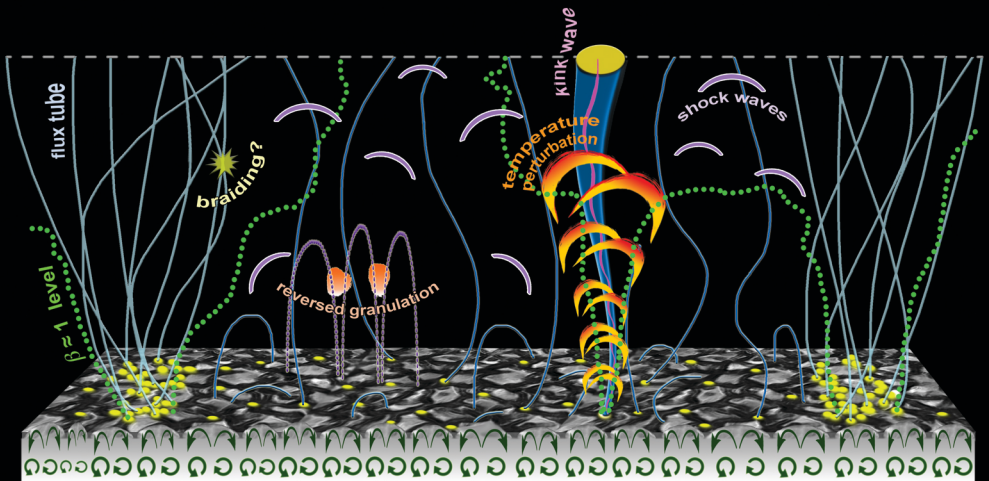


Dynamics of magnetic bright points in the lower solar atmosphere



Shahin Jafarzadeh

International Max Planck Research School
on Physical Processes in the Solar System and Beyond
at the Universities of Braunschweig and Göttingen

Dynamics of magnetic bright points in the lower solar atmosphere

Dissertation
for the award of the degree

“Doctor rerum naturalium” (Dr.rer.nat.)

of the Georg-August-Universität Göttingen

within the doctoral program PROPHYS
of the Georg-August University School of Science (GAUSS)

submitted by

Shahin Jafarzadeh

from Tehran, Iran

Göttingen, 2013

Thesis Committee

Prof. Dr. Sami K. Solanki

Max-Planck-Institut für Sonnensystemforschung, Katlenburg-Lindau, Germany

Prof. Dr. Stefan Dreizler

Institut für Astrophysik, Georg-August-Universität Göttingen, Germany

Dr. Alex Feller

Max-Planck-Institut für Sonnensystemforschung, Katlenburg-Lindau, Germany

Members of the Examination Board

Reviewer: Prof. Dr. Stefan Dreizler

Institut für Astrophysik, Georg-August-Universität Göttingen, Germany

Second Reviewer: Prof. Dr. Sami K. Solanki

Max-Planck-Institut für Sonnensystemforschung, Katlenburg-Lindau, Germany

Additional Reviewer: Prof. Dr. Oskar F. H. von der Lühe

Kiepenheuer-Institut für Sonnenphysik, Albert-Ludwigs-Universität Freiburg, Germany

Further members of the Examination Board:

Prof. Dr. Manfred Schüssler

Max-Planck-Institut für Sonnensystemforschung, Katlenburg-Lindau, Germany

Prof. Dr. Laurent Gizon

Institut für Astrophysik, Georg-August-Universität Göttingen, Germany

Prof. Dr. Wolfgang Glatzel

Institut für Astrophysik, Georg-August-Universität Göttingen, Germany

PD Dr. Dieter Schmitt

Max-Planck-Institut für Sonnensystemforschung, Katlenburg-Lindau, Germany

Date of the oral examination: 03.07.2013

Bibliografische Information der Deutschen Nationalbibliothek

Die Deutsche Nationalbibliothek verzeichnet diese Publikation in der Deutschen Nationalbibliografie; detaillierte bibliografische Daten sind im Internet über <http://dnb.d-nb.de> abrufbar.

ISBN 978-3-942171-75-5

uni-edition GmbH 2013

<http://www.uni-edition.de>

© Shahin Jafarzadeh



This work is distributed under a
Creative Commons Attribution 3.0 License

Printed in Germany

Contents

Summary	9
1 Introduction	11
1.1 The solar atmosphere	12
1.2 Solar magnetism	14
1.2.1 Stokes parameters	16
1.3 Photosphere	16
1.3.1 Granules and mesogranules	18
1.3.2 Reversed granulation	18
1.3.3 Magnetic flux tubes	19
1.3.4 Magnetic bright points	20
1.3.5 Network and internetwork regions	22
1.3.6 Supergranulation	24
1.4 Low chromosphere	24
1.5 Energy transport and heating mechanisms	25
1.5.1 Oscillations and waves	26
1.6 Overview sketch	28
2 Instrumentation and data	31
2.1 SUNRISE balloon-borne solar observatory	31
2.1.1 SuFI	32
2.1.2 IMaX	34
2.2 Formation height	34
2.3 Data preparation	38
2.3.1 Phase-diversity reconstruction	38
2.3.2 Image alignment	40
2.3.3 RMS intensity contrast	42
2.4 Inversions	44
3 Structure and dynamics of isolated internetwork Ca II H bright points	47
3.1 Introduction	48
3.2 Observations and data preparation	49
3.2.1 Ca II H images	51
3.2.2 Stokes measurements	52
3.2.3 Image alignment	52
3.3 Analysis	55

3.3.1	Tracking algorithm	56
3.3.1.1	Image processing	57
3.3.1.2	MBP's location and its trajectory	58
3.3.2	Properties of the MBPs	59
3.3.2.1	Size	59
3.3.2.2	Lifetime	60
3.3.2.3	Intensity	61
3.3.2.4	Horizontal velocity	61
3.3.3	Magnetic field	61
3.3.4	Inversions	62
3.4	Results and discussion	62
3.4.1	A case study: Tracking an individual Ca II H MBP	63
3.4.2	Persistent flasher	66
3.4.3	Statistical studies	68
3.4.3.1	Intensity	70
3.4.3.2	Horizontal velocity	72
3.4.3.3	Size	74
3.4.3.4	Lifetime	76
3.4.3.5	Circular polarisation	77
3.4.3.6	Longitudinal magnetic field	77
3.4.4	A relationship between intensity and horizontal velocity	78
3.5	Kink wave excitation due to high-velocity excursions	79
3.6	Conclusions	83
4	Migration of Ca II H bright points in the internetwork	87
4.1	Introduction	87
4.2	Data	89
4.3	Data analysis and results	90
4.3.1	Trajectories	91
4.3.2	Diffusion processes	91
4.3.2.1	Statistics	94
4.3.2.2	Diffusion coefficients	94
4.4	Modelling	97
4.4.1	Migration scenario	97
4.4.2	Monte Carlo simulation	97
4.5	Discussion and conclusions	101
5	Propagation of high-frequency fast waves in small magnetic elements	107
5.1	Introduction	107
5.2	Observations	110
5.3	Method of analysis and a case study	111
5.3.1	Wavelet transform	113
5.3.2	A case study: Wavelet analysis of a MBP	113
5.4	Statistics and wave identification	117
5.4.1	Comparisons and interpretations	120
5.5	Discussion and conclusions	124

6	Inclinations of small quiet-Sun magnetic features	127
6.1	Introduction	128
6.2	Observational data	129
6.3	Analysis and results	132
6.3.1	Inclination from measurements at two heights	133
6.3.1.1	Sources of uncertainty	135
6.3.2	Inversions	137
6.3.3	Statistics and discussion	141
6.4	Conclusions	146
7	Conclusions and outlook	149
	Bibliography	153
	Acknowledgements	181

Summary

In this thesis we have investigated the structure and dynamics of small-scale magnetic bright points (MBPs) in quiet, internetwork regions of the lower solar atmosphere. Such MBPs are associated with small-scale, intense (generally kG) magnetic elements.

The internetwork (IN) areas cover the largest fraction of the solar surface and it has been argued that the IN may contain most of the existing unsigned magnetic flux on the surface at any given time. However, the distribution of the magnetic field's properties in the IN regions is still being debated. Thus, only recently has the presence of kG fields in the IN been confirmed of which the studied MBPs are thought to be manifestations. In addition, interaction between intense magnetic features and convective flows on the solar surface (in particular in IN areas) have been proposed to excite waves which can carry energy to the upper solar atmosphere. The properties of these waves and their contribution to the heating of the upper solar atmosphere is still unclear. Moreover, the migration of the small magnetic elements owing to the convective flows/turbulence is not known (due to, e.g., lack of high spatial and temporal resolution observations not affected by seeing).

We used high spatial and temporal resolution observations, obtained by the SUNRISE balloon-borne solar observatory, to address the above issues. We concentrate on the study of the smallest MBPs visible in the data; whose apparent lack of internal fine-structure facilitates their precise location and tracking in time-series of images. The analyses were performed using an algorithm we developed to identify, locate and track the MBPs as well as to determine their physical properties at any given time.

Within this context, we have made an original contribution to knowledge in four areas:

- In Chapter 3 “Structure and dynamics of isolated internetwork Ca II H bright points”, we have presented the observational properties (i.e., horizontal velocity, diameter, intensity, magnetic field strength and lifetime) of highly dynamic MBPs observed in the SUNRISE Ca II H passband of the SUNRISE Filter Imager (SuFI). Our analysis revealed that the horizontal velocity and the brightness of the MBPs are anti-correlated. Furthermore, we found large excursions (pulses; sometimes supersonic) in the proper motions of the MBPs which may excite kink waves that travel into the upper solar atmosphere. We showed that these waves are marginally energetic enough to contribute to the heating of the quiet corona.
- In Chapter 4 “Migration of Ca II H bright points in the internetwork”, we have studied the trajectories of the horizontal motion of the Ca II H MBPs in both observations and Monte Carlo simulations. We found that the MBPs, whilst migrating over a small part of a supergranule, display mostly super-diffusive trajectories. Their horizontal motion can be described as a random walker (due to turbulence in intergranular lanes and granular evolution) superposed on a systematic velocity (caused

by granular, meso-, and super-granular flows). Our analysis revealed that the diffusion coefficients of the MBPs' motions lie within the range obtained from the decay rates of the magnetic field on the solar surface in MHD simulations.

- In Chapter 5 “Propagation of high-frequency fast waves in small magnetic elements”, we have exposed the upward propagation of high-frequency (up to 30 mHz), fast waves in the lower solar atmosphere. We detected both fast compressible and fast kink waves by employing a wavelet analysis on perturbations in intensity and horizontal displacement of selected MBPs, respectively, sampled in two atmospheric heights. In addition, we found an increase in the intensity amplitudes and a decrease in amplitudes of the horizontal velocities with height. The latter probably implies that most of the kink waves that may have been excited by the pulses found in Chapter 3 do not reach the corona, but dissipate their energy in the lower layers, or are converted to another wave mode. By comparing our results with those from simulations in the literature, we have discussed the possible causes of observing the fast waves. Mode conversion at the level of plasma beta unity (where the sound and Alfvén speeds coincide) as well as the propagation path of the fast magnetic modes can explain best the measured fast sausage modes. The fast compressible waves do not reach the upper solar atmosphere due to the steep gradient in the Alfvén speed with height.
- In Chapter 6 “Inclinations of small quiet-Sun magnetic features”, we have explored the distribution of the inclinations of the magnetic field in selected small magnetic elements. In this work, we introduced a new approach to determine the inclination angle of small-scale magnetic features which offers, for the first time, an opportunity for computing this parameter independently of Stokes profile measurement, that can be adversely affected by noise in the quiet Sun. We found that the nearly vertical magnetic field of MBPs returned by our geometric method is (clearly) incompatible with the predominantly horizontal magnetic fields, computed from inversions of simultaneously recorded Stokes parameters (i.e., the traditional method).

These findings have implications for, e.g., our understanding of the heating mechanisms in the higher layers of the solar atmosphere, estimates of the solar magnetic flux as well as the structure of the convection flows (within a supergranule) advecting small magnetic elements.

We have summarised the final conclusions in Chapter 7, where the potential further investigations have also been indicated.

1 Introduction

Despite the successes that have been achieved so far in our understanding of various solar phenomena, there have remained further challenges, including the distribution of magnetic fields in the quiet-Sun (Borrero and Kobel 2011, 2012), dynamics and structure of small-scale magnetic features in the lower solar atmosphere (e.g., Solanki 1993; de Wijn et al. 2009) and their contribution to the heating of the upper atmospheric layers (due to, e.g., wave excitations as a result of their jerky motions; Choudhuri et al. 1993b; Hasan and van Ballegoijen 2008); as a few examples of not well understood phenomena, among many others.

Among the variety of magnetic features (with different spatial and temporal scales), the small-scale (point-like) magnetic elements are an excellent diagnostic of horizontal dynamics; since their locations can be determined more reliably compared to larger features possessing internal fine structures. In addition, the small-scale magnetic elements have been shown to strongly influence many other solar phenomena (from small to large scales; Solanki and Schüssler 2004) and have been introduced as a key for solving the mysteries of outer atmospheric heating mechanisms (Trujillo Bueno et al. 2004). These features can be best studied in high spatial and temporal resolution observations (since they are small and highly dynamic), not affected by seeing (distortion effects introduced by the Earth's atmosphere).

In order to obtain a better understanding of the solar magnetisms' structure as well as the heating mechanisms in the upper solar atmosphere, we investigate the structure and dynamics of small magnetic elements in the lower solar atmosphere by analysing high-resolution seeing-free data from SUNRISE balloon-borne solar observatory. The migration of such small magnetic elements can be well tracked in intensity images; since their point-like brightenings do not display significant complex sub-structure in high resolution observations. Such investigations lead us to a better understanding of their migration mechanisms and their contribution in the heating of the upper atmospheric layers. Further, we investigate the distribution of magnetic field in such small magnetic elements in a quiet-Sun region.

In this thesis, we first review (in the present chapter) basic concepts and introduce the solar regions and features on which our studies have concentrated. The data, instruments and analysing methods are explained in Chapter 2. Chapters 3-6 represent our studies of bright, point-like magnetic elements in respect with their structure and dynamics, wave propagation, distribution of magnetic fields, and diffusivity behaviours, respectively. In Chapter 7 we draw our conclusions and summarise what we have learnt from our studies, complemented by an outlook on promising future research.

1.1 The solar atmosphere

The energy that is produced in the Sun's core (by $H \rightarrow He$ fusion) travels to the solar surface by means of radiation (in the innermost 70% of the solar radius) and convection (in the outer 30%; e.g., Stix 2002). The outermost layer of the convective zone is populated by granules, the relatively small convective cells (area of $\approx 10^{4.8} - 10^{6.8}$ km²; Hirzberger et al. 1997). Granules are examples of overturning convection cells, i.e., hot plasma rises to the solar surface at their centres, cools down and sinks back on the sides (e.g., Nordlund et al. 2009). While the vertical velocity of these convective flows decreases rapidly with height, the gas within them moves horizontally with a speed of few kilometres per seconds; sometimes exceeding the local sound speed of $7 - 8$ km s⁻¹ (Solanki et al. 1996a; Bellot Rubio 2009). The intergranular regions, where the cool plasma plunges back down into the solar interior, are relatively darker narrow lanes compared to the brighter (hotter) neighbouring granules.

The solar surface is often defined as the layer whose continuum optical depth, τ , at 5000 Å, is unity, i.e. $\log\tau_{5000} = 0$. Note that the optical depth is a wavelength-dependent function. Geometrical heights are often determined with respect to a layer corresponding to $\log\tau_{5000} = 0$ averaged over quiet-Sun regions. The optical depth depends on atmospheric parameters such as temperature, density, electron pressure and is usually non-uniform over the solar surface (Nelson 1978; Nordlund et al. 2009). The magnetic field also influences it significantly through its influence on the other listed atmospheric parameters.

Above the solar surface, the solar atmosphere is traditionally divided into three or four distinct layers based on their physical properties: photosphere, chromosphere, transition region and corona. The traditional description of the solar atmosphere, very approximately, defines variation of the physical properties of the atmospheric layers based on somewhat averaged physical parameters from (simplified) plane-parallel models. In the actual Sun, the physical conditions in each layer of the atmosphere (more importantly, in the chromosphere and corona) largely differ over different regions based on, e.g., the strength and configuration of the magnetic field (Withbroe and Noyes 1977) and hence, they are very different from such simple traditional pictures that are, for the sake of simplicity, reviewed in the following paragraph.

According to such time-independent plane-parallel models (e.g., Vernazza et al. 1981; Fontenla et al. 1993), the total density of atoms, molecules and ions as well as the total gas pressure decrease roughly exponentially with height. The temperature, that decreases from $\approx 16 \times 10^6$ K at the Sun's core to about 6000 K (on average) at the solar surface displays, however, a different behaviour. It first continues decreasing down to ≈ 4000 K at ≈ 500 km above the solar surface. This is the minimum temperature in the Sun, the so-called "temperature minimum", at least in averaged plane-parallel models, and is the upper boundary of the first atmospheric layer, i.e., the photosphere, where the bulk of the radiative energy flux (mostly corresponding to the visible frequency range) that leaves the Sun is emitted. Note that the minimum temperature may also reach down to values below 3000 K in extreme situations (Leenaarts et al. 2011). In a 1-D picture, above the temperature minimum, the temperature increases through the whole atmosphere, first relatively slowly (within the low- and mid-chromosphere) but then steeper in higher layers (within the upper chromosphere and transition region), reaching to the extremely hot (≈ 1 MK)

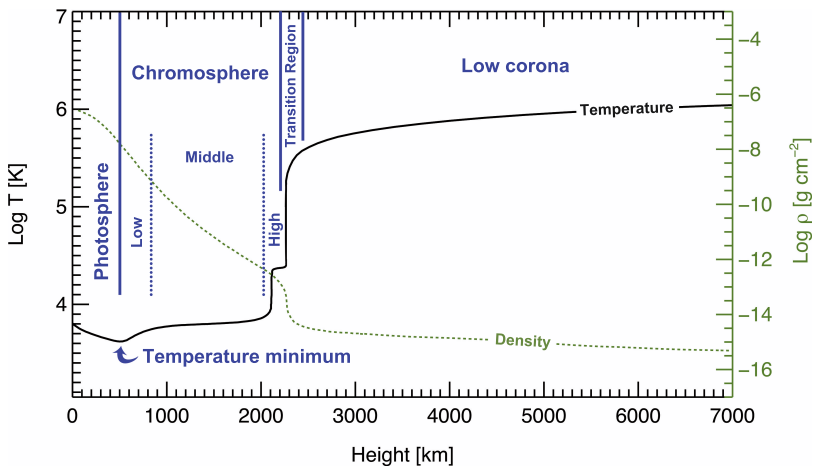


Figure 1.1: One dimensional stratification of temperature (black, solid curve) and density (green, dashed line) in the solar atmosphere. The approximate geometrical heights of the main distinct layers of the solar atmosphere (with respect to $\log\tau_{5000} = 0$) are labelled. The temperature and density profiles are taken from Reeves et al. (1977), Vernazza et al. (1981) and Avrett and Loeser (1992).

and transparent corona. Figure 1.1 shows a one-dimensional temperature stratification in the solar atmosphere along with the density profile (from simple plane-parallel models), labelled with the four layers: photosphere, chromosphere, transition region and low corona. The temperature profiles for the photosphere and the chromosphere were taken from Vernazza et al. (1981) and for the low corona from Reeves et al. (1977). The density profiles, extrapolated to the higher layers, are borrowed from Avrett and Loeser (1992). We remind the reader again that these 1D profiles have been obtained from fitting relatively low resolution lines and continua, mainly in the UV, and moreover, may only be valid for the averaged quantities. These profiles are much more complex for the actual, extremely dynamic Sun whose atmosphere is far from homogeneous; and it is not clear if any part of the Sun actually has a temperature profile following these low-resolution models. Moreover, the boundaries between the different layers are not sharp and cannot be well defined (Solanki and Hammer 2002). In fact, height structures of the solar atmosphere obtained from observations are inconsistent with such models and strongly depend on the magnetic field configuration in different solar regions (e.g., Zhang et al. 1998). The structure of the Sun from the core to the low corona is schematically illustrated in Fig. 1.2.

Different heating mechanisms have been proposed for the extraordinary high temperature of the upper solar atmosphere (see Sect. 1.5).

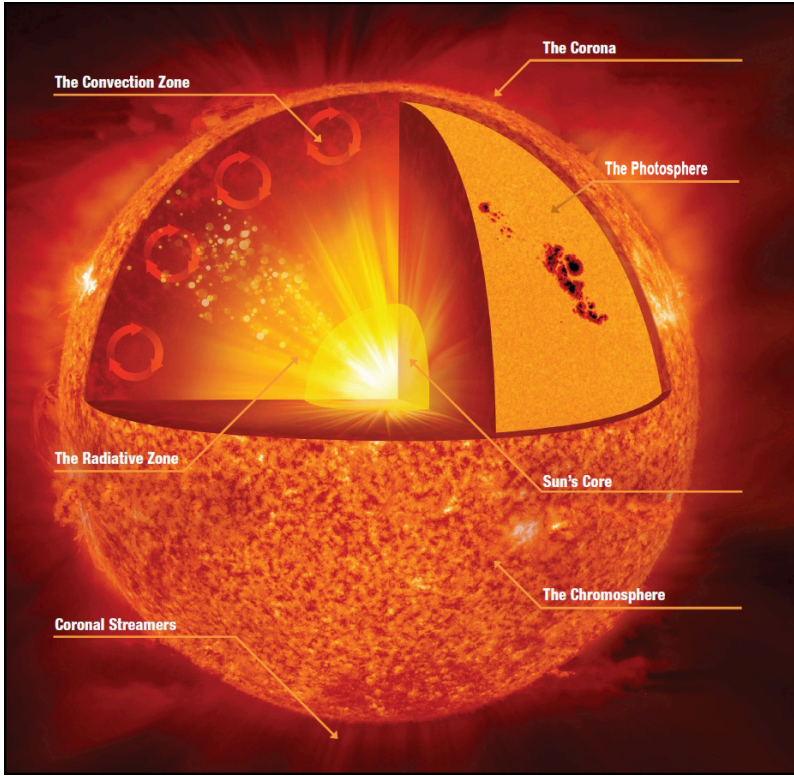


Figure 1.2: Sun's structure. The distinct internal and atmospheric layers are labelled (see main text). Image courtesy of NASA/Jenny Mottar (adapted).

1.2 Solar magnetism

Solar magnetism is considered to be the key for answering many secrets in solar physics, including the upper atmospheric heating (de Wijn 2012). The solar magnetic field is believed to be generated at the bottom of the convection zone through the solar cycle dynamo (see, e.g., reviews by Choudhuri 2003; Charbonneau 2005). The magnetic field lines then rise through the convection zone due to buoyancy and finally emerge through the solar surface (Moreno-Inertis 1986; Schüssler et al. 1994; Caligari et al. 1995). They manifest themselves in the photosphere on all spatial scales (e.g., Stenflo 1989; Solanki 1993, 2001), from smaller than the currently achieved highest spatial-resolution to the largest manifestations covering an entire hemisphere (de Wijn et al. 2009). For a review on the solar magnetic field from the bottom of the convection zone through the whole atmosphere we refer to Solanki et al. (2006); and to a more recent review by Fan (2009)

for the magnetic field in the convection zone.

The strength of the line-of-sight component of the magnetic field in the photosphere has been measured over decades (e.g., Babcock and Babcock 1952; Solanki 2009), from its first observations by Hale (1908) in sunspots (i.e., relatively dark regions of strong magnetic field on the solar surface). Such measurements have been often based on the so-called Zeeman effect as a result of interaction between the magnetic field and atoms in the solar atmosphere; leading to splitting of atomic energy levels, and hence, splitting of the observed absorption/emission spectral lines (Zeeman 1897). Besides the magnetic field strength, the full magnetic vector (i.e., (1) the field strength B , (2) the inclination angle, the angle with respect to the solar surface normal, γ , and (3) the azimuth angle in the plane of the solar surface, ϕ) can be reconstructed from observations of intensity through a magnetically sensitive passband in different polarisation states, i.e., Stokes parameters (Wittmann 1974; Auer et al. 1977; see also, e.g., Borrero et al. 2011).

Alternatively, the magnetic field can be measured using the so-called Hanle effect that is based on the polarisation variation of light in a weak magnetic field (i.e., when the emitted light depends on the atoms subject to the magnetic field with a particular direction; Hanle 1924). Unlike the Zeeman effect, the Hanle effect is sensitive to the collisional de-excitation of the excited atoms (e.g., Trujillo Bueno 2001). Hanle effect provides a better tool for measuring weak magnetic fields whose Zeeman splitting is too small compared to the Doppler width of the spectral line (Solanki 1993).

The magnetic field extended to the upper solar atmosphere can be measured by, e.g., Zeeman and/or Hanle effect in the chromospheric or the coronal spectral lines (Solanki et al. 2003; Lagg et al. 2004; Tomczyk et al. 2004; Lin et al. 2004), however, the much weaker magnetic field and much lower signal-to-noise ratio in the outer atmospheric layers compared to the photosphere make the direct measurements of the magnetic field in the corona difficult (Lin et al. 2000). Other approaches for measuring the coronal magnetic field have also been employed based on, e.g., solar radio observations (White 2002). The magnetic field in the chromosphere can be better determined in regions with stronger fields (e.g., Eibe et al. 2002; Centeno et al. 2010; Harvey 2012). Alternatively, the magnetic field can be extrapolated through the whole atmosphere from photospheric magnetograms using potential or force-free fields (Wiegelmann et al. 2005, and references therein; see also a recent review by Wiegelmann and Sakurai 2012).

The solar magnetic field exhibits a cyclic behaviour, such that, the number of large magnetic features on the solar surface, such as sunspots and pores, (which are often considered as proxies of the magnetic activity level of the Sun) varies in a period of 11 years on average (e.g., Hathaway 2010; Solanki and Krivova 2011). However, there are exceptions to such cyclic variations such as the Maunder minimum (when no sunspot appeared on the solar surface for nearly 70 years; Eddy 1976) as well as secular changes occurring in much larger periods (e.g., Lockwood et al. 1999; Solanki et al. 2000; Ogurtsov et al. 2002; Usoskin and Kovaltsov 2004). Note that even in periods with no appearance of large-scale magnetic features (often referred to as minimum solar activity), the Sun is very far from a static state and the magnetic concentrations are distributed over the whole solar atmosphere. For details on the long-term behaviour of the solar activity see a recent review by Usoskin (2013).

1.2.1 Stokes parameters

Polarised light is described by four Stokes parameters denoted by I , Q , U and V (Unno 1956; Stenflo 1971). Stokes I denotes the total intensity of the light. Therefore, in the mathematical description, Stokes I has always a positive or zero value (zero when there is no light). The other three Stokes parameters, i.e., Stokes Q , U and V , represent different states of the light's polarisation (Q and U denotes different linear polarisations; V refers to circular polarisation), such that,

$$\begin{aligned} Q &= I_{\text{linear}}(\chi = 0) - I_{\text{linear}}(\chi = \pi/2), \\ U &= I_{\text{linear}}(\chi = \pi/4) - I_{\text{linear}}(\chi = 3\pi/4), \\ V &= I_{\text{circular}}(\text{right}) - I_{\text{circular}}(\text{left}), \end{aligned} \quad (1.1)$$

where I_{circular} is the circularly polarised light and χ is the angle between the electric vector of the linearly polarised radiation (I_{linear}) and a reference direction (e.g., Solanki 1993). The integration of squares of Stokes Q , U and V is always equal to, or less than the square of the Stokes I , corresponding to totally or partially polarised light, respectively (del Toro Iniesta 2003):

$$\frac{Q^2}{I^2} + \frac{U^2}{I^2} + \frac{V^2}{I^2} \leq 1. \quad (1.2)$$

Equation 1.2 specifies a sphere (so-called Poincaré sphere; with unity radius) whose every single point (in or on the sphere), described by a Stokes vector, represents a polarised state of light. Such a sphere is depicted in Fig. 1.3a, adapted from del Toro Iniesta (2003). If this figure represents the Stokes vector at the Sun's disc-centre, the axis of Stokes V , that is perpendicular to the QU plane (a plane parallel to the solar surface), points to the observer. The arrows reaching to the sphere's surface (blue) and ending in a point inside the sphere (green) represent sample Stokes vectors corresponding to fully and partially polarised light, respectively.

Note that Stokes V is sensitive to the direction of the magnetic flux and can represent two opposite polarities corresponding to the flux pointing towards or away from the observer. Hence, if on sufficiently small spatial scales (i.e., smaller than spatial resolution of observations) the opposite polarities are mixed, the Stokes V signals are cancelled.

Comparison of the Fig. 1.3a and the magnetic field vector drawn in Fig. 1.3b shows the relationship between the magnetic vector and the Stokes parameters at solar disc centre: Stokes V (the circular polarisation) corresponds to the magnitude of the longitudinal (vertical) component of the magnetic field, while Stokes Q and U together (i.e., the linear polarisation) correspond to its transversal (horizontal) components. Values of these three Stokes parameters specify the inclination angle γ as well as the azimuth angle ϕ ; but with 180° ambiguity for the ϕ (Auer et al. 1977). Note that these pictures are highly qualitative, e.g., the relationship between Stokes Q , Stokes U and longitudinal component of the magnetic field is more complex than above description.

1.3 Photosphere

The solar photosphere is a highly dynamic environment where motions with a wide range of spatial and temporal scales are observed (Spruit et al. 1990). This layer of the atmosphere consists of both low and high plasma- β media, where either the magnetic or the gas

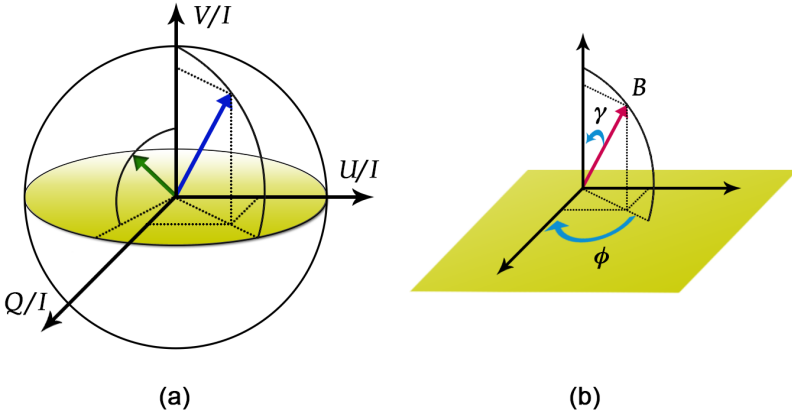


Figure 1.3: a) Polarisation vector on (blue arrow) and within (green arrow) the Poincaré sphere (see main text). Adapted from del Toro Iniesta (2003). b) Vector magnetic field, represented by its components the field strength (B), inclination (γ) and azimuth angle (ϕ).

pressure is dominant ($\beta = P_{gas}/P_{magnetic} \approx 8\pi P_{gas}/B^2$; Rosenthal et al. 2002; Nordlund 2003). Regions with $\beta \approx 1$ are of particular interest since the acoustic and Alfvén speeds coincide at these levels (Bogdan et al. 2003; Cally 2007). We will later (in Chapter 4) discuss the importance of such regions that influence characteristics of wave propagations in the solar atmosphere.

The magnetic field is most reliably measured in the photosphere (i.e., inferred from measurements of the Stokes parameters), where observations of magnetically sensitive lines such as Fe I 5250 Å can reveal the polarisation signals through the Zeeman and Hanle effects. These polarisation signals result in origin and physical properties of many magnetic features in the solar photosphere. However, it has been shown that higher-resolution observations as well as newer analysis techniques have resulted not only in more detailed information but also in often (unexpectedly) different properties (Solanki 2009).

Depends on the required accuracy, either Local Thermodynamic Equilibrium (LTE) or non-LTE can approximate the photosphere, where the densities are large (compared to the higher atmospheric layers) and temperature slowly decreases with height. LTE obviously represents an approximate thermodynamic (thermal, mechanical, chemical and radiative) equilibrium in a small region about any point in the photosphere where changes in parameters, such as temperature, are slow (e.g., Mihalas 1978). In LTE conditions, only radiation (not matter) can deviate from the thermodynamic equilibrium situations. Media with larger densities are better approximated by the LTE conditions (del Toro Iniesta 2003), hence, it is expected that in regions (in the solar atmosphere) close to the temperature minimum and beyond, the LTE assumption will break down (i.e., non-LTE). Note that the departure from LTE does not have a sharp boundary in the solar atmosphere and depends on, e.g., the choice of model atmosphere (Solanki 1998). These conditions

should be kept in mind when the physical parameters in the solar photosphere and above are determined.

1.3.1 Granules and mesogranules

Granules are the topmost part of the convection cells protruding into the photosphere; first observed by Herschel (1801). Their appearances and disappearances are either instantaneous (appearance when rising hot plasma reaches the surface; disappearance when the cool cell completely sinks back below the surface) or as results of other granulations' merging/fragmentations (Nordlund et al. 2009, and references therein). Such hot rising and cool sinking plasmas in the granular and intergranular areas, respectively, result in a large intensity contrast at the solar surface, normally described by the root-mean-square (rms) of the intensity fluctuations, ΔI_{rms} (e.g. Roudier and Muller 1986; Sánchez Cuberes et al. 2000; Danilovic et al. 2008; Abramenko et al. 2012) and are referred to as the granulation contrast (Danilovic et al. 2008):

$$\Delta I_{rms} = \sqrt{\frac{\sum (I - I_{mean})^2}{N I_{mean}^2}}, \quad (1.3)$$

where I_{mean} represents the mean intensity of the image and N is the number of data points with intensity values I . The sum is taken over all data points of the image.

Figure 1.4 shows the granulation patterns at high-spatial resolution observed in an internetwork region (i.e., a region with relatively small magnetic concentrations; see Sect. 1.3.5) of the quiet-Sun disc-centre by the Swedish Solar Telescope (SST; Scharmer et al. 2003). It is seen that the granules have different sizes with irregular shapes; and from a single frame it is not clear whether they present any conspicuous organisation even at larger scales. However, a closer inspection of their evolution has revealed larger structures of about 7000 km in diameter representing reproductive sequences. In such a sequence, some of the the granules (in internetwork areas) first expand, then fragment and expansion of the fragmented cells and fragmentation of the fragmented cells continue for some time. These structures are termed mesogranules (November et al. 1981; Straus et al. 1992). Another convective structure (similar to granulation) on much larger scales, the so-called supergranulation, will be described in Sect. 1.3.6.

1.3.2 Reversed granulation

In the upper photosphere, roughly at heights above 100 – 200 km, the granulation brightness is reversed with height (e.g., Rutten et al. 2004). The cooling of up-flowing gas above the granules (due to its expansion) as well as the radiative heating of sideways flowing gas above the intergranular lanes (causing a temperature increase towards the radiative equilibrium temperature; Cheung et al. 2007) result in the intensity enhancements above the lanes, so-called “reversed granulation” (Nordlund 1984; Leenaarts and Wedemeyer-Böhm 2005). Right panel of Fig. 1.5 shows an example of this effect in simulations from Cheung et al. (2007) in a height corresponding to $\tau_{5000} = 0.1$. The granulation pattern corresponding to the same area but sampled at the solar surface (at $\tau_{5000} = 1$) is shown in the left panel.

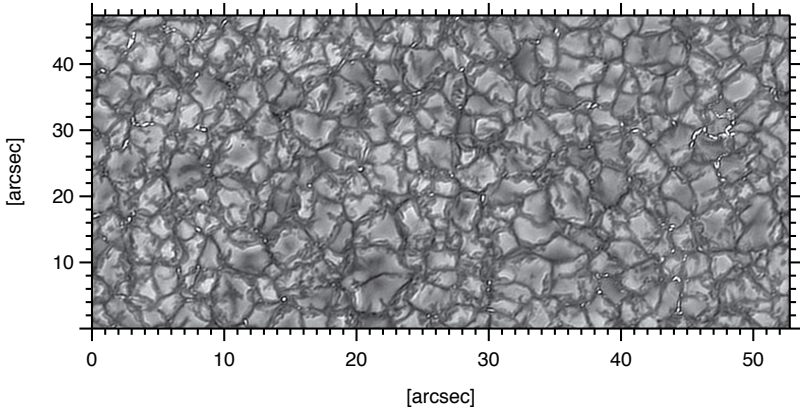


Figure 1.4: Granular pattern observed in Ca II H wide-band of the Swedish Solar Telescope. Image courtesy of Johann Hirzberger.

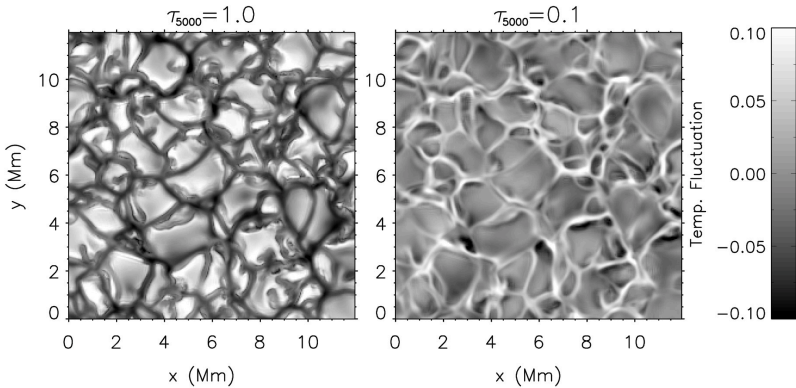


Figure 1.5: Reversed granulation effect (right) sampled a few hundred kilometres higher in the solar atmosphere than the granulation pattern (left). Simulations from Cheung et al. (2007).

1.3.3 Magnetic flux tubes

The magnetic field in the solar photosphere is inhomogeneous and is found in discrete concentrations at all spatial scales (Zwaan 1987). At small-scales, the concentrations of intense magnetic fields are mostly found in intergranular regions where strong down-flows occur. Such strong field concentrations are best described by the flux tube theory (Spruit 1976, 1977, 1981b; Solanki et al. 1996b). Their formation can be modelled as a sequence of steps (e.g., Schüssler 1990): (1) Magnetic field lines are first advected by the horizontal

convective flows towards the intergranular lanes. (2) A convective down-flow occur along the field lines (convective collapse) and the gas within the magnetic feature cools by radiation, thus leading to a reduction in the gas pressure within the atmospheric layers of the magnetic feature. (3) The bundles of magnetic field lines is then compressed by the larger gas pressure in the surroundings, so that the field in the bundle is strengthened. Hence, the pressure exerted by the sufficiently strong field suppresses the convection within the magnetic concentration. (4) This increases the magnetic pressure inside the bundle of field lines, so that the total pressure is finally in balance with the surroundings again. Therefore, the magnetic field lines are clumped into tight (nearly parallel) bundles forming the flux tubes in the narrow intergranular regions. Figure 1.6 illustrates, very schematically, the flux tube's formation sequence along a vertical cut.

By definition, a (cylindrical) flux tube, extending into the solar atmosphere, is considered thin when its radius (R) at each atmospheric layer is smaller than the local pressure scale height, H_p (Defouw 1976). Pressure and magnetic field strength are (approximately) homogeneous across a thin flux tube's cross-section. See, e.g., Yelles Chaouche et al. (2009) who showed that an extended thin tube model (Pneuman et al. 1986; Ferriz-Mas and Schüssler 1989) reproduces concentrated magnetic features in MHD simulations rather well.

In pressure equilibrium between inside and outside the flux tube,

$$p_{out} = p_{in} + \frac{B^2}{8\pi}, \quad (1.4)$$

where p_{out} and p_{in} are the gas pressures outside and inside the flux tube respectively. The second term on the right-hand side of the Eq. 1.4 represents the magnetic pressure inside the tube. The magnetic field outside the flux tube is considered to be zero. By assuming a constant temperature inside and outside the tube at each atmospheric layer and in hydrostatic equilibrium (for an isothermal atmosphere) the gas pressure p , and hence magnetic field strength B , decrease exponentially with height, z ($p = p_0 e^{-z/H_p}$ and $B = B_0 e^{-z/2H_p}$; p_0 and B_0 represent the pressure and field strength at $z = 0$). If the magnetic flux is constant with height (i.e., magnetic flux conservation; $BA = \text{constant}$ for a thin flux tube with an area A at each atmospheric level), the exponential decrease of B with height results in an exponential increase of the area ($A = A_0 e^{z/2H_p}$), i.e., the flux tubes expand with height.

Using the flux tube model of Solanki (1986), an expansion rate of ≈ 3 is approximated for a height of about 500 km from the solar surface (i.e., the temperature minimum). Note that the relative expansion rates of large and small flux tubes are similar (Solanki et al. 1999).

Note that in addition to the flux tubes, there are also magnetic fields represented by low-lying loops (e.g., Martínez González et al. 2007; Ishikawa et al. 2008; Ishikawa and Tsuneta 2009; Martínez González and Bellot Rubio 2009; Danilovic et al. 2010a) and turbulent field (e.g., Pietarila Graham et al. 2009).

1.3.4 Magnetic bright points

Magnetic bright points (MBPs) represent small-scale magnetic elements, i.e., cross-sections of thin flux tubes (Dunn and Zirker 1973; Mehlretter 1974; Solanki 1993). They are good

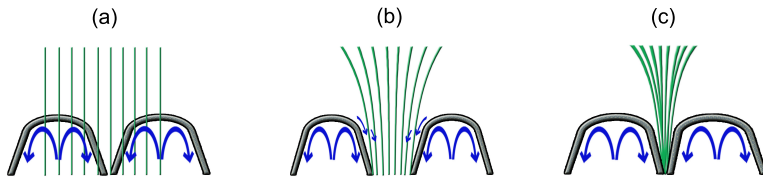


Figure 1.6: Formation sequence of a thin flux tube as seen in a vertical cut: (a) advection of magnetic field lines by granular convective flows, (b) convective collapse within the magnetic concentration, and (c) compression of the bundles of the magnetic field lines and field intensification. The vertical lines represent magnetic field lines. The convection cells along with their motions are shown in the background.

tracers of magnetic elements in intensity images.

The MBPs appear bright since the evacuation inside the flux tube (due to the increase in magnetic pressure; see Sect. 1.3.3) lowers the optical depth inside the tube (Wilson depression) and hence, the hotter gas inside the tube (compared to the external gas at equal optical depth; heated by radiation from the walls of the tube, sampled in deeper geometrical heights) radiates excess energy, compared to the surroundings intergranular areas (Spruit 1976). The walls at deeper optical depth are hot since the temperature increases rapidly with depth below the solar surface. For $\tau \gg 1$, the density of energy flux inside the flux tube, F_i , is much smaller than that in the surroundings, F_e (energy transfer carried by convection is very small inside the tube). Therefore, radiation from the part of the hot walls of the tube above the Wilson depression is the main means of outwards energy transfer. Unlike the top ($\tau \lesssim 1$) hot walls of the tube that is transparent to the radiation, the bottom part of the flux tube (where $\tau \gg 1$) is thermally insulated from hot convective flows of deeper layers (Schrijver and Zwaan 2000; cf. Deinzer et al. 1984a,b; Vögler et al. 2005). Depicted in Fig. 1.7 is a (not to scale) sketch showing this brightness enhancement's concept, inspired from a similar sketch by Schrijver and Zwaan (2000).

Note that only concentrated kG fields can produce sufficiently deep Wilson depressions to allow sufficient excess radiation to enter the magnetic feature resulting in a visible brightening of a MBP (Rutten et al. 2001; Vögler et al. 2005; Riethmüller 2013; Riethmüller et al. 2013).

The bright points (BPs), by definition, should refer to bright point-like elements (depends on spatial resolution of observations). However, not all referenced BPs in the literature are actual point-like features nor do they correspond to magnetic elements (e.g., Steffens et al. 1996; Carlsson and Stein 1997; Wellstein et al. 1998; Muller et al. 2000; Crockett et al. 2010). Instead, they often refer to small-scale (not necessarily point-like) brightenings (magnetic or non-magnetic), sometimes with a non-uniform intensity distribution. The latter effect biases precise locations of the BPs based on, e.g., centre-of-gravity of intensity, which is crucial when the dynamics and motions are to be measured. In the following, we will refer only to small (actual point-like) magnetic features that are seen in intensity images as bright points (MBPs; diameters smaller than 0.3 arcsec).

Chapter 3 of this thesis presents an extensive study of the structure and dynamics of these

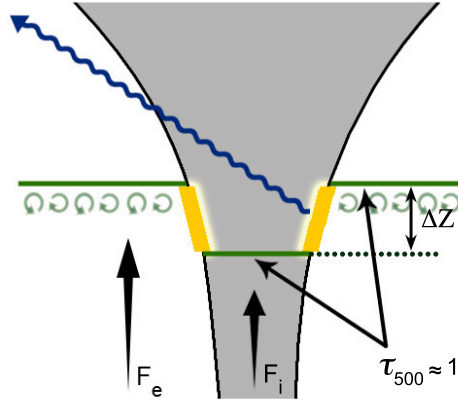


Figure 1.7: Sketch of a thin flux tube (shaded, gray) radiating from hot walls (shining, yellow blocks). The Wilson depression, ΔZ , is shown as geometrical difference between the same level of optical depth ($\tau_{5000} \approx 1$) inside and outside of the flux tube (see text). Small green arrows illustrate the convection. The cartoon is not to scale. Inspired by Schrijver and Zwaan (2000).

MBPs.

1.3.5 Network and internetwork regions

While large magnetic features such as sunspots, pores and plages represent the active Sun in the photosphere, the magnetic field in the quiet-Sun is categorised into two groups, each associated with an area on the Sun: network and internetwork (e.g., de Wijn et al. 2009; Solanki 2009). The network corresponds to regions where concentrated strong fields form groups of small-scale magnetic elements (Stenflo 1973). These regions normally represent several MBPs in intensity images concentrated in a relatively small areas. The relatively large areas between the network patches are so-called internetwork regions (Livingston and Harvey 1971, 1975).

For a long time, the internetwork areas were thought to be only associated with very weak magnetic fields (Livingston and Harvey 1971; Zirin 1985, 1993; cf. Kholenko et al. 2003; Sánchez Almeida 2003). Only in recent years, high-spatial resolution observations of the internetwork regions, have suggested existence of strong (kG) magnetic elements in these areas (e.g., Lagg et al. 2010). However, the distribution of the magnetic fields from the recent-years observations of the internetwork areas have been mostly interpreted as horizontal field (e.g., Lites et al. 2008; Orozco Suárez et al. 2007; Ishikawa and Tsuneta 2009; Orozco Suárez and Bellot Rubio 2012; Bellot Rubio and Orozco Suárez 2012); meaning so much horizontal flux in internetwork areas. Conversely, it has been argued in the literature that the magnetic field in the internetwork is strongly vertical than suggested

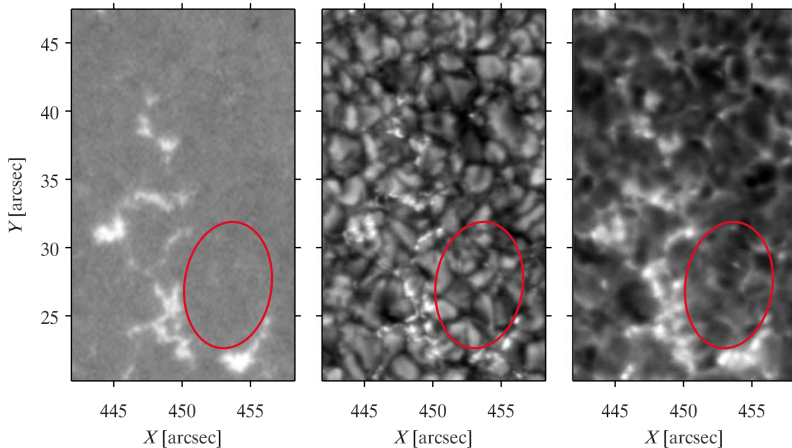


Figure 1.8: Example of network areas (bright patches) and an internetwork region (bordering on the network; indicated by the red ellipses) shown in Fe I 6302 Å line-of-sight magnetogram (left), *G*-band filter (middle) and Ca II H passband (right); observed by Hinode/SOT. Adapted from de Wijn et al. (2009).

by the above studies. Such results are based on Monte Carlo simulations (making use of MHD simulations; Borrero and Kobel 2011, 2012).

Considering that the internetwork covers most of the solar surface, it may contain most of the existing unsigned magnetic flux at any given time on the surface (Sánchez Almeida 2004). Using 3D simulations, Trujillo Bueno et al. (2004) claimed discovery of hidden magnetic fields in internetwork areas whose total magnetic energy was found to be larger than that found in network regions. Hence, the correct estimation of the magnetic field distribution in these areas is crucial and has implications for, e.g., chromospheric and coronal heating (see Sect. 1.5).

Figure 1.8 shows a small region of the quiet-Sun disc-centre in *G*-band (middle), sampling the photosphere, and Hinode Ca II H bandpass (right), sampling few hundreds of kilometres higher in the atmosphere. The line-of-sight magnetogram (representing the longitudinal component of the magnetic field) of the same field-of-view is shown in the leftmost panel. The network of magnetic concentrations, seen as enhanced patches in the magnetograms, represent the network areas. These regions are also observed in the *G*-band and Ca II H images as enhanced brightness areas. Note that such brightenings are more diffuse in Ca II H filtergrams compared to the *G*-band, since the former wavelength samples higher up in the atmosphere (roughly corresponding to the temperature minimum) where the magnetic flux tubes are larger; due to the expansion with height. Part of an internetwork area bordering the network patches is indicated by the red ellipses in all panels of Fig. 1.8.

In Chapter 5 we will investigate the discrepancy between traditionally measured magnetic fields from inversion methods (i.e., where the parameters are obtained by modifying

a model atmosphere until the synthesised and observed data agree; see Sect. 2.4 for a detailed description) and the results of the simulations. We will propose a new, reliable, approach to determine the orientation of selected magnetic flux tubes with respect to an axis perpendicular to the solar surface, so-called inclination angle, and show how they are incompatible with the results of inversions. This study reveals how the horizontal magnetic flux (at the position of selected MBPs) could be overestimated when the traditional inversion methods were used in internetwork areas.

1.3.6 Supergranulation

A very similar structure to that of granules but on much larger scales (size of $\approx 1.5 - 3 \times 10^4$ km) is observed on the whole solar surface (Leighton et al. 1962; Schrijver et al. 1997; Hathaway et al. 2000). These structures (patterns), named supergranulation cells (SG), consist of many granules (and several mesogranules) and are located at the same locations as the internetwork regions. The red ellipse in Fig. 1.8 is likely part of a typical supergranule (internetwork) surrounded by network patches.

Similar to the granules (and the mesogranules), the SGs are interpreted as convective features (e.g., Schrijver et al. 1997; Rast 2003; but also see Gizon et al. 2003 and Schou 2003, who presented a wave-based interpretation). The convective flows have been found to be horizontally move from their centres towards the supergranules' boundaries (i.e., network areas) with horizontal speeds of $0.3 - 0.5 \text{ km s}^{-1}$ (Leighton et al. 1962; Simon and Leighton 1964; De Rosa and Toomre 2004) reaching up to 1 km s^{-1} (Shine et al. 2000). This is a systematic horizontal flow that advects granules (or mesogranules) and any other features trapped in this area, e.g., magnetic elements, from the SG's centre towards the network regions (Orozco Suárez et al. 2012). The vertical component of the supergranular flow was found to be much smaller (an average of 0.01 km s^{-1} up-flow at SG's centre; a mean down-flow speed of 0.005 km s^{-1} at the SG's boundaries) compared to the horizontal component (e.g., Duvall and Birch 2010). For a recent review on the solar convection and supergranulation, we refer to Rieutord and Rincon (2010).

We will study the advection of small MBPs within the SGs in detail in Chapter 6; where we will also address the relationship between the MBPs' diffusivity and their positions in the SGs and/or in the network areas.

1.4 Low chromosphere

In a standard plane-parallel model of the solar atmosphere (e.g., Vernazza et al. 1981; Fontenla et al. 1993), the chromosphere is the middle layer, where the temperature starts increasing from its lowest layer (i.e., the temperature minimum). The shallower temperature increase in the low-to-mid chromosphere is complemented by a dramatic rise in mid-to-high chromospheric regions of such a model. Observations of these different chromospheric layers (carried out in different wavelength bands) look very different and somewhat incompatible (Solanki 2004). This has made the chromosphere one the least understood region in the solar atmosphere, one whose contribution in the heating mechanisms of the outer layers (including the energy transport processes) is still an open and debated question (Ulmschneider and Musielak 2003; Ulmschneider et al. 2005). In this work,

we will only concentrate on the low chromosphere, close to the temperature minimum, where (similar to the upper photosphere) the assumption of LTE breaks down. These atmospheric layers are best sampled by, e.g., the Ca II H spectral line (e.g., Khokhlova 1959; Rutten and Uitenbroek 1991).

1.5 Energy transport and heating mechanisms

The heating mechanisms deal with generation, transportation and dissipation of the energy that heats the chromosphere and the corona. They can be classified based on whether they consider the magnetic field and on time-scales (Narain and Ulmschneider 1996). Both HD (hydrodynamic) and MHD (magneto-hydrodynamic) oscillations in field-free and magnetised regions, respectively, have been investigated as different heating mechanisms in the literature (e.g., reviews by Biermann 1948; Narain and Ulmschneider 1990; Ulmschneider and Kalkofen 2003; Reale 2010).

Acoustic waves are an example of the energy transport mechanism in non-magnetised areas (Erdélyi 2004). The acoustic waves are good approximations of the HD energy transport in relatively short time-scales. (Narayanan 2013) and can contribute to heating of the quiet chromosphere through, e.g., forming shocks as a result of amplitude increase with height due to the density decrease (i.e., shock dissipation; e.g., Ulmschneider 1970; Erdélyi 2006).

The MHD heating mechanisms, on the other hand, include the energy transport by slow and fast MHD waves, magneto-acoustic and magneto-acoustic-gravity waves and Alfvén waves as well as the energy dissipation by current sheets (e.g., Galsgaard and Nordlund 1996; Roberts 2000). While the former MHD waves are examples of alternating current (AC) heating mechanisms (corresponding to relatively small time-scale perturbations; rapid driving motions), braiding of the field lines leading to nanoflares (Parker 1988) as well as thin elongated current sheets (tangential discontinuities in the magnetic field, formed by MHD turbulence; Rappazzo et al. 2008) represent direct current (DC) heating mechanisms; as a result of external (gradual) driving forces on longer time-scales compared to transportation and dissipation times (Priest and Forbes 2000; Klimchuk 2006; Reale 2010). Both AC and DC can dissipate energy in the corona in the form of, e.g., resonant absorption and Joule heating (Ohmic heating; heat released by dissipation of electric currents), respectively, and hence, they both can contribute in coronal heating (e.g., Milano et al. 1997; Erdélyi 2004; Antolin et al. 2008; van Ballegooijen et al. 2011). However, other dissipation mechanisms in the corona for both AC and DC are also proposed (see a review by Klimchuk 2006).

The dissipated energies have to balance the energy losses in different solar atmospheric layers and in different solar regions. Unlike the chromosphere that radiation is the principal energy loss mechanism, the highly ionised corona has three major energy loss terms: radiation, thermal conduction and mass flow (Withbroe and Noyes 1977). The chromospheric and coronal energy losses obtained for different solar regions of, e.g., quiet-Sun, active regions and coronal holes, are summarised in Table 9.1 of Aschwanden (2004).

1.5.1 Oscillations and waves

Oscillatory motions have been observed in different layers of the solar atmosphere, in both field-free and magnetised areas, over a wide range of frequencies (Narayanan 2013). Section 1 in Chapter 5 provides a general overview of these oscillations in magnetic elements.

In particular, in the absence of magnetic fields in the internetwork regions in the photosphere, where pressure and gravity are the dominant restoring forces, outward propagating longitudinal waves (i.e., acoustic waves) can be generated at the top of the convection zone from the turbulent motions constituting the convection (Lighthill 1952; Stein 1967; Goldreich and Kumar 1990; Bogdan et al. 1993). These acoustic waves can propagate upwards and contribute to the heating of the higher layers if their frequency is larger than the cutoff acoustic frequency of $\approx 5 - 6$ mHz in the photosphere (Ulmschneider 1971; Wang et al. 1995b; Kalkofen et al. 2003). In addition, gravity waves can be produced within turbulent convective flows, where different kinds of instabilities exist (Mihalas and Toomre 1981, 1982). The gravity waves, with relatively low frequencies compared to the acoustic waves, can propagate in the convectively stable atmosphere (mostly horizontally with subsonic velocities; Stodilka 2008), whereas they cannot propagate within the convection zone due to the convective instability. Following Brund (1927), Stein (1967) provided a critical frequency (Eq. 2 in their paper) above which the internal gravity waves cannot propagate.

In the photospheric magnetic elements, in addition to gravity and pressure, the magnetic field also acts as a restoring force. Therefore, in addition to the longitudinal (compressible) acoustic waves and gravity waves, transversal (incompressible) MHD waves, produced by the interaction between convective motions and the magnetic field (e.g., in magnetic flux tubes), can also propagate along the tubes (e.g., Rosenthal et al. 2002; Bogdan et al. 2003). These interactions may result from the (1) buffeting of the flux tubes by the surrounding granules (kink mode), (2) the tubes' compression by convective forces from opposite sides (sausage mode), or (3) twisting the flux tubes by rotating flows around the tubes (torsional wave) (Spruit 1982; Solanki 1993). Depicted in Fig. 1.9 are these three wave modes in a cylindrical thin flux tube from Solanki (1993), originally taken from Thomas (1985).

The upward propagating acoustic and MHD waves can be well observed at heights corresponding to the temperature minimum and the low chromosphere that are best sampled by observations in Ca II H/K passbands (Carlsson and Stein 1997; Hasan and van Ballegoijen 2008).

So-called H_{2V}/K_{2V} grains, associated to Ca II H/K emission peaks, are believed to be produced by the propagating acoustic waves in magnetic-field-free areas (Rutten and Uitenbroek 1991; Carlsson and Stein 1997). The acoustic waves amplitude (A_w) increases much more rapidly than the sound speed (c_S) in the solar atmosphere; since, e.g., a roughly 4 orders of magnitude smaller density (ρ) in the low chromosphere compared to the solar surface results in approximately 2 orders of magnitude larger A_w , while less than a factor of two change in temperature (T) increase causes c_S to remain almost unchanged (assuming no mechanical energy lost; $A_w \propto \rho^{-1/2}$; $c_S \propto T^{1/2}$; Carroll and Ostlie 1996). As a result, the wave amplitude exceeds the local sound speed and hence a shock wave develops. The shock waves cause significant density change over a short distance that in

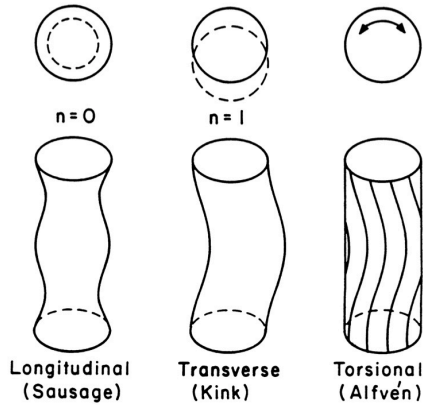


Figure 1.9: Illustration of the three MHD wave modes (see main text) along a thin flux tube in an un-stratified medium; from Solanki (1993).

return produces large heating (Bird 1964; Erdélyi 2006).

The propagation of high-frequency MHD waves along the magnetic flux tubes have been claimed to be responsible for extreme intensity enhancements of Ca II H MBPs (from numerical simulations; Hasan and van Ballegoijen 2008).

Waves are termed as “slow”, “intermediate” or “fast” when their propagation speed is smaller than, equal to or larger than the local Alfvén speed, respectively (Edwin and Roberts 1982; Rosenthal et al. 2002). These relative velocities depend on the plasma- β of the medium they propagated in (Bogdan et al. 2003).

If the MHD waves are much faster than the local Alfvén speed, they may not dissipate (or reflect) in the low chromosphere and might penetrate to the upper chromospheric layers and beyond. MHD simulations have shown that these fast waves can reach the transition region where their reflections may form both outward and inward propagating Alfvén waves (Cally and Hansen 2011). Such a fast-to-Alfvén mode conversion was shown by Cally and Hansen (2011) to be dependent on magnetic field inclination and does not occur for exactly vertical magnetic field.

Using different atmospheric models, it has been proposed that rapid pulse-like horizontal motions of MBPs (i.e., speeds larger than 2 km s^{-1} occurring in short intervals) due to forcing by rapid convective flows, excite magneto-acoustic kink waves along the flux tubes that can transfer energy to the upper chromosphere and/or corona (Spruit 1981a; Choudhuri et al. 1993a,b). Chapter 3 of this thesis presents a thorough study of the structure and dynamics of Ca II H MBPs whose jerky (sometimes supersonic) motions appear to marginally produce enough energy needed for heating the quiet corona, if the thereby excited kink waves can reach there. Such waves are detected and their propagation within the solar atmosphere is investigated in Chapter 4.

In Chapter 4 we will study characteristics of MHD waves in selected small MBPs whose intensity and horizontal displacement fluctuations reveal upward propagation of high-frequency fast waves of both compressible and incompressible modes.

1.6 Overview sketch

Illustrated in Fig. 1.10 is a very simple overview sketch of the selected features and events in the lower solar atmosphere (not to scale) that are discussed in Chapters 3 – 6. Most of these phenomena have been briefly described in this chapter.

Summarising, the convective flows of hot plasma in sub-surface regions (depicted as small, green curved arrows) carry energy, produced in the Sun's core, to the solar surface ($\tau_{5000} \approx 1$), where the plasma partly loses the energy and sinks back into the convection zone. The topmost part of these convective cells are seen (at the base of the photosphere) as irregularly shaped bright features (where hot plasma rises), i.e., granules, and intergranular dark lanes in between, where the cool plasma plunges back down into the interior. At larger scales, the supergranular convective flows are shown using the large green arrows at the bottom. The MBPs, i.e., manifestations of magnetic field concentrations, are shown as small (roundish) yellow features located in the intergranular lanes. The corresponding flux tubes are only drawn for a few magnetic elements (the blue and black nearly vertical lines). These flux tubes are often bent due to, e.g., propagation of kink waves along the magnetic field lines. In addition, a few low-lying magnetic loops are also plotted. The concentration of magnetic elements (here seen as MBPs) is much larger in network areas compared to the internetwork region as illustrated in Fig. 1.10. To keep the figure simple, the flux tube expansion as well as the reversed granulation effect are only displayed for one and two cases, respectively. The propagation of transversal kink waves is schematically depicted along the expanding flux tube. Furthermore, temperature perturbations (up to about 900 K) as a result of propagating compressive acoustic waves are represented by the yellow-red arc-shaped patterns; inspired from simulations by Hasan and van Ballegoijen (2008). As shown in Fig. 1.10, the concentrated (kG) magnetic elements, manifested as MBPs in an intensity image, are also observed in internetwork areas. Therefore, the $\beta \approx 1$ level also lies below the solar surface at the position of kG MBPs in the internetwork region. This level is highly dependent upon the magnetic fields and structures a complex surface in the atmosphere. However, for simplicity, we have only depicted a side-view of a very rough surface at positions of a few MBPs. In fact, in the internetwork regions, the $\beta \approx 1$ level is located much higher up in the atmosphere except at the location of MBPs.

Braiding of the flux tubes (due to random motions of their footpoints on the solar surface) leading to nanoflares (drawn in Fig. 1.10) was proposed by Parker (1988) as an important contributor to coronal heating. However, such events have not been directly observed yet. Please note that there are many other features/events present in the lower quiet-Sun atmosphere that are not shown in this overview sketch; since we only aim to focus on studying the mentioned phenomena.

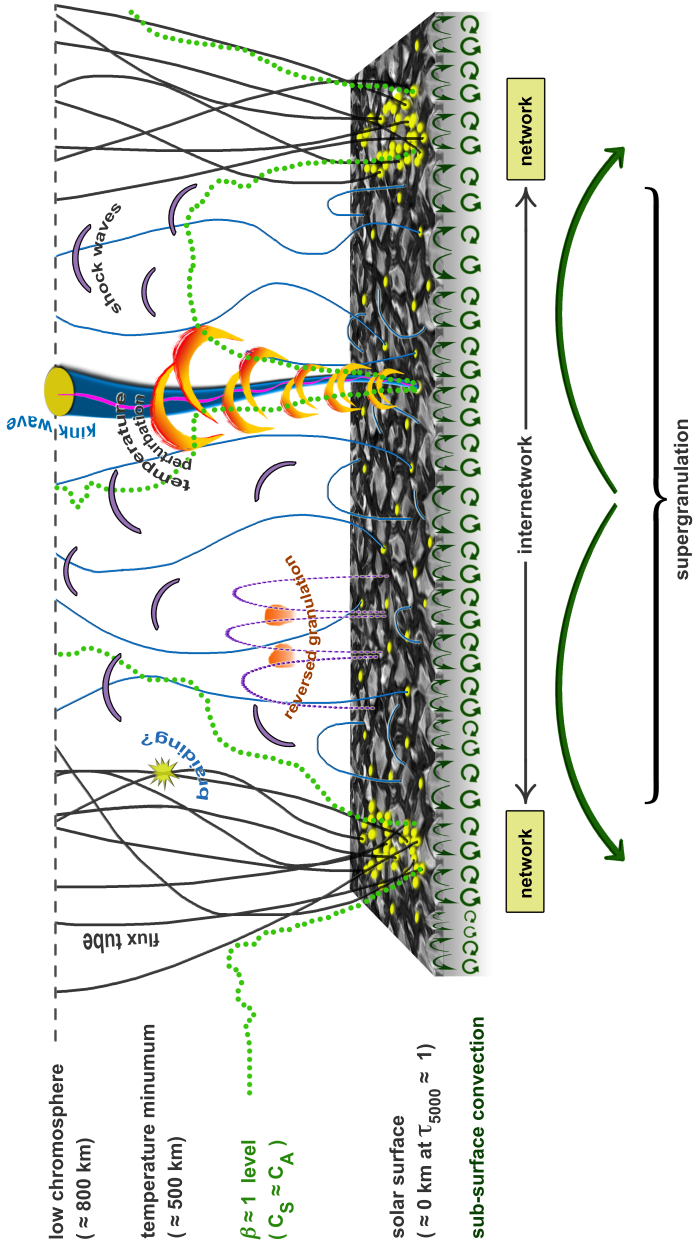


Figure 1.10: Simple sketch of the lower solar atmosphere including features/events studied in the present work. The cartoon represents a side-view of a quiet-Sun area. (Caption is continued on following page.)

Figure 1.10: (caption continued from preceding page): Base of the photosphere (i.e., solar surface at $\tau_{5000} \approx 1$) is shown as a granulation pattern, originally observed by IMaX/SUNRISE. The small and large green arrows below the surface schematically show the direction of granular and supergranular convective flows, respectively. The MBPs are indicated as small yellow circles located in intergranular lanes with larger concentrations in network regions compared to internetwork areas (corresponding to the supergranulation). The solid, often bent, vertical lines represent thin flux tubes in both network (black lines) and internetwork (blue line) areas. A few low-lying magnetic loops have also been illustrated by blue lines in the internetwork region. For simplicity, the flux tubes' expansion is illustrated only for one of the cases, where propagation of longitudinal acoustic waves along the tube axis (wavy purple line) as well as transversal kink waves around the tube are depicted. The yellow and red colours of the arc-shaped patterns represent temperature perturbation due to acoustic wave propagation (inspired from simulations by Hasan and van Ballegoijen 2008). The $\beta = 1$ level, where sound and Alfvén speeds coincide, is shown very schematically, only for few cases (see main text). The energy produced by, e.g., waves or braiding of the magnetic flux tubes, may be transferred to the upper solar atmosphere. The reversed granulation effect is illustrated only for two cases (for simplicity) from a side-view cut. The figure is not to scale.

2 Instrumentation and data

High spatial and temporal resolution observations are the key for studying the dynamics of small magnetic bright points (MBPs) in the lower solar atmosphere; whose evolution occurs on small spatial and time scales (e.g., de Wijn et al. 2009). We use observations from the SUNRISE balloon-borne solar observatory which have enabled us to reach an unprecedented high spatial resolution on the solar surface with the near-ultraviolet photospheric and (low-) chromospheric images as well as Doppler- and magnetograms. These observations, not affected by the seeing introduced by the Earth's atmosphere, are of particular interest when proper motions of the MBPs are considered; since the effect of distortion (i.e., differential seeing-induced deformations in different frames of an image sequence) is ruled out for such stratospheric (balloon) observations.

In this chapter, the SUNRISE observatory and its on-board instruments, the obtained data as well as methods used for retrieving the physical parameters (e.g., magnetic vector) are briefly described.

2.1 SUNRISE balloon-borne solar observatory

The SUNRISE balloon-borne solar observatory (Solanki et al. 2010; Barthol et al. 2011) comprises a 1-m Gregory telescope equipped with two main post-focus science instruments: SuFI (SUNRISE Filter Imager; Gandorfer et al. 2011), a multi-channel UV filter imager, and IMaX (Imaging Magnetograph eXperiment; Martínez Pillet et al. 2011), a Fabry-Pérot (filter-based) vector magnetograph. The images were actively aligned (between SuFI and IMaX) and stabilised during the whole observations using a Correlating Wavefront Sensor (CWS; Berkefeld et al. 2011) and an Image Stabilisation and Light Distribution (ISLiD; Gandorfer et al. 2011) system units, respectively. The residual pointing jitter was reduced using a fast tip-tilt mirror controlled by the CWS. The low-order wavefront aberrations caused by the optical system were pre-corrected by an adaptive optics system (Berkefeld et al. 2011). These aberrations are further corrected using post-processing techniques (see Sect. 2.3.1).

The SUNRISE telescope has a field-of-view (FOV) of 180 arcsec (about 0.1 of the solar disc's diameter; Barthol et al. 2011). Figure 2.1 shows an image of the payload and the balloon right before launch, borrowed from Barthol et al. (2011).

The observatory had its first flight between 8 – 13 June 2009 around the north pole (launched from Kiruna, northern Sweden, and landed on Somerset island, northern Canada) at a mean cruise altitude of 36 km. Being within the Arctic circle, the payload of this stratospheric balloon-borne observatory, carried by a $\approx 1 \text{ Mm}^3$ balloon with helium gas, could point to the Sun during the entire flight. Figure 2.2 shows the trajectory of the



Figure 2.1: SUNRISE balloon-borne solar observatory before launch in Kiruna (northern Sweden). From Barthol et al. (2011).

SUNRISE flight.

2.1.1 SuFI

SuFI, the SUNRISE Filter Imager, consists of a UV sensitive (down to 2000 \AA), fast read-out camera with 2048×2048 pixels (an image scale of $0.0207 \text{ arcsec/pixel}$), a filter wheel holding five violet and near-UV filters, as well as a mechanical shutter for exposure control (Gandorfer et al. 2011). To correct the wavefront deformations, the SuFI camera's FOV is divided into two parts, recording the same solar region in focus and defocus modes (see Sect. 2.3.1). Therefore, the SuFI images have a FOV of $14 \times 40 \text{ arcsec}$. Characteristics of the five filters, i.e., 2140, 3000, OH 3120, CN 3880 and Ca II H 3968 \AA , are summarised in Table 2.1 (from Solanki et al. 2010 and Gandorfer et al. 2011).

SuFI acquired a total of ≈ 150000 filtergrams in all five passbands during the entire flight. However, only 55685 of the images were recorded while the CWS was in closed-loop mode (i.e., while the current pointing location was continually modified to maintain the correct pointing location within $\pm 45 \text{ arcsec}$).

Depending on the light level entering the SuFI camera as well as the filter being used at any given time, different exposure times were assigned. The light level is dependent upon the position on the solar disc that the telescope is pointing to (the light level decreases from centre to limb) as well as the intensity (contrast) level of the observed target. Moreover, the light level decreases towards shorter wavelengths. To cope with the latter effect, except for Ca II H line, the combination of two filters at each filter position is used to prevent



Figure 2.2: Trajectory of the SUNRISE flight from Kiruna (northern Sweden) to Somerset Island in northern Canada. From Barthol et al. (2011).

unwanted contributions from leakage at longer wavelengths. To give some idea of typical exposure times, 30000, 300, 200, 100 and 1000 ms exposures were typically employed for the 2140, 3000, 3120, 3880 and 3968 Å passbands, respectively (Gandorfer et al. 2011). During the SUNRISE flight, different observing programs were performed. Depending on each observing mode, a number of SuFI filters were used. Hence, different time-scales (cadences) ranging between 2 – 12 sec were obtained for a given filter, whenever the 2140 Å filter (with exposure time of 30 sec) was not included.

For more details on SuFI we refer the reader to the paper by Gandorfer et al. (2011).

Table 2.1: Characteristics of SUNRISE/SuFI filters; from Solanki et al. (2010) and Gandorfer et al. (2011).

Central Wavelength (Å)	FWHM (Å)	Number of Images
2140	100	442
3000	50	11598
3120	12	10034
3880	8	14552
3968	1.8	19059

2.1.2 IMaX

IMaX, the Imaging Magnetograph eXperiment, is a spectropolarimeter operating in the magnetically (Zeeman) sensitive Fe I 5250.2 Å line (Landé factor $g = 3$; Martínez Pillet et al. 2011). It comprises two cameras (1000 × 1000 pixels; spatial sampling of 0.0523 arcsec/pixel), simultaneously observing the same solar region (i.e., dual-beam mode). IMaX uses two nematic liquid-crystal modulators to obtain all four Stokes parameters (I , Q , U and V) in various wavelength positions inside the spectral line plus a continuum point. IMaX achieved an effective spectral resolution of 85 mÅ using a tunable, solid-state, narrow-band (FWHM ≈ 1.0 Å) Fabry-Pérot filter.

The obtained data differ in the number of wavelength positions and/or Stokes parameters in different observing programs. In addition, the number of accumulations at each wavelength position varies in different observing modes. The polarisation states (Stokes parameters) include one of these two cases: (1) only Stokes I and V , for the case of longitudinal observations (labelled L for longitudinal), and (2) all four Stokes parameters, for the case of full Stokes vector (labelled V for vector). Therefore, each IMaX dataset is designated by one of these labels followed by the number of wavelength positions and then the number of accumulations separated by a dash. Table 2.2 summarises characteristics of the IMaX observing modes (from Solanki et al. 2010 and Martínez Pillet et al. 2011).

Table 2.2: Characteristics of SUNRISE/IMaX observing modes; from Solanki et al. (2010) and Martínez Pillet et al. (2011).

Observing Mode	Cadence (sec)	Wavelength Positions* (mÅ)	Continuum Positions* (mÅ)	Number of Images
V5-6	33	-80, -40, +40, +80	+227	1005
V5-3	18	-80, -40, +40, +80	+227	600
V3-6	20	-60, +60	+227	39
L12-2	31	-60, +60	+227	123
L3-2	8	-192.5 to +192.5 each 35	+192.5	315

* From the line-centre (5250.2 Å).

IMaX provides two-dimensional (50×50 arcsec²) vector magnetograms, Dopplergrams (line-of-sight velocity maps) as well as intensity frames in different wavelength positions sampling different heights in the solar photosphere. Further physical information from the Stokes parameters are retrieved by inverting the measured Stokes vectors using numerical solutions of the Unno-Rachkovsky radiative transfer equations (see Sect. 2.4). For more details on IMaX we refer the reader to the paper by Martínez Pillet et al. (2011).

2.2 Formation height

The wavelength and band-width of a filter determined the range of heights in the solar atmosphere sampled by the filter (Rutten 1990; Uitenbroek and Briand 1995). In order to

understand the results obtained from observations made with such a filter, it is necessary to know the physical properties of the medium representing in the observed images. Hence, the range of formation heights (or their average value) should be computed prior to the analysis of the images observed through each filter. The formation height is defined as the height above the solar surface at which $\tau_{5000} = 1$ (Uitenbroek 2003).

The so-called ‘‘Response Function’’ (RF) and ‘‘Contribution Function’’ (CF) are 2 approaches that are usually used to determine where in the solar atmosphere the spectral lines (or a specific part of the lines) are formed (e.g., Kucera et al. 1998). While the RF derives the sensitivity of the line to various perturbations (e.g., disturbances of temperature, magnetic field or velocity) at any given atmospheric height (Beckers and Milkey 1975; Landi Degl’Innocenti and Landi Degl’Innocenti 1977; Grigor’eva et al. 1991), the CF provides the height of line formation using a function that describes the contribution of a given height to the emergent intensity (Wittmann 1974; Caccin et al. 1977). The CF to emergent intensity has been shown not to be a sufficient tool for estimating the formation height (in particular for the weak lines) since it includes the bound-free and free-free processes that are responsible for the continuous intensity and not for the shape of the line profile (Magain 1986; Grossmann-Doerth et al. 1988). Instead, the CF to line depression, representing the bound-bound process alone, can provide a better estimation of the formation height (Grossmann-Doerth et al. 1988; Solanki and Bruls 1994; also see Gurtovenko et al. 1991).

To this end, we first synthesise a particular spectral line (or blend of lines) in a model atmosphere and determine the corresponding CFs by solving the radiative transfer and statistical equilibrium equations. Then, we convolve the CFs at each height by the transmission profile of the corresponding filter.

SUNRISE provided observations of quiet-Sun. Therefore, we chose to carry out the CF computations in some of the models described by Fontenla et al. (1993), namely FALC, FALF or FALP representing an averaged quiet-Sun, bright regions of the quiet-Sun (i.e., network) or a typical active region plage, respectively. Depending on the approximate atmospheric layer that the lines are expected to sample, one of the conditions, either LTE or non-LTE are assumed. To compute the CFs and hence the formation heights of the spectral lines of interest, we ran the 1D version of the RH-code of Uitenbroek (2001) which is based on the Multi-level Accelerated Lambda Iteration (MALI) scheme of Rybicki and Hummer (1991, 1992).

In Sect. 3.2.1 we will compare the three models and show that of the three selected models, FALP represents best the atmosphere inside the MBPs, i.e., the features mainly studied in this thesis. In Sects. 3.2.1, 5.2 and 6.2 the formation heights (CFs) of SuFI Ca II H, SuFI 3000 Å and IMAx Fe I 5250.2 Å (continuum and line-core) are provided.

The photospheric SuFI 3120 and 3880 Å passbands clearly represent the granulation (similar to SuFI 3000 Å), however, they sample different atmospheric layers that are dependent upon, e.g., the density and strength of the spectral lines they include. The formation height of the broad 2140 Å passband is estimated to be around 100 km above the solar surface (at $\tau_{5000} = 1$; Solanki et al. 2010). However, we have not computed the formation heights of these three SuFI passbands using the RH-code, since we have not used them in our investigations.

As an example, the sequence of formation heights’ determination for the SuFI Ca II H line using FALC and FALP model atmospheres are shown in Figs. 2.3 and 2.4, respec-

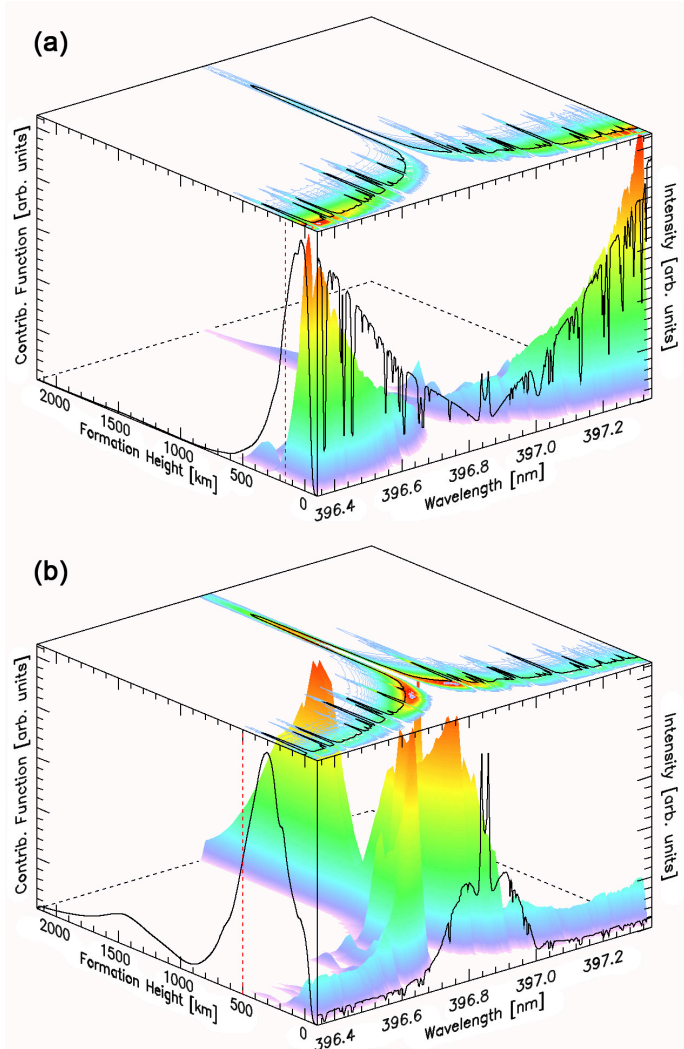


Figure 2.3: Determination sequence of contribution functions (CFs) of the Ca II H line (a) and synthesised SuFI Ca II H bandpass (b) in the FALC model atmosphere (see main text). Panels on the right of the cubes: The spectral lines. Inside the cubes: Contribution functions (CFs) computed using the RH-code. Left panels: Integrated CFs over wavelength. The dashed (red) vertical line indicates the mean formation height. Panels on top of the cubes: Contour plot of the CFs. Different colours imply different strengths of the CF, as indicated in the body of the cube. The solid (black) line shows the averaged CFs over geometrical heights plotted as a function of wavelength.

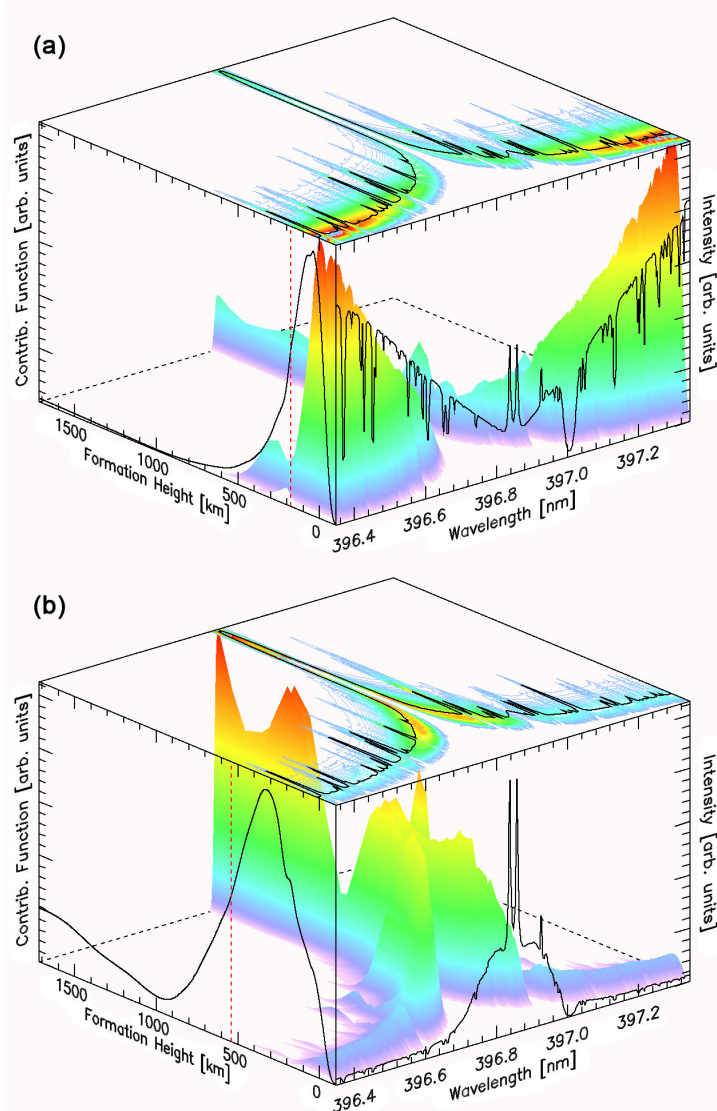


Figure 2.4: Same as Fig. 2.3, but for the FALP model atmosphere.

tively. In both figures, panels ‘a’ and ‘b’ correspond to the synthesised line before and after convolution with the transmission profile of the SuFI Ca II H filter, respectively. All cubes represent the plots of the synthesised lines (right panels), the CFs (3D structures inside the cube whose strengths have been highlighted by different colours), integration of the CFs over wavelength (left panel) and projection as well as the average of the CFs over heights plotted versus wavelength (coloured contour plot and solid, black line; top panel). The dashed (red) vertical lines in the left panels indicate the mean formation height of the computed spectral lines shown in the right panels of the cubes (i.e., either before or after application of the filter profile).

2.3 Data preparation

SUNRISE provided high-quality, high-resolution, multi-wavelength data sampling different heights in the lower solar atmosphere at a resolution of around 100 km at the solar surface. The Sun was completely quiet during the entire SUNRISE flight. The data represent the quiet-Sun at high spatial and temporal resolution and are ideal for studying the complex and diverse behaviour of the magnetic fields in, e.g., small-scale, dynamic structures manifested as magnetic bright points in intensity images (Solanki et al. 2012).

IMaX covers 50×50 arcsec² of the FOV of the SUNRISE telescope (180 arcsec in diameter) leaving room for the CWS to correct the location of the observing target at any given time within ± 45 arcsec. SuFI provides a smaller FOV of about 14×40 arcsec (somewhat less than half of the SuFI camera), to obtain simultaneous information for post-facto phase-diversity reconstruction on the other half of the detector (see Sect. 2.3.1). Figure 2.5 shows the FOV of these instruments relative to the telescope FOV (panel ‘b’) and relative to a continuum image of the solar disc (panel ‘a’).

Both SuFI and IMaX data are corrected for wavefront aberrations (caused by the optical system) via post-facto phase-diversity reconstruction techniques. The images are then aligned whenever needed. They are not, however, corrected for straylight since its effect from the Earth’s atmosphere is negligible for SUNRISE, although instrumental straylight very likely still is present to a certain extent (A. Feller, priv. communication). This is supported by the straylight analyses of other space-based telescopes combined with their post focus instruments (e.g., Mathew et al. 2007, 2009; Danilovic et al. 2008; Wedemeyer-Böhm and Roupe van der Voort 2009).

2.3.1 Phase-diversity reconstruction

In the absence of 99% of the Earth’s atmosphere (i.e., in the absence of seeing in the case of SUNRISE), optical systems (i.e., telescope and post-focus instruments) can also distort incoming wavefronts (due to, e.g., misalignments), resulting in blurred and distorted images (Martínez Pillet et al. 2011). Therefore, the observed images should be restored by the (known) wavefront deformations.

All images observed by SUNRISE (from both SuFI and IMaX instruments) were reconstructed using the Phase Diversity (PD) technique (Gonsalves and Chidlaw 1979; Paxman et al. 1992; Löfdahl and Scharmer 1994). In this method, the wavefront deformations are derived from a pair of simultaneously taken images of the same target with a known aber-

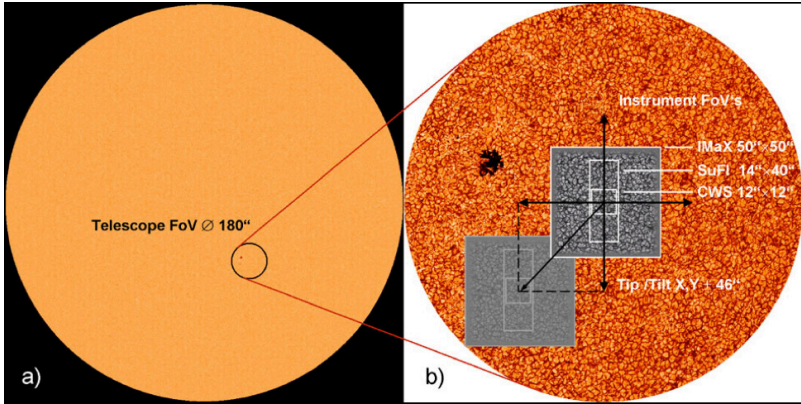


Figure 2.5: Field-of-view (FOV) of the SUNRISE telescope indicated as a small circle on the solar disc (a). FOV of the SuFI and IMaX science instruments as well as the Correlating Wavefront Sensor (CWS) are compared to the telescope's FOV of 180 arcsec in panel 'b'. From Barthol et al. (2011).

ration between the images: while both images are affected by an unknown aberration induced by the optical system, one of the images is in addition defocused by a certain amount (i.e., the known aberration).

Estimating the wavefront deformation in this way, may however, be affected by, e.g., noise, resulting in small-scale perturbations in the restored wavefront. In these cases, PD reconstructions of bursts (speckle series) of focused-defocused images can reduce the noise effect (Löfdahl et al. 1998).

SuFI simultaneously recorded focused and defocused images on the same detector by dividing the detector into 2 equal parts using two parallel and inclined glass plates located about the secondary (science) focus. The coating on the surface of these two plates were chosen such that half of the light is transmitted through both plates without any reflection (forming the focused image) and the other half is transmitted after two reflections between the plates. This reflected, optically delayed light (resulting in a longer path compared to the light forming the focused image) creates a defocused image. Therefore, half of the SuFI camera recorded the focused images, while the other half (simultaneously) recorded the defocused images of the same target; for later PD reconstructions.

IMaX, however, recorded defocused images only after completing each observing run (i.e., recording all accumulated images corresponding to all wavelength positions and all polarisation states) using the two cameras. These focused-defocused images were only obtained for the continuum wavelengths by inserting a plastic plate in front of one of the cameras (to defocus the incident light). The number of integrations were the same as in the subsequent observing run to obtain a similar signal-to-noise ratio. Therefore, the observed images can be deconvolved from the point spread function (PSF) of the instrument evaluated by the PD technique, applied to the continuum images.

The reconstruction of the SuFI and IMaX data are described in detail by Hirzberger

et al. (2011) and Martínez Pillet et al. (2011), respectively.

Different versions of the data have been prepared since the SUNRISE flight. Four different versions exist of the SuFI data:

- level-0: Raw data, including both focused and defocused images on one frame of 42×42 arcsec².
- level-1: Data that are flat-fielded and corrected for dark current, but not PD reconstructed.
- level-2: PD reconstructed data employing individual wavefronts for each frame.
- level-3: PD reconstructed data using averaged wavefront errors obtained from the permanent in-flight measurements.

The IMAx data comprises three versions:

- level-0: Raw data.
- level-1: Data corrected for dark current, flat-field and the instrumental effects (i.e., the instrumental polarisation), but not reconstructed.
- level-2: Reconstructed data using an averaged wavefront; the reconstruction is done by deconvolution of the PSF of the telescope and instrument derived from the intermittent in-flight PD measurements.

SuFI level-3 data correspond to IMAx level-2 data, both of whose reconstructions are based on an average wavefront.

All non-reconstructed Stokes profiles from IMAx have a 1σ noise level of about 10^{-3} on average, as computed from the continuum filter positions. After the PD reconstruction (while spatial resolution is increased by a factor of 2), the noise level increases by (approximately) a factor of 3. The noise levels of Stokes Q , U , and V for both non-reconstructed and PD reconstructed V5-6 data are summarised in Table 6.1.

2.3.2 Image alignment

A precise image alignment is crucial when analysing images (simultaneously) observed in different wavelengths and/or with different instruments (e.g., Shimizu et al. 2007). Depending on the spatial sampling of the images, orientation and alignment of the instruments or filters in the filter-wheel of the instrument, the image alignment may include scaling, translation, rotation and/or flipping with respect to a reference image.

In the case of SUNRISE, images obtained in different channels of the SuFI as well as the SuFI-IMAx images need to be aligned (since they are taken using different filters/cameras), while the images observed in different wavelength positions of the IMAx (taken using the same camera and same filter) do not need any further alignment.

We precisely aligned images using a cross-correlation technique applied on common sets of manually selected features in images representing similar visual pictures (e.g., granular patterns). The basic steps of the routine are outlined below:

1. Select two images that look similar: All SuFI passbands, except the Ca II H line, as well as the IMAx Stokes I continuum represent granular patterns including, sometimes, other small-scale features such as MBPs (depending on intensity contrasts). The SuFI Ca II H filtergrams represent similar structures (e.g., reversed granulations) as seen in images sampled by the innermost wavelength positions of the IMAx Stokes I .
2. Clip the pair of images to the same size (i.e. to roughly a common FOV); by visually selecting common small-scale features.
3. Align the images around a common point, e.g., a bright point. This procedure secures a more precise selection of initial guess parameters in the following step.
4. Find the transformation parameters (i.e., shifts and scales in both x and y directions as well as the rotation angle) for one of the images (the target image) with respect to the other image (the reference image). These parameters are calculated by manually selecting the common points on both images and then iteratively applying a cross-correlation approach and minimising the differences using the Powell function. In this procedure, the initial (guess) coefficients of the transformation are approximated from the selected common points by performing a polynomial spatial warping. The initial warping is then tweaked until a maximum in the cross-correlation is found using the Powell minimisation routine (with a maximum number of iterations of 200).
5. Transform the “target image” based on the transformation parameters.

Whenever the image alignment between SuFI and IMAx frames is performed, they are re-sampled to a common plate scale of one of the instruments, dependent upon the primary dataset under analysis. The IMAx images should be rotated by 270° followed by a transposition prior to the alignment to achieve an approximate co-orientation with SuFI filtergrams. Since the innermost wavelength positions of IMAx sample heights roughly corresponding to the mid-to-high photosphere, their intensity (Stokes I) images look similar to those recorded in SuFI Ca II H filtergrams. Therefore, IMAx images (sampling both continuum level and upper photosphere) are used for aligning images observed in SuFI passbands that samples heights close to the continuum level (i.e. 2140-3880 Å; all representing granular patterns) and Ca II H images sampling, roughly, a height corresponded to the temperature minimum.

Two examples illustrating the selection of points common to both images are shown in Fig.2.6. The selected points are indicated by yellow squares around them. Prior to the selection of the common points in these examples, IMAx images were re-sampled to the SuFI image scales, the images were cropped to a roughly common FOV, and they were aligned around a common point. The common points’ selection is shown for pairs of SuFI 3000 Å and IMAx Stokes I continuum images in the left and right panels of Fig.2.6a, respectively. A similar procedure is presented in Fig.2.6b for an average of the -40 and $+40$ mÅ wavelength positions of the IMAx Stokes I (left) and SuFI Ca II H 3968 Å (right). The former image corresponds to the inner flanks of IMAx Fe I 2520.2 Å and will be considered as a proxy for the IMAx line-core intensity. Note the location

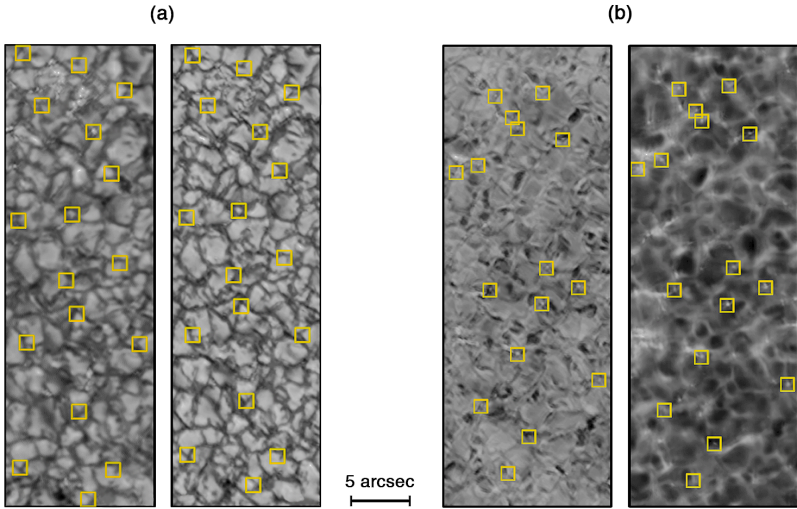


Figure 2.6: Examples of common points' selection in pair of images (see main text). a) SuFI 3000 Å (left) and IMAx Stokes I continuum (right). b) Average of two innermost wavelength positions of IMAx Fe I 5250.2 Å (left) and SuFI Ca II H 3968 Å (right).

difference between the approximate common points, e.g., the lowermost selected points, in both pairs of images. Examples of the aligned images, obtained in all SuFI passbands as well as IMAx Stokes I continuum are shown in Fig. 2.7. The image sizes become significantly smaller compared to the original SuFI image size of 14×40 arcsec² when all images are co-aligned simultaneously; due to different offsets between the SuFI images. Therefore, in the following chapters, we will align only those pairs of images that are of interest for the analysis; thus keeping the largest possible FOV.

2.3.3 RMS intensity contrast

The rms (root-mean-squared) intensity contrasts are determined to characterise intensity variations between bright and dark regions in an image (e.g., Danilovic et al. 2008). Higher intensity contrast facilitates easier feature identification (e.g., detecting a MBP) and its tracking in time-series of images (Berger et al. 1998a; Crockett et al. 2009; Criscuoli et al. 2012).

Table 2.3 summarises example values of the computed mean rms intensity contrasts of the SUNRISE images from Hirzberger et al. (2010) and the contrast of MBPs from Riethmüller et al. (2010). The mean rms intensity contrasts of the SuFI images, presented in Table 2.3, were measured from a level-3 dataset observed at disc-centre quiet-Sun on 9 June 2009 (Hirzberger et al. 2010). The rms contrast of the IMAx 5250.2 Å image was computed from a continuum dataset and is expectedly lower than those of the SuFI images due to its longer wavelength. Therefore, it is expected that small bright features such

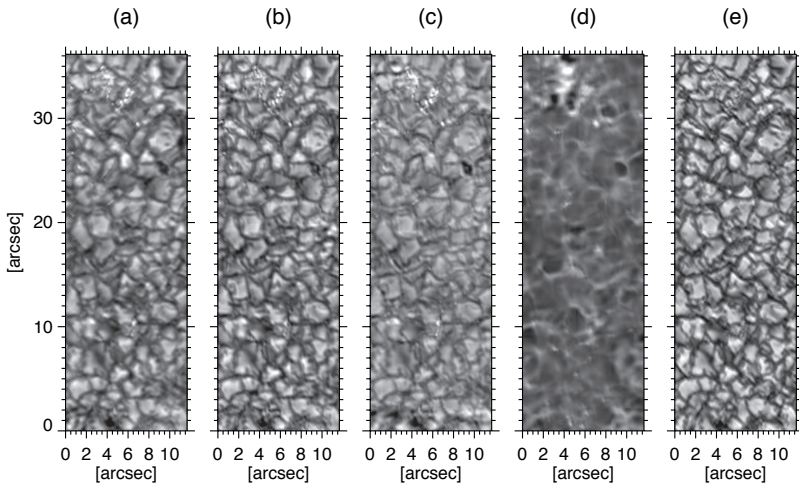


Figure 2.7: Examples of SuFI and IMAx co-aligned images: (a) SuFI 3000 Å, (b) SuFI 3120 Å, (c) SuFI 3880 Å, (d) SuFI Ca II H 3968 Å, and (e) IMAx 5250.2 Å continuum intensity (Stokes I).

as MBPs are better visible in higher contrast images, as is also evident from the ratio of the MBPs' rms contrast to that of granulations given in the Table 2.3 (from Riethmüller et al. 2010).

Table 2.3: Sample values of rms intensity contrast of the SUNRISE images (middle column; from Hirzberger et al. 2010). Ratio of the MBP contrasts to those of granulations, from Riethmüller et al. (2010), are shown in the rightmost column. All contrasts correspond to quiet-Sun disc-centre observations.

Wavelength (Å)	RMS Contrast	Contrast Ratio
2140	27.8	4.7
3000	20.0	2.4
3120	19.5	1.8
3880	17.3	3.3
3968	20.1	4.0
5250.2*	13.5	0.8

* Continuum point corresponding to 5250.4 Å

2.4 Inversions

Physical information stored in each pixel can be extracted by inverting the Stokes profiles (recorded by IMAx), such that, the observed and synthetic spectra (computed with models representing the structure of the solar atmosphere) are compared (e.g., Auer et al. 1977; Skumanich and Lites 1987; Ruiz Cobo and del Toro Iniesta 1992; Bellot Rubio et al. 2000). This comparison provides information used for modifying the initial model atmosphere; since the Stokes profiles are sensitive to perturbations of the atmospheric parameters (Ruiz Cobo and del Toro Iniesta 1994). Note that the inversion methods may also introduce ambiguities in the results (e.g., in the magnetic field's azimuth angle) since all parameters cannot be efficiently sampled (Bellot Rubio et al. 2000). However, some methods that solve the azimuth ambiguity have been developed (e.g., Wang 1997; Wang et al. 2001; Metcalf et al. 2006). The accuracy and reliability of the atmospheric parameters determined from the inversion methods have been discussed by, e.g., del Toro Iniesta and Ruiz Cobo (1996).

We applied the SPINOR inversion code (Frutiger et al. 2000; Berdyugina et al. 2003) to the SUNRISE/IMAx Stokes profiles pixel by pixel. It is a height-dependent inversion code based on the STOPRO routines (Solanki 1987), i.e., the spatially coupled inversion technique of van Noort (2012); van Noort et al. (2013) has not been applied to them. The way such methods work can be summarised by the following steps:

1. Synthesise Stokes profiles of the observed spectral line(s) in an initial model atmosphere (described by a number of physical parameters, such as magnetic vector, temperature, gas and electron pressures, density, microturbulence velocity and line-of-sight velocity, all as a function of optical depth) by solving the radiative transfer equations of the Zeeman-split lines.
2. Compare the synthesised (theoretical) Stokes profiles with those obtained from the observations through a chi-squared (χ^2) merit function (Bellot Rubio et al. 2000).
3. Modify (iteratively) the initial model atmosphere through, e.g., a Levenberg-Marquardt algorithm (i.e., a minimisation method in least squares or nonlinear curve fitting; Press et al. 2007), until the χ^2 reaches an acceptable minimum (i.e., repeating steps 1 and 2 by modifying the model atmosphere at the beginning of each iteration until χ^2 is minimised). Note that different minimisation methods may be used in different inversion codes, e.g., the code presented by Lagg et al. (2004) uses the genetic algorithm PIKAIA (Charbonneau 1995) to minimise goodness of the fit to the observed profiles.

Figure 2.8 schematically illustrates an inversion procedure.

The initial atmospheric model of the solar photosphere is normally chosen from either the Milne-Eddington approximation (e.g., Martínez Pillet et al. 1997) or a standard atmospheric model, e.g. the HSRA (Harvard Smithsonian Reference Atmosphere; Gingerich et al. 1971). While the former model assumes a source function linear with optical depth (τ) and other parameters independent of τ (Unno 1956; Orozco Suárez et al. 2010), the latter employs a model in which physical parameters vary with τ (Asensio Ramos et al. 2012). Milne-Eddington based inversions solve the RTE analytically and provide a faster

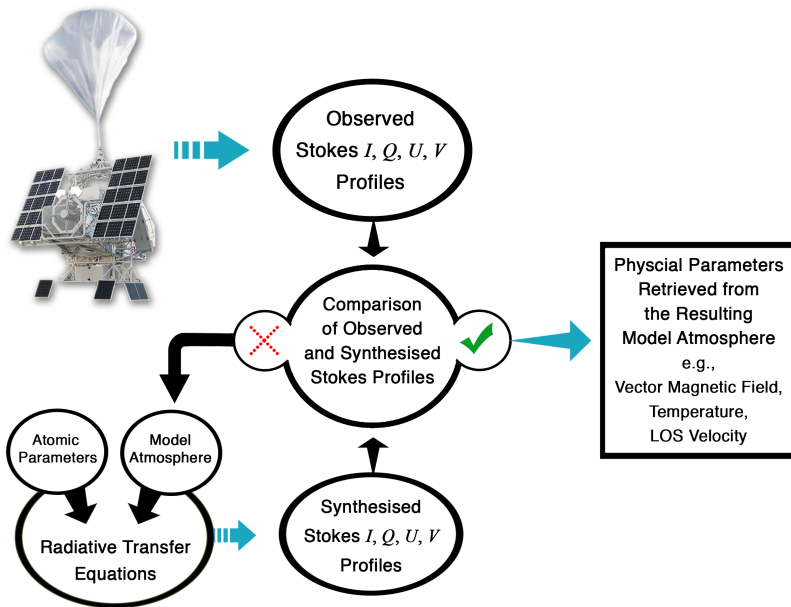


Figure 2.8: Simple block scheme of inversion techniques (see main text).

and simpler treatment of the RTE compared to the numerically solved RTE of the height dependent inversions (del Toro Iniesta and Ruiz Cobo 1996).

When the physical quantities at several optical depths (so-called nodes; Ruiz Cobo and del Toro Iniesta 1992) are provided, the algorithm makes simultaneous modifications at all depths in the iterative solution. Each node adds an extra set of free parameters to the inversion code (Borrero and Solanki 2008). It is mainly useful if it results in a better fit to the observed Stokes profiles and if it provides more physical insight. Figure 2.9 shows example maps of the observed Stokes profiles (from PD reconstructed data; obtained on 9 June 2009) along with the maps of the magnetic field vector, LOS velocity and temperature computed using the SPINOR code with one node at $\tau_{5000} = 1$ (i.e., when all physical parameters, except the temperature, are considered constant with height). A boxcar filter of 3×3 pixels has removed most of the residual noise from the maps. Note that due to the highly inhomogeneous distribution of the magnetic field, the signal-to-noise ratio (SNR) of Stokes Q , U and V varies strongly from one spatial pixel to another. Hence, the atmospheric (in particular magnetic) parameters returned by the inversion code are not equally reliable in all pixels, since the code results an arbitrary value when fitting to noise. Such biases may therefore appear in the parameters returned by an inversion code at low SNR (the uncertainties increase rapidly with decreasing SNR in the polarised Stokes profiles).

Furthermore, we will use the results of two other inversions of the same dataset for

comparison. These were carried out using the SIR (Ruiz Cobo and del Toro Iniesta 1992) and VFISV (Borrero et al. 2011) codes (see Chapter 6). While SIR (similar to SPINOR) is a height-dependent inversion code considering the HSRA model atmosphere (for SUNRISE data; Guglielmino et al. 2012), the VFISV inversion code is based on the Milne-Eddington approximation of the solar atmosphere. The magnetic strengths and field inclination angles retrieved from the three inversion codes are presented (partly) in Chapter 3 and also in Chapter 6 where the inversions of differently treated datasets (with different noise levels) are discussed.

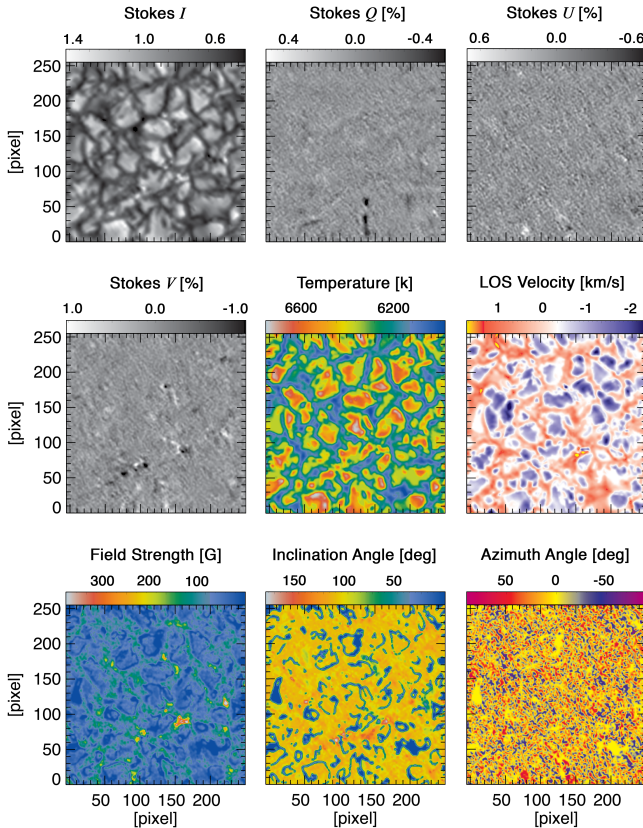


Figure 2.9: Results of the SPINOR inversion for a small area of the IMAx FOV (see main text). The Stokes maps include all the five wavelength positions of a V5-6 dataset. All parameters are computed for $\tau_{5000} = 1$.

3 Structure and dynamics of isolated internetwork Ca II H bright points observed by SUNRISE

This chapter appeared as S. Jafarzadeh^{1,2}, S. K. Solanki^{1,3}, A. Feller¹, A. Lagg¹, A. Pietarila⁴, S. Danilovic¹, T. L. Riethmüller¹ and V. Martínez Pillet⁵, 2013, *A&A*, 549, A116.

Abstract We aim to improve our picture of the low chromosphere in the quiet-Sun internetwork by investigating the intensity, horizontal velocity, size and lifetime variations of small bright points (BPs; diameter smaller than 0.3 arcsec) observed in the Ca II H 3968 Å passband along with their magnetic field parameters, derived from photospheric magnetograms.

Several high-quality time series of disc-centre, quiet-Sun observations from the Sunrise balloon-borne solar telescope, with spatial resolution of around 100 km on the solar surface, have been analysed to study the dynamics of BPs observed in the Ca II H passband and their dependence on the photospheric vector magnetogram signal.

Parameters such as horizontal velocity, diameter, intensity and lifetime histograms of the isolated internetwork and magnetic Ca II H bright points (MBPs) were determined. Mean values were found to be 2.2 km s^{-1} , 0.2 arcsec ($\approx 150 \text{ km}$), $1.48 \langle I_{Ca} \rangle$ and 673 sec, respectively. Interestingly, the brightness and the horizontal velocity of MBPs are anti-correlated. Large excursions (pulses) in horizontal velocity, up to 15 km s^{-1} , are present in the trajectories of most MBPs. These could excite kink waves travelling into the chromosphere and possibly the corona, which we estimate to carry an energy flux of 310 W m^{-2} , sufficient to heat the upper layers, although only marginally.

The stable observing conditions of Sunrise and our technique for identifying and tracking MBPs have allowed us to determine reliable parameters of these features in the internetwork. Thus we find, e.g., that they are considerably longer lived than previously thought. The large velocities are also reliable, and may excite kink waves. Although these wave are (marginally) energetic enough to heat the quiet corona, we expect a large

¹ Max-Planck-Institut für Sonnensystemforschung, Max-Planck-Str. 2, 37191, Germany

² Institut für Astrophysik, Georg-August-Universität Göttingen, Friedrich-Hund-Platz 1, 37077, Germany

³ School of Space Research, Kyung Hee University, Yongin, Gyeonggi 446-701, Republic of Korea

⁴ National Solar Observatory, 950 N. Cherry Avenue, Tucson, Az 85719, USA

⁵ Instituto de Astrofísica de Canarias, C/Vía Lactea, s/n 38205, La Laguna, E-38200, Tenerife, Spain

additional contribution from larger magnetic elements populating the network and partly also the internetwork.

3.1 Introduction

The solar chromosphere is both, heavily structured and highly dynamic. One of the important contributors to the low chromosphere's structuring and dynamics in high spatial resolution images are bright points (BPs). They are also an excellent diagnostic since due to their apparent lack of internal fine structure, they are ideal tracers of horizontal motions of magnetic features. Such BPs, however, can have a rather diverse set of physical causes. Here we discuss particularly small BPs seen in the strong chromospheric lines such as Ca II H.

Acoustic waves, thought to be one of the heating mechanisms of the quiet chromosphere from simulations (e.g., Carlsson and Stein 1997) and observations (e.g., Rutten and Uitenbroek 1991; Kneer and von Uexkull 1993; Hofmann et al. 1996; Cadavid et al. 2003; Beck et al. 2008; Bello González et al. 2010) appear as bright, short-lived points in Ca II H/K filtergrams that are sufficiently spectrally narrow to isolate the H_{2V}/K_{2V} emission peak. These bright points are normally referred to as H_{2V}/K_{2V} grains. With the help of radiation-hydrodynamic numerical simulations Carlsson and Stein (1997) explained the origin of these point-like brightening as high-frequency p -modes. Lites et al. (1993) found no clear correlation between the Stokes V signal and the occurrence of K_{2V} grains, observed in the Ca II H passband, in contrast to Sivaraman and Livingston (1982), who had concluded that these grains are associated with a weak magnetic field of 20 G on average. Cadavid et al. (2003) found that most K-line brightenings occur 2 minutes before or after G -band darkening events in roughly the same positions in an internetwork area. They concluded that the timing and coupling of these chromospheric brightenings and photospheric darkenings are due to a pre-existing acoustic wave pattern with four minute periodicity. They also showed that the K_{2V} grains are not associated with any detectable magnetic flux in the simultaneously observed magnetograms. The time delay of about two minutes is roughly consistent with the travel time of sound from the photosphere to the chromosphere (Hoekzema et al. 2002).

In addition to the short-lived acoustic H_{2V}/K_{2V} grains, other bright, point-like structures are observed in the low solar chromosphere and around the temperature minimum¹. These include the brightest parts of the (1) "reversed granulation" (Rutten et al. 2004), which appears as bright arcs all over internetwork areas, concentrated to brighter point-like structures in some regions, (2) magnetic bright, point-like features in both network and internetwork areas, and (3) "persistent flashers", i.e., BPs which appear (when intermittent magnetic patches are squeezed together) and disappear (when the magnetic concentrations become less dense; as imposed by the granular flows) during their lifetime (Brandt et al. 1992; de Wijn et al. 2005; Rutten et al. 2008).

¹ Note that the term "bright point" has been interchangeably used in the literature for chromospheric phenomena such as brightenings associated with magnetic features, or K-grains (e.g., Steffens et al. 1996), and for bright, point-like features in the other layers of the solar atmosphere, e.g., X-ray bright points in the corona, or photospheric magnetic bright points. Here we restrict ourselves to the chromospheric features.

Earlier studies of BPs in the quiet Sun mostly concentrated on the dynamics of network BPs. These have been well-studied at the atmospheric layers we sample, i.e., from the upper photosphere to the low chromosphere (e.g., Lites et al. 1993; Wellstein et al. 1998). They are connected to photospheric BPs (e.g., Riethmüller et al. 2010) with concentrated kilo-Gauss, nearly vertical magnetic elements described by flux tubes (e.g., Spruit 1976; Solanki 1993; Yelles Chaouche et al. 2009), and have been often referred to as MBPs (magnetic bright points; e.g., see Muller et al. 2000; Möstl et al. 2006) or GBPs (when identified in the G -band passband; e.g., Berger and Title 2001; Steiner et al. 2001; Sánchez Almeida et al. 2001, 2010; Schüssler et al. 2003; Shelyag et al. 2004; Bovelet and Wiehr 2008).

The chromospheric internetwork MBPs are more challenging and less studied. The few previous investigations of internetwork Ca II H MBP dynamics (e.g., Al et al. 2002; de Wijn et al. 2005), although of considerable value, suffer from the comparatively limited spatial resolution of the employed data. A complete observational picture of the dynamics of these bright point-like features obtained at high spatial resolution, including the intensity, horizontal velocity, size and lifetime distributions, is so far unavailable. Providing such a picture for the smallest elements currently observable is the aim of this chapter.

Here we characterise the time-dependent properties, including the dynamics of the MBPs observed in the low chromospheric layers sampled by the SUNRISE Filter Imager (SuFI) Ca II H filter, centred at 3968 Å. We measure their magnetic property with the help of simultaneous full Stokes photospheric observations in the Imaging Magnetograph eXperiment (IMaX) Fe I 5250.2 Å passband. Several criteria are considered to define the particular breed of Ca II H MBPs probed in this work.

This chapter is organised as follows: in Sect. 3.2, we describe the data and their preparation prior to analysis. In Sect. 3.3, our methods for studying the temporal evolution of the identified SUNRISE Ca II H MBPs, as well as their magnetic correspondence measurements are explained. The results of our investigations and related discussions are presented in Sect. 3.4, followed by the conclusions in Sect. 3.6.

3.2 Observations and data preparation

Several simultaneous image sequences obtained by the SUNRISE Filter Imager (SuFI; Gandorfer et al. 2011) and the Imaging Magnetograph eXperiment (IMaX; Martínez Pillet et al. 2011) on board the SUNRISE balloon-borne solar telescope (Solanki et al. 2010; Barthol et al. 2011; Berkefeld et al. 2011) are used for this study.

Table 3.1 summarises the SuFI and IMaX observations used in this study. In this table, we present exposure time and observing cadence of each image sequence and for all wavelengths recorded by SUNRISE. However, only the SuFI Ca II H (centred at 3968 Å), SuFI CN (centred at 3880 Å) and IMaX Fe I 5250.2 Å images were used for this chapter. Image sequences that were not observed in a certain wavelength and/or data that were not available (e.g., not yet reduced) at the time of this investigation, are indicated by dashed lines.

Table 3.1: Log of observations.

Central Wave- length (\AA)	FWHM of Filter (\AA)	9 June 2009			11 June 2009			13 June 2009				
		Exp.** (ms)	Cad.** (s)	Exp. Cad. (ms) (s)								
3000	50	500	12	500 12	-	-	130 8	130 7	-	-	-	-
3120	12	150	12	150 12	-	-	250 8	250 7	-	-	-	-
3880	8	80	12	80 12	65	4	70 8	70 7	75	3	75	3
3968	1.8	960	12	960 12	500	4	500 8	500 7	500	3	500	3
5250.2	0.085	250	33	250 33	-	-	-	-	250	33	250	33

* All times in UT

** Exposure Time

*** Cadence

3.2.1 Ca II H images

The primary time series in this investigation consist of SuFI images (Hirzberger et al. 2010) taken in the Ca II H filter (centred at 3968 Å with FWHM \approx 1.8 Å). The series were recorded on 2009 June 9 (at 0 and 1 UT, both with 12 sec cadence), June 11 (at 15, 20 and 21 UT, with 4, 8 and 7 sec cadences, respectively) and June 13 (at 1 UT, with 3 sec cadence) in quiet-Sun regions close to disc-centre. We employ level 3 data, i.e., images that have been phase diversity reconstructed with averaged wave front errors (cf. Hirzberger et al. 2010, 2011).

To obtain an estimate of the formation height of the radiation passing through the SUNRISE/SuFI Ca II H passband, we determined the contribution functions (CF) by means of the 1D RH-code (Uitenbroek 2001). This code solves both radiative transfer and statistical equilibrium equations in non-LTE for a given atmospheric model. We used a four-level plus continuum Ca II H model atom (Uitenbroek 2001) and three different atmospheric models, FALC, FALF and FALP, which respectively describe an averaged quiet-Sun area, bright regions of the quiet-Sun and a typical plage region (Fontenla et al. 1993, 2006). For all atmospheric models, the intensity profiles (synthetic spectra) of the Ca II H line, computed with the RH-code from the atomic model, as well as the determined contribution functions to line depression (e.g., Grossmann-Doerth et al. 1988) were convolved with the transmission profile of the SUNRISE/SuFI Ca II H filter. Figure 3.2a shows the Ca II H spectra before convolution with the transmission profile (dashed curve) for FALC (red line), FALF (green line) and FALP (blue line). Figure 3.2b displays the convolved profiles. The latter model represents higher H_{21}/H_{2R} emission peaks around the line-core compared to the other models due to excess heating related to the magnetic field, just as in MBPs (e.g., Skumanich et al. 1975; Ayres et al. 1986; Solanki et al. 1991). For a comparison of Ca II K line shapes in different model atmospheres see Fig. 7 of Fontenla et al. (2009). The mean intensity contrast of FALP relative to FALC (\approx 1.43; determined from the convolved spectra) is similar to that of small, internetwork SUNRISE Ca II H MBPs under study (see Sect. 3.4.3.1). Integration of the (filter-profile convolved) CF over wavelength gives the contribution of each height to formation of the signal seen in the SUNRISE Ca II H bandpass. Plotted in Fig. 3.2c are the computed CFs for the SUNRISE filter versus geometric height for the three model atmospheres. The CFs have multiple peaks and cover a wide range of heights from below the surface to the mid-chromosphere. The vertical dotted lines in Fig. 3.2c indicate the average formation heights (cf., Leenaarts et al. 2012), lying at 437, 456 and 500 km for FALC, FALF and FALP, respectively. The sudden drop of the CF's curve for FALP at \approx 1700 km is due to the rapid increase in the temperature at the top of the chromosphere.

The SUNRISE/SuFI Ca II H filter is narrower than that of *Hinode* (centred at 3968.5 Å with FWHM \approx 3.0 Å; Tsuneta et al. 2008), so it samples higher layers in the quiet-Sun compared to the *Hinode* Ca II H passband with an average formation height of 247 km. (cf. Carlsson et al. 2007).

The photon noise is the most prominent noise source in intensity and hence it is assumed as the only noise contribution in the measurements. The noise introduced by instrumental effects into the SUNRISE observations is much smaller and not considered further. The photon noise is calculated by measuring the high frequencies derived from the Fourier power spectrum of the reconstructed images (after apodization). A value of 0.01 $\langle I_{Ca} \rangle$ was

measured as the averaged photon noise in our Ca II H images.

3.2.2 Stokes measurements

Full Stokes vector (I, Q, U, V) data recorded in parallel to the Ca II H sequences by IMAx in the magnetically sensitive photospheric Fe I 5250.2 Å line at a cadence of 33 sec were also analysed whenever available. The Stokes vector was measured in four wavelength positions in the line located at $-80, -40, +40$ and $+80$ mÅ from line centre and at $+227$ mÅ in the continuum. The noise level was $3 \times 10^{-3} I_c$ after phase-diversity reconstruction ($V5 - 6$ data; Martínez Pillet et al. 2011).

In order to study the magnetic properties of the investigated MBPs, following Solanki et al. (2010) and Martínez Pillet et al. (2011), we averaged over Stokes V at the 4 wavelength positions inside the line, normalised to the local quiet-Sun continuum intensity (I_c). To avoid cancellation effects, the sign of the two red wavelength points was reversed prior to averaging. This wavelength averaged Stokes V will be called CP in the following.

The total linear polarisation (LP) was also computed from the Stokes Q and U profiles ($LP = \sqrt{Q^2 + U^2}$), averaged over the four wavelength positions in the line. To do this, we first average the Stokes Q and U profiles over the wavelength positions with the same sign (i.e., the two outermost and two innermost wavelength positions), then compute the LP for each averaged position, and finally calculate the mean value of the two LP s. The CP and LP were determined from the non-reconstructed data (with a factor of 2 lower spatial resolution and, more importantly, a factor of 3 lower noise compared to the reconstructed data), which were flat-fielded and corrected for instrumental effects.

The noise level for LP was computed from the IMAx Stokes Q and U frames of the continuum wavelength and the LP was corrected for the offset produced due to squaring the Stokes profiles. Furthermore, to increase the signal-to-noise ratio (SNR), an average over a 3×3 pixels area centred at the corresponding location of the MBP on the aligned IMAx images was performed on Stokes Q, U and V profiles, at each wavelength position, prior to computing the CP and LP signals. The 3σ level of the Stokes profiles decreases due to the averaging over four wavelength positions and it is additionally reduced due to the spatial averaging of the polarisation signals. The reduction in the noise by a factor of 3 due to the spatial smoothing over 3×3 pixels was not fully achieved due to coherent noise, probably caused by image jitter. The final computed value of the 3σ noise levels for CP and LP normalised to I_c is on average 1×10^{-3} .

Areas where the CP signal is greater than the computed 3σ noise level are defined as magnetic regions (patches).

3.2.3 Image alignment

Since the Ca II H images form the primary data set considered in this chapter, the IMAx $50'' \times 50''$ images (936×936 pixels in size and with an image scale of 0.0523 arcsec/pixel) were cropped to the field of view (FOV) of the SuFI Ca II H images covering 712×1972 pixels (with an image scale of 0.0207 arcsec/pixel) after interpolating the images to an approximately common scale and orientation.

Furthermore, the images were properly aligned by applying a cross-correlation technique on common sets of manually selected features in two image series having the closest

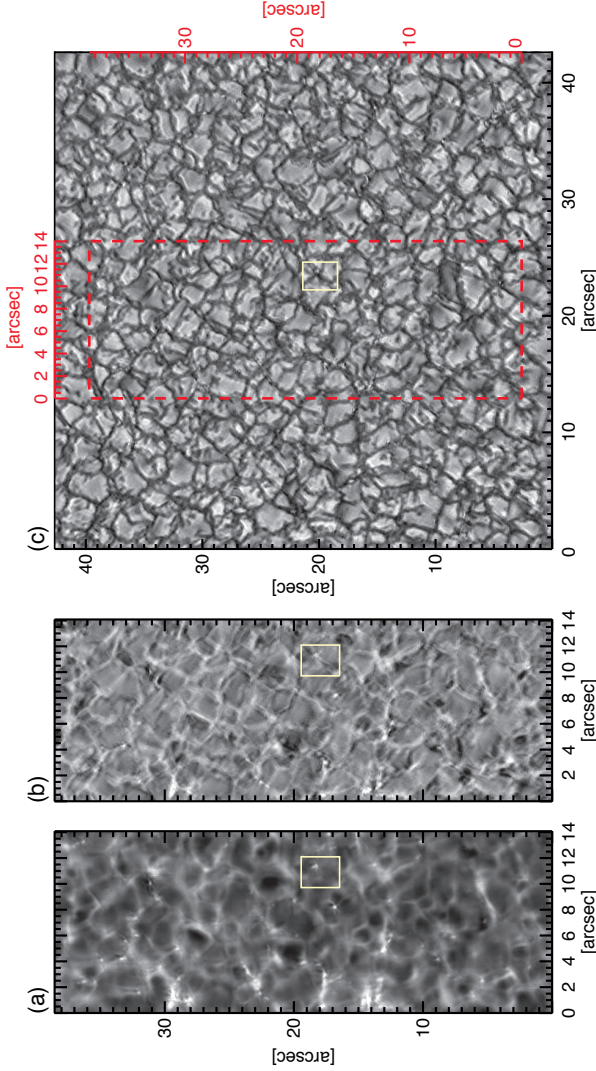


Figure 3.1: Example of co-spatial and co-temporal images from both SuFI and IMAx instruments on board the SUNRISE balloon-borne solar telescope. (a) SuFI Ca II H image. (b) Average of two line-positions at -40 *mathrmmA* and $+40$ *mathrmmA* from the Fe I 5250.2 Å line-core. Plotted is the part of the full FOV overlapping with the SuFI Ca II H image. (c) Full field of view of the continuum position of the IMAx Fe I 5250.2 Å line. The red dashed-line in this image illustrates the co-aligned area in common with the SuFI Ca II H image. The yellow box (solid-line) includes a sample Ca II MBP studied here; its temporal evolution and parameter fluctuations are presented in Fig. 3.4 and Fig. 3.5, respectively. The common coordinate system adopted for the present analysis is given below and to the left of panels a and b, as well as above and to the right of panel c.

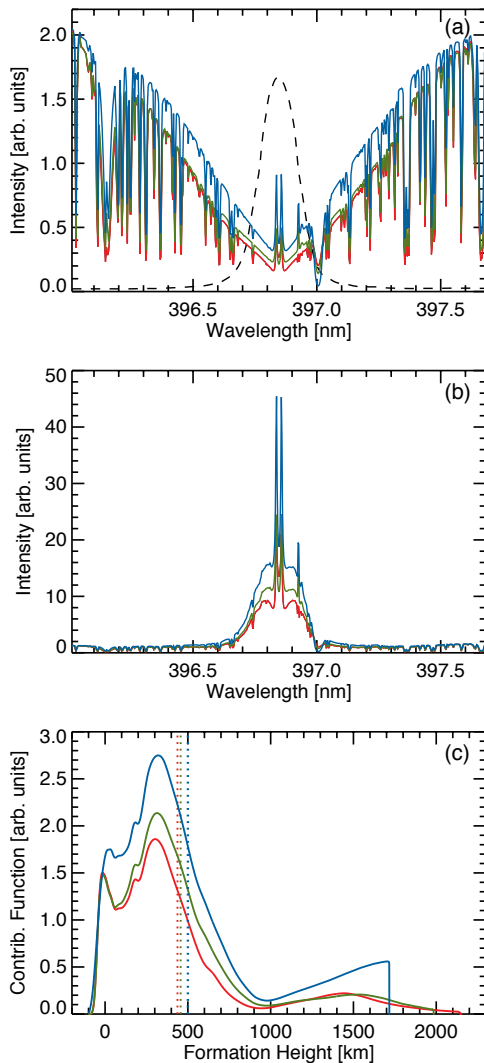


Figure 3.2: (a): Intensity profiles (synthetic spectra) of Ca II H line for three atmospheric models (see text). The dashed curve represents the transmission profile of the SUNRISE/SuFI Ca II H filter. (b): Results of the convolution of the spectra with the transmission profile shown in panel (a). (c): Line depression contribution functions for the SUNRISE/SuFI Ca II H bandpass vs. height. The vertical lines indicate the corresponding average heights of formation. Red, green and blue lines in all panels represent the FALC, FALF and FALP model atmospheres.

formation heights: Ca II H and the average of the -40 and $+40$ \AA line-positions of the IMAx Stokes I . The latter corresponds to the inner flanks of Fe I 5250.2 \AA and is a proxy for the line-core intensity. The differences in solar position of the manually selected features were iteratively minimised using the Powell minimisation function. The resulting cross-aligned images show good alignment within the spatial resolution of the observations. After co-alignment, the IMAx images were given the same coordinate system as the SuFI Ca II H images for each image sequence, so that any spatial structure, e.g., a MBP, is addressable by the same coordinates in all images. Note that the SuFI and IMAx data have different cadences, hence, we selected those Ca II H images whose observing times are closest to the IMAx line-core observations.

Figure 3.1 shows example frames of SuFI Ca II H (left), IMAx line-core (as described above; centre) and the IMAx Stokes I continuum (right) after the co-alignment.

3.3 Analysis

In Sect. 3.1, we reviewed point-like brightenings observed around the temperature minimum, i.e., H_{2V}/K_{2V} grains, product of reversed granulation, MBPs and persistent flashers. They are in many respects similar to the MBPs considered here, but many of the BPs in the literature also differ in important ways. In the present work, we investigate the SUNRISE/SuFI Ca II H MBPs which (1) are located in internetwork areas, (2) are intrinsically magnetic (as far as we can determine), (3) are not oscillations or wave-like features, (4) are not the product of reversed granulation, (5) are actual bright point-like features, i.e., have a roughly circular shape, (6) are brighter than the mean intensity of the image and (7) do not interact with other MBPs (i.e., merge or split) in their observed lifetimes. These conditions restrict us to internetwork, magnetic, non-interacting and small bright points seen in the height sampled by the SUNRISE/SuFI Ca II H passband. These MBPs turn out to be the smallest Ca II H MBPs observed so far. The small size is partly due to the upper limit of 0.3 arcsec that we set. This facilitates precise tracking and avoids any ambiguities due to a changing shape and/or varying distribution of the brightness over the internetwork MBPs. In order to isolate MBPs with the above properties, we set the following criteria:

- (1) All the MBPs are investigated in quiet internetwork areas where no significant large bright features, i.e., no obvious magnetic structure representing the network, are present in the immediate vicinity, i.e., within 3 arcsec.
- (2) The magnetic properties of the MBPs are determined from the simultaneous photospheric magnetograms (Stokes V signals) obtained from the SUNRISE IMAx instrument. Only MBPs with CP above 3σ during at least half of the MBPs' lifetime are considered. This criterion is imposed whenever simultaneous IMAx observations are available (see Table 3.1).
- (3) Criterion (2) ensures that the analysed MBPs are not due to non-magnetic phenomena such as acoustic waves. Since the magnetic information is not available for the image sequences observed on 11 June 2009, we perform a further test for these time series proposed by Cadavid et al. (2003). They found a delay between photospheric intergranular darkenings and H/K -line brightenings. We investigate such an

occurrence for our candidate MBPs by comparing the aligned simultaneous SuFI images in the CN 3880 Å and Ca II H passbands. Thus, a MBP is included only if its brightening is not preceded by a CN darkening.

- (4) The bright arc-shaped features caused by the reversed granulation may in some cases produce point-like brightenings and hence may lead to false MBP detection. These arcs and associated BPs are, however, short-lived. Therefore, in order to avoid misidentification, we exclude BPs with lifetimes less than 80 seconds (de Wijn et al. 2005).
- (5) We set an upper limit of 0.3 arcsec, i.e 2 times the spatial resolution of the SUNRISE data, for the MBP diameter. This size threshold limits the identified bright features to actual point-like features with roughly circular shapes.
- (6) A MBP is considered to be detected only if its intensity (i.e., contrast) in a Ca II H image, at any given time, rises above the mean intensity of the entire frame ($\langle I_{Ca} \rangle$).
- (7) Finally, MBPs which merge with other features or split into several MBPs (or magnetic elements) during their lifetimes are excluded. In order to sort out MBPs affected by such interactions an additional careful manual inspection is made of the temporal evolution of each MBP.

3.3.1 Tracking algorithm

Identification and tracking of Ca II H MBPs, i.e., determining their positions and other parameters in consecutive frames, is not straight forward as pointed out by de Wijn et al. (2005). We employ a tracking algorithm based on a particle tracking approach developed by Crocker and Grier (1996). This method has been widely used and has been confirmed as a precise approach in colloidal studies for identifying and tracking small roughly point-like features on a noisy and variable background (e.g., Crocker and Grier 1996; Weeks et al. 2000; Jenkins and Egelhaaf 2008), conditions very similar to the Ca II H images.

After the MBPs were automatically identified in all frames, we again visually checked each MBP in each image in order to catch and discard misidentifications, i.e., the interacting MBPs. Then, starting from the frame in which a particular MBP was first identified we tracked the selected MBP automatically backward and forward in time for as long as all criteria listed above were met.

The brightness, size and shape of a MBP change as it migrates. The tracking algorithm must deal with changing properties and distinguish the MBP from noise and other transient bright, point-like features (e.g., caused by a passing wave) in the immediate surroundings of the candidate MBP.

A region slightly larger than the area that the selected MBP is moving in (i.e., a typical area of $3'' \times 3''$) is cropped from the whole field of view. This smaller subframe generally includes fewer non-interesting bright features that may cause difficulties to the tracking procedure.

The algorithm is then initialised by determining all local intensity minima and maxima in the first subframe (the reference frame), followed by two steps applied to all images of the whole time series: (1) image restoration and (2) locating the MBP and linking the locations into trajectories.

3.3.1.1 Image processing

In order to facilitate precise tracking of the identified MBPs, the image is restored to correct for inhomogeneities such as non-uniform background solar intensity, noise and geometric distortion due to rectangular pixels. The restoration includes a correction for sudden brightenings in the immediate surroundings of the MBP, e.g., caused by a passing wave. This effect includes local intensity peaks of varying levels which in principle cannot be distinguished from the MBP even by applying an intensity threshold. In this study, we follow a sophisticated method based on the algorithm developed by Crocker and Grier (1996) to track suspended particles. The algorithm restores the image by applying a convolution kernel in which (1) the low-frequency modulation of the background intensity with a non-uniform brightness is subtracted from the entire image after boxcar averaging over a circular region with a diameter of $2w + 1$ pixel, where $2w$ is an even valued integer slightly larger than a single MBP's apparent diameter in pixels, and (2) purely random noise with a correlation length of $\lambda_n \approx 1$ (i.e., assuming single pixel instrumental noise; Jenkins and Egelhaaf 2008) is suppressed without blurring the image. The latter step is performed by convolving each image with a Gaussian kernel. In order to maintain consistency with our MBP definition, we set the former size threshold $2w$ slightly larger than the maximum diameter of the defined MBPs (i.e., 0.3 arcsec) which equals 20 pixels. Assuming a fixed size of $2w$ for the MBPs, we compute both these steps with the convolution kernel

$$K(i, j) = \frac{1}{K_0} \left[\frac{1}{B} \exp\left(-\frac{i^2 + j^2}{4\lambda_n^2}\right) - \frac{1}{(2w + 1)^2} \right], \quad (3.1)$$

where K_0 and B are normalisation constants. Thus, the filtered image (A_f) after the restoration is given by

$$A_f(x, y) = \sum_{i, j=-w}^w A(x - i, y - j) K(i, j), \quad (3.2)$$

where $A(x, y)$ is the original image, (x, y) and (i, j) are pixel coordinates in the image and kernel, respectively. As an example, panel (b) in Fig. 3.3 shows the result of such an image restoration applied to the original image shown in panel (a). Berger et al. (1995) restored *G*-band images by applying a somewhat similar kernel from a “blob finding” algorithm used to identify GBPs, followed by a further intensity enhancement of dilation and erosion processing.

To summarise, we applied a real-space, spatial bandpass filter by (wavelet) convolution of the Ca II H images with (1) a “large kernel” to cut off low spatial frequencies (i.e., eliminating the larger scale residual noise of the bright, extended background structures; the second term in Eq. (3.1)), and (2) a “small kernel” to truncate high frequency noise (the first term in Eq. (3.1)); while retaining information of a characteristic size $(2w + 1)$. As a result, we enhanced the MBP's intensity profiles at the expense of other image components, e.g., passing waves and reversed granulation. However, the enhanced images were only used to locate the MBPs and to measure their sizes. They were not used in subsequent measurements of the MBP intensity (i.e., contrast), since the restoration procedure may introduce spurious high spatial frequency artifacts in intensity. The contrast

values of the MBPs are instead measured from the original Ca II H images, by referencing their accurate positions and sizes obtained from the restored images.

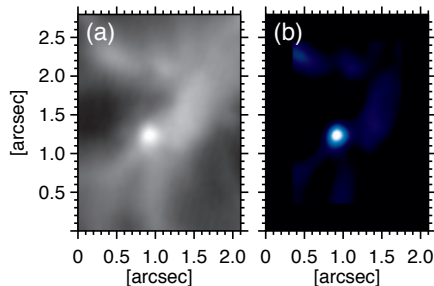


Figure 3.3: A cropped subframe including a visually selected MBP (panel *a*) is restored after its background is subtracted off and noise is reduced (panel *b*).

3.3.1.2 MBP's location and its trajectory

The position of the maximum intensity in the identified (selected) MBP in the reference frame is assigned the initial coordinates of the MBP. These initial coordinates are then assumed to be at the centre of a circular window with a fixed diameter of 20 pixels \approx 0.4 arcsec (i.e., a window slightly larger than the maximum allowed size of the MBPs with diameter of 0.3 arcsec). If more than one pixel has the same maximum intensity value, the pixel halfway between them is selected instead. Then, (1) the centre of gravity of the intensity is computed for pixels inside the circular window as new coordinates of the MBP, (2) the circular centroid is moved to the new coordinates and (3) the coordinates are iteratively checked and refined if the new centre is found to have a larger offset than 0.5 pixel from the current circular window centroid.

In the next step, the selected MBP in the reference frame is compared with the automatically identified MBP in the vicinity of its position in both the preceding and the following frames. Finally, the locations of a MBP in all consecutive frames are linked together to describe its trajectory.

The displacement of a MBP between consecutive already analysed frames can be used as an input in the tracking algorithm and is useful when a MBP disappears and re-appears as happens for the so-called ‘‘persistent flashers’’. This allows the missing points to be interpolated in the trajectory. Figure 3.4 illustrates an example of a time series for a selected MBP and its corresponding trajectory as computed by the tracking algorithm. Time proceeds row by row and from left to right.

Normally, the standard image processing and tracking algorithms locate a MBP with an uncertainty of $1/N$ of a pixel (Hunter et al. 2011), where N is the diameter of the MBP in pixels. Crocker and Grier (1996) did an error analysis for the tracking technique employed here and came to the conclusion that the error for locating the objects (MBPs in our case) can have a minimum value somewhat better than 0.05 pixel. However, considering the fact that the size and intensity variation of such MBPs may affect this pre-

cision (Hunter and Weeks 2012), we (over-) estimate that our algorithm is able to locate the MBPs within half a pixel (Crocker and Grier 1996).

3.3.2 Properties of the MBPs

For each MBP in every frame, in addition to the location, a number of further parameters were determined, as described below. Some quantities, such as intensity and size (diameter), are dependent upon the threshold used to identify the MBP or compute these parameters, since the threshold defines which pixels are included in the measurements. This point should be kept in mind when the results obtained in the following are compared with the other, previously found values. The difference in the spatial resolutions of different observations, however, is also considerable and very likely has a significantly stronger effect.

A MBP is considered to be detected if its intensity (i.e., contrast) in a Ca II H image, at any given time, rises above the mean intensity of the entire frame ($\langle I_{Ca} \rangle$). Although this criterion may cause the relatively low contrast MBPs (i.e., the ones which are less bright than the mean intensity of the whole image, but have locally high contrast) to be missed, it reduces the chance of false detections.

We discard interacting MBPs to avoid falsely assigning different features to the same MBP in the course of its lifetime. This criterion may bias the lifetime distribution to shorter lifetimes since the longer lived MBPs are statistically more likely to interact with other features. In addition, limiting ourselves to non-interacting MBPs may introduce a bias in the proper motion speeds, although this is not clear. Thus, such non-interacting MBPs may move slower since the chances for interaction increases for the faster moving MBPs that travel a greater distance. Conversely, the process of interaction could slow the MBPs down, so that the selected MBPs may be biased towards higher proper motions.

The reader should keep all such biases (caused by the selection criteria) in mind when the properties of our selected MBPs are compared with previous findings (where different selection criteria were applied and which therefore suffer from different biases).

3.3.2.1 Size

We apply two methods to measure the MBP sizes.

Method (1): The size (diameter) of a MBP is given by the radius of a circle with the same area as the MBP. Following Crocker and Grier (1996), the effective radius R of a SUNRISE Ca II H MBP with arbitrary shape is calculated as the root mean square (rms) of intensity-weighted distances of all pixels within a MBP from its location i.e., its centre of gravity of intensity obtained as in Sect. 3.3.1.2. This calculation is carried out within the circular window defined in Sect. 3.3.1.2, which, by construction, is always larger than the MBP (and the MBP's intensity will have dropped to below the threshold in all directions within this circle). This radius is misleadingly called "Radius of Gyration" in the particle tracking algorithm. It is misleading because it is not related to gyration or rotation of a particle or a MBP. Given its success in following point-like sources on a noisy and variable background, we believe that this is an appropriate method for measuring the size of Ca II H MBPs since it remains largely unaffected by a sudden brightening due to, e.g., a passing wave, etc. Hence, it is our method of choice.

Method (2): Sizes of MBPs are estimated based on the Full Width at Half Maximum (*FWHM*) of the intensity peak at the location of the MBP.

The *FWHM* of a 2D Gaussian fit to the intensity profile of photospheric MBPs has been widely used for estimating their sizes (e.g., Title and Berger 1996; Sánchez Almeida et al. 2004). The 2D Gaussian functions must deal with the narrow and dark intergranular lanes in which the photospheric MBPs typically reside. Unlike the photospheric MBPs, the Ca II H MBPs are embedded in a relatively dark internetwork area with passing bright waves. In addition, the higher contrast of Ca II H images compared to photospheric passbands (e.g., *G*-band) as well as the fact that the Ca II H data sample higher layers of the solar atmosphere, imply a larger size and more shape variation of the detected MBPs. In particular, the shape variations decrease the quality of the fits with any specific 2D Gaussian function to the identified Ca II H MBPs. An alternative approach is to measure the area across the intensity profile of the MBP when it drops to half of its intensity peak (maximum) value. Assuming a roughly circular shape of the MBPs and hence a circular level set for the Gaussian distribution, the (mean) *FWHM* of a MBP is calculated as the diameter of a circle with the same area as measured.

The latter definition (interpretation with a *FWHM*) results in diameter that are on average 21% larger and more variable than the ones obtained from the tracking algorithm. We prefer the definition based on the tracking algorithm (*method 1*), since it deals better with sudden brightenings of the image when travelling bright waves cross the MBP. At such moments *method 2* can give an arbitrarily large size. Therefore, the size values used in this chapter are based on the first definition.

3.3.2.2 Lifetime

The birth and death times of many MBPs were not observable in our image sequences mainly because of the relatively short time series as well as the relatively small field-of-view. Therefore, the lifetime was computed only for those MBPs that were born and died within the course of the time series and which did not enter or leave the field-of-view during the time series. A MBP is considered to be born when its brightness first rises above $\langle I_{Ca} \rangle$ and is considered dead when its intensity is observed to permanently drop below $\langle I_{Ca} \rangle$, i.e., it does not rise again to above this detecting threshold for 160 sec (i.e., 2 times our lifetime threshold) in the following frames. These additional frames are considered in order to avoid underestimating the lifetimes of MBPs with repetitive brightenings, e.g., the persistent flashers. If a MBP reappears within 30 pixels (i.e., about twice our MBP's size threshold) of its original location within 160 sec we consider it to be the same MBP. If these conditions are not met then we assume the new brightening to belong to a new MBP.

The relatively short time series biases the measurements towards shorter lifetimes and hence the lifetime distribution must be corrected (see Sect. 3.4.3.4). Two possible sources of uncertainty of the measured lifetime are the exposure time of the SuFI Ca II H images (i.e., 1 sec) and the observing cadence. The latter parameter differs for different time series used in this study and thus we consider an average value of the cadences presented in Table 3.1, weighted by the number of MBPs identified in each image sequence. Therefore, the Ca II H MBPs' lifetimes reported in this chapter have an overall uncertainty of 9 sec.

3.3.2.3 Intensity

The mean value of the intensity inside the area of each detected MBP is referred to as its absolute intensity. The intensity values are measured from the original phase-diversity reconstructed Ca II H images, by referencing their accurate positions and sizes obtained from the restored images (described as in Sect. 3.3.1.1, Sect. 3.3.1.2 and Sect. 3.3.2.1). The contrast of the MBP is then determined by normalising its intensity to the mean intensity of the entire Ca II H frame that the MBP is observed in, i.e., we form the contrast relative to the average quiet-Sun.

3.3.2.4 Horizontal velocity

The instantaneous horizontal velocity (v) was determined by taking the difference between the locations of a MBP (known to sub-pixel accuracy) in two consecutive frames and dividing by the time between frames. The statistical uncertainty in measuring this frame-to-frame horizontal velocity (σ_v) was computed from the error propagation analysis. We can then assess the mean value of the horizontal velocity $\langle v \rangle$ and its uncertainty for each MBP, consisting of n time steps (frames), using the weighted mean (Wall and Jenkins 2003),

$$\langle v \rangle = \frac{\sum_{j=1}^n (v_j / \sigma_j^2)}{\sum_{j=1}^n (1 / \sigma_j^2)}, \quad (3.3)$$

where v_j and σ_j^2 are the j th determined instantaneous horizontal velocity (v) and its variance, respectively. The best estimate of the uncertainty of $\langle v \rangle$ is then,

$$\sigma_{\langle v \rangle} = \sqrt{\frac{1}{\sum_{j=1}^n (1 / \sigma_j^2)}}; \quad (3.4)$$

We also use Eqs. (3.3) and (3.4) to calculate the total mean value of the horizontal velocity and its uncertainty. Note that we do not take the normal average of the velocity values to determine the mean velocities (for each MBP or the mean over all MBPs), since different velocity values have different uncertainties. This latter effect arises because of different distances a MBP may travel in equal time steps and/or different time steps due to (1) a variable cadences within an image sequence caused by missing or discarded images, and/or due to (2) a temporarily undetected MBP. Such an analysis results in an average uncertainty (weighted average over all MBPs) of 0.02 km s^{-1} in the horizontal velocities.

3.3.3 Magnetic field

The magnetic properties of the Ca II H MBPs were investigated by comparing with maps of CP and LP determined as described in Sect. 3.2.2. In order to avoid noise introducing false detections, isolated single pixels lying above 3σ were not counted as signal. The magnetic regions lying above 3σ are outlined in Fig. 3.4 by red and yellow contours for opposite polarities of the CP . A Ca II H MBP is then considered magnetic if it overlaps with the computed photospheric magnetic patches for more than 50% of its lifetime. The magnetic field is generally still present at times when it is not associated with the MBP but

either lies below the 3σ threshold, or just fails to overlap with the MBP. The MBP shown in Fig. 3.4 seems to be almost completely inside a magnetic patch of negative polarity for most of the time. However, there are times (e.g., at the time 3041 sec from UT midnight) when this MBP is observed just outside the boundary of the magnetic patch.

The peak values of CP and LP over a MBP's area is considered as corresponding polarisation degrees of the MBP measured from the spatially smoothed non-reconstructed data (obtained as described in Sect. 3.2.2).

3.3.4 Inversions

We use the results of SIR code (Stokes Inversion based on Response functions; Ruiz Cobo and del Toro Iniesta 1992) inversions of the IMAx Fe I 5250.2 Å Stokes vector carried out by L. R. Bellot Rubio. The code numerically solves the radiative transfer equation (RTE) along the line of sight (LOS) for the Zeeman-induced polarisation of light under the assumption of local thermodynamic equilibrium (LTE). The code deals with all four Stokes parameters (I , Q , U , V), any combinations of which are fitted for any arbitrary number of spectral lines. Then, the differences between the observed and synthetic Stokes profiles are iteratively minimised by modifying an initial model atmosphere. Details of the employed SIR inversions can be found in the paper by Guglielmino et al. (2012).

The Harvard Smithsonian Reference Atmosphere (HSRA; Gingerich et al. 1971) is used as the initial model atmosphere. The temperature has two nodes and the inversions recover the temperature stratification in layers between $\log(\tau) - 4$ and 0 (where τ is the optical depth of the continuum at 5000 Å). Stray light is not taken into account for this inversion and a magnetic filling factor of equal to unity is assumed. This implies that the magnetic field strength from the SIR code is a lower limit of the true value.

3.4 Results and discussion

A total of 107 Ca II H MBPs were identified in 6 different image sequences obtained by the SuFI instrument, where each MBP is counted only once during its lifetime. We found a relatively low MBP average number density of 0.03 (Mm)^{-2} corresponding to $\approx 1.8 \times 10^5$ MBPs at any given time on the whole solar surface. This number is roughly an order of magnitude smaller than the number of granules on the solar surface at any given time. This low number can be due to the rather restrictive identification criteria, in particular that we consider only small isolated MBPs (comparable in size with the SUNRISE spatial resolution) that do not merge or split while they migrate. These criteria restrict our sample mainly to internetwork MBPs. The parameters intensity contrast, horizontal velocity and size, were calculated for each MBP at every time step. The lifetime was measured only for 47 MBPs whose birth and death times were both observable. The MBP is considered magnetic if the average of the local Stokes V signal within a 3×3 pixel box around its corresponding location is higher than the 3σ level over at least 50% of the detected MBP lifetime.

3.4.1 A case study: Tracking an individual Ca II H MBP

Here, we study the evolution of one of the identified MBPs in detail. Snapshots of the Ca II H intensity in the region around the MBP as well as overlaid contours of CP are plotted in Fig. 3.4. The MBP moves within an area of roughly 1×2 arcsec² in the course of its lifetime of 1321 ± 13 sec (see its trajectory in the bottom right frame). The MBP is located almost always inside a magnetic patch, except for a few moments such as the one that occurs at time 3041 sec (all times are given relative to UT midnight). At this time, the MBP lies mainly outside the boundary of the magnetic patch, however, a small part of its area overlaps with $CP > 3$ signal. Note the irregular intervals between the frames. Figure 3.5 illustrates the temporal behaviour of physical parameters of the MBP. It has a mean intensity of $1.65 \pm 0.01 \langle I_{Ca} \rangle$ and moves with a mean proper motion velocity of 1.86 ± 0.08 km s⁻¹.

The frame-by-frame intensity variation (thin curve) is plotted in panel (a). The intensity curve smoothed by a boxcar averaging of 5 frames is overplotted (red in the online version). In order to estimate the effect of transient brightenings, e.g., passing waves, on the MBP's intensity variation, we overplot the variation of the averaged intensity within the MBP (smoothed by a 5-frames boxcar averaging; blue dashed curve) measured in the restored images, i.e., the images from which the larger wave-like features are subtracted (see Sect.3.3.1.1); the curve is in arbitrary units. A comparison between the two smoothed intensity curves validates the intrinsic intensity variation of the MBP. Panel (b) represents the variation of horizontal velocity smoothed over 5 frames by weighted averaging, described in Sect. 3.3.2.4 (thick curve; red in the online version). The thin vertical solid lines indicate the error bars. The values of intensity and horizontal velocity vary by a factor of nearly 2 and 3, respectively.

Close inspection of panels (a) and (b) reveals an anti-correlation between these two quantities for the MBP. The vertical dashed lines mark the times when the intensity maxima and minima fall together with minima and maxima in horizontal velocity, respectively. However, two peaks in the horizontal motion plot and the corresponding dips in intensity plot, indicated by vertical dot-dashed lines, show a small time delay. An anti-correlation between the intensity and horizontal velocity is also observed in some other MBPs, sometimes also with a small time delay. All MBPs do not show it.

Panel (c) in Fig. 3.5 illustrates the evolution of the MBP's diameter, which is found to be constant to within 10 – 15 %.

The CP (obtained as described in Sect. 3.2.2 and normalised to the continuum intensity $\langle I_c \rangle$ averaged over the full IMAx FOV), plotted in panel (d), is always above the 3σ noise level, which demonstrates the magnetic origin of this MBP.

The variation of total linear polarisation (LP ; see Sect. 3.2.2), normalised to $\langle I_c \rangle$, is plotted in panel (e). The dashed and dotted lines in panel (e) show the 3σ and 2σ noise levels. The LP is almost always below the 1σ level (indicated by the dot-dashed line), implying that the linear polarisation signal detected at the position of the small MBP is not significant at the 1σ level. Nevertheless, inversions return a strongly inclined field for such a MBP with inclination angles between 78 and 90° in the course of its lifetime. This result, however, is probably affected by noise as we find by comparing with inclinations derived from the locations of the MBP in images sampling different heights in the atmosphere (Jafarzadeh et al., in preparation).

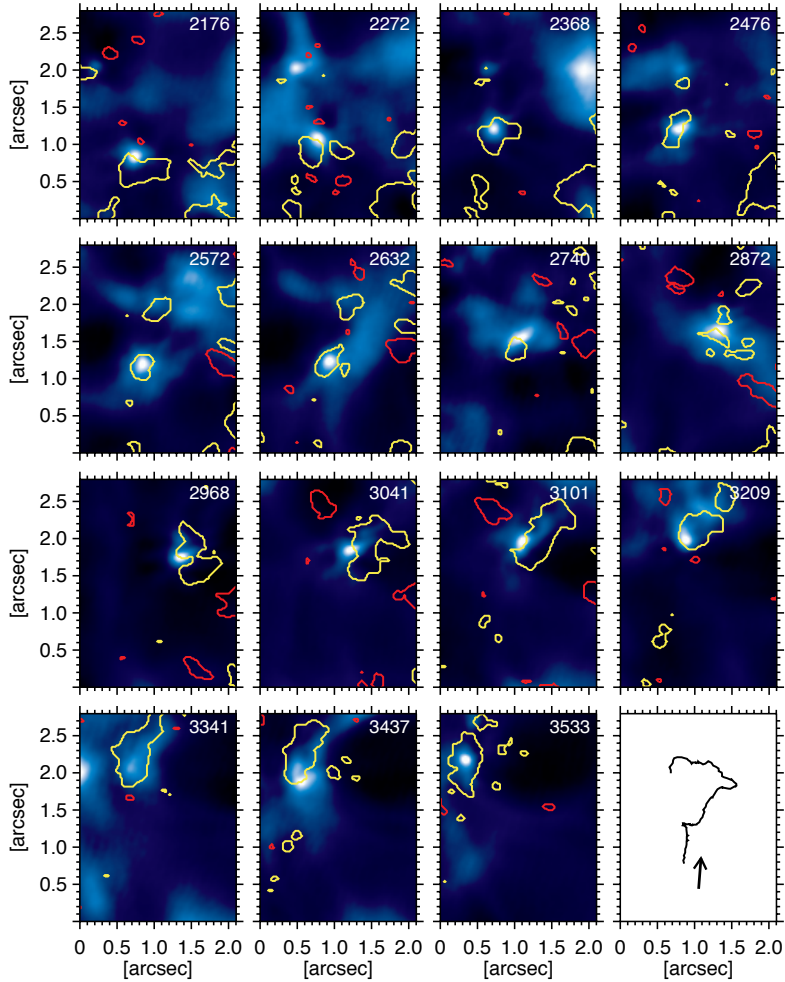


Figure 3.4: Temporal evolution of a selected MBP (Lifetime: 1321 sec), observed on 9 June 2009 in the SUNRISE/SuFI Ca II H passband. Time proceeds row by row and from left to right within each row. The red and yellow contours outline magnetic regions with opposite polarities of the line-of-sight magnetic field component and match the 3σ level in Stokes V . In the bottom-right panel, the trajectory of the MBP is plotted. The arrow marks the sense of the motion. The time from UT midnight, in seconds, is shown in the upper-right corner of each frame. Note the irregular intervals between frames.

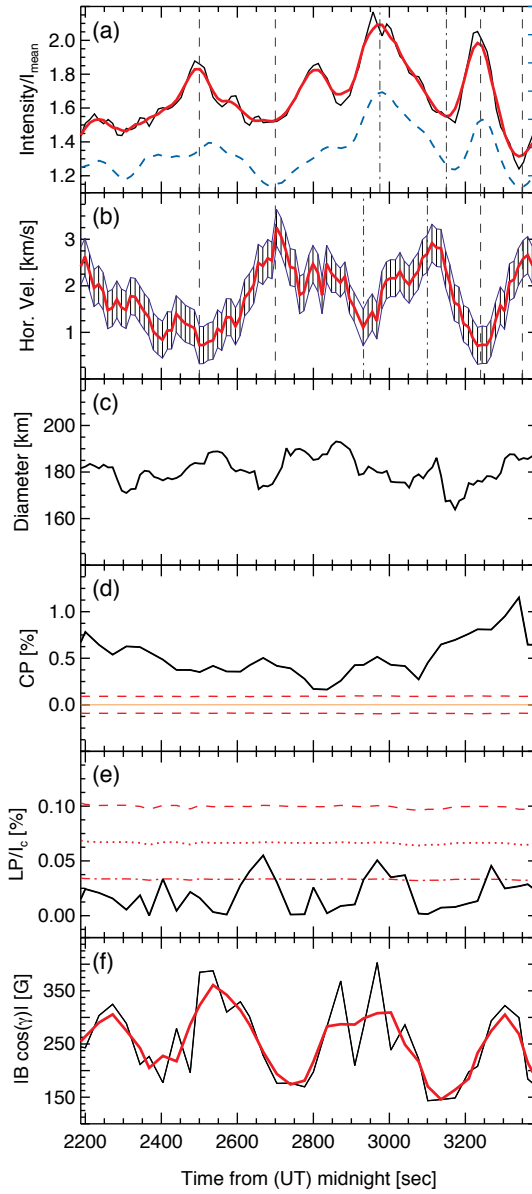


Figure 3.5: (Caption on the following page.)

Figure 3.5: Evolution of (a) the intensity contrast, (b) horizontal velocity, (c) diameter, (d) CP , a measure of the strength of Stokes V , (e) total net linear polarisation LP , and (f) field strength of the selected MBP shown in Figs. 3.1 and 3.4. CP and LP are normalised to Stokes I continuum. In panel (a) and (f), the thin curves respectively represent the time variation of average intensity and the unsigned longitudinal magnetic field within the MBP while the smoothed thick lines (red in online version) show a 5-frames boxcar average. They are both normalised to the mean intensity of the image. The (blue) dashed curve in panel (a) represents the smoothed average intensity within the MBP, in arbitrary unit, from the restored images (see main text). Evolution of horizontal velocity, smoothed within 5 frames by weighted averaging, is plotted as the thick line (red in the online version) in panel (b) while the thin vertical solid lines indicate the error bars. The vertical dashed lines in the two upper panels serve to guide the eye to the general anti-correlation between intensity and horizontal velocity (see main text). The 3σ noise levels for both CP and LP , are drawn as dashed-lines in panels (d) and (e), while the dotted and dot-dashed lines in panel (e) are the 2σ and 1σ noise levels, respectively. The unsigned longitudinal magnetic field depicted in panel (f) was computed from the SIR inversions (see main text).

The values of the field strength multiplied by the absolute value of the cosine of the inclination angle $|B \cos(\gamma)|$ (i.e., the unsigned longitudinal component of the magnetic field) returned by the SIR inversion code are plotted in panel (f). We plot the variations of $|B \cos(\gamma)|$ since this value is retrieved more reliably than B (see Sect. 3.4.3.6). $|B \cos(\gamma)|$ varies between 108 and 361 G assuming that the magnetic feature is spatially resolved. If this particular MBP is spatially unresolved by SUNRISE (Riethmüller et al. 2013), which is likely given the low CP value, these field strength values are the lower limits.

Figure 3.6 shows a $|B \cos(\gamma)|$ map of the MBP at time 3304 sec from UT midnight. $|B \cos(\gamma)|$ at the position of this small internetwork MBP reaches a maximum value of 322 G at this point in time. The over-plotted solid contours show the field strength levels of 100, 200 and 300 G. The location of the Ca II H MBP is overlaid (dashed contour). The maximum intensity of the MBP, indicated by a cross, is offset by 0.05 arcsec (20% of the diameter of the MBP) relative to the location of the highest $|B \cos(\gamma)|$. This offset may represent a small inclination of the flux tube from the vertical direction, since the Ca II H brightness and $|B \cos(\gamma)|$ are determined at different heights. We will consider inclinations of magnetic elements in a separate chapter. A small observing time difference between the SuFI Ca II H and IMAx images can also be a reason for such an offset.

3.4.2 Persistent flasher

Among the 107 analysed MBPs 7 are similar to those named persistent flashers by Brandt et al. (1992). Their main difference to the majority of the selected MBPs is the occurrence of intensity variations about the detection limit ($\langle I_{Ca} \rangle$) which give rise to the apparent succession of flashes.

An example of such a MBP is shown in Fig. 3.7, which shows the Ca II H intensity at 6 times within an area of 2×2 arcsec². The contours outline magnetic regions with CP above the 3σ level. The temporal variations of different parameters of the MBP are

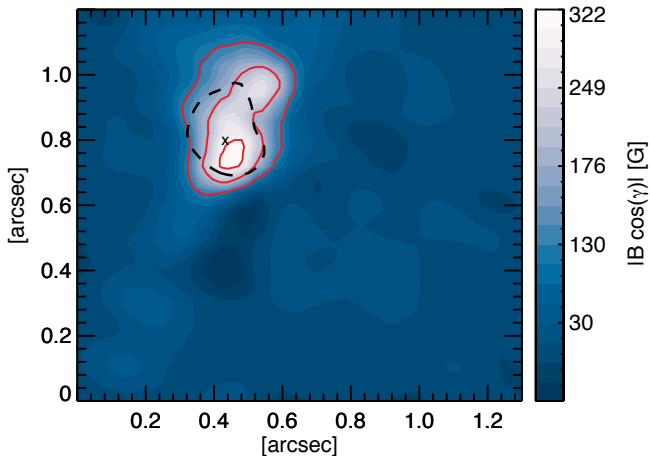


Figure 3.6: Map of the unsigned longitudinal component of magnetic field, $|B \cos(\gamma)|$, centred on the MBP shown in Fig. 3.4 at time 3304 sec from UT midnight. The solid contours indicate the height-independent $|B \cos(\gamma)|$ at 100, 200 and 300 G. The Ca II H MBP's area is indicated by the dashed contour.

plotted in Fig. 3.8. From panel (a) it is evident that between two bright phases the intensity of the MBP drops below the intensity limit of the detection giving it the appearance of flashing, although its intensity variations are no larger, in a relative sense, than those of the MBP displayed in Fig 3.5. Interestingly, an anti-correlation between the intensity and the horizontal velocity in panel (b) is also seen for this persistent flasher. The flasher travels with a mean proper motion velocity of $2.82 \pm 0.06 \text{ km s}^{-1}$. The size is constant within a range of 10% (panel (c)). We cannot rule out that the large excursion of the size at the beginning of the plotted time series is due to a false detection at the very beginning of the MBP's identification. Similar to the other MBPs under study, CP always lies above the 3σ noise level, also for the persistent flasher; see Fig. 3.8d. Again, the LP signal lies almost always below the σ level (dot-dashed line). Therefore, the same conclusion as for the MBP studied in Sect. 3.4.1 can be made here of the field inclination. The $|B \cos(\gamma)|$, plotted in panel (f), has a mean value of 190 G, smaller than the majority of the normal, non-flasher MBPs under study.

In this investigation, the few “persistent flashers” (6% of all identified MBPs) clearly have a magnetic origin, with horizontal velocities of 2.4 km s^{-1} on average. This makes the persistent flashers about equally mobile as the other Ca II H MBPs (see Sect. 3.4.3.2). The flashers differ from the normal MBPs mainly in that they (the flashers) tend to be less bright. The persistent flashers are on average 47% less bright than the other MBPs studied here (see Sect. 3.4.3.1). This causes the occurrence of intensity variations (\approx of a factor of 3) around our detection limit and hence the intermittent appearance of the MBP. We conclude that persistent flashers are less bright, but otherwise normal MBPs.

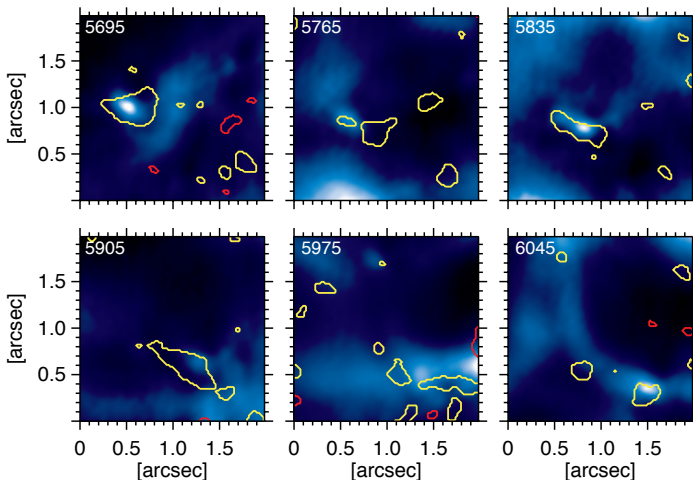


Figure 3.7: Temporal evolution of a MBP similar to the persistent flasher of Brandt et al. (1992). Time proceeds row by row from left to right in each row. The yellow and red contours indicate magnetic patches of opposite polarities. The time in seconds, from UT midnight, is given in the upper-left corner of each frame.

3.4.3 Statistical studies

Table 3.2 summarises the number and mean values of the MBPs studied here. The mean lifetime value is to our knowledge the longest obtained for Ca II H MBPs so far (see Sect. 3.4.3.4), although it is a lower limit due to the finite lengths of the employed time series. This reflects the excellent quality of the SUNRISE/SuFI observations. The mean diameter is influenced by our criteria to only concentrate on the isolated and point-like features which do not display any internal fine structure.

Distributions of the intensity, horizontal velocity and size of all 107 MBPs, as well as the lifetime of the 47 MBPs for which it is available, are presented in Fig. 3.9. Before discussing these properties in detail, we point out that all of the MBPs for which simultaneous polarimetric observations were available ($\approx 50\%$ of all MBPs) are clearly associated with magnetic fields (see Sect. 3.4.3.5). It is useful to bear this in mind when reading the following sections.

The difference in the spatial resolutions and scattered light between different sets of data in the literature is considerable and may well be a dominant cause of discrepancies between various studies. In addition, observing in different wavelengths and hence sampling different heights in the solar atmosphere affects the results. The same is true for the variation in the lengths of observed image sequences. Finally, differences in definition of MBPs may also influence the results (e.g., thresholds used).

Mean values of MBP physical parameters determined here are compared with past findings in Table 3.3. In this table, because of the common origin and the similarity in appearance of the MBPs in *G*-band, TiO-band and Ca II H/K passbands (de Wijn et al.

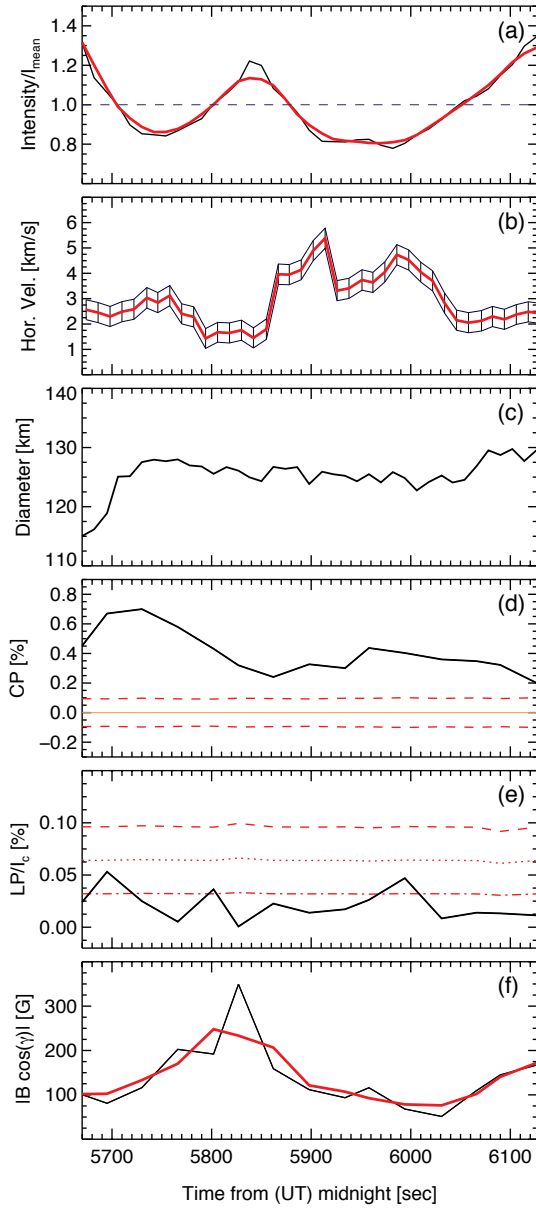


Figure 3.8: The same as Fig. 3.5, but for the persistent flasher shown in Fig. 3.7.

2008), we have also included G -band and TiO passbands, which normally sample lower regions of the solar atmosphere than Ca II H/K. However, the sampled heights depend on the filter widths. Thus, the measured Ca II H/K signal also gets contributions from the lower layers of the atmosphere. The average horizontal speed of non-magnetic K-grains is also listed in this table in order to illustrate the difference to MBPs.

3.4.3.1 Intensity

The distribution of all 5677 measured instantaneous intensity contrasts of the 107 MBPs is represented by the outlined histogram in Fig. 3.9a. Its exponential fit with an e-folding width of $0.22 \langle I_{Ca} \rangle$ is overlaid as a red, dot-dashed line (fit limited to the range of 1.45 to $2.7 \langle I_{Ca} \rangle$).

The intensity contrast distribution shows a lower limit of $0.69 \langle I_{Ca} \rangle$ and the brightest detected MBP reaches a maximum value of $2.86 \langle I_{Ca} \rangle$. The mean contrast value, averaged over all MBPs and all time steps is $1.48 \langle I_{Ca} \rangle$. The few intensity values less than $\langle I_{Ca} \rangle$ belong to persistent flashers whose intensity drops below the detection limit ($\langle I_{Ca} \rangle$) at some moments of time, so that the average is low, although in between they are clearly visible.

The filled histogram in Fig. 3.9a is the distribution of the lifetime average of intensity contrast of each individual MBP of all 107 MBPs.

A comparison with values in the literature is summarised in Table 3.3. Such a comparison is not straightforward because observations at different wavelengths, with different filter widths and different spatial resolution give a range of contrasts. Also, none of the non-SUNRISE studies of Ca II H or K BPs provides their average contrasts. Berger et al. (1995) showed that the intensity of their GBPs, on average, reaches 1.27 relative to the quiet-Sun average. A range of $0.8 - 1.8 \langle I_{QS} \rangle$ was reported for the same wavelength by Sánchez Almeida et al. (2004) at an estimated spatial resolution of 135 km

Table 3.2: Summary of averaged properties of the Ca II H MBPs

Parameter	Mean value ^a	No. of MBPs
Intensity	$1.48 \pm 0.3 \langle I_{Ca} \rangle$	107
Horizontal Velocity	$2.2 \pm 1.8 \text{ km s}^{-1}$	107
Diameter	$0.2 \pm 0.02 \text{ arcsec}$	107
Lifetime	$673 \pm 526 \text{ sec}$	47
CP ^b	$0.32 \pm 0.21 \%$	53
$ B \cos(\gamma) $ ^b	$142 \pm 87 \text{ G}$	53

^a The uncertainty estimates were calculated from the standard deviations of the parameters' distributions. For formal errors see main text.

^b From SUNRISE/IMaX

CP : Circular polarisation degree, described as in Sect. 3.2.2; $|B \cos(\gamma)|$: unsigned longitudinal component of magnetic field.

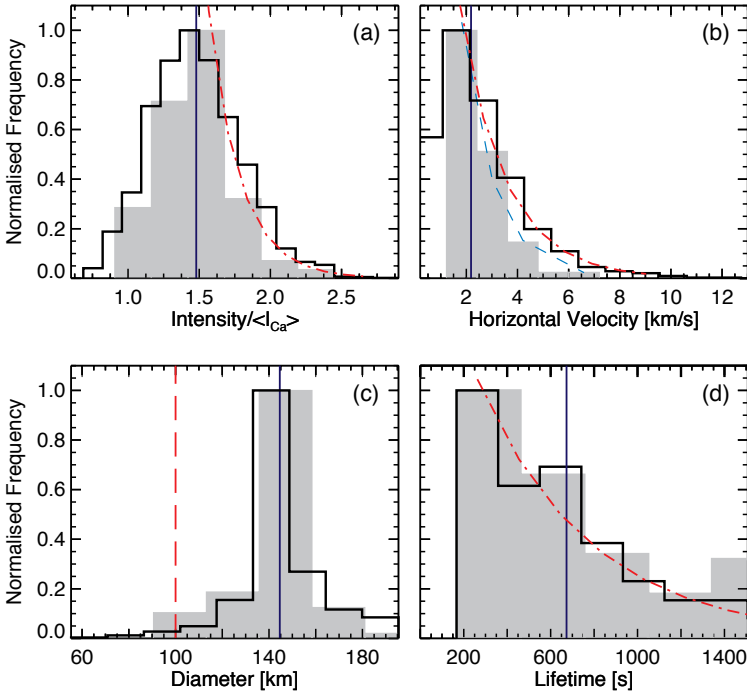


Figure 3.9: Statistical properties of the detected SUNRISE Ca II H MBPs. (a): Distribution of mean intensity contrast for all 5677 individual measurements (black, outlined histogram) and of the time averaged contrast of all 107 MBPs (grey, filled histogram). (b): Distribution of all 5570 individual measurements of horizontal velocity (black, outlined histogram) and of the values averaged over their respective lifetimes of the 107 studied MBPs (grey, filled histogram). (c): Histogram of mean size (diameter) of all 107 MBPs (grey, filled histogram) and all 5677 individual measurements (black, outlined histogram). The vertical dashed line indicates the spatial resolution achieved by the SUNRISE telescope. (d): Histogram of lifetimes of 47 MBPs (black, outlined histogram) and of corrected lifetimes (grey, filled histogram; see main text). The vertical solid lines indicates the mean values of the distributions. The fits (dot-dashed and dashed curves) are explained in the main text.

on the Sun. Note that the lower boundary of this range means that these BPs are darker than $\langle I_{QS} \rangle$ implying that the GBPs were bright only with respect to the intergranular lanes surrounding them. A mean value $1.17 \langle I_{QS} \rangle$ was obtained by Möstl et al. (2006) for magnetic GBPs.

Riethmüller et al. (2010) studied the peak contrast of the MBPs observed in different passbands of the SUNRISE observatory between 2140 Å and 5250.2 Å, including Ca II H 3968 Å. They found mean values of the peak contrast equal to 1.11, 1.35, 1.52, 1.60, 1.89 and 2.31 $\langle I_{QS} \rangle$ for 5250, 3120, 3000, 3880, 3968 and 2140 Å, respectively. Their mean contrast value of the Ca II H MBPs is somewhat larger than the 1.48 we measured in this study. This difference partly reflects the different criteria employed to identify the MBP studied (we restrict ourselves to smaller MBPs). Moreover, they measured the peak contrast of each MBP, which is expected to be higher than the contrast averaged over a MBP's area as we determined.

3.4.3.2 Horizontal velocity

The distribution of the instantaneous proper motion velocity of all individual 5570 frame-to-frame measurements made in this study is given by the outlined histogram in Fig. 3.9b. The red, dot-dashed line is the exponential fit to this histogram (for velocities larger than 1.8 km s^{-1}) with an e-folding width corresponding to a horizontal velocity of 1.8 km s^{-1} . However, lower velocities ($< 1 \text{ km s}^{-1}$) are under-represented relative to the exponential fit, suggesting that the MBPs tend not to stay at a given spot. The distribution displays a tail reaching up to 10 km s^{-1} . There are a few measurements at higher velocities which lie outside the range of this histogram reaching up to 15.5 km s^{-1} . Using the values of temperature, density and gas pressure of the VAL-C atmospheric model (Vernazza et al. 1981) at the average formation height of the SUNRISE Ca II H MBPs (500 km), the sound speed is estimated to be between 6.5 and 7 km s^{-1} . Thus, Fig. 3.9b implies that about 3.5% of the time the MBPs' motion is supersonic.

The distribution of the mean value (lifetime average) of the horizontal velocity of each MBP is over-plotted (filled histogram). The exponential fit to this histogram (with an e-folding width corresponding to a horizontal velocity of 1.3 km s^{-1}) is plotted as a blue, dashed line. Power law fits were found to be unacceptable for both these distributions. The statistics reveal that the mean horizontal velocity of the MBPs studied in this work varies between 1.2 and 6.6 km s^{-1} (mean values for individual MBPs) with an average value of 2.2 km s^{-1} (averaged over all MBPs).

We remind the reader that the value of the frame-to-frame velocity is biased by the measurement error in positioning the MBPs (see Sect. 3.3.1.2). An upper limit on the velocity induced by this error is about 0.7 km s^{-1} . The effect of this error is greatly decreased when computing the velocities averaged over the lifetimes of individual MBPs, as mentioned above (see Sect. 3.3.2.4).

As summarised in Table 3.3, the measured horizontal velocities of the Ca II H MBPs are larger than the velocities of MBPs in the photosphere, which are quoted as 0.06 km s^{-1} (van Ballegooijen et al. 1998), $1 - 1.4 \text{ km s}^{-1}$ (Möstl et al. 2006), although higher horizontal velocities of up to 5 km s^{-1} for a few indicated BPs have been reported in the literature (Berger and Title 1996). Note that van Ballegooijen et al. (1998) determined horizontal velocities by tracking corks so that these refer to averaged motions of clusters of

Table 3.3: Comparison of the mean values of properties of BPs obtained in this study with values in the literature.

Reference	Telescope (Diffraction Limit)	Passband (FWHM)	Pol. Info. ^a	Feature ^b	Intensity [$\langle I_{GS} \rangle$]	H. Velocity [km s^{-1}]	Diameter [arcsec]	Lifetime [s]
This study	SUNRISE (0'10)	Ca II H (1.8 Å)	Yes	MBP	1.48	2.2	0.2	673
Riehmüller et al. (2013)	SUNRISE (0'10)	CN (8.0 Å) ^c	Yes	MBP	-	-	0.45	-
Keys et al. (2011)	DST (0'12)	G-band (9.2 Å)	No	MBP	-	1.0	-	91
Abramenko et al. (2010)	NST (0'11)	TiO (10 Å)	No	IBP	-	-	≈0.16	< 120
Crockett et al. (2010)	DST (0'12)	G-band (9.2 Å)	No	MBP	-	-	0.31	-
Riehmüller et al. (2010)	SUNRISE (0'10)	Ca II H (1.8 Å) ^c	Yes	MBP	1.89	-	-	-
Möstl et al. (2006)	SST (0'1)	G-band (11.6 Å)	No	MBP	1.17	1.11	0.28	263
de Wijn et al. (2005)	DOT (0'2)	Ca II H (1.3 Å)	No	IBP	-	-	-	258
Sánchez Almeida et al. (2004)	SST (0'1)	G-band (10.8 Å)	No	GBP	0.8-1.8	-	0.25	225
Nisenson et al. (2003)	DOT (0'2)	G-band (10 Å)	No	GBP	-	0.89 ^d	-	552
Berger and Title (2001)	SVST (0'2)	G-band (12 Å)	Yes	GBP	-	1-5 ^e	0.145	-
Wellstein et al. (1998)	VTT (0'3)	Ca II K (0.3 Å)	No	NBP	-	6.6	-	-
Steffens et al. (1996)	VTT (0'3)	Ca II K (0.3 Å)	No	K-grain	-	50	-	-
Berger et al. (1995)	SVST (0'2)	G-band (12 Å)	No	GBP	1.27	-	0.35	-
Muller et al. (1994)	Pic du Midi (0'25)	5750 Å (60 Å)	No	NBP	-	1.4	-	1080 ^f
Soltau (1993)	VTT (0'3)	Ca II K (0.3 Å)	No	IBP	-	2.5	-	-
Muller (1983)	Pic du Midi (0'25)	5750 Å (60 Å) ^c	No	IBP	-	-	-	540

^a Polarisation (magnetic field) information^b IBP: Internetwork Bright Point; NBP: Network BP; MBP: Magnetic BP; GBP: G-band BP^c See main text for other passbands^d rms velocity^e From Berger and Title (1996)^f From Muller (1983), who found this value for NBPs.

BPs instead of isolated ones. However, our value is significantly smaller than the average of 6.6 km s^{-1} (Wellstein et al. 1998) and 49 km s^{-1} (Steffens et al. 1996) reported for the Ca II H internetwork K-grains as well as $7-10 \text{ km s}^{-1}$ horizontal velocities of the network BPs found by Wellstein et al. (1998). Whereas the somewhat larger values we find compared to the GBPs may be acceptable (e.g., caused by swaying of magnetic flux tubes), the huge range of values quoted for the chromosphere (Ca II H and K observations) shows how difficult it is to compare these values. Obviously, the different measurements refer to very different kinds of features. In particular, K-grains refer to a wave phenomenon and cannot be compared with the magnetic features studied here. There still remains the discrepancy with the large value for network BPs published by Wellstein et al. (1998). Possible explanations for this are: (a) Network BPs (NBPs) move much faster than internetwork BPs (IBPs). (b) Because Wellstein et al. (1998) had no magnetic information, their measurements may have been affected by misidentification of passing waves even in the case of NBPs. We obtained stable results only after applying a careful filtering technique. (c) Proper motion velocities derived from ground-based observations tend to be exaggerated due to differential seeing-induced deformations in different frames of the time series.

Since we are unaware of any studies (e.g., in the *G*-band) suggesting higher horizontal velocities of network BPs than internetwork MBPs, and due to the much larger horizontal velocities found by Wellstein et al. (1998) than of photospheric BPs, we conclude that explanations (b) and (c) are more likely than (a).

3.4.3.3 Size

The distribution of the MBP diameters obtained from all 5677 individual measurements are represented by the outlined histogram in Fig. 3.9c. The MBPs' diameters range between 85 and 195 km or ≈ 0.11 and ≈ 0.27 arcsec, with a mean value of 150 ± 15 km ($\approx 0.2 \pm 0.02$ arcsec).

The filled grey histogram represents lifetime averages. Both histograms exhibit a rather narrow peak centred at ≈ 150 km corresponding to a diameter of ≈ 0.2 arcsec. This narrowness of the peak reflects our size criterion in which a SUNRISE Ca II H MBP was defined as a bright, point-like feature with a maximum diameter of 0.3 arcsec at any given time. On the other hand, the MBPs' size distribution extends down to the resolution reached by SUNRISE of roughly 100 km in the best time series. Therefore, the typical diameter of the MBPs studied here is between 0.15 and 0.25 arcsec. Possible explanations for the missing smaller MBPs in our statistics (down to the theoretical resolution limit) are: (a) Resolution of the Ca II H images is somewhat larger (e.g., 0.2 arcsec) than the best resolution reached by SUNRISE. (b) The smaller features are not bright enough to be identified by our detection procedure. (c) The smaller features are not long-lived enough to be considered as a MBP based on our restricted criteria (see Sect. 3.3).

Comparing the diameters obtained here with those reported in the literature is not straight forward, since they depend on the spatial resolution of the employed observations, the level of solar activity in the observed area (internetwork, network, plage, etc.) and on the technique used to determine the size. In this study, in order to avoid the effect of fine structure, we have set an upper limit on the size, so that we do not include the larger features that are also present in the SUNRISE data. We review the reported values of the

BP sizes observed in the photosphere and the low chromosphere in Table 3.3. However, it is important to remember that the magnetic field of magnetic elements expands with height. Therefore, under the assumption that the brightness structures scale with the size of the magnetic features, a MBP seen in the Ca II H passband should be larger than in the *G*-band, and larger still than in the TiO band (which corresponds essentially to the continuum outside sunspot umbrae) under the same observing conditions.

Using the network flux-tube model of Solanki (1986) and the thin-tube approximation (Defouw 1976) we estimate the ratios of the flux tube diameter at the different heights of the atmosphere sampled by the red continuum (TiO band), the *G*-band (roughly 50 km higher; Carlsson et al. 2004) and Ca II H (≈ 440 km higher; see Sect. 3.2.1). We obtain 1 : 1.1 : 2.6, respectively, assuming the approximate mean formation heights. However, these ratios represent a lower limit of the size ratios, since the Ca II H MBPs form in higher layers due to the effect of higher H_{2V}/H_{2R} emission peaks around the Ca II H line-core (see Sect. 3.2.1). One should keep these expansion rates in mind when comparing the size of MBPs in different layers. Note that the Wilson depression affects all layers and does not, to first order, affect this ratio.

Berger et al. (1995) reported a range of FWHM between 0.17 and 0.69 arcsec, with an average value of 0.35 arcsec for photospheric *G*-band BPs. Using the same telescope and the same passband, Berger and Title (2001) noted a much smaller mean value of 0.145 arcsec. This latter value is well below the theoretical diffraction limit, 0.2 arcsec, of the telescope they used (*SVST*; Swedish Vacuum Solar Telescope) and hence smaller than the spatial resolution of their observations. This diameter probably reflects the threshold they used to obtain the size. In any case it suggests that they probably did not resolve most of the BPs in their sample. Later, Sánchez Almeida et al. (2004) obtained a diameter of 0.25 arcsec on average (for GBPs), in data from a telescope with a higher diffraction-limit. Crockett et al. (2010) employed one-dimensional intensity profiling to detect magnetic GBPs and found a diameter distribution peaked at 0.31 arcsec which is in agreement with that of Berger et al. (1995). Their largest GBPs were 1 arcsec in diameter. Recently, Riethmüller et al. (2013) studied the photospheric BPs from the SUNRISE/SuFI CN 3880 Å passband and found an average diameter of 0.45 arcsec with a distribution of sizes ranging from 0.24 to 0.78 arcsec. A relatively small mean value of 0.16 arcsec was reported for internetwork BPs observed in high spatial resolution images taken in the TiO band (Abramenko et al. 2010). An excessively large value of the diameter has been reported for the Ca II K MBPs, observed in internetwork areas (Soltau 1993). He reported a diameter of 2.5 arcsec and considered it as an indication of a preferred size for the magnetic features. Obviously, either he considered very different features than we did or his spatial resolution was very low.

Based on the estimated expansion rates of a thin flux tube in the lower solar atmosphere, a photospheric GBP, i.e., the cross-sectional area of the flux tube in the height sampled by *G*-band, with a diameter of 0.35 arcsec (i.e., the largest mean value of a GBP's diameter reviewed here) expands to a diameter of 0.8 – 1.3 arcsec at the height sampled by Ca II H passband, assuming nearly vertical flux tubes. Such an expansion with height may lead to Ca II H/K MBPs with diameters as large as 2.5 arcsec (Soltau 1993) corresponding to relatively large GBPs, which, although rare, are observed (e.g., Berger et al. 1995; Crockett et al. 2010).

3.4.3.4 Lifetime

Histogram of the lifetime for the 47 MBPs for which both birth and death times were observable are shown in Fig. 3.9*d*. The red, dot-dashed line is an exponential fit with e-folding time of 526 sec, roughly 9 *min*. The condition that only MBPs with lifetimes longer than 80 sec are considered in this study, in principle limits the left side of the distribution. As mentioned in Sect. 3.3, this lifetime threshold of 80 sec was introduced to exclude point-like brightenings caused by superpositions of waves and reversed granulation (de Wijn et al. 2005). However, the shortest lifetime we found is 167 sec, so that in practice this limit should not influence the deduced lifetimes. This result suggests that either there is a lower limit to the lifetime of MBPs, or one of the other criteria by which we isolate our MBPs also discarded shorter lived MBPs.

The longest lived MBP in our sample lasted 1507 sec. This is only slightly shorter than the longest image sequence we have used in this study and therefore, the length of our image series restricts the longest lifetime we can determine. This causes the number of longer lived MBPs to be underestimated. Therefore, following Danilovic et al. (2010*b*), we correct the lifetime distribution by multiplying it with a weight of

$$\frac{(n-2)}{(n-1-m)}, \quad (3.5)$$

where m is the number of frames that the MBP lives and n is the total number of frames in the observed time series (shown in shaded grey in Fig. 3.9*d*). This results in a somewhat higher mean lifetime of 673 sec, i.e., roughly 11 *min*.

In an earlier study, de Wijn et al. (2005) discussed that tracking the Ca II H MBPs in internetwork regions is harder than in the network due to the larger, more dynamic granules in the internetwork regions that cause crashing into the flux tubes. They concluded that this interaction can disturb the processes that cause the brightness of MBPs and hence make them invisible. They reported a mean lifetime of 258 sec for their internetwork Ca II H MBPs. The mean lifetime of 673 sec for internetwork Ca II H MBPs that we have obtained from the SUNRISE data with a higher resolution, is a factor of 2.6 larger than their value and is indicated by a vertical line in the lifetime histogram illustrated in Fig. 3.9*d*. At least a part of this difference could be due to the effect of variable seeing on the results of de Wijn et al. (2005), which can lead to significant underestimates of the lifetime.

Abramenko et al. (2010) showed that the majority ($\approx 98.6\%$) of photospheric BPs, identified in high resolution images, have a lifetime less than 120 sec. This implies either a fundamental difference between photospheric and chromospheric MBPs. Alternatively, it is due to the difficulty of reliably identifying internetwork MBPs in the visible continuum due to the generally low contrasts, particularly in the absence of polarisation information. Alternatively, it may be the effect of variable seeing in the observations of Abramenko et al. (2010). Nisenson et al. (2003) found an averaged lifetime of 9.2 *min* for their isolated, network GBP, which is comparable with our finding for isolated internetwork Ca II H MBPs. de Wijn et al. (2008) reported a mean lifetime of 10 *min* for the magnetic internetwork elements they studied in the quiet-sun. Although this is in a good agreement with what we obtained here, only 20% of their magnetic internetwork elements are related to BPs. They do not say if these BPs differ from the remaining magnetic features. In a lower resolution observation (≈ 0.3 arcsec), Muller (1983) found a mean value of 1080 sec

for network BPs and an average lifetime of 540 sec for internetwork BPs, both observed in the photospheric 5750 Å passband. In addition, they also found a range of 180–600 sec for the lifetime of Ca II K BPs. Although at lower spatial resolution and affected by variable seeing, the result for the internetwork BPs is in agreement with our findings. Note that they also restricted themselves to the study of “point-like” BPs by setting an upper limit of 0.5 arcsec for the BPs’ diameters.

Except for the results reported by Muller (1983) and Nisenson et al. (2003), the lifetimes we find for internetwork MBPs are significantly larger than those in the literature, both in the photosphere and the chromosphere. This may well be due to the stable conditions provided by SUNRISE. An alternative explanation for the longer lifetimes obtained in the SUNRISE data could be that through our criteria that allow a MBP to disappear and appear again, we are sometimes falsely assigning two or more features to the same MBP in the course of its lifetime. However, it has only a small effect on our lifetime distribution, as we found by recalculating the distribution without applying this criterion (only the few persistent flashers are affected). To test this situation, we consider the magnetic polarity of each MBP for which this information is available. We find that every MBP always maintains the same polarity during its lifetime. This supports our identifications. Our criterion to restrict our MBPs in size may conceivably lead to a bias in lifetimes (if smaller MBPs are longer lived). The agreement between our result and the one found by Muller (1983), who also set an upper limit on BP sizes, may support such an interpretation.

3.4.3.5 Circular polarisation

Plotted in Fig. 3.10 is the distribution of all (unsigned) CP values (described as in Sect. 3.2.2) measured in individual snapshots of all 53 MBPs for which simultaneous IMAx observations were available (see Table 3.1). The 3σ noise level is indicated by the vertical dashed line. The exponential fit to the distribution (restricted to $CP \geq 0.2\%$) is overlaid (red dot-dashed line). It has an e-folding width of 0.21 CP [%]. The vertical solid-line indicates the mean value of CP , which corresponds to 0.32%.

Our mean value of CP , from the spatially smoothed non-reconstructed IMAx data, is smaller, by a factor of about 8, than that of Riethmüller et al. (2013), who measured this quantity at the position of their MBPs from the phase-diversity reconstructed IMAx data. Hence, their larger photospheric CN MBPs with diameters between 0.24 – 0.78 arcsec show much stronger polarisation signals compared to our small-scale, low chromospheric elements with diameters of 0.11 – 0.27 arcsec. Note that due to the flux tube’s expansion with height, our small Ca II H MBPs are considered to have an even smaller size at the height sampled by the photospheric CN passband. Our measured CP values (at the position of small MBPs) from non-reconstructed data are roughly a factor of 2 smaller than those computed from the phase-diversity reconstructed images.

3.4.3.6 Longitudinal magnetic field

As a final result, we perform an analysis of the Stokes profiles using the SIR code to compute the unsigned longitudinal component of magnetic field, $|B \cos(\gamma)|$ (see Sect. 3.3.4). We show $|B \cos(\gamma)|$ since this value is retrieved more reliably than B , whose values can be adversely affected by noise in Stokes Q and U . However, we should keep in mind

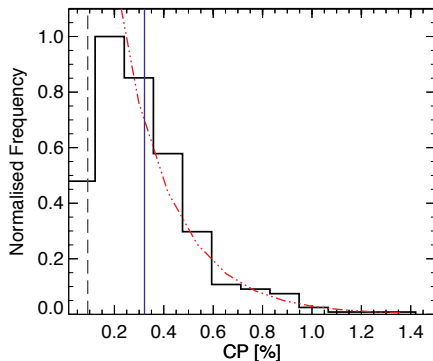


Figure 3.10: Histogram of the CP at the corresponding positions of the SUNRISE Ca II H MBPs in the photosphere. The dashed line marks the 3σ noise level. The red, dot-dashed line corresponds to an exponential fit and the vertical solid-line indicates a mean values of 0.32% CP .

that the $|B \cos(\gamma)|$ values may not be completely reliable, since the MBPs either are not fully spatially resolved or the polarisation signals of the small MBPs under study are too close to the noise level. The former issue causes the inversion code to underestimate the true field strength. The second issue is caused by the sometimes extreme line weakening of the highly temperature and magnetically sensitive IMAx Fe I 5250.2 Å line (Sheeley 1967; Stenflo 1975; Shelyag et al. 2007; Lagg et al. 2010; Riethmüller et al. 2010, 2013). The fact that such point-like magnetic features are bright, suggests that they are the cross-sections of kG magnetic elements whose field strengths are underestimated, very likely because their true diameters in the photosphere are below the SUNRISE spatial resolution. A more thorough discussion is provided by Riethmüller et al. (2013).

Figure 3.11 depicts the distribution of $|B \cos(\gamma)|$ for the MBPs observed on 9 June 2009. This histogram shows a mean value of 142 G indicated by a vertical line in Fig. 3.11. An exponential fit to the points with $B > 100$ G results in an e-folding width of 87 G. A similar conclusion as for the CP distribution is made when our longitudinal magnetic field is compared with that of Riethmüller et al. (2013), who found stronger fields ranged between 25 – 1750 G and with a mean value of 544 G.

3.4.4 A relationship between intensity and horizontal velocity

The only statistically significant correlation obtained from data of all MBPs was found between the maximum values of intensity and maximum proper motion velocity of all identified MBPs.

The maximum intensity values of all identified MBPs are plotted versus their maximum horizontal velocities in Fig. 3.12. The linear regression fit to the data (red solid line) shows an inverse correlation between maximum intensity and maximum proper motion velocity of the MBPs with a correlation coefficient of -0.49 . The blue dot-dashed lines in this plot indicate the confidence bands with 95% confidence level which show an interval

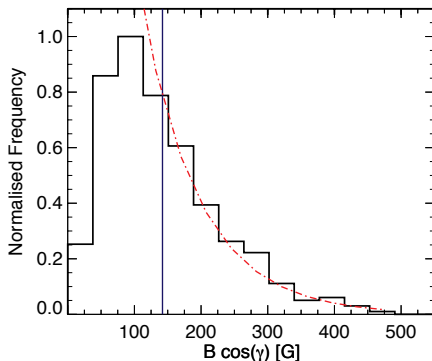


Figure 3.11: Histogram of the unsigned longitudinal component of magnetic field, $|B \cos(\gamma)|$, from the SIR inversion. The red, dot-dashed line represents an exponential fit to the right wing of the distribution, i.e., for $B > 100$ G. The vertical line indicates the mean field strength value.

estimate for the entire regression line. Clearly, the faster a MBP moves, the less bright it is. In particular, the combination of very bright and very mobile MBPs is not present.

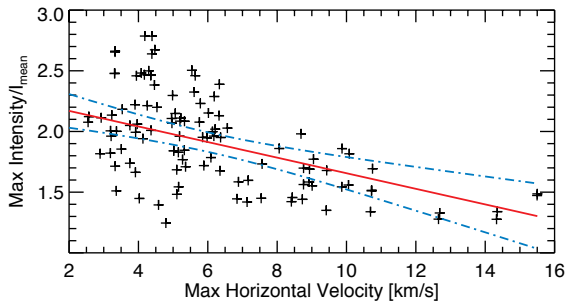


Figure 3.12: Relationship between the maximum horizontal velocity and the maximum intensity of the identified MBPs. The solid (red) line illustrates a linear regression fit to the data with 95% confidence bands (blue dot-dashed lines) around it.

3.5 Kink wave excitation due to high-velocity excursions

We assume that the migration of our Ca II H MBPs is a proxy for the motion of the cross-section of the underlying magnetic elements or flux tubes in the layer sampled by the SUNRISE/SuFI Ca II H passband, i.e., the cross-sections of magnetic elements at around the height of the temperature minimum/low chromosphere.

Furthermore, we found that all studied MBPs have velocity variations similar to the one plotted in Fig. 3.5*b*. In particular, the maximum (peak) velocity observed for each MBP is often much larger than its mean value and is reached for only a brief time. This corresponds to the occurrence of intermittent pulses in the horizontal velocity. In Fig. 3.13 the mean and the peak values of horizontal velocity of all identified MBPs are plotted versus their observed lifetimes. In both plots, higher velocities are mostly observed for shorter lived MBPs. The peak horizontal velocity ranges between 2.6 and 15.5 km s⁻¹, with a mean value of 6.2 km s⁻¹ for all MBPs. In addition, Fig. 3.13*b* shows that almost all MBPs move fast at least once during their lifetimes. The horizontal solid (red) and dot-dashed (blue) lines in both panels in Fig. 3.13 indicate the rough limits distinguishing fast, intermediate and slow MBP motions, with fast motions implying mean proper motion speed ≥ 3 km s⁻¹ and intermediate motions between 2 and 3 km s⁻¹. These limits were chosen following Choudhuri et al. (1993a) and Kalkofen (1997).

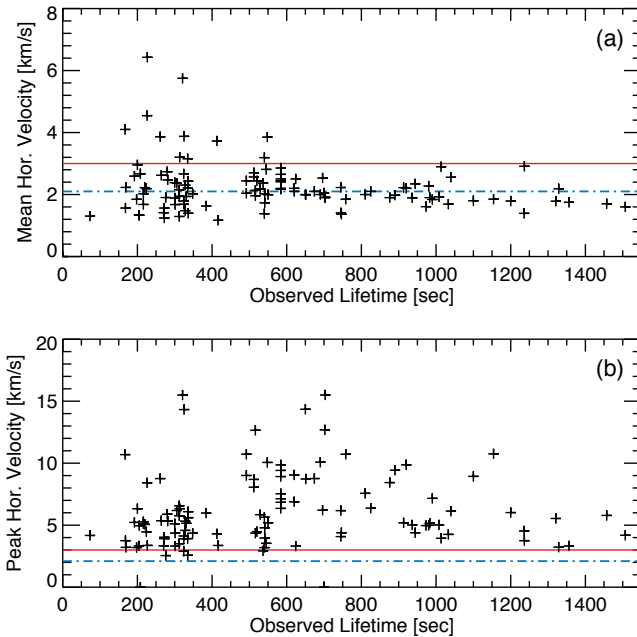


Figure 3.13: (a) The mean horizontal velocity, and (b) maximum (peak) horizontal velocity versus the observed lifetimes of the studied MBPs. The horizontal solid (red) and dot-dashed (blue) lines indicate the approximate limits for fast and intermediate MBP velocities, respectively (see main text).

Note that vibration-induced image jitter introduced by instrumental effects (i.e., due to brief loss of pointing-lock of the telescope) into the SUNRISE observations is much smaller than our observed jerky motions (Berkefeld et al. 2011).

Rapid horizontal motions are of interest in particular if they occur as a pulse, i.e., in combination with a rapid acceleration, since such motions have been proposed to excite magneto-acoustic kink waves along flux tubes (Spruit 1981a; Choudhuri et al. 1993a). Such transversal kink waves transport energy and can travel into the upper chromosphere without significant reflection (Spruit 1981a). Although the reflection at the transition layer decreases the energy flux transported by the kink wave, it may be interesting for quiet coronal heating (Choudhuri et al. 1993b). These early results have been given a strong boost by results of De Pontieu et al. (2007) that transverse magneto-hydrodynamic (MHD) waves along spicules, which may propagate along extensions of MBPs to higher layers, carry sufficient energy to heat the corona. According to Choudhuri et al. (1993a), proper motions of MBPs faster than $\approx 2 - 3 \text{ km s}^{-1}$ (happening within a time shorter than $\approx 100 \text{ sec}$) are particularly effective in exciting kink waves.

This mechanism can be imagined as the rapid jostling of flux tube by granules in the photosphere which impulsively excites oscillations in the tube (Hasan et al. 2000). Then, the oscillations (waves) propagate upwards while their velocity amplitudes increase exponentially until they reach values comparable to the tube speed for kink waves in chromospheric layers, where the kink waves become nonlinear (e.g., Kalkofen 1997). In the middle of the chromosphere, these transversal kink waves may couple to the longitudinal magneto-acoustic waves (Ulmschneider et al. 1991) and dissipate by forming shocks (e.g., Zhugzhda et al. 1995).

Choudhuri et al. (1993a,b) carried out a theoretical analysis of the transversal kink waves induced by the flux tubes footpoints. They derived the following expression that gives a rough estimate of total energy flux (F_E) carried by the kink waves:

$$F_E \approx 6.5 \times 10^{26} \left(\frac{\rho_0}{10^{-7} \text{ g cm}^{-3}} \right) \left(\frac{A_0}{10^5 \text{ km}^2} \right) \left(\frac{v_0}{1 \text{ km s}^{-1}} \right)^2 \cdot \left(\frac{H}{250 \text{ km}} \right) \left(\frac{F(\lambda)}{\lambda^2} \right) n f \text{ ergs cm}^{-2} \text{ s}^{-1}, \quad (3.6)$$

where ρ_0 is the atmospheric density, A_0 is the cross sectional area of the flux tube (i.e., area of the MBP), v_0 is the maximum velocity of a horizontal pulse, and H is the scale height. The parameters n and f in Eq. (3.6) represent the number density of MBPs and the frequency of motions (i.e., pulses), respectively. λ is a dimensionless parameter related to the rapidity of a MBP, i.e., a measure of the strength of the MBP motion. This parameter is determined by $\lambda = v_0/(\omega_c L)$, where ω_c is the cut off frequency at a certain layer in the atmosphere and L is the MBP displacement within the pulse duration. The dimensionless function $F(\lambda)$ is the asymptotic energy which depends on the employed atmospheric model. Choudhuri et al. (1993b) examined three different models and finally concluded that an isothermal atmosphere is a reasonable model for kink waves propagation in the solar atmosphere induced by rapid flux tube footpoint motions. Therefore, we employ the isothermal atmosphere model in our calculations.

Since we are aiming for a rough estimate of the energy flux generated by our high-velocity Ca II H MBPs, we are satisfied with approximate values of the various parameters entering Eq. (3.6). Following Wellstein et al. (1998), we take the scale height H in an isothermal atmosphere of 7000 K (as an upper limit), equal to $\approx 150 \text{ km}$. At the height of formation of the SUNRISE/SuFI Ca II H MBPs (i.e., a height corresponding roughly to the

Table 3.4: Characteristics* of Ca II H MBPs pulses and estimated values of energy flux for different velocity bins.

Velocity Bin [km s ⁻¹]	N_p	v_0 [km s ⁻¹]	t_p [s]	A_0 [km ²]	L [km]	f [mHz]	λ	$F(\lambda)$	F_E [erg cm ⁻² s ⁻¹]
2 – 3	252	2.5	42	16000	55	4.00	1.5	0.33	4.1×10^4
3 – 4	206	3.5	43	16500	61	3.00	1.9	0.48	5.9×10^4
4 – 5	135	4.4	43	17100	70	2.00	2.1	0.54	6.1×10^4
5 – 6	84	5.4	47	17600	70	1.00	2.6	0.70	5.0×10^4
6 – 7	31	6.4	42	16900	81	0.50	2.6	0.71	2.4×10^4
7 – 8	15	7.5	33	18300	72	0.20	3.4	0.98	1.4×10^4
8 – 9	20	8.4	38	18600	80	0.30	3.5	1.00	2.4×10^4
9 – 10	11	9.5	40	18600	74	0.20	4.3	1.25	1.4×10^4
10 – 11	7	10.4	22	18600	74	0.10	4.7	1.39	1.0×10^4
11 – 12	2	11.4	47	25000	46	0.03	8.2	2.58	2.7×10^3
12 – 13	2	12.4	28	19800	70	0.03	5.9	1.81	3.5×10^3
14 – 15	3	14.2	49	19700	76	0.04	6.2	1.90	6.5×10^3
15 – 16	2	15.7	33	22300	65	0.03	8.0	2.49	4.8×10^3
2 – 16	770	4.1	42	16800	63	-	-	-	3.1×10^5

* N_p : Number of pulses; v_0 : Mean horizontal velocity; t_p : Mean lifetime; A_0 : Mean area; L : Mean displacement; f : Frequency of pulse occurrence; λ : Rapidity parameter; $F(\lambda)$: Asymptotic energy; F_E : Net flux

temperature minimum), we use the density from the VAL-C atmospheric model (Vernazza et al. 1981): $\rho_0 \approx 6 \times 10^{-9}$ g cm⁻³.

For the acoustic cutoff frequency at the temperature minimum we use 3×10^{-2} s⁻¹ (Spruit 1981a).

Then, we analyse the horizontal velocity variations of each MBP and look for significant pulses, i.e., when the proper motion velocity exceeds a certain limit for a maximum duration of 100 sec. We compute the pulses occurring in 1 km s⁻¹ wide velocity bins between values of 2 and 16 km s⁻¹. The pulse parameters, i.e., the peak horizontal velocity and the area of each MBP at that time, as well as the displacement which the MBP suffers during each pulse, are recorded. The frequency of pulses for each bin is then computed as the ratio of the number of pulses in the bin and the integrated lifetime over all MBPs. As mentioned earlier, the identified MBPs in this study have a number density of 0.03 (Mm)⁻².

The parameters v_0 , A_0 and L are computed as the average over all the peak horizontal velocities, all the areas and all the displacements determined for all pulses in all MBPs within each velocity bin, respectively. We extrapolate the plot of $F(\lambda)$ versus λ from Fig. 6 in Choudhuri et al. (1993a) to obtain the value of $F(\lambda)$ for the computed λ s. The values of the obtained parameters for each velocity bin are presented in Table 3.4. The

integrated energy flux is then computed over all velocity bins larger than a given speed. We do the analysis for two speed limits: one for $v = 3 \text{ km s}^{-1}$ and one for $v = 2 \text{ km s}^{-1}$ representing fast and intermediate MBP motions, respectively (Choudhuri et al. 1993a; Kalkofen 1997).

We find an integrated value of $F_E \approx 2.7 \times 10^5 \text{ erg cm}^{-2}\text{s}^{-1}$ (or $\approx 270 \text{ W m}^{-2}$) for pulses with $v \gtrsim 3 \text{ km s}^{-1}$ and a marginally larger value of $F_E \approx 3.1 \times 10^5 \text{ erg cm}^{-2}\text{s}^{-1}$ (or $\approx 310 \text{ W m}^{-2}$) for pulses with $v \gtrsim 2 \text{ km s}^{-1}$. These estimated values of total energy flux are compatible with the estimated energy flux density of $1 - 3 \times 10^5 \text{ ergs cm}^{-2}\text{s}^{-1}$ ($100 - 300 \text{ W m}^{-2}$) required to heat the quiet corona and/or drive the solar wind (Hollweg 1990; Hansteen and Leer 1995). Our value is a lower limit since we only considered small, internetwork magnetic elements.

Table 3.4 is in agreement with the finding of Choudhuri et al. (1993b), that faster motions, though more infrequent, provide more substantial contributions compared to the slower ones (cf. Eq. 3.6).

Note that if the formation height of the Ca II H channel were to lie lower, e.g., in the mid photosphere where the atmospheric density is much higher, $\rho_0 \approx 5 \times 10^{-8} \text{ g cm}^{-3}$, then the energy flux estimated based on Eq. (3.6) would be about one order of magnitude larger.

Muller et al. (1994) reported a very much larger value of $F_E = 2000 \text{ W m}^{-2}$ for their photospheric network BPs with $v > 2 \text{ km s}^{-1}$ whereas Wellstein et al. (1998) found a value of $F_E = 440 \text{ W m}^{-2}$ for their K_{2V} BPs with mean horizontal velocity of 6 km s^{-1} . The latter value is highly affected by the formation height assumption of 1100 km for their Ca II K passband, and may not be relevant in any case since it is unclear which fraction of their features really is magnetic. The results of Muller et al. (1994) suggest that it would be worthwhile to follow also larger MBPs as found in the network in SUNRISE data.

3.6 Conclusions

In this chapter, we have provided observational properties of intrinsically magnetic and highly dynamic small bright point-like features in the SUNRISE Ca II H passband. MBPs of the type studied here, i.e., with diameters below 0.3 arcsec, are present mainly in the internetwork. We have, for simplicity, further restricted our analysis to those MBPs that do not merge or split in the course of their observed lifetime. They cover only 5% of the Sun's surface and radiate on average 1.48 times more than the average quiet-Sun in the 1.8 \AA broad SUNRISE Ca II H filter, so that 7.5% of the radiative energy losses in lower chromospheric layers are due to such features (assuming Ca II H to be representative of other spectral lines formed in that layer). This is negligible. However, motions of these features may be responsible for kink waves travelling into the corona, and for the braiding of field lines leading to nanoflares (Parker 1988), so that studying them can potentially help us in our understanding of chromospheric and possibly coronal heating mechanisms.

We applied a set of stringent criteria in order to separate the MBPs we wish to study from all other bright, point-like features. In particular, we only consider MBPs smaller than 0.3 arcsec. This limited us to a smaller number of MBPs, but ensured that they are not oscillations or wave-like features, nor the product of reversed granulation.

Nearly all the MBPs for which we could test this were found to be associated with significant photospheric magnetic field. This result agrees with that of de Wijn et al. (2005),

who showed, although at lower spatial resolution, that internetwork Ca II H BPs were located inside magnetic patches. They also found a good spatial coincidence between their Ca II H MBP patches and the ones they found in *G*-band images. This is also the case in the SUNRISE data (Riethmüller et al. 2010).

These small MBPs in internetwork areas have long lifetimes with a mean value of 673 sec, much longer than any values in the literature for Ca II H MBPs, but in good agreement with the mean lifetime of about 9 *min* for photospheric internetwork BPs (Muller 1983) as well as a mean lifetime of 10 *min* for the internetwork magnetic elements (IME; de Wijn et al. 2008), of which only 20% are associated with *G*-band and Ca II H BPs. Our internetwork features appear to live less long than (photospheric) network BPs which last on average 1080 sec (Muller 1983), however, a comparable mean lifetime of 9.2 *min* for network GBPs was found by Nisenson et al. (2003). In addition, we showed that the Ca II H MBPs move horizontally with an average speed of 2.2 km s⁻¹. We suspect that the much higher horizontal velocities reported by Wellstein et al. (1998) and Steffens et al. (1996) refer to a different type of feature, which is probably non-magnetic. Furthermore, an inverse correlation between the maximum values of intensity and horizontal velocity of the identified MBPs was observed, i.e., the MBPs are brightest when they are at rest.

It was shown that in addition to the considerable mean values of the horizontal velocity of the subsonic MBPs, almost all SUNRISE Ca II H MBPs move with a much larger peak horizontal velocity (up to 15.5 km s⁻¹) for at least a short period of time. On average a MBP spends 3.5% of its life travelling at a supersonic speed. These motions are not regular but often correspond to pulses of rapid horizontal motion. Such jerky, pulse-like motions efficiently give rise to kink waves travelling along a magnetic flux tube according to Choudhuri et al. (1993a,b). They calculated that the efficiency of kink wave excitation depends on the rapidity of the MBP motion with respect to the cutoff frequency of the atmosphere. We computed a rough estimate of the energy flux generated by the rapid MBP motions (i.e., for pulses with $v \gtrsim 2$ km s⁻¹) of $\approx 3.1 \times 10^5$ erg cm⁻²s⁻¹ (or ≈ 310 W m⁻²), which is sufficient to heat the quiet corona (energy flux density of $1 - 3 \times 10^5$ ergs cm⁻²s⁻¹ or 100 - 300 W m⁻²; Withbroe and Noyes 1977; Hollweg 1990; Hansteen and Leer 1995) if the kink pulses propagate into the corona and dissipate their energy there. Our estimated value is an order of magnitude lower than the energy flux transported by Alfvén waves estimated by De Pontieu et al. (2007) from observations of type II spicules (4 to 7 kW m⁻²). However, the mechanisms by which these different energy fluxes are generated may be different. Hasan and van Ballegooijen (2008) argued that the heating in Ca II H MBPs, caused by weak shocks occurring at short time intervals (less than 100 sec) in magnetic flux tubes, is in contrast with the long-period waves which are considered as the spicules driver (De Pontieu et al. 2004). Also, by restricting ourselves to small MBPs, we may be missing the magnetic features carrying the most energy into the upper atmosphere.

The mean value of the unsigned longitudinal component of magnetic field, $|B \cos(\gamma)|$, in the MBPs was found to be 142 G, reaching 500 G only rarely. These values may be influenced by some of the MBPs not being fully spatially resolved (Riethmüller et al. 2013) and/or the polarisation signals lying close to the noise level at some times, as can be seen in Fig. 3.10.

All distributions of the parameters studied here, except that of diameter, display an exponential fall-off towards larger values, implying random stochastic processes. The shape of the size histogram is partly determined by our restriction to features smaller than

0.3 arcsec, and may well be affected by the fact that many of these features could be unresolved in the photosphere, as is suggested by their weak fields (see Riethmüller et al. 2013).

We identified 7 persistent flashers (Brandt et al. 1992) in our sample of MBPs. We find that the flashers are normal MBPs that differ mainly in that they have smaller average values of intensity, so that their brightness drops below the threshold at some moments in time and they seem to disappear temporarily.

We expect that granular and intergranular motions are primarily responsible for the horizontal motions of the corresponding flux tubes rooted in intergranular lanes. Interestingly, the lifetime distribution of our Ca II H MBPs (range between 167 and 1507 sec) is comparable with that found by Hirzberger et al. (1999) for granules, who showed a range of 168 – 1800 sec for granular lifetimes with only a relatively small number of long-lived granules with lifetimes longer than 1200 sec. However, they found a mean lifetime of about 360 sec for the granules which is smaller than the lifetime of our Ca II H MBPs. In addition, the existence of horizontal convective supersonic flows at the boundaries between granules and intergranular lanes (e.g., Cattaneo et al. 1989; Solanki et al. 1996a; Nordlund et al. 2009; Bellot Rubio 2009; Vitas et al. 2011) may explain our observations of fast motions MBPs and supersonic pulses which can be due to the impact of fast granular flows on the flux tubes.

Summarising, we studied the structure and dynamics of the smallest currently observable magnetic bright features at the height sampled by the SUNRISE/SuFI Ca II H passband (i.e., a height corresponding roughly to the temperature minimum). We determined and discussed the statistical distributions of the MBPs' properties including intensity, horizontal velocity, size, lifetime, polarisation signals as well as magnetic field strength. We found an anti-correlation between the maximum proper motion velocity and the peak intensity values of the MBPs. With the help of an advanced image processing technique, selecting the actual MBPs based on stringent criteria and using data unaffected by seeing from SUNRISE, we provided accurate horizontal velocity profiles of the Ca II H MBPs. These profiles revealed indications of fast pulses (i.e., rapid MBP motions on short time scales) which may contribute to coronal heating by exciting kink waves in the corresponding flux tubes. The energy flux that we estimate following Choudhuri et al. (1993a,b) is marginally sufficient to heat the quiet corona. Note that we restricted ourselves to small internetwork magnetic elements, so that we are probably including only a small fraction of the energy flux in our estimate. Hence, in addition to other possibilities of coronal heating, e.g., braiding of field lines leading to nanoflares (Parker 1988), the jerky motions of the MBPs studied in this work, can excite waves that potentially carry enough energy to contribute to the heating of the quiet corona. Future work will aim at detecting such waves.

4 On the migration of Ca II H bright points in the internetwork

To be submitted to A&A by S. Jafarzadeh^{1,2}, R. H. Cameron¹, S. K. Solanki^{1,3}, A. Pietarila⁴, A. Feller¹, A. Lagg¹ and A. Gandorfer¹.

Abstract The migration of magnetic bright point-like (MBP) features in the lower solar atmosphere reflects the dispersal of magnetic flux as well as the horizontal flows of the atmospheric layer they are embedded in.

We analyse trajectories of the proper motion of intrinsically magnetic, isolated internetwork Ca II H MBPs (mean lifetime 461 ± 9 sec) to obtain their diffusivity behaviour. We use high spatial and temporal resolution image sequences of quiet-Sun, disc-centre observations obtained in the Ca II H 3968 Å passband of the Sunrise Filter Imager (SuFI) onboard the Sunrise balloon-borne solar observatory. Small MBPs in the internetwork are automatically tracked. The trajectory of each MBP is then calculated and described by a diffusion index (γ) and a diffusion coefficient (D). We further explore the distribution of the diffusion indices with the help of a Monte Carlo simulation.

We find $\gamma = 1.69 \pm 0.08$ and $D = 257 \pm 32 \text{ km}^2\text{s}^{-1}$ averaged over all MBPs. Trajectories of the MBPs are classified as super-diffusive, i.e., $\gamma > 1$, with the determined γ being the largest obtained so far. A direct correlation between D and time-scale (τ) determined from trajectories of all MBPs is also obtained.

We discuss a simple scenario to explain the diffusivity of the observed MBPs while they migrate within a small area in a supergranule (i.e., an internetwork area). The relatively short lived MBPs are described as random walkers (due to granular evolution and intergranular turbulence) superposed on a systematic (background) velocity, caused by granular, mesogranular and supergranular flows.

4.1 Introduction

The study of small-scale, magnetic bright point-like features (MBPs) in the lower solar atmosphere has gained in interest over the last two decades since many of them trace the

¹ Max-Planck-Institut für Sonnensystemforschung, Max-Planck-Str. 2, 37191, Germany

² Institut für Astrophysik, Georg-August-Universität Göttingen, Friedrich-Hund-Platz 1, 37077, Germany

³ School of Space Research, Kyung Hee University, Yongin, Gyeonggi 446-701, Republic of Korea

⁴ National Solar Observatory, 950 N. Cherry Avenue, Tucson, Az 85719, USA

kG magnetic features that connect the photosphere with higher layers of the atmosphere. MBPs are among the smallest potentially spatially resolved structures seen in the photosphere (e.g., Berger and Title 2001; Möstl et al. 2006; Sánchez Almeida et al. 2010; Riethmüller et al. 2010) and chromosphere (e.g., Rutten and Uitenbroek 1991; Steffens et al. 1996; Leenaarts et al. 2006; Jafarzadeh et al. 2013a). Their motion is important for braiding of the magnetic field in the corona which plays an important role for coronal heating according to Parker (1972, 1983, 1988); cf. Gudiksen and Nordlund (2002, 2005a,b); Peter et al. (2004).

Dispersion of the MBPs, i.e., their non-oscillatory motion on the solar surface, is thought to be due to photospheric flows, e.g., expansion and evolution of granules and supergranules, differential rotation and meridional flows (Hagenaar et al. 1999). Such motions are commonly described in terms of a diffusion process (e.g., Leighton 1964; Lawrence and Schrijver 1993; Dybiec and Gudowska-Nowak 2009; Ribeiro et al. 2011), whose efficiency is expressed by a diffusion coefficient (D) representing the rate of increase of the area that the MBP diffuses across per unit time. This process can be characterised by the relation $(x - x_0)^2 \propto t^\gamma$, where $(x - x_0)^2$ represents the squared displacement (sd) of the tracked MBP between its location x at any given time t and its initial position x_0 . γ is normally named the diffusion index. Motions with $\gamma < 1$, $\gamma = 1$ and $\gamma > 1$ are called sub-diffusive, normal diffusive (random walk) and super-diffusive whose sd grows slower than linear, linearly, or faster than linear with time, respectively (Dybiec and Gudowska-Nowak 2009).

Normal diffusion historically has been the first known class of diffusive processes. It characterises a trajectory which consists of successive random steps and is described by the simplest form of diffusion theory (e.g., Fick 1855; Einstein 1905; Lemons and Gythiel 1997). Brownian motion is an example of a normal diffusive process. Leighton (1964) discussed the random walk interpretation of magnetic concentrations in the solar photosphere. He estimated the diffusion coefficient for granules and supergranules to be roughly $10^4 \text{ km}^2 \text{ s}^{-1}$. He found that this rate is comparable with the dispersal rate of the magnetic regions in the photosphere; and hence concluded that convective flows are responsible for random walk of the magnetic concentrations (cf. Jokipii and Parker 1968; Lawrence and Schrijver 1993; Muller et al. 1994).

Sub-diffusive motion of magnetic elements in an active region in the photosphere was first reported by Lawrence and Schrijver (1993). Later, Cadavid et al. (1999) found that although the motion of magnetic network G-band MBPs in the photosphere is random if their lifetimes are larger than 25 minutes, MBPs with lifetimes less than 20 minutes migrate sub-diffusively. The sub-diffusivity was explained by the trapping of MBPs at stagnation points (i.e., points with zero horizontal velocity; sinks of flow field) in the inter-cellular pattern (Simon et al. 1995). In agreement with Cadavid et al. (1999), Hagenaar et al. (1999) stated that the diffusion index obtained from tracking magnetic elements may depend on the time-scale and also vary in time.

There are only few observational reports of super-diffusion in the lower solar atmosphere. Berger et al. (1998b) found indications of slight super-diffusivity among other normal diffusive G-band MBPs in network regions. Later, in two high spatial and temporal resolution image sequences, Lawrence et al. (2001) found a significant number of super-diffusive MBPs between normal ($\gamma = 1$) and Richardson diffusion (i.e., $\gamma = 3$). Recently, Abramenko et al. (2011) observed super-diffusivity of photospheric TiO MBPs

in high spatial resolution time series. They reported the presence of super-diffusivity (as the only observed diffusion regime) for both quiet-Sun and active regions. Such super-diffusivity was latter confirmed by Chitta et al. (2012) by tracking MBPs observed in wideband H α .

Diffusivity of MBPs is thought to be related to the turbulent convection on and below the solar surface (Nordlund 1985). In addition, it has been shown that stronger magnetic fields and larger magnetic elements result in smaller diffusion coefficients (Schrijver 1989; Schrijver et al. 1996). Furthermore, numerical simulations have suggested that lower magnetic fluctuation levels are associated with larger deviations from the normal diffusion (Pommois et al. 1999; Zimbardo et al. 2000).

In summary of the above, the mobility of small MBPs has been described as dependent on temporal and spatial scales, magnetic field strength as well as the level of (sub-) photospheric turbulent convection.

We present measurements of the motion of small MBPs seen in the high-resolution Ca II H images of the SuFI instrument aboard the SUNRISE balloon-borne solar observatory. The MBPs under study are located in the quiet-Sun internetwork areas sampled at a height corresponding roughly to the temperature minimum. In particular, we track the motion of these small and intrinsically magnetic features (Jafarzadeh et al. 2013a, hereafter Paper I) in time series of filtergrams and calculate their trajectories. We compute the *sd* for each trajectory and measure the corresponding power exponent (i.e., the diffusion index) as well as the diffusion coefficient.

In Sect. 4.2, we outline the dataset used to produce the time-series. Section 4.3 represents the analysis method of the trajectories of the MBPs as well as the diffusion study results. In Sect. 4.4 we explore the role played by the distribution of diffusion indices. Finally, the concluding remarks are discussed in Sect. 4.5.

4.2 Data

We used part of the datasets described in Paper I. The sets consist of six time series of intensity images obtained in the Ca II H passband (centred at 3968 Å with FWHM \approx 1.8 Å) of the SUNRISE Filter Imager (SuFI; Gandorfer et al. 2011) on board the SUNRISE balloon-borne solar observatory (Solanki et al. 2010; Barthol et al. 2011; Berkefeld et al. 2011).

Table 4.1 lists the employed image sequences. All images were phase diversity reconstructed employing averaged wavefront errors (cf. Hirzberger et al. 2010, 2011), i.e., they correspond to level 3 data. For all images the field of view is $\approx 15 \times 41$ arcsec² (712 \times 1972 pixels) in size, with an image scale of 0.021 arcsec/pixel. All data refer to quiet regions close to solar disc centre.

Figure 4.1 illustrates two snapshots from two different time series. We have indicated 4 MBPs by yellow boxes whose trajectories will be studied here in details. The left image in Fig. 4.1 contains a small network area in the upper part of the field-of-view that is excluded from our further analysis which concentrates on internetwork MBPs.

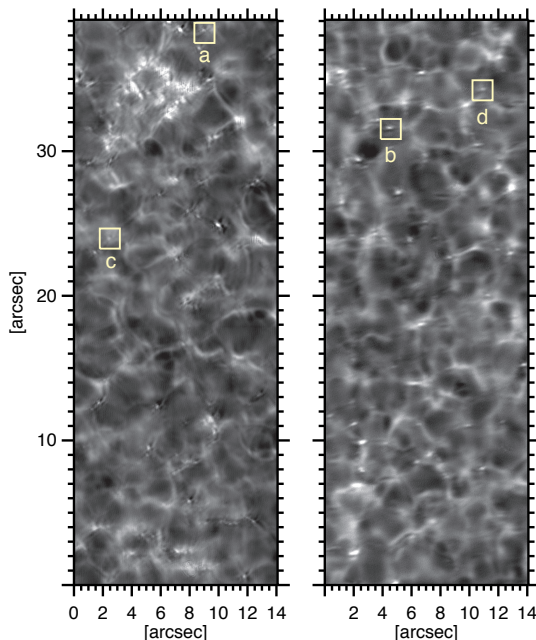


Figure 4.1: Two examples of SuFI/SUNRISE Ca II H filtergrams. Left: Observed on 9 June 2009, at 01:54:43 UT. Right: Obtained on 11 June 2009, at 21:05:20 UT. The yellow boxes include selected MBPs whose trajectories are shown in Fig. 4.2.

Table 4.1: Log of observations.

Date	Time Interval (UT)	No. of frames	Cadence
9 June 2009	00:36 - 00:59	117	12 sec
9 June 2009	01:32 - 02:00	136	12 sec
11 June 2009	15:22 - 15:44	312	4 sec
11 June 2009	20:09 - 20:19	78	8 sec
11 June 2009	21:00 - 21:09	83	7 sec
13 June 2009	01:46 - 01:59	255	3 sec

4.3 Data analysis and results

We analyse trajectories of the Ca II H MBPs studied in Paper I. According to the definition introduced in Paper I, a Ca II H MBP is an isolated (no merging, no splitting and no fine-structure resolved) bright, point-like feature in the height range sampled by the SuFI

Ca II H 3968 Å passband. The MBPs are included in this study if they (1) are located in an internetwork area around disc centre, (2) are intrinsically magnetic (for those cases that we have co-spatial & nearly co-temporal magnetograms), (3) have a lifetime longer than 80 sec, (4) have a roughly circular shape with a diameter smaller than 0.3 arcsec, and (5) are neither due to acoustic waves nor associated with “reversed granulation” (cf. Rutten et al. 2004).

The identified (selected) MBPs are tracked using the algorithm described in Paper I. Furthermore, the trajectories of the MBPs are computed and the modes of motion for each trajectory are further investigated.

4.3.1 Trajectories

The trajectory of a MBP can be reconstructed by linking the string of x and y positions marking the MBP’s location in each frame. These MBPs have a mean lifetime of 673 ± 9 sec, when measured only for those MBPs whose birth and death times are observable within the course of the time series and inside the images field-of-view (Jafarzadeh et al. 2013a). The observed lifetime was found to be 461 ± 9 sec on average when all MBPs are considered. The shortest and longest lifetimes are 167 ± 8 sec and 1321 ± 13 sec, respectively. Four examples of trajectories of SUNRISE Ca II H MBPs are illustrated in Fig. 4.2 (upper panels).

Linking the MBP positions into a trajectory is only possible if the MBP’s displacement in two consecutive frames is sufficiently smaller than the typical distance between the detected MBPs. This latter condition ensures that interacting MBPs or those that show apparent merging or splitting behaviours are excluded. This criterion may cause us to miss the fastest moving MBPs. However, a particular MBP may disappear and reappear again in a short time interval, such as the so called “persistent flashers” (Brandt et al. 1992; Jafarzadeh et al. 2013a). Therefore, these possible absent times were considered in the tracking algorithm, while a final visual inspection guaranteed the exclusion of interacting MBPs in these special cases. For details on the locating and tracking procedures of the MBPs, we refer the reader to Jafarzadeh et al. (2013a).

4.3.2 Diffusion processes

The trajectories of MBPs, $\mathbf{r}(t)$, for a diffusive process can be parametrised by their self-diffusion coefficients D based on the Einstein-Smoluchowski equation (Crocker and Grier 1996),

$$\langle |\mathbf{r}(t_0 + t) - \mathbf{r}(t_0)|^2 \rangle = 2dD\tau, \quad (4.1)$$

where τ is the elapsed time and d indicates the trajectory’s dimension. The term $\mathbf{r}(t_0 + t) - \mathbf{r}(t_0)$ gives the displacement of the MBP at a given time $t_0 + t$, from its first observed location at time t_0 . In its original definition, the left hand side of the above equation is the mean of the squared displacement, whose value is computed by averaging all squared displacements (sd) in the system, i.e., all squared displacements over all MBPs. However, this latter averaging can result in the mixing of different diffusive processes and is not ideal for studying different motion types that the MBPs may have (Dybiec and Gudowska-Nowak 2009).

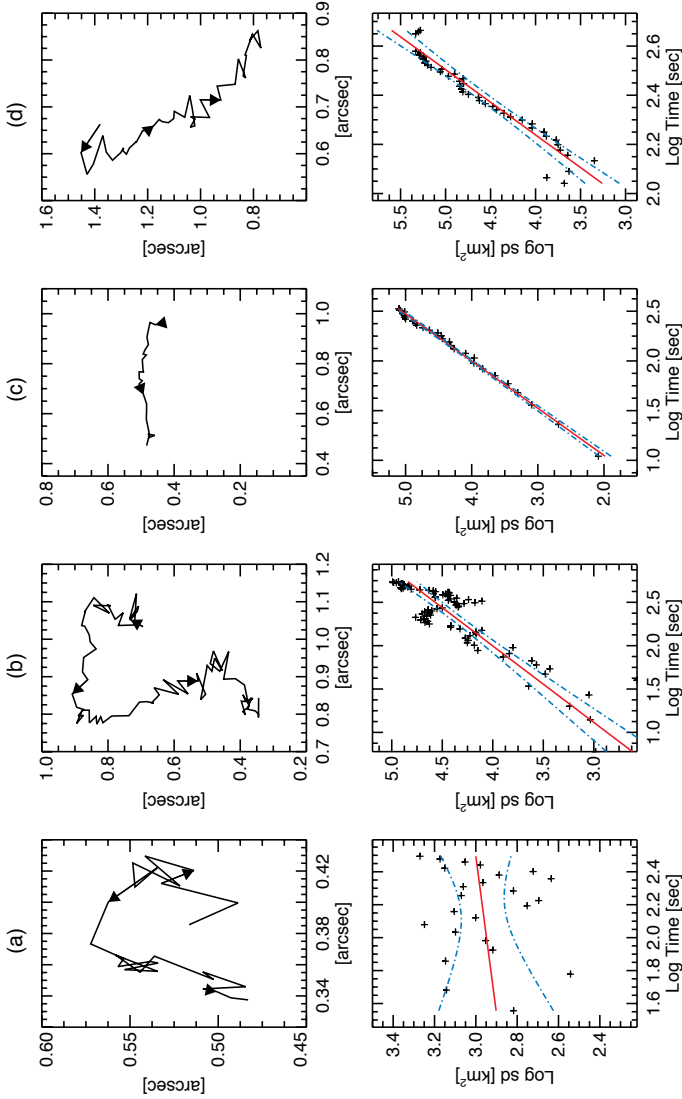


Figure 4.2: Trajectories (top) and log-log plots of the squared displacement (sd) versus time (bottom) of the four MBPs identified in Fig. 4.1 as ‘a’-‘d’, marked at the top of the upper panels. Arrows on the trajectories indicate the direction of the MBP’s motion. The red (solid) lines are the best linear fits to the sd data points (crosses) vs. time and the blue, dot-dashed lines show the 95% confidence bands around the linear fit. The linear fits result in a MBP with $\gamma=0.10 \pm 0.47$ (a), a slope (or γ) of 1.13 ± 0.18 (b), a MBP with $\gamma=2.10 \pm 0.11$ (c), and a MBP with a high power exponent γ of 3.76 ± 0.57 (d). The uncertainties are computed from the 95% confidence bands.

In its general form, diffusion is characterised by scaling of the variance of positions or alternatively the sd with time (Ribeiro et al. 2011),

$$sd(\tau) = C\tau^\gamma, \quad (4.2)$$

where C is the proportional constant. The power exponent γ (i.e., diffusion index) is the scaling factor of the sd and, by definition, can be used to classify distinct diffusion regimes as,

$$\begin{cases} \gamma < 1, & \text{Sub-diffusive process} \\ \gamma = 1, & \text{Normal diffusive process (Random walk)} \\ \gamma > 1, & \text{Super-diffusive process} \end{cases} \quad (4.3)$$

Since diffusive processes in which the sd grows linearly with time ($\gamma = 1$) are named “normal”, deviations from linearity result in “anomalous” diffusion. Trajectories for which the sd grows slower or faster than linearly with time are said to lie in the sub- or super-diffusion regimes, respectively. Diffusive processes with $\gamma = 2$ and $\gamma = 3$ are often referred to as ballistic and Richardson diffusion, respectively.

In order to compute the γ , we calculate the sd of each MBP in each image (i.e., at every time step) from its observed position in the first image it is present in. The diffusion index of the MBP can be conveniently captured by the slope of $sd(\tau)$ on a log-log scale. The standard deviation of the slope is also computed within 95% confidence intervals. Therefore, the true value of the slope and hence of γ lies within this confidence interval with a 95% probability.

Once γ is known, the diffusion coefficient D is calculated from the constant of proportionality C of Eq. 4.2 for each MBP separately. Following Abramenko et al. (2011), the diffusion coefficient, D , representing the rate of area in unit time that a MBP moves across, is estimated as the coefficient of turbulent diffusion described by Monin and Ia-glom (1975) as a function of time-scale,

$$D(\tau) = \frac{1}{2d} \frac{d}{d\tau}(sd(\tau)). \quad (4.4)$$

From the Eq. 4.2, it follows

$$D(\tau) = \frac{C\gamma}{2d} \tau^{\gamma-1}, \quad (4.5)$$

where $d = 2$ for our 2-dimensional trajectories.

In practice, C can be computed from the constant term of the linear equation obtained from the least squares fit to the log-log plot of the $sd(\tau)$ for each MBP (i.e., the lower panels of Fig. 4.2; $C = 10^{\text{intercept}}$), γ is the slope of the fit and τ represents the MBP’s lifetime.

Figure 4.2 displays the trajectory and $sd(\tau)$ plots of four selected MBPs indicated as (a)-(d) in Fig. 4.1, marked at the top of the upper panels of Fig. 4.2. MBP (a) in Fig. 4.2 represents one of the few MBPs (lifetime 312 ± 13 sec) with a small $\gamma = 0.10 \pm 0.47$. Although this is not the best example in our data, we chose to show its trajectory (top panel) as well as its log-log plot (bottom panel) here, because it was the only MBP with $\gamma < 1$ in the selected frames shown in Fig. 4.1. The 95% confidence intervals are plotted as the confidence bands (blue, dot-dashed lines) around the linear fits (red, solid-line) to

the data points. As can be seen in the upper left panel, the MBP moves over a small distance and in fact, it stays almost at the same position for some time before making a short jump to the next location. In fact, it moves by less than 0.1 arcsec from its initial position, i.e., by less than its own width (size) of 0.16 arcsec. The MBP (b) in Figs. 4.1 and 4.2, whose lifetime is 548 ± 8 sec, provides an example whose slope of the linear fit (the red solid line in the bottom panel), $\gamma = 1.13 \pm 0.18$, is consistent with normal diffusion. This particular MBP displays a peculiar behaviour. The MBP first tends to move quickly from its initial position. Later it changes its general direction and comes closer to its initial coordinates again. Had it disappeared after, e.g., 300 sec, a larger γ would have been obtained. The $sd(\tau)$ plots of the MBPs (c) and (d) in Figs. 4.1 and 4.2 (lifetimes 336 ± 13 sec and 461 ± 8 sec) result in $\gamma = 2.10 \pm 0.11$ and $\gamma = 3.76 \pm 0.57$, respectively. Although the two trajectories look rather similar in the upper panels of Fig. 4.2, they are different in the sense that the MBP (d) seems to be randomly pushed to the sides, while moving away from its point of origin, while the MBP (c) maintains roughly a smooth migration path. The large γ for example (d) comes from the fact that it gets accelerated, i.e., moves on average faster with time.

4.3.2.1 Statistics

Figure 4.3 shows the statistical distribution of the diffusion indices γ of all 103 MBPs in the analysed SUNRISE/SuFI data (black histogram). The histogram is peaked close to $\gamma = 2$ and has a mean value of 1.69 (indicated by a vertical dashed-line) with the distribution's standard deviation equal to 0.80. 88% of these MBPs have $\gamma > 1$ and only 12% exhibit $\gamma \leq 1$.

The red histogram illustrates the statistics of diffusion indices resulting from a Monte Carlo simulation. We describe and discuss this simulation in Sect. 4.4.2.

4.3.2.2 Diffusion coefficients

Table 4.2 summarises the computed diffusion coefficients, D , for the MBPs 'a-d' (in Figs. 4.1 and 4.2) along with their lifetimes and diffusion indices, γ . D increases with increasing γ for these four examples.

Table 4.2: Diffusion parameters of four example MBPs.

MBP	Lifetime [sec]	γ^*	D^{**} [km ² s ⁻¹]
a	312 ± 13	0.10 ± 0.47	0.08 ± 0.01
b	548 ± 8	1.13 ± 0.18	35.8 ± 1.2
c	336 ± 13	2.10 ± 0.11	203.6 ± 14.7
d	461 ± 8	3.76 ± 0.57	811.7 ± 35.6

* Diffusion index

** Diffusion coefficient

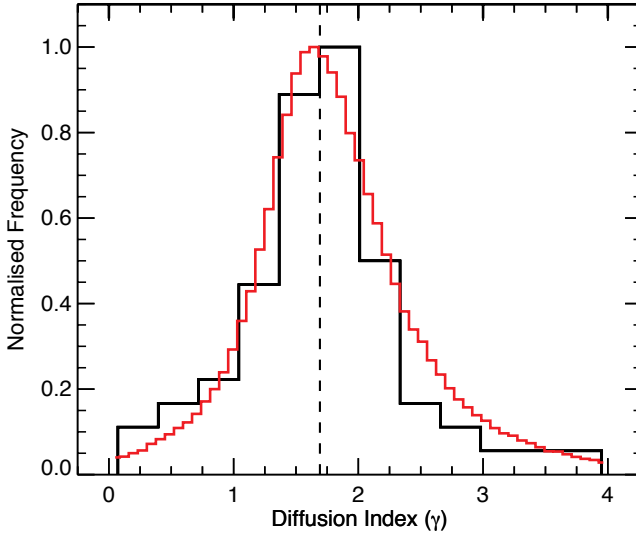


Figure 4.3: Distribution of the diffusion index γ obtained from the SUNRISE/SuFI data (black histogram), normalised to unity maximum value. The vertical dashed line indicates the mean value of γ . The red histogram shows the result of a Monte Carlo simulation for the observed MBP (see main text, Sect. 4.4, for details).

The computed D obtained from all SUNRISE/SuFI Ca II H MBPs are plotted as a function of γ in a linear-log plot in Fig. 4.4 (black crosses). A power-law fit to the data (i.e., $\gamma = 28.9 D^{2.8}$) is overplotted as a (green) dashed line.

The red line is obtained from the same Monte Carlo simulation as the red histogram in Fig. 4.3. In Fig. 4.4 the simulated line has been shifted (upward) to the observed trend (discussed in Sect. 4.4.2). The blue vertical lines indicate the error bars of the simulated trend.

A mean value of $D = 257 \pm 32 \text{ km}^2\text{s}^{-1}$ was obtained from the dispersal of the SUNRISE (internetwork) Ca II H MBPs.

Plotted in Fig. 4.5 is $D(\tau)$ on a log-log scale. The black, solid line shows the best linear fit to the data points obtained from the SUNRISE Ca II H MBPs. Interestingly, we observe a direct correlation between the D and time-scale (τ) which is consistent with the results on super-diffusive internetwork MBPs in the quiet-Sun found by Lawrence et al. (2001) (blue, solid line) and Abramenko et al. (2011) (green, dashed line). The results from all three studies are consistent with each other. We also found a direct relationship between D and displacement (\sqrt{sd}) values (not shown), similar to that of Abramenko et al. (2011).

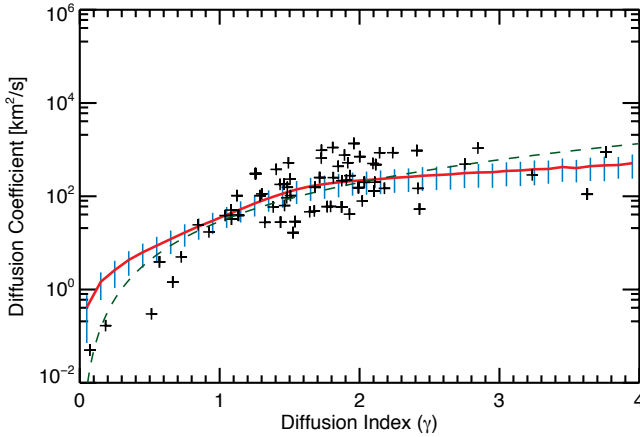


Figure 4.4: Linear-log plot of diffusion coefficient, D , versus diffusion index, γ . Black crosses indicate the diffusion parameters calculated from trajectories of the SUNRISE Ca II H MBPs. The green, dashed line shows a power-law fit to the data points (see main text). The solid (red) curve is obtained from a Monte Carlo simulation. Error bars to the simulated values are shown as vertical (blue) lines (see Sect. 4.4.2 for details).

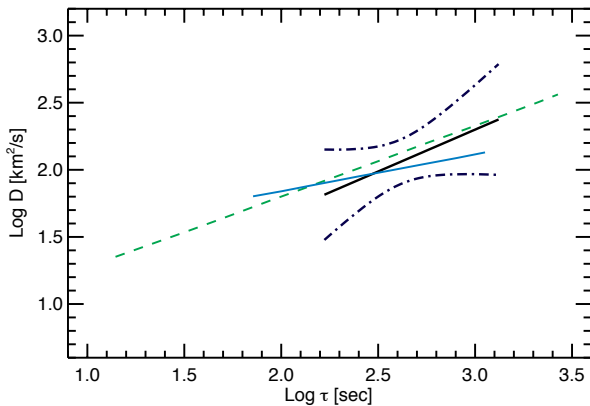


Figure 4.5: Log-log plot of diffusion coefficients (D) as a function of time-scale (τ). Black, solid line: A linear fit to the data points determined from trajectories of the SUNRISE Ca II H MBPs. The 95% confidence bands to the fit are overplotted as dot-dashed lines. For comparison, similar plots (for the quiet-Sun regions) from Lawrence et al. (2001) (blue, solid line) and Abramenko et al. (2011) (green, dashed line) are overlaid.

4.4 Modelling

The histogram of the diffusion index (i.e., Fig. 4.3) is peaked close to $\gamma = 2$, with wings reaching into $\gamma < 1$ and $\gamma > 3$. Furthermore, more than one third (39%) of the γ computed for SUNRISE/SuFI MBPs are around $\gamma = 2$ (within their uncertainties). The fact that our longest lived MBP has a lifetime of 22 min (with each MBP being observed for ≈ 8 min on average) leads us to speculate that the broad wings of the distribution are due to the relatively small number of individual frames (steps) we have observed each MBP, i.e., the width of the distribution is due to realisation noise caused by relatively short lifetimes of the MBPs. Clearly, the longer the motion of a MBP can be followed the more precisely the sd can be fit. This can be clarified by making a simple model of the horizontal velocity of a MBP. Recall that we are dealing with internetwork MBPs, which can lie anywhere in a supergranule (SG).

4.4.1 Migration scenario

The MBPs are located in a complex turbulent medium. Correspondingly, the observed horizontal velocity of a MBP can be broken up into several components. In general, a variety of motions advect the MBPs, acting on different time and spatial scales. These motions range from turbulence in intergranular lanes (acting on the order of a few seconds), via the expansion and motion of granules (on the order of a few minutes), meso- and super- granular flows (on the order of an hour and about 1 day, respectively) to differential rotation and meridional flow.

Given the relatively small field-of-view of all analysed time-series and their locations close to disc centre, the influence the meridional circulation and differential rotation can be neglected.

The relatively short lifetimes of the MBPs under study that move only over a fraction of a meso-/super- granule (in the course of ≈ 8 min, on average) implies that the short-lived small-scale motions (i.e., intergranular turbulences and granular evolutions) are primarily responsible for the random walk components of the MBPs' motion. On the other hand, we expect that the meso- and super-granular flows as well as motions imparted by constantly expanding, contracting and splitting granules on passively advected MBPs can be considered to be systematic.

Note that granules can contribute in a way to both random (v_r) and systematic (v_s) components of the MBPs' horizontal velocity, since the speeds imparted on MBPs due to granular evolution (slowly) change in the course of a MBP's lifetime.

In addition, it is worth to mention that a part of the motion of the Ca II H MBPs can be due to kink waves excited at such magnetic elements. However, we do not search for any periodicity in the motion of the MBPs and the effects of the kink waves are considered to be included in the random motion's component.

4.4.2 Monte Carlo simulation

Assuming an explanation as proposed in Sect. 4.4.1, we explore the statistical distribution of the diffusion index γ (shown in Fig. 4.3) and its relationship with D (plotted in Fig. 4.4)

obtained from the SUNRISE/SuFI data with the help of a Monte Carlo simulation.

We allow 30000 randomly generated “MBPs” to move along the perpendicular x and y axes in $2D$ space and in time t . The x and y axes represent the directions of the random motions of a MBP, while the systematic direction is defined with the x axis. As in Sect. 4.4.1 the latter can be taken to represent mainly mesogranular, supergranular and granular flows. The random motions are thought to be largely associated with granular and turbulent intergranular flows (on short time-scale). The random walk is modelled assuming a discrete time-step of Δt (coherence time), over which the velocity is assumed to be constant. The Δt and ratio of the random to systematic velocities (v_r/v_s) are treated as initial free parameters of the simulation.

We performed the Monte Carlo simulations for MBPs with lifetimes between 160 and 1320 sec. 30000 realisations were analysed for each lifetime. For each run of the simulation (for a particular lifetime), the trajectories of the 30000 simulated MBPs were determined in the same way as for the observed MBPs, described in Sect. 4.3.1, and are further analysed to compute their diffusion indices using a method similar to that applied to the SUNRISE/SuFI Ca II H MBPs as described in Sect. 4.3.2 (i.e., slope of the log-log plot of the $sd(\tau)$ for each MBP; computed from the simulated MBP’s trajectory). Therefore, for any set of the two free parameters, we obtain a distribution of diffusion index γ for the 30000 simulated MBPs with a given lifetime.

Integration of the individual simulated histograms corresponding to each lifetime results in a distribution of γ calculated for MBPs with different lifetimes, similar to the distribution obtained from the observations. To compare with the observed distribution, the histogram resulting from the simulation is re-binned to match the resolution of the one obtained from the observations. Then, the free parameters are tuned until the best match between these two histograms (i.e., one obtained from the observations and one calculated from the Monte Carlo simulation) occurs. The chi-square, χ^2 , is computed as a measure of the best match between the two histograms. Since we compare the distributions of the two binned datasets, the quantity χ^2 is measured as (Press et al. 2007):

$$\chi^2 = \sum_i \frac{(O_i - C_i)^2}{O_i + C_i}, \quad (4.6)$$

where O_i and C_i indicate the i^{th} observed and computed (simulated) bin of the histograms. Plotted in Fig. 4.6 is the coherence time Δt as a function of the ratio of velocities v_r/v_s for all χ^2 values. The Δt and v_r/v_s combination giving the smallest χ^2 value was found to be 62 ± 3 sec and 1.6 ± 0.03 . Note that the absolute values of the velocity are not constrained by the histogram of γ . Therefore for simplicity we used $v_r = 1 \text{ km s}^{-1}$.

The result of the simulated distribution of γ based on these parameters (integrated over all simulated distributions with different lifetimes) is plotted in Fig. 4.3 as a red histogram. A comparison with the black histogram, which represents the distribution of diffusion index obtained from the observations (i.e., from the SUNRISE/SuFI data), shows that the simulated distribution is stronger than that of the observations in the (far) wing at $\gamma > 2.5$ but it is weaker for $\gamma < 1$.

In the next step, we determine the absolute values of these random and systematic velocities using the diffusion coefficient D . Given the determined ratio of the velocity components as well as the coherence time, we compute D in the same way as for the

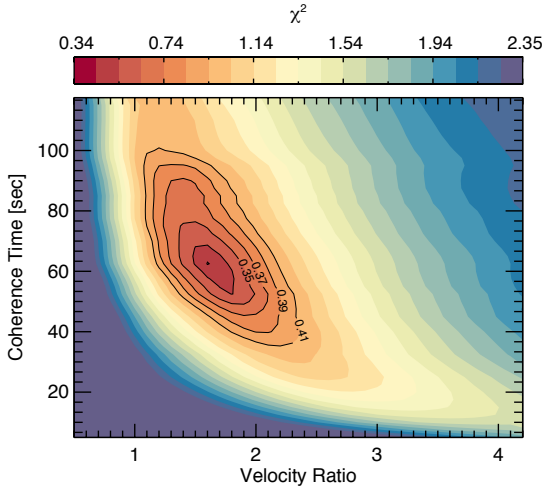


Figure 4.6: Results of a chi-square (χ^2) test for finding the best match between the distributions of the diffusion index from observations and Monte Carlo simulations of the MBPs located in a supergranule’s bulk. The contours guide the eye to the best χ^2 value, giving the appropriate coherence time Δt for the random velocity and the ratio of random-to-systematic velocities v_r/v_s of the MBPs under study.

observed data, described in Sect. 4.3.2.2. Then, we overplot the computed D versus γ for the simulated data on the same linear-log plot as for the observed data. For simplicity, we average the D values in each γ bin and overplot its standard deviation as an error bar for each point. The plot of $\log(D)$ versus γ in Fig. 4.4 shows similar trends for both simulated and observed data, but originally with an offset in the direction of $\log(D)$.

We have only one free parameter left in the simulation, namely v_s , with which to shift the $\log(D)$ versus γ curve. We recall that an arbitrary value for v_r had been used so far. Therefore, we tuned v_r , while keeping v_r/v_s and Δt fixed, until we found the best agreement between the observed and computed plots of $\log(D)$ versus γ . The output of the simulation giving the best agreement with the observations is overplotted as a red line (along with the error bars; vertical blue lines) on the observed data (black crosses) in Fig. 4.4. The v_r giving the best fit was found to be $1.2 \pm 0.1 \text{ km s}^{-1}$ on average. Consequently, the systematic flow tends to move with a velocity of $0.75 \pm 0.06 \text{ km s}^{-1}$.

Finally, we take these best-fit values and do the simulation once again but for a larger range of lifetimes, i.e., from 80 sec, representing the criterion for minimum lifetime of the MBPs under study, to three times longer than the maximum lifetime of the observed MBPs from the SUNRISE/SuFI data. A plot of γ versus lifetime resulting from this simulation is illustrated in Fig. 4.7. The background brightness follows the number density of MBPs with a particular γ . A vertical cut at a given lifetime indicates the histogram density of the γ distribution at the chosen lifetime. The solid lines mark percentiles, i.e., fixed values of the integrals over the histogram density in the vertical direction starting at the bottom.

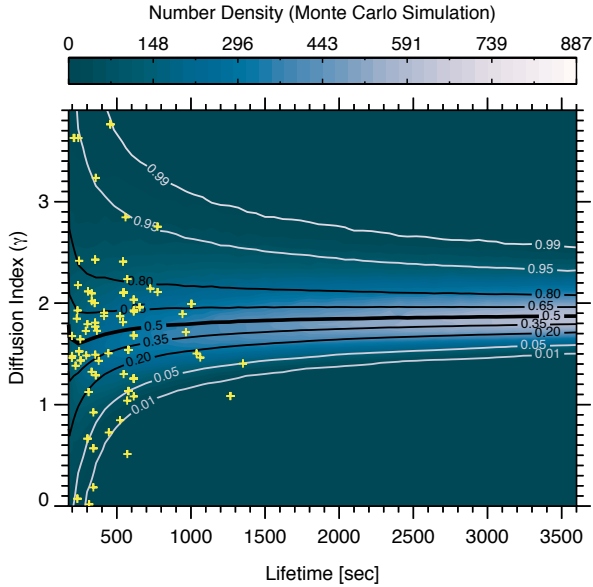


Figure 4.7: Evolution of the diffusion index histogram with increasing lifetime of the MBPs. The background brightness is a measure of the number density of MBPs with a certain γ obtained from a Monte Carlo simulation. The solid lines indicate the percentiles of the distributions (see main text for details). The observed data points from the SUNRISE/SuFI data are overlaid on the simulated plot and are marked by yellow crosses.

Each yellow cross represents an observed MBP from the SUNRISE/SuFI data. At the left side of this plot, where most of our observed data points are located, the lifetimes are shorter and correspond to much fewer time-steps than the right side. The left part of the plot displays a wider distribution of γ , with the histograms having extended tails, similar to the tails of the observed histogram in Fig. 4.3. Insufficient sampling on the left part of the diagram enhances the effect of the random velocity, so that an individual MBP can display a γ rather far removed from the expectation value.

There are only few data points (as seen in Fig. 4.7) that have γ values which are highly unlikely according to the simulations, e.g., outside the 5% and 95% percentile curves. One source of these outlying MBPs may be the fact that we considered a uniform systematic flow dragging the MBPs with it, whereas in reality the flow speed (caused by the contraction, expansion or explosion of the granules as well as the meso- and super-granular flows) is expected to vary. However, the simulated histogram includes almost all of the data points and hence can explain most of the observations. Interestingly, the four data points whose locations lie outside the outermost (1%) contour of the simulation in Fig. 4.7 all have small γ . One possibility to explain the excess of low γ MBPs is that these are lying at the borders of the SGs, where sub-diffusive and random walk MBPs are expected;

due to inflows from opposite directions (from neighbouring SGs).

To summarise, the observations are consistent with the MBPs being random walkers superposed on a systematic flow. Therefore, while the motion of MBPs has a random component due to intergranular turbulence, birth and death of neighbouring granules, the MBP is transported by a systematic velocity on a larger spatial-scale, e.g., due to the constant evolution of long-lived granules, or the contributions of meso- and supergranules to the large-scale velocity field felt by the magnetic element underlying the MBP.

We found a coherence time of 62 ± 3 sec which is comparable with a value of 68 sec computed from the given size (length scale) of our features (i.e., 150 km on average) as well as the mean horizontal velocity of the MBPs under study (i.e., 2.2 km s^{-1}) reported by Jafarzadeh et al. (2013a). This implies that MBPs move on average a distance corresponding to their own diameter before being forced to move in another direction.

4.5 Discussion and conclusions

We analysed the trajectories of 103 isolated (i.e., displaying no merging or splitting) internetwork MBPs (≈ 0.2 arcsec in diameter on average; Jafarzadeh et al. 2013a) in the quiet-Sun observed in the Ca II H 3968 Å passband of SUNRISE/SuFI. We performed a diffusion analysis on the trajectories of MBPs to distinguish between MBPs with different types of motions. We do not, however, search for oscillations or wave-like motions.

In order to avoid potentially mixing MBPs in different diffusion regimes and to get a better insight into the character of motion, we performed the diffusion analysis to all individual trajectories separately (Dybiec and Gudowska-Nowak 2009).

We used the same MBPs as in Paper I where they were identified using stringent criteria; which gives us confidence that these MBPs are good tracers of small-scale magnetic elements in the upper layers of the photosphere and the lower chromosphere. These intrinsically magnetic features can be considered to represent the cross-sections of nearly vertical flux tubes (Jafarzadeh et al. 2013b) whose positions are influenced by different external forces and are restricted to intergranular lanes. Therefore, although they are not perfect tracers of the horizontal flows, the spatial and temporal scaling of the MBPs' dynamics can still indicate the presence of turbulence in their migration's path (Lawrence et al. 2001).

We should note that the relatively small field of view ($\approx 15 \times 41$ arcsec), short time series (less than 28 min) and the restrictive criteria applied to select these small MBPs have limited our sample to a relatively small number of 103 isolated MBPs (a number density of $0.03 (Mm)^{-2}$; Paper I). However, selecting only point-like features has allowed us to locate the MBPs more accurately.

We found a mean diffusion index (or diffusion power-law exponent), γ , of 1.69 ± 0.08 averaged over all MBPs. The γ histogram is peaked close to this value and ranges from $\gamma \approx 0$ to $\gamma \approx 4$ (see Fig. 4.3). We suspect that, however, this wide range in the γ distribution does not reflect the presence of different diffusion regimes (i.e., sub-, normal or super-diffusive; as described in Sect. 4.3.2), but that it is possibly due to realisation noise (around the mean value representing a single diffusion category) due to our relatively short lived MBPs (mean lifetime ≈ 8 min).

We further explored the distribution of the diffusion index with the help of a Monte

Carlo simulation (see Sect. 4.4.2). It demonstrated that the migration of internetwork MBPs is consistent with a random walk (due to intergranular turbulences and granular evolution) superposed on a systematic velocity (caused by granular as well as meso- and super-granular flows). We note that a part of the motion of the magnetic Ca II H MBPs can be due to kink waves excited at such magnetic elements; whose effects were considered to be included in the random motion's component. The simulation clarified and confirmed that the deduced γ values of almost all MBPs are consistent with a single underlying γ of 1.69 ± 0.08 and that the large scatter of γ values of individual MBPs is indeed caused by the short lifetimes of these MBPs and the associated realisation noise.

Hence, the dispersal of the studied Ca II H MBPs in the quiet-Sun is mainly interpreted as super-diffusive. Note that excluding the network regions in the present study most likely has also excluded most MBPs located at stagnation points and hence, sub-diffusive MBPs have not been observed.

This result is in agreement with those reported by Lawrence et al. (2001), who found $\gamma = 1.13 \pm 0.01$ (on average) for MBPs, using high spatial and temporal resolution images in a region of enhanced magnetic activity. Super-diffusivity has been also reported by Abramenko et al. (2011) and Chitta et al. (2012) in recent investigations. They reported values of the diffusion index in a given type of region by averaging the displacements over all MBPs. Abramenko et al. (2011) obtained $\gamma = 1.48$ for quiet-Sun, $\gamma = 1.53$ for plage and $\gamma = 1.67$ for coronal hole areas, while Chitta et al. (2012) reported a diffusion index of 1.59 for their relatively short-lived MBPs (with a mean lifetime of about 3 – 4 min) observed in quiet-Sun regions. The mean γ for the quiet-Sun obtained in both studies are roughly consistent with the average $\gamma = 1.69 \pm 0.08$ that we found in the present work, although their values are slightly smaller. This may have to do with the fact that earlier γ values were obtained from ground-based observations and could be affected by differential seeing-induced deformations (introducing artificial turbulences), while we determined $\langle \gamma \rangle$ using the SUNRISE/SuFI data unaffected by seeing.

Lepreti et al. (2012) used the same datasets as Abramenko et al. (2011) to determine γ (for time-scales < 400 sec) for pair dispersion of MBPs (i.e., from measuring the mean-square separation of pairs of MBPs). They found same γ (≈ 1.48) for such pairs of MBPs observed in all the three regions (i.e., quiet-Sun, plage and coronal hole areas), from which, they interpreted the diffusivity properties as the results of the local correlations in the turbulence's inertial range. In addition, Lepreti et al. (2012) concluded that the diffusivity of individual MBPs studied by Abramenko et al. (2011) (that differs in the three regions) depends on the detailed structure of the flows.

Some published values of γ , of the diffusion coefficient (D) as well as of the mean lifetimes of the investigated features are compared with those obtained in this study in Table 4.3. Since the effect of atmospheric seeing is important, it is indicated if the observations are space, ground or balloon-based. The types of solar regions that were investigated can be deduced from the names of the features. With the exception of the investigations finding super-diffusive motions, discussed earlier, almost all other authors interpreted their results as indicative of normal or sub-diffusive processes. Berger et al. (1998b) did find a $\gamma = 1.34 \pm 0.06$. However, they interpreted it as in terms of normal diffusion with a slight indication for super-diffusivity, since the area coverage of their network MBPs as a function of time could be well explained by a Gaussian model. Cadavid et al. (1999) found normal diffusion ($\gamma = 1.10 \pm 0.24$) for time-scales longer than 25 min

and sub-diffusive MBPs ($\gamma = 0.76 \pm 0.04$) on time-scales shorter than 22 min, both based on tracking MBPs in a network area.

Manso Sainz et al. (2011) found, however, a mean value of 0.96 (nearly corresponding to normal diffusion) averaged over a wide distribution of γ for magnetic internetwork elements. We suspect that such a small value is due to their criterion of tracking only the footpoints of small-scale magnetic loops. The motion of such freshly emerged field is only partly driven by flows at the solar surface, to a significant extent it also reflects the dynamics and subsurface structure of the emerging field. Hence their results may not be directly comparable with ours.

As stated earlier, our Monte Carlo simulation describes the motion of our MBPs as the superposition of a directed systematic velocity v_s and a random velocity v_r . A comparison of the model output with observations of the horizontal motion of the Ca II H MBPs allowed us to determine both the random and systematic components as well as the effective coherence time of the random walk flows. We determined the mean values of these velocities to be $v_r \approx 1.2 \pm 0.1 \text{ km s}^{-1}$ and $v_s \approx 0.75 \pm 0.06 \text{ km s}^{-1}$. A coherence time of $62 \pm 3 \text{ sec}$ was found for the random velocity.

The random component of the velocity, obtained here, is consistent with that computed for the rms value of the horizontal transport of the magnetic concentrations in the intergranular areas (Cameron et al. 2011).

Horizontal flows in SGs can be measured through, e.g., tracking of markers (so-called corks) added on frames of image-sequences. Spruit et al. (1990) tracked corks over a mesogranule and found a cork velocity of 1.0 km s^{-1} as they move towards the mesogranular boundaries (on time-scales of about 10 – 30 min). They showed that the flow speed decreases when approaching the mesogranular boundaries, reaching to a minimum of about 0.5 km s^{-1} . This range of systematic velocities caused by granular (and/or meso- and super-granular) flows is comparable with that of found in the present work. Our determined systematic velocity is slightly larger than the mean horizontal flow velocity of $\approx 0.4 \text{ km s}^{-1}$ within SGs, reported by Title et al. (1989); Wang et al. (1995a); Hathaway et al. (2002) and those reported for the mesogranular flows ($\approx 0.3 \text{ km s}^{-1}$; Leitzinger et al. 2005). The v_s obtained in our investigation is in a good agreement with that of Del Moro et al. (2007), who found a horizontal flow speed of $0.75 \pm 0.05 \text{ km s}^{-1}$ inside a SG via cork tracking.

We also determined a mean diffusion coefficient (D ; the area that a MBP moves across per unit time) of $257 \pm 32 \text{ km}^2 \text{ s}^{-1}$ averaged over all studied MBPs. The diffusion coefficient values reported in the literature, summarised in Table 4.3 lie between 19 and $350 \text{ km}^2 \text{ s}^{-1}$. One source of such a large range could be due to the fact that different values could refer to different features. Schrijver et al. (1996) noted the diffusivity dependency of flux concentrations on the flux they contain, since the smaller concentrations move faster compared to the larger ones. Tracking small features on relatively short time-scales is another source of bias, since the potential effects of larger scales (e.g., supergranular flows) are detected more clearly when measuring for a sufficiently long duration (Schrijver et al. 1996). By tracking magnetic concentrations in a large FOV of MDI magnetograms, Hagenaar et al. (1999) found that the diffusion coefficient, $D = 70 - 90 \text{ km}^2 \text{ s}^{-1}$, determined for time intervals less than $1.0 \times 10^4 \text{ sec}$ is smaller than that measured on time-scales longer than $3.0 \times 10^4 \text{ sec}$, which gives $220 \leq D \leq 250 \text{ km}^2 \text{ s}^{-1}$. They interpreted such a difference (using a model) as the effect of supergranular flow that acts as a negligible

Table 4.3: Comparison of the mean values of diffusion index γ and diffusion coefficient D of small magnetic elements obtained in this study with some of those in the literature.

Reference	Base of Observations	Telescope/Spacecraft	Feature ^a	Lifetime ^b [sec]	γ	D^b [km^2s^{-1}]
This study	Stratospheric balloon	SUNRISE	IMBP	461	1.69	257
Chitta et al. (2012)	Ground	SST	IMBP	180 – 240	1.59	(≈ 90) ^c
Abramenko et al. (2011)	Ground	BBSO/NST	IMBP/NMBP ^d	(10 – 2000)	1.48	(19 – 320)
Manso Sainz et al. (2011)	Space	Hinode	IMBP	< 900	0.96	195
Utz et al. (2010)	Space	Hinode	IMBP	150	(≈ 1)	350
Lawrence et al. (2001)	Ground	SVST	NMBP? ^e	9 – 4260	1.13	-
Cadavid et al. (1999)	Ground	SVST	NMBP	18 – 1320	0.76	-
Hagenaar et al. (1999)	Space	SOHO	1500 – 3450 MBPL	1.10 < 1.0×10^4	- (≈ 1)	70 – 90
Berger et al. (1998b)	Ground	SVST	> 3.0×10^4 sec NMBP ^d	(100 – 3800)	1.34	60
Lawrence and Schrijver (1993)	Ground	BBSO	AME ^d	($\approx 1.8 \times 10^5$)	0.92	250

^a IMBP: Internetwork Magnetic Bright Point; NMBP: Network MBP; AME: A Magnetic Feature; MBPL: Magnetic Bright Points from a Large FOV, e.g., full solar disc.

^b Mean values; otherwise a range is given whenever it was available.

^c Values in parentheses are not directly reported in the papers, but are computed from the given plots/tables.

^d See their paper for other types of regions.

^e MBPs in a region of enhanced magnetic activity.

drift in short time-scales. Cadavid et al. (1999) discussed the mismatch between different reported diffusion coefficients in the literature due to the assumption of normal diffusion for all investigated features in most of the studies to date. Berger et al. (1998b) determined $D = 60.4 \pm 10.9 \text{ km}^2\text{s}^{-1}$ for network MBPs by assuming, for simplicity, Gaussian (normal) diffusion (i.e., $D = sd/2d\tau$), whereas the γ they obtained, $\gamma = 1.34 \pm 0.06$, corresponds to the super-diffusive regime. They also found a $D = 285 \text{ km}^2\text{s}^{-1}$ in quiet-Sun internetwork regions by tracking corks. Chae et al. (2008) reported the smallest value of $D = 0.87 \pm 0.08 \text{ km}^2\text{s}^{-1}$ determined for magnetic elements from Hinode/SOT magnetograms. This unusually small value, however, could reflect their somewhat different method of diffusivity measurements, by solving the equation of magnetic induction. Later, Utz et al. (2010) found $D = 350 \pm 20 \text{ km}^2\text{s}^{-1}$ for magnetic internetwork MBPs observed by the same telescope (i.e., Hinode/SOT). They obtained this value in the framework of the normal diffusion process. Manso Sainz et al. (2011) used the same instrument and found $D = 195 \text{ km}^2\text{s}^{-1}$ for footpoints of small-scale internetwork magnetic loops. We speculated that this relatively small value compared to that found in the present work is due to the fact that they considered only freshly emerged small loop footpoints.

Note that larger D values (compared to those mentioned above) have been also obtained from other techniques. For instance, a range of $D = 500 - 700 \text{ km}^2\text{s}^{-1}$ was determined by Simon et al. (1995) using a kinematic model of diffusion generated by supergranulation. Roudier et al. (2009) estimated $D = 430 \text{ km}^2\text{s}^{-1}$ using floating corks on a relatively large scale (larger than $2.5 Mm$).

Cameron et al. (2011) described the decay of the magnetic field by turbulent diffusion through 3D radiative MHD simulations that were run in a $6000 \times 6000 \text{ km}^2$ (from 800 km below the surface at $\tau_{5000 \text{ \AA}} = 1$ to 600 or 840 km above for different runs). They characterised the decay in terms of diffusion coefficients and found D to lie in the range of $100 - 340 \text{ km}^2\text{s}^{-1}$ for different upper boundary conditions (i.e., vertical or potential for the magnetic field, open or closed for the flows, 600 or 840 km above the optical surface for the height of the simulation box). Interestingly, the mean value of $D = 257 \pm 32 \text{ km}^2\text{s}^{-1}$ we obtained from the dispersal of SUNRISE Ca II H MBPs lies within the range deduced from MHD simulations by Cameron et al. (2011). In addition, the determined D value is within the range of diffusion coefficients observed over a much longer durations and larger areas (see Schrijver and Zwaan 2000, Table 6.2).

Furthermore, we found a direct correlation between D and time-scale (τ) computed from trajectories of all MBPs (see Fig. 4.5). Note that the dependency of $D(\tau)$ on γ is not surprising though, since it follows the relationship expressed in Eq. 4.5. The $D(\tau)$ trend we obtained from our super-diffusive MBPs tends to be steeper than those measured by Lawrence et al. (2001) and Abramenko et al. (2011) for internetwork super-diffusive features. Abramenko et al. (2011) compared such a relationship with other types of regions (e.g., network areas, active regions and a coronal hole area) and other diffusion regimes reported in the literature. They showed that such a direct correlation between D and τ is only observed for the case of super-diffusion ($\gamma > 1$). D s Constant with time for $\gamma = 1$ (Schrijver et al. 1996; Berger et al. 1998b; Hagenaar et al. 1999) as well as anti-correlations between D and τ (Berger et al. 1998b; Cadavid et al. 1999) for $\gamma < 1$ are also observed.

Recently, Orozco Suárez et al. (2012) studied the horizontal velocity of both convective flows and internetwork magnetic elements (IMEs) over a SG during a 13-hour unin-

errupted observing campaign. They found that the IMEs are almost at rest at the centre of the SG where they start accelerating while radially moving outward. The IMEs tend to decelerate while approaching the SG's boundaries.

We speculate that a hypothetical long-lived MBP (that may appear or disappear at any location in body of a SG) would gently accelerate over the SG's bulk due to mass conservation assuming a constant upflow over most of the SG's area and to systematically advect such a MBP towards the SG's borders. In addition, granular and mesogranular flows (that act on shorter spatial scales) would impart it with additional velocity components that change as these convection cells evolve. Trajectory of such a MBP is expected to follow a super-diffusive regime, although with a lower γ than expected from the SG flow alone, due to the random motions imparted mainly by granular evolution (which for a very long-lived MBP contributes mainly to v_r) and intergranular turbulence. This MBP would start decelerating when approaching the SG's boundary. Once the MBP finds itself in the network region, it is trapped in the sinks (stagnation points) due to inflows from opposite directions, i.e., from neighbouring SGs. The ever evolving granular flows will keep acting on small spatial scales. The trajectory of the MBP at this stage of its evolution is likely to be best explained by a normal and/or sub-diffusion processes.

This scenario may explain why the sub- and normal- diffusive MBPs were almost the only diffusion regimes reported in the literature before ≈ 2000 (Berger et al. 1998b; Cadavid et al. 1999; Lawrence et al. 2001): older studies most likely concentrated on network areas. For ground-based observations, another effect is also important: the residual aberrations and distortions due to variable seeing introduce an artificial turbulent motion into image time series, which leads to artificially small γ s. It is worth noting that lower resolution observations need not lead to smaller γ values and in fact, the larger scale flows (e.g., supergranular flows) would be detected better compared to smaller scale motions. This latter effect results in a larger γ value.

To summarise, we characterised the motions of SUNRISE Ca II H MBPs by turbulent diffusion theory. The MBPs (mean lifetime ≈ 8 min) were observed in seeing-free high-resolution image sequences in an internetwork area of the quiet-Sun. A mean diffusion index of $\gamma = 1.69 \pm 0.08$ as well as a mean diffusion coefficient of $D = 257 \pm 32 \text{ km}^2\text{s}^{-1}$ were obtained. The γ corresponds to super-diffusion which describes the MBPs as features whose squared displacement (sd) from the first observed location grows faster than linearly with time. It is, to our knowledge, the largest γ value for MBPs reported in the literature so far. The latter parameter (D) lies within the range of decay rate of the magnetic field from MHD simulations and is among the largest D values obtained for small-scale magnetic features found in the literature. We found that D increases as the time-scale increase, but always lies in the range of those obtained by other investigations for larger spatial extend and longer durations. The migration of relatively short-lived features like MBPs tend to be constructed by a superposition of random motions due to granular evolution and intergranular turbulence and a systematic granular, mesogranular and supergranular flows.

5 Propagation of high-frequency fast waves in small magnetic elements observed by SUNRISE/SuFI

To be submitted to A&A by S. Jafarzadeh^{1,2}, S. K. Solanki^{1,3}, M. Stangalini^{1,4}, R. H.-Cameron¹, S. Danilovic¹ and A. Gandorfer¹.

Abstract We characterise waves in small solar magnetic elements and investigate their propagation.

We use the wavelet transform to analyse oscillations of horizontal displacement as well as intensity of magnetic bright points (MBPs) in the 3000 Å and Ca II H 3968 Å passbands of the filter imager on the Sunrise balloon-borne solar observatory.

We find evidence for upward propagating waves at high-frequencies (up to 30 mHz). The measured time-lags are consistent with a speed of 36 ± 4 km s⁻¹ for kink waves as well as 144 ± 4 and 24 ± 4 km s⁻¹ for fast compressible waves, once the height difference between the two layers is considered. A decrease in horizontal velocity amplitudes as well as an increase in intensity amplitudes with height are also observed.

Both compressible and incompressible (kink) waves have been found in small-scale magnetic features. The two types of waves have different, although overlapping, distributions of periods. The differences in phases between the two observed heights reveal upward propagation of short period fast waves of both kinds in the selected MBPs. Such fast waves can be explained best as the results of mode conversion at the level of plasma beta unity (where the sound and Alfvén speeds coincide) as well as the propagation path of the fast magnetic mode.

5.1 Introduction

Wave phenomena in solar magnetic features have been proposed as a prime means of transferring the energy from the solar interior and lower atmosphere, needed to maintain the high temperatures of the mid and upper solar atmosphere as well as to power the solar

¹ Max-Planck-Institut für Sonnensystemforschung, Max-Planck-Str. 2, 37191, Germany

² Institut für Astrophysik, Georg-August-Universität Göttingen, Friedrich-Hund-Platz 1, 37077, Germany

³ School of Space Research, Kyung Hee University, Yongin, Gyeonggi 446-701, Republic of Korea

⁴ Dipartimento di Fisica, Università di Roma, via della Ricerca Scientifica 1, 00133 Rome, Italy

wind (e.g., Choudhuri et al. 1993b; De Pontieu et al. 2007; Straus et al. 2008; Taroyan and Erdélyi 2009; Vigeesh et al. 2009; Bello González et al. 2009; McIntosh et al. 2011; Jafarzadeh et al. 2013a). Most observations of propagating waves in magnetic structures are either restricted to the chromosphere and higher layers or to large features, such as sunspots. Here, we present observations of short-period waves propagating along thin, magnetic flux tubes in the lower solar atmosphere, whose transported energy is thought to be responsible for the intensity enhancements of magnetic bright points (MBPs) seen in strong chromospheric lines such as Ca II H (Hasan and van Ballegooijen 2008).

The oscillations in the magnetised solar atmosphere are represented by different modes of oscillation, depending on their compressive/non-compressive and magnetic nature, (Edwin and Roberts 1983; Hasan and Sobouti 1987; Bogdan et al. 2003; Roberts 2006; Kato et al. 2011), and occur in propagating or standing states (Rosenthal et al. 2002; Dorotovic et al. 2013). The magnetic fields act as a guide for MHD waves connecting different layers of the solar atmosphere. Stangalini et al. (2011) showed that the longitudinal acoustic waves in the photosphere are propagated along the magnetic field lines and their leakage to the upper atmospheric layers is dependent upon the inclination of the magnetic field.

Magnetic waves excited in a thin flux tube, are generally classified, for simplicity, according to their propagation speeds: (1) Alfvén waves propagating with the local Alfvén speed, e.g., inside a flux tube, (2) axisymmetric, longitudinal magneto-acoustic mode which propagates with the tube speed c_T that is smaller than both sound c_S and Alfvén c_A speeds ($c_T = c_S c_A / \sqrt{c_S^2 + c_A^2}$), and (3) non-axisymmetric, transversal kink waves propagating with a speed between that of the surroundings and c_A (e.g., Spruit 1982; Solanki 1993; Roberts and Ulmschneider 1997; Cranmer and van Ballegooijen 2005; De Pontieu et al. 2007; Khomenko et al. 2008; Jess et al. 2009; Morton et al. 2011; Pietarila et al. 2011; Mathioudakis et al. 2012). Within thicker flux tubes additional wave modes also propagate: the fast and the slow mode, travelling at speeds that depend on the ratio of c_A/c_S and on the direction of propagation relative to the field lines (the slow MHD waves propagate only along field lines, while the fast waves can propagate in all directions). In general, both modes are compressible. The slow mode is closely related to the tube mode (longitudinal magneto-acoustic mode; e.g., Kato et al. 2011). While the slow modes dissipate in the chromosphere by forming shocks (e.g. Ulmschneider 1970; Erdélyi 2006), a fraction of the fast waves may penetrate into the upper solar atmosphere (due to their higher phase speeds, which reduce the occurrence of shocks). Hence, the fast waves (and the Alfvén waves) are of interest for understanding the heating mechanisms of the outer solar atmosphere, while the slow waves may contribute in heating of the low-to-mid chromosphere. Note that the fast waves may also be refracted due to the large gradient of the Alfvén speed (Nutto et al. 2012).

While each of these waves may propagate along a flux tube, coupling between different modes may also occur (Roberts 2004; Khomenko et al. 2008). Numerical simulations of wave propagation in the lower solar atmosphere have shown coupling of fast and slow magneto-acoustic waves in regions where the acoustic and Alfvén speeds nearly coincide, i.e., where the plasma- $\beta \approx 1$ ($\beta \equiv 8\pi p/B^2$; Bogdan et al. 2003). This level has been called the “equipartition level” (Cally 2007), where equipartition between magnetic and thermal energy density is achieved. At other places, the waves with magnetic dominated and acoustic natures are decoupled. The modes of such waves in low and high β media are summarised in Table 4 of Bogdan et al. (2003). At the equipartition level, part of the

energy contained in the acoustic branch can be channelled to the magnetic branch and vice versa, while, the waves are also partly transmitted through the conversion layer without changing their physical natures, but with exchanging the fast and slow labels. The former and latter cases are normally referred to as “mode conversion” and “mode transmission”, respectively (Cally 2007). The fraction of energy transmitted or converted depends on the attack angle of the wave itself, the wavelength and the width of the conversion layer (Schunker and Cally 2006; Hansen and Cally 2009; Stangalini et al. 2011). In addition to the fast and slow waves whose physical nature depends on the level of plasma- β , (transverse) Alfvén waves may propagate in both $\beta > 1$ and $\beta < 1$ regions (Rosenthal et al. 2002; Bogdan et al. 2003).

Both incompressible (kink) and compressible (e.g., sausage) waves are thought to be excited in the magnetic elements by the interaction of the flux tubes with surrounding granules (Hasan and Kalkofen 1999). Very recently, by exploiting the high spatial resolution provided by SUNRISE/IMaX, Stangalini et al. (2013) have reported the interaction between longitudinal and horizontal velocity oscillations in small magnetic elements in the solar photosphere.

MHD simulations have also shown that strong localised pressure pulses can excite fast and slow magneto-acoustic waves propagating along the magnetic flux tubes (Shibata 1983). Also p -modes and convective motions can locally drive magneto-acoustic waves in magnetic structures (Khomenko and Calvo Santamaria 2013). Spruit (1981a) and Choudhuri et al. (1993b) proposed that rapid, pulse-like motions of the flux-tube footpoints produce kink waves along the tubes that can propagate into the upper solar atmosphere. The energy that such jerky motions can potentially carry, may contribute to the heating of the quiet corona (e.g., Hasan et al. 2000; Hasan and van Ballegoijen 2008; Jafarzadeh et al. 2013a). Cranmer and van Ballegoijen (2005) found that the energy of incompressible, transversal kink waves, propagating along flux tubes, are transformed into the volume filling Alfvén waves above the height where individual flux tubes merge (i.e., in the chromosphere). However, according to their model that 95% of such Alfvénic waves are reflected at the transition region. The propagating mechanisms of the magneto-acoustic and kink waves in small magnetic element (in the lower solar atmosphere) has been studied in detail in 2D (e.g., Khomenko et al. 2008) and 3D (e.g., Vigeesh et al. 2012) simulations.

Please note that we have reviewed the propagation of waves only in the lower solar atmosphere. Waves in the upper layers of the atmosphere have also been observed, e.g., in coronal loops (Aschwanden et al. 1999; De Moortel et al. 2002; Wang et al. 2003, cf. Nakariakov and Verwichte 2005 for a review), in quiet-Sun with frequencies up to 100 mHz using the *TRACE* spacecraft (DeForest 2004) or in spicules from Hinode/SOT with an average frequency of 19 mHz (Okamoto and De Pontieu 2011) and many others.

In addition, different excitation mechanisms have been proposed or speculated upon for the same wave mode observed at different heights from the solar surface. For instance, the excitation of kink waves observed in the lower solar atmosphere has been attributed to buffeting of the flux tubes carrying them by the surrounding granular flows (Hasan and van Ballegoijen 2008), while, small-scale magnetic reconnection in the chromosphere has been proposed to drive the kink modes detected in the higher atmosphere (He et al. 2009).

Note that we have only focused on the wave propagating within magnetic elements.

In non-magnetised areas, waves such as acoustic, gravity and surface gravity (generating resonant modes of oscillation as p -modes, g -modes, and f -modes below the solar surface, respectively) also exist (Deubner and Gough 1984). Propagation of, e.g., acoustic waves in non-magnetised atmosphere, can also transmit energy contributing to the heating of the chromosphere (Carlsson and Stein 1997; Erdélyi et al. 2007).

In this chapter, we investigate the propagation of high-frequency waves in the lower solar atmosphere by analysing both horizontal displacement oscillations of MBPs and their intensity perturbations at two sampled heights observed at high spatial and temporal resolution by the SUNRISE balloon-borne solar observatory. We detect high-frequency fast waves, both compressible and incompressible, propagating at the selected MBPs in the lower solar atmosphere. In Sect. 5.2 we introduce the data used in this analysis. In Sect. 5.3 we describe our analysis methods that retrieve the observational properties of the waves. We provide the results and corresponding interpretations in Sect. 5.4. The results are discussed and conclusions are drawn in Sect. 5.5.

5.2 Observations

High spatial and temporal resolution observations of quiet-Sun disc centre at 3000 \AA (FWHM $\approx 50 \text{ \AA}$) and $\text{Ca II H } 3968 \text{ \AA}$ (FWHM $\approx 1.8 \text{ \AA}$) were carried out using the SUNRISE Filter Imager (SuFI; Gandorfer et al. 2011) aboard the SUNRISE balloon-borne solar observatory (Solanki et al. 2010; Barthol et al. 2011; Berkefeld et al. 2011) on 9 June 2009. Simultaneous full Stokes observations in the magnetically sensitive $\text{Fe I } 5250.2 \text{ \AA}$ line by the Imaging Magnetograph eXperiment (IMaX; Martínez Pillet et al. 2011) on board SUNRISE provided the photospheric magnetograms which were used to determine the magnetic properties of features observed in the other passbands.

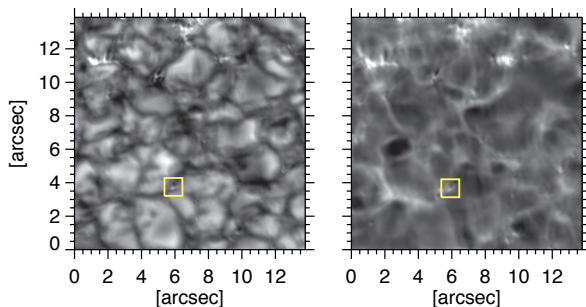


Figure 5.1: Images in the SUNRISE/SuFI 3000 \AA (left panel) and $\text{Ca II H } 3968 \text{ \AA}$ (right panel) passbands. The yellow boxes include a sample magnetic bright point studied here.

The seeing-free 3000 \AA and Ca II H image sequences employed in this work share a common field-of-view of $14 \times 40 \text{ arcsec}$, and were both recorded with a cadence of 12 sec. The recordings at the two wavelengths are offset by 1 sec in time (3000 \AA images follow Ca II H filtergrams).

Figure 5.2 shows a small part of a snapshot in each wavelength. A MBP is marked whose horizontal displacement fluctuations as well as intensity oscillations are studied here.

We estimate the heights of formation of the 3000 Å band and Ca II H line profile by computing their contribution functions (CFs) using the RH radiative transfer code (Uitenbroek 2001). The code provides the contribution of each height to the emission at a certain wavelength by solving both radiative transfer and statistical equilibrium equations in a given atmospheric model. Following the discussions in Jafarzadeh et al. (2013a) (hereafter referred to as Paper I), we use the FALP model atmosphere (Fontenla et al. 1993) to describe the MBPs after convolving the CFs at different wavelengths by the spectral profile of the relevant SuFI filter. For more details of similar implementations we refer the reader to section 2.1 in Paper I. For comparison, the CFs resulting from the FALC model atmosphere (that represents an averaged quiet-Sun region) are also determined. The CFs for 3000 Å line profile are computed for the continuum and in LTE (Local Thermodynamic Equilibrium) conditions, while the radiative transfer and statistical equilibrium equations are solved for the Ca II H line to calculate the line-depression CFs (Magain 1986; Grossmann-Doerth et al. 1988) in non-LTE. Plotted in Fig. 5.2 are the CFs for the two passbands and both atmospheric models. We show this figure here, although some of the results can already be found in Paper I in order to highlight the difference between the CFs and average formation heights of the 3000 Å and Ca II H passbands of SUNRISE/SuFI. The vertical dashed lines indicate the corresponding average formation heights weighted by the CFs. An average height difference of ≈ 450 is determined between images observed in 3000 Å and Ca II H passbands; from the mean heights of formation. The sudden drop of the Ca II H CF for the FALP at ≈ 1700 km is due to the rapid temperature increase in the upper chromosphere, leading to the ionisation of Ca⁺.

5.3 Method of analysis and a case study

We study wave-like phenomena in the lower solar atmosphere by analysing oscillations in both horizontal displacement and intensity of small-scale magnetic features, the intensity oscillations being a tool to investigate the presence of compressive modes in the magnetic elements. Knowledge of the precise position of such elements versus time is a must in such analyses, which requires seeing-free observations. We focus on magnetic, bright, small point-like features (i.e., MBPs) similar to the ones studied in Paper I. Consequently, the accurate locations as well as intensity of such MBPs are determined using the same algorithm as described in detail in Paper I.

In order to determine whether any of the detected waves are propagating (and to measure the speed of propagation) we need to track horizontal displacements and intensity oscillations in both passbands, 3000 Å and Ca II H.

We found 7 MBPs whose trajectories could be precisely tracked in both 3000 Å and Ca II H image sequences for a sufficiently long time, i.e., longer than 5 min. This latter criterion improves the frequency resolution in the observed oscillations. The number of MBPs investigated here is lower than the SUNRISE Ca II H BPs studied in Paper I with lifetimes longer than 5 min because of the relatively low contrast in the 3000 Å filtergrams compared to the Ca II H images (Riethmüller et al. 2010). We dropped all those MBPs that could not be precisely tracked at both filter positions over their complete lifetimes.

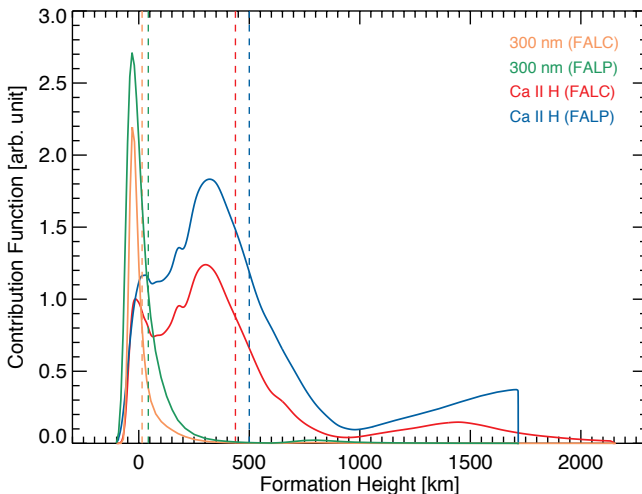


Figure 5.2: Contribution functions for the SUNRISE/SuFI 3000 Å and Ca II H passbands from the RH radiative transfer code, for two atmospheric models (see text). The vertical dashed lines indicate the corresponding (weighted) average formation heights.

By restricting ourselves to the smallest MBPs we may have discarded the longer lived ones (if larger MBPs have longer lifetimes).

Please note that although uncertainties introduced by the locating algorithm as well as instrumental vibration-induced image jitter may bias the final analysis, their effects are much smaller than the motions of the MBPs under study. Jafarzadeh et al. (2013a) found an average uncertainty of 0.02 km s^{-1} in the determined horizontal velocities of similar MBPs. This is much lower than the mean amplitude of the Ca II H MBP horizontal velocities of 1.3 km s^{-1} in the present study. The power spectra of the residual image jitter (in both horizontal and vertical directions) measured for the SUNRISE observatory shows a frequency range of about 10 – 150 Hz (Berkefeld et al. 2011) which is much higher than the sub-Hertz frequencies of the waves under study (see Sect. 5.4). Hence, the effect of instrumental vibration-induced jitter is negligible in our analysis, except for smearing the images. Moreover, we observe clear phase-lags between the oscillations observed in the two heights (see Sect. 5.3.2) that cannot be due to the jitter or random motions.

The maximum intensity over all pixels of the MBPs is measured at any given time. Jafarzadeh et al. (2013a) obtained an average photon noise of $0.01 \langle I_{Ca} \rangle$ in the Ca II H images as a mean uncertainty in determining the intensity that is much smaller (by a factor of 15) than the mean amplitude of the Ca II H intensity oscillations. The 1 sec time difference between the two time-series (i.e., 3000 Å and Ca II H image sequences) were corrected by adding the corresponding phase angle.

5.3.1 Wavelet transform

We perform a wavelet analysis (Daubechies 1990; Torrence and Compo 1998) in order to simultaneously localise the spectral power in both time and frequency domains. The wavelet transform is especially suitable for searching for transient oscillations and for studying wave propagation within the solar atmosphere in the presence of non-stationary signals (Baudin et al. 1994, 1996; Bloomfield et al. 2004; McIntosh and Smillie 2004; Jess et al. 2007).

The wavelet (W) is defined as the convolution of the time-series with a mother function that is a window (envelope) whose variable width enables the analysis to capture both low/high frequencies and long/short durations simultaneously. We employ the Morlet mother function with a dimensionless frequency $\omega_0 = 6$ using a wavelet algorithm developed by Grinsted et al. (2004). This function satisfies the balance between frequency and time localisation (Farge 1992) and hence is suitable for investigating propagation of waves with different ranges of frequencies. The Morlet function is a complex wavelet, consisting of a plane wave modulated by a Gaussian window, described as

$$\psi_0(\eta) = \pi^{-1/4} e^{i\omega_0\eta} e^{-\eta^2/2}, \quad (5.1)$$

where $\eta = s t$ is a dimensionless time that stretches the wavelet in time t by changing its scale s .

The wavelet power spectrum of a time-series is defined as $|W(s)|^2$. The cross-spectrum (or cross wavelet power spectrum) of two time-series is then determined by multiplying the wavelet of a time-series with the complex conjugate of the other one. The cross-spectrum highlights times and regions with strong common power in the two time-series. Furthermore, the cross-correlation between the wavelet power spectra of the two time-series is examined by wavelet coherence, which is the square of the cross-spectrum normalised by the individual power spectra (Grinsted et al. 2004). The coherence level varies between 0 (representing incoherent oscillations) and 1 (for coherent oscillations). Power spectra are determined of all four time-series (horizontal displacement and intensity oscillations at the two sampled heights). Cross power and coherence are computed between the time-series of a given type of oscillation sampled at different heights.

We also measure the phase difference between such pairs of time-series, since phase lags provide information on wave propagation. These phase-lags are estimated from the complex arguments of the cross spectra. To ensure the reliability of the results we will only consider those cases in which the wavelet coherence of the oscillations at the two heights is above 0.7.

5.3.2 A case study: Wavelet analysis of a MBP

Figures 5.3a-d show the wavelet power spectra of the horizontal velocity perturbations and intensity oscillations observed in the Ca II H and 3000 Å passbands for the MBP highlighted in Fig. 5.2. The colour-scale represents the power in arbitrary units. The areas with bleached colours represent the so-called cone-of-influence (COI) which defines regions that are subject to edge effect. Hence, only the computed values outside the COI are considered for the analysis.

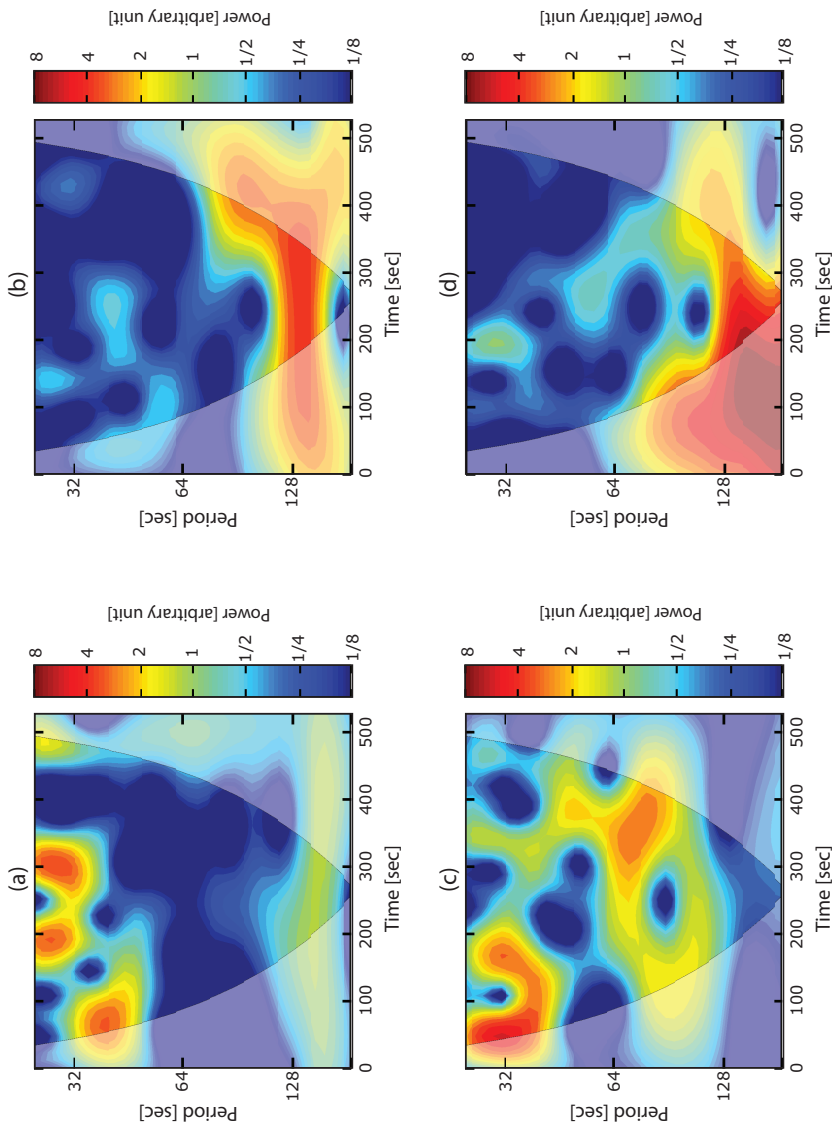


Figure 5.3: (Caption on the following page.)

Figure 5.3: Wavelet power spectra of oscillations in a small magnetic bright point. (a) For horizontal displacement oscillations observed in SUNRISE/SuFI Ca II H time-series. (b) For intensity oscillations in SUNRISE/SuFI Ca II H time-series. (c) For horizontal displacement oscillations observed in SUNRISE/SuFI 3000 Å image sequences. (d) For intensity perturbations in SUNRISE/SuFI 3000 Å image sequences. The cone-of-influence area is shown by the identified washed-out colours (see main text).

This sample MBP has a lifetime of 528 ± 9 sec (For details on determining the lifetime and its uncertainty of similar MBPs we refer the reader to Sect. 3.2.2 of Jafarzadeh et al. 2013a). The wavelet analysis of the oscillations revealed periodicities with a wide range of values, 25 – 187 sec, for this magnetic element.

Both panels ‘a’ and ‘c’ in Fig. 5.3 show several power peaks indicating the occurrence of (horizontal displacement) oscillations with different periods at different times. The correlations between these high power patches are shown by the wavelet coherence, represented in Fig. 5.4a. We can see from this figure that in the period range 25–50 sec, there are three high-coherent patches at $t \sim 80$ sec, $t \sim 200$ sec and $t \sim 480$ sec. In all cases, the strong features in panel ‘a’ of Fig. 5.3 (corresponding to the oscillations observed in Ca II H) seem to occur after their corresponding features in panel ‘c’ (representing the oscillations seen in the 3000 Å bandpass). The power patches in intensity oscillations are displayed in Figs. 5.3b and 5.3d along with their wavelet coherence shown in Fig. 5.4b. In the latter situation, much of the power is concentrated at longer periods compared to the horizontal velocity perturbations.

In all plots only small areas outside the COI correspond to high power values. However, they are sufficient for identifying the oscillatory motions. Moreover, we are interested in the correlations of the oscillations between the two sampled heights. Wave parameters obtained from oscillations in one layer could be biased by the poor repetitive power.

Please note that the wavelet coherence attains large values in areas which do not necessarily represent the high power patches in individual wavelet power spectra, in particular for horizontal displacements. Therefore, the individual power spectra are not a particularly good guide to the presence of correlated oscillations at the two heights, with the wavelet coherence providing better information on wave propagations.

The phase angle between the two layers can be deduced from the small arrows on both plots of wavelet coherence (Figs. 5.4a and 5.4b). Arrows pointing to the right and to the left represent in-phase and anti-phase oscillations in the two layers, respectively. Downward pointing arrows indicate that the oscillations in Ca II H lead the oscillations in 3000 Å images, which would imply downward propagating waves. For simplicity, we have only over-plotted the arrows (i.e., the phase-lags) for those regions whose coherence levels exceed 0.5. We take a larger coherence level of 0.7 as a lower limit for the reliable correlation between the two oscillations. The 0.7 coherence levels are indicated by solid (black) contours in Figs. 5.4a-b. In all positions outside the COI and for coherence levels exceeding 0.7, the arrows tend to point upwards (i.e., positive phase-angle) indicating that the oscillations observed in Ca II H images follow the ones seen in 3000 Å filtergrams (sampling the lower layer in the solar atmosphere compared to Ca II H), and hence, the waves propagate upwards.

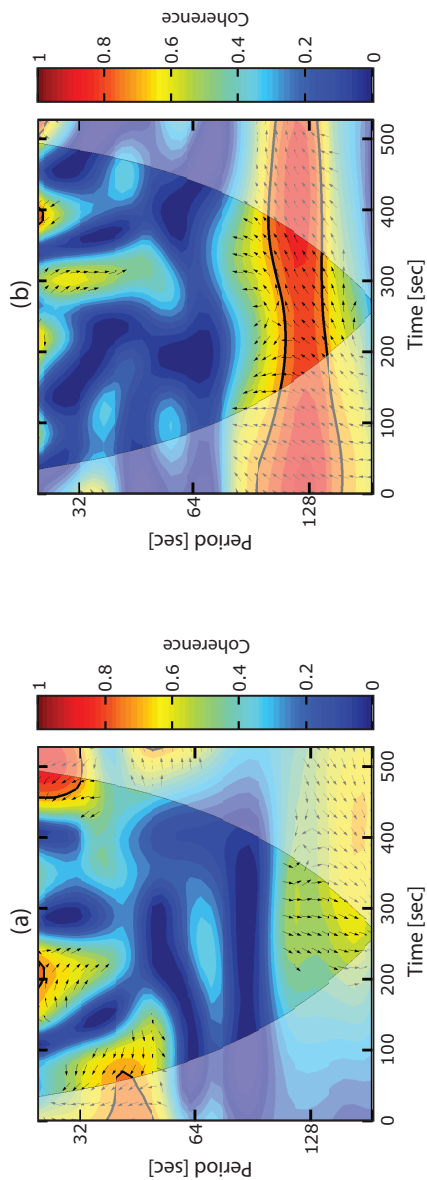


Figure 5.4: Wavelet coherence between perturbations in 3000 \AA and Ca II time-series for horizontal displacements oscillations (a) and for intensity oscillations (b). The arrows indicate the phase-lag between the two time-series observed at the two sampled heights; with in-phase oscillations marked by arrows pointing right and Ca II leading 3000 \AA by 90° depicted by arrows pointing straight down. The 0.7 coherence level is indicated by black solid contours.

Different angles of the upward pointing arrows represent different phase angles between the oscillations in the two layers and can be converted to time-lags τ (i.e., the wave travel-time) for specific frequencies using

$$\tau = \frac{\varphi}{2\pi f}, \quad (5.2)$$

where φ and f are the phase-lag and frequency values, respectively.

We compute the time-lags corresponding to all points in the wavelet coherence (e.g., Fig. 5.4) which are located outside the COI and for coherence levels exceeding 0.7. The propagation speed of the wave (c_w) can then be calculated for each frequency by its corresponding τ and the height difference h between the two heights sampled by the analysed data, i.e., $c_w = h/\tau$.

5.4 Statistics and wave identification

Plotted in Figs. 5.5 and 5.6 are 2D histograms of phase-angle versus period from wavelet coherence of horizontal velocity and intensity oscillations, respectively, of all 7 investigated MBPs. All phase-angle values obtained from all 7 analysed MBPs enter Figs. 5.5 and 5.6, as long as their coherence exceeds 0.7 and the coherences are located outside the COI. Examples are all phase-angles obtained from the wavelet coherence spectra satisfying the above criteria in Figs. 5.4a and b.

The background colours in Figs. 5.5 and 5.6 represent the sample density. For robust statistics unbiased by outliers with a small probability of occurrence (due to, e.g., spurious coherence between the two oscillations), the extreme outliers, i.e., the values lying outside the clusters of most of the other data points, are determined. We separate concentrated regions from the extreme outliers using the Grubbs statistical significance test (Grubbs 1969). This test estimates a criterion corresponding to the largest deviation from the mean value in units of the standard deviation σ of the data points in the 2D histograms. Regions with smaller number density than this criterion are considered to host the outliers whose small probability of occurrence compared to the rich cluster of other data points may bias the further interpretations (Press et al. 2007). The dot-dashed contours in Figs. 5.5 and 5.6 indicate the estimated Grubbs' criteria of 4.4σ and 5σ , respectively, from the mean values of the concentrated regions.

We find occurrence of short period (high-frequency) oscillations: (1) a period range of 30 – 75 sec for horizontal velocity perturbation (with the distribution's peak at 62 sec) and (2) periods between 30 and 195 sec for intensity fluctuations (with two peaks of the distribution at 41 and 135 sec). The phase-angle distributions show almost only positive values, meaning the propagation of wave-like phenomena from the height sampled by 3000 Å passband (i.e., lower layer) towards the height sampled by the Ca II H filter. However, about 15% of all occurrence in the intensity histogram have a negative phase-angle that can represent a downward propagation. In addition to the main peaks of this histogram at 41 and 135 sec, the distribution shows concentrations of occurrences/points peaking at 72 sec and a less densely populated region between 160 and 190 sec. These regions get completely separated for a coherence level of, e.g., 0.8. We cannot, however, verify whether these separated regions represent distinct dispersion relations due to, e.g.,

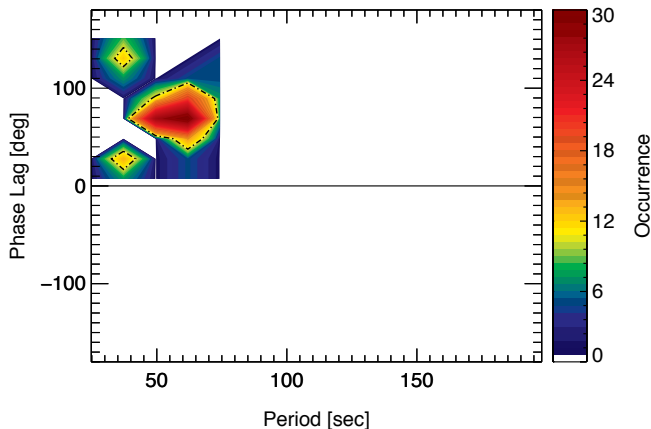


Figure 5.5: 2D histogram of phase-lag versus period from wavelet coherence of horizontal velocity oscillations between 3000 \AA and Ca II H passbands with coherence levels exceeding 0.7. Positive phase-lags represent upward propagations.

different waves with different modes or natures. The wave speeds corresponding to these regions might provide such information.

Using Eq. 5.2, we obtained a travel-time of 12 sec for the peak of the histogram of the horizontal displacement (Fig. 5.5). The travel-times calculated for the two major peaks of the intensity fluctuations' 2D histogram (Fig. 5.6) are 3 and 18 sec.

We now want to see whether the time delay is compatible with what we expect from acoustic waves. We follow Lawrence et al. (2011); Lawrence and Cadavid (2012) and assume that the trend connecting the peaks in Fig. 5.6, or a part of that, represents the acoustic dispersion relation, we can estimate the height difference between the two layers by using the wave travel-time τ computed using Eq. 5.2 and a sound speed $c_S \approx 7 - 8 \text{ km s}^{-1}$. In this case we get $\Delta h \approx 20 - 60 \text{ km}$, a height difference which is small compared to the $\approx 450 \text{ km}$ estimated from radiative transfer (see Sect. 5.2). A somewhat larger c_S as may result in a hot magnetic element is not able to resolve this discrepancy. This is also evident by looking at the phase lag expected for acoustic waves assuming a height difference of 450 km, overplotted in Fig. 5.6 (dashed line). The phase lag is much larger than that observed in the MBPs at all frequencies. This means that either the waves in the magnetic features propagate much faster than sound, or the heights determined from the CFs are wrong.

In order to identify which of these causes is responsible for the observed discrepancy, we apply a similar analysis as carried out so far, but based on the Fourier transform, to intensity oscillations of both, 3000 \AA and Ca II H time-series in a relatively large FOV (i.e., $14 \times 5 \text{ arcsec}^2$) of quiet-Sun. This area was chosen based on a visual inspection in which only a relatively small number of MBPs (with no other larger magnetic structures) appeared in the whole selected FOV and for the entire time-series.

We perform the Fourier transform on the entire length of the time-series recorded by

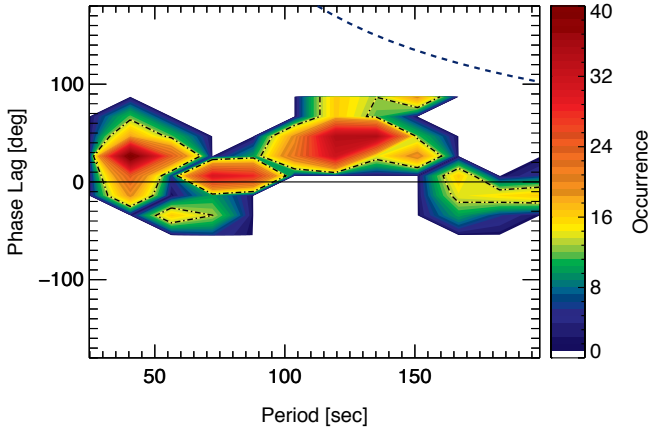


Figure 5.6: Same as Fig.5.5 but for the intensity oscillations. The dashed curve represents the dispersion relation of acoustic waves (see main text).

individual pixels separately and compute phase-lags between the time-series from their cross spectrum. In the averaged quiet-Sun, the acoustic wave is expected to be dominant, with $c_S \approx 7 - 8 \text{ km s}^{-1}$. The acoustic or other compressible waves propagating in any magnetic elements in the selected quiet-Sun FOV may have a different behaviour (i.e., guided by the magnetic field lines; meaning that the acoustic waves are modified to magneto-acoustic waves travelling at the tube speed along the flux tubes). However, their contribution to the obtained phase-lag is very small, since they only cover a very small fraction of the whole FOV. The phase-lag can be converted into a time-lag using Eq. 5.2 for each Fourier frequency.

Figure 5.7 shows a 2D histogram of phase versus frequency. Figure 5.7 illustrates the unwrapped phase-diagram, i.e., the phase-diagram that is corrected for phase jumps of 360° . Acoustic waves with frequencies larger than the corresponding cut-off-frequency can propagate within the atmosphere. We found acoustic waves in the high-frequency range of $4 - 38 \text{ mHz}$ that are propagating upwards. The lower boundary of the frequency range ended at the cut-off frequency of the acoustic waves; while they are all marginally below the Nyquist frequency ($\approx 42 \text{ mHz}$). A nearly linear trend can be clearly observed. We assume that this ridge is due to acoustic waves. The slope of this ridge is given by the best fit black solid line. The yellow error bars indicate the standard deviation of the scatter data points along the phase-lag axis (they do not represent the uncertainty of the slope). The slope reflects the travel time of the acoustic wave between the two layers and is equal to $57 \pm 2 \text{ sec}$. From there, we find a height difference of $430 \pm 30 \text{ km}$ between layers of the quiet solar atmosphere sampled by the 3000 \AA and Ca II H passbands. The error comes from the uncertainty in determining the slope and in the sound speed of $7.5 \pm 0.5 \text{ km s}^{-1}$.

For comparison, we have over-plotted the expected phase difference ($\Delta\varphi$) versus frequency (f) for intensity oscillations between the two layers, based on three different models explained by Centeno et al. (2006): (1) Linear adiabatic (vertical) wave propagation

in an isothermal non-stratified atmosphere (red, dashed-line), Eq. 5.2. (2) In a stratified atmosphere including gravity (white, dot-dashed line):

$$\Delta\varphi = (\Delta h \sqrt{\omega^2 - \omega_{ac}^2})/c_S, \quad (5.3)$$

where $\omega = 2\pi f$, $\omega_{ac} = \gamma g/2c_S$ is the acoustic cutoff frequency, $g = 274 \text{ m s}^{-2}$ is the gravity (assumed to be constant) and $\gamma = 5/3$ is ratio of the specific heats for an adiabatic propagation.

(3) Same as model 2 but for radiative losses with Newton's law of cooling (dark blue, long dashed line; originally developed by Souffrin 1972):

$$\Delta\varphi = \Delta h \sqrt{\frac{h_R + \sqrt{h_R^2 + h_I^2}}{2}}, \quad (5.4)$$

where

$$h_R = \frac{\omega^2(1 + \omega^2 \tau_R^2 \gamma)}{gH_0(1 + \omega^2 \tau_R^2 \gamma^2)} - \frac{1}{4H_0^2}, \quad (5.5)$$

$$h_I = \frac{\tau_R \omega^3 (\gamma - 1)}{gH_0(1 + \omega^2 \tau_R^2 \gamma^2)}, \quad (5.6)$$

$H_0 = c_S^2/(\gamma g)$ is the pressure scale height and τ_R is the radiative time-scale.

We obtained the best fits from the three models on the observed trend using $c_S = 7.5 \text{ km s}^{-1}$, $\tau_R = 12 \text{ sec}$ and $\Delta h \approx 450 \text{ km}$. Such best fits from the theory also confirm the height difference of $\approx 430 \text{ km}$ we found from Fourier analysis of the acoustic wave's propagation.

The height difference of $430 \pm 30 \text{ km}$ between atmospheric layers sampled by the Ca II H and 3000 Å passbands, obtained from analysing the acoustic waves in the quiet atmosphere, reliably confirms the value of $\approx 450 \text{ km}$ estimated from CFs (see Sect. 5.2). Since the difference in formation height between 3000 Å and Ca II H hardly changes, even slightly increases, then going to a hotter model, we conclude that the problem lies in assigning the intensity oscillations in the MBPs to acoustic waves.

Using a height difference of $\approx 430 \pm 30 \text{ km}$ and the time-lags computed from the largest occurrence of the phase-lag versus period diagrams (i.e., Figs.5.5 and 5.6), we obtained an upward propagation speed of 144 ± 4 and $24 \pm 4 \text{ km s}^{-1}$ for the intensity oscillations and a value of $36 \pm 4 \text{ km s}^{-1}$ for the kink perturbations.

Further, we found a decrease in amplitudes of the horizontal velocities (with a factor of 1.5), while an increase in the intensity amplitudes (with a factor of 7.2) were observed.

5.4.1 Comparisons and interpretations

Theoretical models and numerical simulations of magneto-acoustic and kink waves in photospheric magnetic flux concentrations may be a better way for the interpretation of the observed propagating waves. However, we should keep in mind that such theoretical investigations have been often confined to a simplified atmosphere whose characteristics may differ, to some extent, from the actual solar atmosphere. We review relevant models/simulations in the following that may provide a better understanding of our observations of the propagating, high-frequency, fast transversal and longitudinal waves in small magnetic elements from SUNRISE/SuFI. Note that the primary drivers of perturbations in

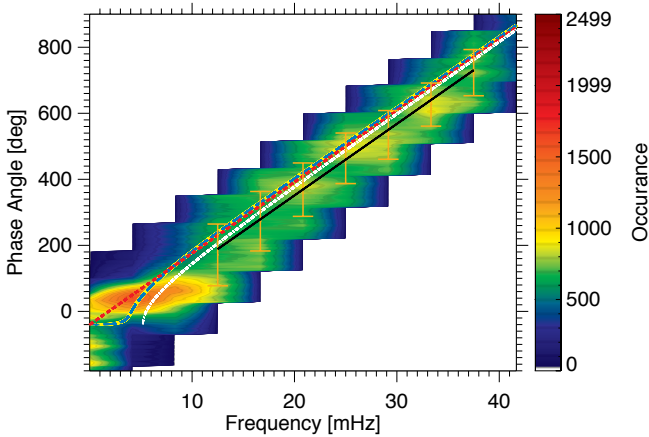


Figure 5.7: Histogram of the unwrapped phase spectrum between the 3000 Å and Ca II H intensity images in a $14 \times 5 \text{ arcsec}^2$ quiet-Sun area; from Fourier transform analysis of individual pixels. The slope, indicated by (black) solid line along with the scatter 1σ error bars, represents the propagating acoustic wave travel-time. The fits represent propagation for linear wave in an isothermal non-stratified atmosphere (red, dashed line), stratified atmosphere including gravity (white, dot-dashed line), and for a model considering radiative losses (dark blue, long dashed line).

the following reviews are often motivated by observations of the motions of magnetic bright points as a proxy for magnetic elements.

Wave excitation models by Hasan et al. (2000): They modelled excitation of oscillations at the footpoint of magnetic flux tubes in the network areas by analytically solving the Klein-Gordon equation. They showed that excitation of kink waves, due to short-duration pulses at the base of the flux tubes, can produce intermittent chromospheric emissions. Such kink waves have been shown to potentially carry enough energy to contribute to the coronal heating (e.g., Choudhuri et al. 1993b; Jafarzadeh et al. 2013a). Hasan et al. (2000) found that these transversal waves cannot represent a major contribution to the chromospheric heating unless they are excited by high-frequency motions (periods of 5 – 50 sec). They speculated that such high-frequency motions could be due to intergranular turbulence (below the photospheric base) that would not be observable from the ground due to the seeing effect. They noted that these high-frequency perturbations are likely to produce Alfvén waves that propagate along the magnetic field lines and dissipate energy in the chromosphere.

Numerical simulation by Bogdan et al. (2003): As a continuation of the work by Rosenthal et al. (2002), Bogdan et al. (2003) extensively studied the propagation of magneto-acoustic-gravity waves within the photospheric and low chromospheric regions of a 2D magnetised atmosphere. In their numerical simulations, uniform waves are generated at a spatially localised source in the photosphere, confined to a 400 km region within the flux element (at 180 km below the surface), with a driving frequency of 42 mHz (a

period of 23.8059 sec). The propagation of both horizontal and vertical perturbations were studied separately. In addition, they investigated the wave propagations in magnetic elements with different field strengths, such that the $\beta = 1$ layer was located below or above the wave sources. They concluded that the slow and fast magneto-acoustic-gravity waves are decoupled in the low- and high- β mediums and their coupling, leading to mode conversion and/or mode transmission, is restricted to the areas with $\beta = 1$, where the gas and magnetic pressures are comparable. They also discussed that the intermediate Alfvén waves, that propagate in both low- and high- β regions, may remain coupled with the fast mode through the whole $\beta < 1$ domains. Note that they approximated the magnetic fields using a potential field that may not provide accurate boundaries of the flux tubes with the surroundings.

MHD models by Hasan and van Ballegooijen (2008): As a continuation of earlier works by Hasan et al. (2003) and Hasan et al. (2005), Hasan and van Ballegooijen (2008) proposed that the intensity enhancement of Ca II H BPs are due to a heating process caused by dissipation of high-frequency, slow magneto-acoustic waves (i.e., frequencies > 10 mHz) launched as kink waves at the base of the magnetic flux tubes. Propagation of both slow and fast magneto-acoustic waves were indeed observed in their simulations. They explained the generation of each wave based on the mode conversion and mode transmission at the $\beta = 1$ level where (1) horizontal (transverse) motions at the base of the photospheric flux tubes (producing slow, MHD, kink waves in $\beta > 1$ regions) are partially converted to slow (longitudinal) acoustic waves propagating along magnetic field lines in $\beta < 1$ regions, (2) the slow, MHD, kink waves in the $\beta > 1$ medium are partially transmitted as kink, MHD, fast waves in the $\beta < 1$ regions, and (3) absorption of the p -mode (i.e., a fast, longitudinal wave in $\beta > 1$ within the magnetic flux tubes) produced in the immediate vicinity of the flux tubes is converted to a kink fast mode (in layers with $\beta < 1$). Hasan and van Ballegooijen (2008) showed that while the latter fast transverse waves rapidly travel to the upper layers of the atmosphere, the former (slow, compressive acoustic) wave forms shocks at chromospheric heights (i.e., compressional heating as a result of an amplitude increase with height due to the density stratification) accompanied by large temperature perturbations (around 900 K) representing the intensity enhancement of the Ca II H BPs. They concluded that high-resolution space observations are needed to confirm the existence of such high-frequency fast magneto-acoustic waves; and/or the Alfvén waves predicted by Hasan et al. (2000).

Numerical simulation by Nutto et al. (2012): They investigated the unexpectedly small time-lags measured between two photospheric layers at a strong magnetic field concentration, similar to those of observed by, e.g., Finsterle et al. (2004). They consider a dynamic atmosphere (i.e., convectively unstable, time-dependent and magnetic) in their numerical simulations and excite waves for different cases, i.e., propagations of both spherical and plane-parallel waves, excited from different locations with respect to small magnetic elements. They found that when one of the height levels (at which the waves are observed), or even both of them, are above the $\beta = 1$ level, the wave travel-time significantly decreases. They explain such a decrease in time-lag as the effects of: (1) convergence of formation heights inside the strong magnetic elements, (2) mode conversion above the $\beta = 1$ level, and (3) propagation path of the fast magnetic mode. They conclude that the velocity field includes the signature of both slow acoustic and fast magnetic modes in the regions where $\beta < 1$. Unlike Hasan and van Ballegooijen (2008) that primarily launched

the wave by buffeting the base of the flux tube in their MHD model (while the p -mode generated in the immediate vicinity of the flux tube would also penetrate into the tube), the wave source in the simulations of Nutto et al. (2012) has (only) an acoustic nature. Therefore, the incident fast acoustic wave at the $\beta = 1$ level, is partially converted to the fast magnetic wave and is partially transformed as the slow acoustic wave propagating in the $\beta < 1$ regions. Nutto et al. (2012) also noted that the dynamic and complex $\beta = 1$ level in the actual solar atmosphere may cause several $\beta = 1$ levels above each other, hence, several mode conversions inside the flux tubes may occur.

The formation height inside magnetic elements of the 3000 Å bandpass is expected to decrease due to spectral line weakening in magnetic elements, whereas the enhanced brightness of the Ca II H line-core in magnetic elements is associated with the strengthening of the line emission, which leads to an increase in the effective formation height inside the magnetic elements (Jafarzadeh et al. 2013a). Hence, in our data we expect the formation height to diverge rather than to converge, as suggested by Nutto et al. (2012).

In addition, Nutto et al. (2012) showed that the fast (sausage) waves do not propagate upwards, but they turn sideways. This effect could explain the small time-lags they observed between the two photospheric layers at the magnetic feature.

Summarising, simulations have shown that both fast and slow magneto-acoustic waves can be generated at the base of magnetic (thin) flux tubes due to sudden impacts from the sides while moving in intergranular lanes (Bogdan et al. 2003; Hasan and van Ballegoijen 2008). Such bursts can be due to, e.g., expansion or explosion of the neighbouring granules as well as the intergranular turbulence, with a large range of speeds that can generate waves with a wide range of frequencies. The turbulence in the intergranular areas were speculated to be responsible for the high frequency range of the generated waves (Hasan et al. 2000). The pulse-like events (sometimes super-sonic; Jafarzadeh et al. 2013a) can excite transversal kink waves along the flux tubes as a slow mode in the $\beta > 1$ regions. In addition, the interaction of the magnetic elements with the convective flows generates acoustic waves that propagate along the field lines as a fast mode in the high- β regions. Note that the condition whether the waves sources are located in the $\beta > 1$ or $\beta < 1$ domains depends on magnetic field strength, however, we expect that the MBPs studied in the present work are kG features (otherwise their brightness excess could not be observed; e.g., Rutten et al. 2001; Vögler et al. 2005; Riethmüller 2013; Riethmüller et al. 2013) and hence the $\beta = 1$ level should locate close to (below or above) the solar surface (the lower layer in our observations sampled by 3000 Å passband). When these separated waves, i.e., (1) the slow MHD and (2) the fast magneto-acoustic wave, reach to the $\beta = 1$ surface, the two modes become coupled (alike) and both mode conversion (i.e., exchanging the physical nature of the waves from being magnetic to acoustic or vice versa) and mode transmission (i.e., changing the labels from slow to fast or vice versa without changing the nature) may occur. These mode conversions and transmissions may occur only to a part of each incident wave to the $\beta = 1$ level whose fraction depends on, e.g., the attack angle. As a result, the following separated waves can emerge from the $\beta = 1$ level propagating in the $\beta < 1$ regions: (1) slow (compressible) acoustic wave, (2) fast, (transversal, incompressible), MHD kink wave, and (3) fast (transversal, compressible), magnetic sausage wave.

Therefore, one could speculate observations of fast kink and fast compressible waves as the results of: (1) mode transmission at the $\beta = 1$ level (transmitted from slow kink

waves in $\beta > 1$ to fast kink mode in $\beta < 1$ regions), and (2) mode conversion at the $\beta = 1$ surface (converted from fast, compressible acoustic waves in $\beta > 1$ to fast, compressible MHD waves in $\beta < 1$ mediums), respectively.

The relatively short lifetimes of the MBPs under study did not allow us to (reliably) detect low-frequency waves.

Another important cause of small wave travel-times between the two atmospheric levels at magnetic features (resulting fast compressible, sausage waves in our study) was shown by Nutto et al. (2012) as a consequence of determining phase-lags between vertically separated but horizontal sensing layers. This latter effect is a result of velocity perturbations in wide regions of the atmosphere (owing to vertical orientation of wave fronts of the refracted fast waves in the regions where $\beta < 1$ as well as to high phase speed) which are in phase along vertical lines of sight (Nutto et al. 2012). Nutto et al. (2012) explained the fast mode's refraction (in the $\beta < 1$ mediums) as a consequence of the steep gradient in the Alfvén speed and continuous changes of the phase speed along the wave fronts.

Similar to our findings, both fast kink (incompressible) and fast compressible waves were also observed by Morton et al. (2012) along magnetic flux tubes close to disc-centre, quiet-Sun sampled in the mid-chromosphere. They interpreted these two kinds of waves in magnetic flux tubes as (1) fast MHD kink mode, measured from transverse displacement of the magnetic structures, and (2) fast MHD sausage mode, manifested as intensity perturbations. They found propagation speeds of $\approx 60\text{--}90\text{ km s}^{-1}$ for the kink oscillations as well as a range of $\approx 50\text{--}320\text{ km s}^{-1}$ measured from the intensity perturbations. We suspect that our observations may represent the lower solar atmosphere's counterparts of the fast waves (of both kinds) observed in the mid to upper chromosphere by Morton et al. (2012). However, the typical periods of 180 – 210 sec for the fast kink waves as well as 90 – 190 sec for the fast propagating intensity perturbations measured by Morton et al. (2012) are somewhat larger than those of obtained here. From our point-like magnetic elements whose size is close to the spatial resolution of the data, we cannot (directly) investigate any relationship between the size and intensity variations to verify manifestation of the sausage mode in the intensity perturbations.

5.5 Discussion and conclusions

We studied oscillations of horizontal velocity and intensity of small-scale MBPs observed in 3000 Å and Ca II H image sequences from SUNRISE/SuFI. The MBPs observed in the two layers are taken to represent the cross-sectional area of the same nearly vertical flux tubes. Time-series of 7 reliable MBPs were studied in this analysis. Although such a small number of MBPs is not representative of all magnetic elements in general, the obtained properties of such oscillatory motions are secured from seeing-free data.

We computed a height difference of $\approx 450\text{ km}$ between the two atmospheric layers sampled by SuFI 3000 Å and Ca II H passbands by employing the RH radiative transfer code of Uitenbroek (2001). For comparison, we also analysed the intensity oscillations in a $14 \times 5\text{ arcsec}^2$ quiet-Sun area. We calculated the coherence and phase-lags of the two time-series (Ca II H and 3000 Å), obtaining the phase-frequency diagram of the oscillations (Fig. 5.7). Oscillations in the relatively large FOV of the quiet Sun are expected

to correspond to acoustic waves. The phase-frequency diagram for propagating high-frequency acoustic waves resulted in a time-lag of 57 ± 2 sec implying an average height difference of 430 ± 30 km between the two atmospheric layers sampled by SUNRISE/SuFI 3000 Å and Ca II H passbands. This height difference is comparable with that determined from the RH code.

The wavelet transform analysis at small-scale magnetic elements yielded: (1) consistent high-frequency waves up to 30 mHz in both kinds of oscillations (not limited by the Nyquist frequency of ≈ 42 mHz), (2) dominating fast waves with a speed of 36 ± 4 km s⁻¹ in horizontal displacements perturbations (kink mode) and speeds of 144 ± 4 and 24 ± 4 km s⁻¹ manifested in intensity oscillations, compressible fast waves (from the peaks of the phase-period's 2D histograms), (3) positive phase-lags between the oscillations observed in simultaneous observations of 3000 Å and Ca II H (for both horizontal displacement and intensity perturbations), meaning upward propagation of the waves, and (4) presence of a variety of (fast) waves with a range of speeds in intensity oscillations (with an average wave travel-time of 4.3 sec) which may belong to different dispersion relations or different sources (Bogdan et al. 2003). In addition, a slight indication (about 15% of phase-period data points) of downward wave propagation were also observed in the intensity oscillations.

Observations of fast kink and fast sausage (compressible) waves along the magnetic flux tubes were also reported by Morton et al. (2012), but in the mid-chromosphere. The upward wave propagation in small MBPs, studied here, agrees with that of Jess et al. (2012) who found a similar behaviour in intensity oscillations of a larger number of MBPs in both observations and simulations. They investigated the wave propagation in all pixels of a relatively large FOV and concluded that much of the power is concentrated in MBPs.

In agreement with the small time-lags (between the two atmospheric layers) that we found from the wavelet analysis of both intensity and horizontal displacement oscillations, Finsterle et al. (2004) observed that the wave travel time vanishes at the centre of magnetic regions.

Nutto et al. (2012) showed that the steep gradient in the Alfvén speed (and hence the continuous change in phase speed along the wave fronts) causes the fast waves to be refracted. As a consequence, they found that velocity perturbations in a wide area of the atmosphere (due to vertically oriented wave fronts of the refracted fast waves and also because of the long wavelength) result in vanishing the measured time-lags between two atmospheric layers. This results can well explain the fast compressible waves we observed in the present study.

When the magnetic field is slightly inclined, fast waves can be converted to the Alfvén mode in layers well above the $\beta = 1$ level, i.e., the fast wave reflection point (Cally and Hansen 2011). Interestingly, the magnetic field of the MBPs under study has a small inclination relative to nearly vertical line-of-sight, in agreement with those studied by Jafarzadeh et al. (2013b). However, Nutto et al. (2012) showed that fast compressible waves do not propagate upwards, but rather start to propagate sideways (or even downwards) above some certain heights.

Bogdan et al. (2003) explained the character of observed oscillations in the solar magneto-atmosphere using an extensive numerical simulations. They showed that at any given location, a superposition of several distinct waves with different characterisations may be observed. Bogdan et al. (2003) concluded that these waves may propagate in dif-

ferent directions and may come from different locations, e.g., directly from their sources, from the $\beta = 1$ level as a result of the mode conversion, or locally from interaction of any kind of waves with p -modes. Therefore, distinguishing the nature of different waves that we observed in intensity fluctuations may not be straightforward from the observations. We suspect that other causes are perhaps involved in obtaining such a phase-period diagram (i.e., Fig. 5.6) for the intensity fluctuations. Such causes and other possible effects could even result in overestimation of their speeds.

Furthermore, for the measurements made at the two heights (i.e., sampled by 3000 Å and Ca II H passbands), we observed a decrease with height in horizontal velocity amplitudes (by a factor of 1.5) for all 7 MBPs studied here, while, an increase in intensity amplitude (by a factor of 7.2) with height are obtained. The former can imply that the kink waves may not reach the corona, either dissipating their energy in lower layers, or being converted to another wave mode (e.g., Alfvén wave) on the way. The latter (i.e., the increase of the amplitude of intensity fluctuations) is not straightforward to interpret. Model calculations would be required to investigate, e.g., relationship between such intensity oscillations and changes in temperature amplitude.

Summarising, we have observed high-frequency, fast, upward propagating kink and compressible (probably sausage) waves using data from SUNRISE unaffected by seeing. The existence of such high-frequency waves in magnetic elements has been proposed by Hasan and van Ballegooijen (2008), who showed that buffeting of the flux tubes' footpoints by high frequency perturbations by the surrounding granules and intergranular turbulence can excite such high-frequency kink waves along the flux tubes. The mode conversion at $\beta = 1$ level is initially responsible for exciting fast magnetic waves (Bogdan et al. 2003). These fast waves were shown not to reach the higher atmospheric layers, but be refracted due to the large gradient in the Alfvén speed in the regions where $c_A/c_S > 1$ (Nutto et al. 2012). Nutto et al. (2012) found that the resulting propagation path of the refracted wave contains in-phase velocities (along the vertical lines of sight) in a wide height range of the atmosphere. They explained the latter effect as a cause for observing small wave travel-time between two atmospheric layers. This can explain best the fast sausage mode we observed here (measured from small wave travel-times). In addition, the observed kink waves may also not reach the upper solar atmosphere, due to the determined decrease of the horizontal velocity amplitudes with height. This probably implies that such waves may dissipate energy while travelling in the lower solar atmosphere and hence, they can contribute to the energy balance in the (low) chromosphere. Other possibilities could be wave reflection to the lower atmospheric layers or conversion to another wave mode. The computed wave speeds of both kink and sausage modes seem to be affected (overestimated) by other causes. Future work will concentrate on detecting such effects by studying in detail the analysis tool used here under different circumstances, such as studying the effect of different coherence thresholds.

6 Do inversions provide the correct inclinations of small quiet-Sun magnetic features?

To be submitted to A&A by S. Jafarzadeh^{1,2}, S. K. Solanki^{1,3}, A. Lagg¹, L. R. Bellot-Rubio⁴, M. van Noort¹, A. Feller¹, V. Martínez Pillet⁵, S. Danilovic¹ and A. Gandorfer¹.

Abstract Large amounts of horizontal magnetic flux have been reported in the quiet-Sun internetwork, often based on Stokes profile inversions.

Here we introduce a new method to deduce the inclination of magnetic elements and use it to test magnetic field inclinations from inversions.

We determine accurate positions of a set of small, bright magnetic elements in high spatial resolution images sampling different photospheric heights obtained by the Sunrise balloon-borne solar observatory. Together with estimates of the formation heights of the employed spectral bands, these provide us with the inclinations of the magnetic features. We also compute the magnetic inclination angle of the same magnetic features from the inversion of simultaneously recorded Stokes parameters.

Our new, geometric method returns nearly vertical fields (average inclination of around 14° with a relatively narrow distribution having a standard deviation of 6°). In strong contrast to this the traditionally used inversions give almost horizontal fields (average inclination of $75 \pm 8^\circ$) for the same magnetic features. We show that for these magnetic features inversions overestimate the flux in horizontal magnetic fields by an order of magnitude.

The almost vertical field of bright magnetic features from our geometric method is clearly incompatible with the rather horizontal magnetic fields obtained from the inversions. This indicates that the amount of magnetic flux in horizontal fields in the quiet-Sun deduced from inversions is overestimated. These should in particular not be applied to obtain the inclination when there is no clear Stokes Q and U signal. We suggest the proposed measurement as a complementary approach to inversions of Stokes parameters for determining the field inclination.

¹ Max-Planck-Institut für Sonnensystemforschung, Max-Planck-Str. 2, 37191, Germany

² Institut für Astrophysik, Georg-August-Universität Göttingen, Friedrich-Hund-Platz 1, 37077, Germany

³ School of Space Research, Kyung Hee University, Yongin, Gyeonggi 446-701, Republic of Korea

⁴ Instituto de Astrofísica de Andalucía (CSIC), Glorieta de la Astronomía, s/n 18008 Granada, Spain

⁵ Instituto de Astrofísica de Canarias, C/Vía Lactea, s/n 38205, La Laguna, E-38200, Tenerife, Spain

6.1 Introduction

The magnetic field strength distribution in the solar photosphere depends on the location: (1) in active and network regions kG fields dominate (e.g., Stenflo 1973; Solanki 1987; Martínez Pillet et al. 1997; Martínez González et al. 2012), while (2) weak magnetic fields, up to a few hG, are found all over the solar surface. The latter (i.e., weaker) component has been most intensely studied in internetwork (IN) areas, i.e., the supergranular interiors (e.g., Livingston and Harvey 1971, 1975; Lin 1995; Khomenko et al. 2003; Trujillo Bueno et al. 2004; Khomenko et al. 2005; Ishikawa and Tsuneta 2009; Beck and Rezaei 2009; Ishikawa and Tsuneta 2011; Bellot Rubio and Orozco Suárez 2012). Recently, kG fields have been found also in the IN (Lagg et al. 2010). In comparison with the active and network regions, the internetwork covers a much larger fraction of the solar surface and hence may contain most of the existing unsigned magnetic flux on the surface at any given time (Sánchez Almeida 2004). Therefore, measuring reliable magnetic field properties of the internetwork areas is important for our understanding of, e.g., a local dynamo (Vögler and Schüssler 2007; Danilovic et al. 2010a; Stenflo 2012) and the dynamic coupling of the photosphere to the higher atmospheric layers (de Wijn et al. 2009). For recent reviews on the quiet-Sun IN magnetic fields, we refer to de Wijn et al. (2009), Solanki (2009) and Sánchez Almeida and Martínez González (2011).

The characteristics of magnetic fields are traditionally inferred from the influence of the Zeeman effect on spectral lines. Observed Stokes profiles are treated through inversions of the polarised radiative transfer equations to determine, e.g., the strength and inclination angle of the magnetic field relative to the line-of-sight. Such a treatment depends, to a certain extent, on the model and sometimes the initial parameters assumed in the employed inversion code and may fail (i.e., provide wrong results) when the polarisation signals are below or close to the noise level.

High spatial resolution data have indicated that the magnetic field in internetwork areas is mainly horizontal (Lites et al. 1996; Orozco Suárez et al. 2007; Lites et al. 2008; Ishikawa and Tsuneta 2009; Orozco Suárez and Bellot Rubio 2012), while isotropic distributions of the magnetic field vector have also been reported (Asensio Ramos 2009; Bommier et al. 2009) and Stenflo (2010) has argued that the field is on average more vertical than horizontal. The origin of horizontal and vertical magnetic fields in the quiet-Sun have been suggested to lie in the emergence of small bipolar loops and the concentration into flux tubes by convective collapse of the field forming their foot-points, respectively (Ishikawa and Tsuneta 2011). A common origin of vertical and horizontal fields in the internetwork is predicted by modes of the local dynamo (Vögler and Schüssler 2007; Schüssler and Vögler 2008; Danilovic et al. 2010a).

Borrero and Kobel (2011, 2012) have argued that excessive horizontal fields can be returned by inversions of noisy polarisation signals. They found horizontal and hG fields from inverting the observed Stokes profiles (in quiet-Sun internetwork regions), whereas their Monte-Carlo and numerical simulations revealed purely vertical field; with much weaker field strengths ($B < 20$ G) compared to those obtained from inversions. They found that only 30% of the observed regions have sufficiently strong Stokes Q and U signals (i.e., signals sufficiently above the noise level) to allow the reliable determination of the magnetic field vector. de Wijn et al. (2009), Asensio Ramos (2009) and Bommier et al. (2009) have all pointed out the difficulties in obtaining the magnetic inclination

when the polarisation signal is weak and in particular, the Stokes Q and U signals are not well above the noise level. In contrast, Orozco Suárez and Katsukawa (2012), Orozco Suárez and Bellot Rubio (2012) and Bellot Rubio and Orozco Suárez (2012) argued that the mainly horizontal field in the IN deduced from inversions is consistent with their more up-to-date analyses or the higher signal-to-noise ratio data they analysed.

In this chapter, we present a new and simple approach to obtain inclinations of small-scale bright magnetic structures (magnetic bright points; MBPs) using intensity images observed in different layers of the solar atmosphere. Since MBPs are co-located with the magnetic field, the inclination obtained in this manner should correspond to the inclination of the magnetic vector. We therefore call it the magnetic inclination proxy, γ_p . We test this correspondence by determining the inclination using the same method, but from the Stokes V profiles at measurements made at different heights (i.e., by comparing wavelengths at different distances from the line-core in a sufficiently strong spectral line). We use Stokes V due to its larger signal-to-noise ratio (SNR) compared to other Stokes profiles. Furthermore, we compare the inclination angles obtained from our proposed geometric method and those computed from Stokes inversion codes.

The plan of this chapter is as follows: in Sect. 6.2 we briefly review the data used for the study. In Sect. 6.3 we describe the technique used to measure the magnetic field inclination along with the results. We also introduce the inversion codes that we apply to the polarimetric data and discuss the comparison between differently measured inclination angles. We summarise our conclusions in Sect. 6.4.

6.2 Observational data

For most of this study we use high spatial resolution observations acquired on 9 June 2009 (between 01:32:06 and 01:58:43 UT), in the quiet-Sun disc-centre, by the Imaging Magnetograph eXperiment (IMaX; Martínez Pillet et al. 2011) on board the SUNRISE balloon-borne solar observatory (Solanki et al. 2010; Barthol et al. 2011; Berkefeld et al. 2011).

The data consist of the full Stokes vector (I, Q, U and V) measured in five wavelength positions located at $-80, -40, +40, +80$ mÅ and $+227$ mÅ from the centre of the magnetically sensitive Fe I 5250.2 Å line. The first four wavelengths lie within the line, while the last one samples the continuum. The image sequences were obtained at a cadence of 33 sec with a noise level of $\approx 3 \times 10^{-3} I_c$ after phase-diversity (PD) reconstruction ($V5-6$ level 2 data; Martínez Pillet et al. 2011). We also analysed data prior to PD reconstruction (level 1 data), which were flat-fielded and corrected for instrumental effects. They have a noise level of $\approx 1 \times 10^{-3} I_c$. The 1σ noise levels of all Stokes profiles are summarised in Table 6.1 (discussed in detail below).

We prepared two datasets of intensity images, each sampling a different height above the solar surface. We used these two sets of images for determining the proxy of the magnetic field's inclination angle γ_p from measurements at the two heights. One set is composed of IMaX Stokes I continuum images, which sample the continuum formation height. To obtain the second set we form images corresponding to a combination of the line core and the line's inner flanks by averaging the -40 and $+40$ mÅ wavelength positions of the IMaX Stokes I normalised to the continuum intensity. We refer to these

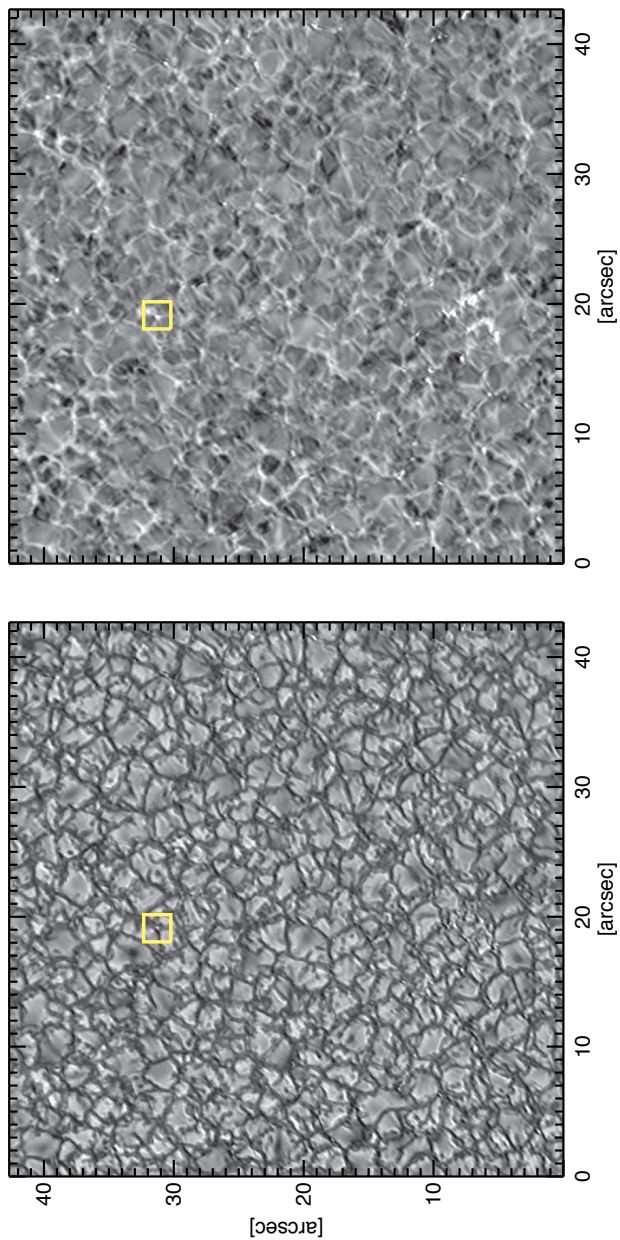


Figure 6.1: Example of co-spatial and co-temporal images from SUNRISE/IMaX. Left: Full field-of-view (after apodization) of the IMaX at the continuum wavelength position next to the Fe I 5250.2 Å line. Right: Average of two line-positions at -40 mÅ and $+40$ mÅ from the Fe I 5250.2 Å line-core. The yellow box encloses a sample magnetic bright point (MBP) studied here.

images as line-core images in the following. Figure 6.1 shows example frames of the IMAx continuum intensity (left) and the IMAx line-core (as described above; right).

We used the RH radiative transfer code of Uitenbroek (2001) to estimate the formation heights of the two layers sampled by the data products introduced in the last paragraph. We employed the code in the LTE mode for two atmospheric models, FALC and FALP, representing the averaged quiet-Sun and plage regions (or magnetic bright points; MBPs), respectively (Fontenla et al. 1993, 2006). Plotted in Fig. 6.2 are the line depression contribution functions (CFs; Magain 1986; Grossmann-Doerth et al. 1988) versus height above continuum optical depth unity ($\tau_c = 1$; optical depth at 5000 Å), obtained by integrating the computed, IMAx filter-profile weighted, CFs over wavelength, for IMAx continuum (red) and IMAx line-core (blue) and for FALC (dashed line) and FALP (solid line) model atmospheres. The vertical lines indicate the mean formation heights. These formation heights result in a $\sim 300 \pm 100$ km height difference between the two layers in magnetic elements.

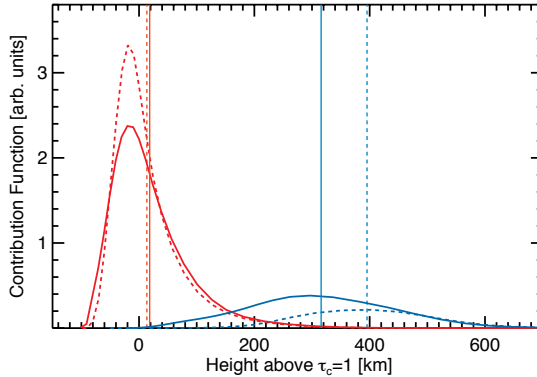


Figure 6.2: Line depression contribution functions for the SUNRISE/IMAx continuum (red) and line-core (blue) positions (see main text). The dashed and solid lines represent the FALC and FALP model atmospheres, respectively. The vertical lines indicate the corresponding weighted mean formation heights (heights above continuum optical depth unity, τ_c).

For a part of the analysis, in order to increase the SNR of the often weak polarisation signals found in the quiet-Sun, we average the Stokes V signals over the four wavelength positions inside the line, normalised to the local quiet-Sun continuum intensity (I_c). To avoid cancellation, the sign of two red wavelength points was reversed prior to averaging. We refer to this quantity as CP in this chapter. Furthermore, we form the total linear polarisation (LP) from the Stokes Q and U signals (i.e., $\sqrt{Q^2 + U^2}$). Similar to CP , we aim to increase the LP 's SNR by averaging over the four wavelength positions. However, because squaring the Stokes profiles also squares the noise, which then no longer cancels through averaging, we do not form the LP for each single wavelength position prior to averaging. The LP is instead computed as

$$LP = \frac{1}{2 I_c} \left(\sqrt{\overline{Q}_{14}^2 + \overline{U}_{14}^2} + \sqrt{\overline{Q}_{23}^2 + \overline{U}_{23}^2} \right), \quad (6.1)$$

where \overline{Q} and \overline{U} are respectively the averaged Stokes Q and U profiles over two wavelength positions with the same sign under normal circumstances, i.e., the outermost (indicated by indices 1 and 4) and the innermost (represented by indices 2 and 3) wavelength positions in the line. The outer and inner wavelength positions are treated separately in order to avoid possible cancellation.

The CP and LP are measures of the level of polarisation and are only used as selection criteria.

In addition to the PD reconstructed data, we also determined the CP and the LP from the less noisy non-reconstructed data (but at the cost of a factor of 2 lower spatial resolution compared to the PD reconstructed data).

An average 1σ noise level of $\approx 6 \times 10^{-4}$ was obtained for CP and LP from the non-reconstructed data. The noise levels were determined as the standard deviations at the continuum position since we do not expect any polarisation signal in the continuum. The Stokes V signals found by Borrero et al. (2010) at this wavelength are restricted to sufficiently few spatial locations not to influence the noise estimate.

We further spatially smooth the CP and LP maps obtained from non-reconstructed data by applying a boxcar average of 3×3 pixels, to additionally reduce the noise in the weakly polarised regions under study without degrading the spatial resolution (the non-reconstructed data are oversampled by this amount). After this step, the 1σ noise levels for both CP and LP are reduced to $\approx 3 \times 10^{-4}$ in the non-reconstructed maps. A spatial smoothing by 9 pixels would be expected to reduce the noise level by a factor of 3 under ideal conditions. However, we found the actual reduction in the noise level is smaller due to the presence of coherent noise caused by image jitter.

In the following, we will use the CP and LP maps only to extract and distinguish the polarisation signal from the noise. By retrieving the magnetic field vector through inversion of Stokes profiles with different noise levels, we will be able to investigate the effect of noise level on the inclination of the magnetic vector, although it must be borne in mind that the data with different noise levels do differ in spatial resolution and sampling from each other.

To summarise, the differently treated datasets are: (1) The non-reconstructed (but flat-fielded and corrected for instrumental effects) images, (2) spatially smoothed non-reconstructed data, obtained by applying a 3-pixel boxcar smoothing, and (3) the higher spatial resolution (by a factor of 2) PD reconstructed images with a higher noise level than the non-reconstructed data. Table 6.1 summarises the 1σ noise levels of CP , LP as well as individual of Stokes profiles for these differently treated datasets.

6.3 Analysis and results

We propose a simple method for determining the magnetic field's inclination angle proxy from high resolution intensity images which works for magnetic features that produce brightness enhancements. We manually select these elements, whose $CP \geq 4\sigma$, in intensity images of differently treated data.

Table 6.1: Summary of 1σ noise levels in the employed data sets

Parameter	PDR*	NR*	SSNR*
Q/I_c	2.6×10^{-3}	8.3×10^{-4}	4.6×10^{-4}
U/I_c	3.6×10^{-3}	1.1×10^{-3}	4.8×10^{-4}
V/I_c	3.3×10^{-3}	1.0×10^{-3}	6.3×10^{-4}
CP	1.7×10^{-3}	5.2×10^{-4}	3.2×10^{-4}
LP	2.2×10^{-3}	6.6×10^{-4}	2.9×10^{-4}

* PDR: PD reconstructed data; NR: Non-reconstructed data; SSNR: Spatially smoothed Non-reconstructed data

In parallel to our measurements at two heights, we also determine the magnetic field vector in the selected features by inverting the observed Stokes profiles.

6.3.1 Inclination from measurements at two heights

The new approach is based on the fact that in addition to the clearly present low-lying loops (e.g., Martínez González et al. 2007; Ishikawa et al. 2008; Ishikawa and Tsuneta 2009; Martínez González and Bellot Rubio 2009; Danilovic et al. 2010a) and a probably truly turbulent field (e.g., Pietarila Graham et al. 2009) there are also magnetic fields that are better represented by slender flux tubes (e.g., Solanki et al. 1996b). Flux tubes describe relatively isolated, concentrated magnetic fields, so-called magnetic elements (MEs). They are rooted in the solar interior and unless they have freshly emerged, they extend into the upper atmospheric layers (Stenflo 1989; Solanki 1993). The cross-section of an intense and thin ME in each layer of the photosphere manifests itself as a bright point (MBP) in intensity images, due to a combination of continuum enhancement and line weakening (e.g., Keller 1992; Kiselman et al. 2001; Nagata et al. 2008). In the lower photosphere the excess brightness of MBPs is due to radiation from subsurface hot walls of the flux tubes (Spruit 1976; cf. e.g., Deinzer et al. 1984b), whereas in the middle photosphere and higher layers it is produced by radiative and non-radiative heating. We take the centre of gravity of the intensity patches of the observed MBPs to represent the locations of the centres of MEs.

Therefore, connecting the MBPs identified in well-aligned intensity images corresponding to two different atmospheric layers (e.g., the solar surface and an upper photospheric layer) can provide its inclination, if they belong to the same ME and if the height difference between the two layers is known. We refer to this inclination angle as γ_p (p for proxy) to distinguish it from the true magnetic inclination γ . We apply this method to small MBPs identified in SUNRISE/IMaX high spatial resolution images in the Fe I 5250.2 Å continuum and in the line-core (as described in Sect. 6.2).

The isolated, small and magnetic bright points are manually selected in both continuum and line-core images. They are required to meet the criteria described in Jafarzadeh et al. (2013a) (hereafter referred to as Paper I) in IMaX line-core images. The application of the same criteria is reasonable for IMaX line-core filtergrams whose intensity variations

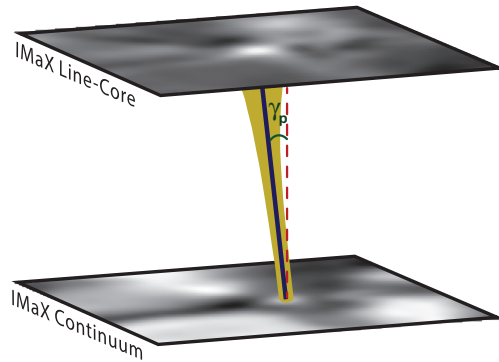


Figure 6.3: A magnetic bright point (MBP; marked in Fig. 6.1) in the continuum and line-core intensity images obtained by *SUNRISE*/IMaX. A schematic flux tube connecting the locations of the MBP at the two photospheric layers (yellow shading) with approximate height difference of 300 ± 100 has been added. The inclination of the axis of this flux tube (solid line) relative to the surface normal (dashed line) is marked as γ_p . The figure is a simplification in that the two images are assigned fixed heights; not to scale, with the vertical axis expanded by a factor of 2.8.

is similar to the Ca II H images analysed in Paper I. We checked this by applying these criteria to overlapping SuFI (Gandorfer et al. 2011) Ca II H images and IMaX line-core images, obtaining a good match. In addition, a MBP is considered magnetic if it is located inside a magnetic patch (i.e., with $CP \geq 4\sigma$ noise level). Therefore, the selected MBPs (a total of 386) only include very small magnetic, bright, point-like features in quiet-Sun internetwork areas, which facilitates an accurate locating procedure. Please note that many of these small MBPs are likely spatially unresolved by *SUNRISE* (Jafarzadeh et al. 2013a; Riethmüller et al. 2013). Larger MBPs that are also found in *SUNRISE*/IMaX (Lagg et al. 2010; Riethmüller et al. 2010) are not considered in this study, since their (normally) non-uniform brightness and internal fine-structure do not facilitate finding a unique and accurate position. The MBP's precise location is computed using an algorithm described in detail in Paper I. The one important difference here, compared to Jafarzadeh et al. (2013a), is that the algorithm crops a small area (i.e., a square with sides of 0.6 arcsec) from each frame containing the manually selected MBP roughly at the centre, prior to the locating process. This facilitates the procedure, particularly, in continuum images. This algorithm determines the location of the MBP, i.e., centre of gravity of intensity down to sub-pixel accuracy. Once the MBP has been located in the upper layer, we then search for a counterpart in the continuum images. We look for compact MBPs in intergranular lanes. The two closest MBPs at each height are assigned to each other, with the further requirement that the Stokes V signal supports this identification.

Figure 6.3 illustrates the identification at two heights of a MBP and the interpolation of the flux tube between the two heights, for the MBP marked in Fig. 6.1. The locations of the MBPs in the two layers, with a height difference of $\approx 300 \pm 100$, are connected by a solid line. The yellow shaded surface illustrates very schematically the flux tube's expansion based on the determined MBP's areas in the continuum and the line-core images. The expansion factor of ≈ 2.8 is comparable to that obtained from the network flux-tube model of Solanki (1986) and the thin-tube approximation (Defouw 1976).

The tangent of the inclination of such a flux tube is then computed by simply dividing the offsets between the locations of the MBP in the continuum and the line-core images by the estimated height difference between those layers. The flux tube illustrated in Fig. 6.3 has an inclination angle of $\gamma_p = 19 \pm 7^\circ$ (see Sect. 6.3.1.1 for an estimate of the uncertainty).

6.3.1.1 Sources of uncertainty

Uncertainty in the determined inclination angles is induced by biases from different sources:

Location of MBP: The technique used to locate the MBPs has an accuracy of 0.05 pixel at best (i.e., when the MBP is ideally small). We employ a more conservative value of 0.5 pixels for the uncertainty, which takes the effect of the MBPs' size and intensity variations into account (Jafarzadeh et al. 2013a). The IMAx pixel size of 0.0523 arcsec thus implies an uncertainty of ~ 19 km, in the horizontal plane.

Estimate of the height difference: The mean formation heights of the IMAx continuum and line-centre (as described in Sect. 6.2) depend on the atmospheric structure, which leads to an uncertainty in the difference between the heights of the two sampled layers (≈ 300 km). To be on the safe side we take a conservative value of ± 100 km for this uncertainty which corresponds to a relative uncertainty of 33%.

Observing-time difference: We formed the line-centre images by averaging the innermost wavelength positions of the IMAx Stokes I normalised to the continuum point (Sect. 6.2). The datasets we used here have a cadence of 33 sec, meaning an average time-difference of ~ 16.5 sec between the IMAx line-centre and the IMAx continuum images. MBPs of the type under study move horizontally with an average speed of 2.2 km s^{-1} (Jafarzadeh et al. 2013a). Assuming that the MBP moves at this speed in a fixed direction during the difference in time between the images introduces on average an offset of ≈ 36 km between the MBPs' locations at the two heights.

The combination of the three uncertainties mentioned above translates into an uncertainty in the inclination angle γ determined from measurements at the two heights. A combination of 40 km uncertainty in the horizontal plane (σ_h) as well as a 100 km error in measuring the height difference between the two layers (σ_z) leads to an average uncertainty of $\sigma_\gamma \approx 7^\circ$ in the determined inclination angles ($\sigma_\gamma \approx \sigma_{h/z} / (1 + h^2/z^2)$), where h and z are the mean values of the horizontal displacement and the height difference between the two layers. $\sigma_{h/z}$ is the uncertainty of h/z determined using σ_h and σ_z .

Another source of errors are Doppler shifts and Zeeman splitting, which can cause the parts of the spectral lines in the IMAx filters to sample a different height than in the absence of these effects. In order to estimate the errors introduced by these effects in a statistical sense we also compared the Ca II H line-core sampled by a 1.8 \AA broad SuFI filter (Gandorfer et al. 2011), which is sufficiently broad not to be affected by typical

Doppler shifts or Zeeman splitting. Typical formation heights were determined by Jafarzadeh et al. (2013a), ≈ 500 km above $\tau_c = 1$. Only the subset of MBPs lying in the narrower SuFI field-of-view can be analysed in this way. Also, a careful sub-pixel alignment of the SuFI images to those from IMAx was carried out. The reversed granulation visible in both, the Fe I line-core images obtained by IMAx and the SuFI Ca II H images, allowed this alignment to be performed within a SuFI pixel. By comparing the centre of gravity of MBP locations in the SuFI Ca II H and in the IMAx continuum, the average and standard deviation of the inclination of γ_p obtained from the Ca II H/IMAx continuum images are 7° and 4° respectively. This agrees well with the values obtained from the IMAx line-core and continuum (14° and 6° , respectively; see Sect. 6.3.3). This smaller inclination obtained from the SuFI/Ca II H-IMAx/continuum combination may have a variety of causes. Firstly, the height difference between Ca II H and the 5250.4 \AA continuum is larger, reducing the effect of errors/uncertainties in deducing the horizontal position on the derived γ_p . Secondly, due to the higher cadence of SuFI the time difference between the images at the two heights is smaller, thus reducing uncertainties due to the motions of magnetic features. Finally, unlike the 5250.2 \AA line-core intensity sampled by IMAx, the Ca II H intensity provided by SuFI is almost unaffected by (reasonable) Doppler shifts and Zeeman splitting, which could affect the location of the brightness peak.

Although the MBPs are manifestations of magnetic elements, the location of the centre of gravity of intensity may have an offset with respect to the strongest magnetic field. This can also bias the measured inclination angles in the magnetic elements based on the detected MBPs in intensity images. Since we studied small MBPs observed close to the quiet-Sun disc-centre we expect such an effect to be relatively small. We tested it by additionally considering Stokes V images obtained at the four wavelength positions at which SUNRISE/IMAx measures within the spectral line. These wavelengths sample four atmospheric layers between the IMAx continuum and the line-centre, whereby they form two pairs of wavelengths with similar formation heights. An average height difference of ≈ 50 km between the two heights was estimated by computing the response functions (RFs) of model atmospheres to the magnetic field strength at the two IMAx wavelength positions $+40$ and $+80 \text{ m\AA}$ from the line-centre, after convolving the spectra with the transmission profile of the IMAx Fe I filter. The model atmospheres were computed at the location of the MBPs (i.e., individually for each MBP) using the SPINOR inversion code (see Sect. 6.3.2). The RFs were obtained by forward calculations using the STOPRO Stokes transfer code (Solanki 1987).

The centre of gravity of magnetic patches (i.e., Stokes V signals greater than 4σ noise level) at the rough positions of the MBPs (detected in the intensity images) were considered as the location of magnetic elements. The centre of gravity of the magnetic patches has an offset of ≈ 1.5 pixels on average from that determined for the MBPs in the IMAx Stokes I continuum images and a mean offset of ≈ 1.2 pixels from the MBPs in the IMAx Stokes I line-core frames. Note that the IMAx continuum samples a lower atmospheric layer compared to the four wavelength positions in the line. Since the magnetic field patches are normally bigger and more amorphous than the MBPs, its centre of gravity were measured within a small circle (diameter of ≈ 0.4 arcsec) centred at the pixel with maximum value. The centre of gravity and the peak value of the magnetic elements in all four wavelength positions of the Stokes V images tend to have an offset of 0.6 pixel on average. The inclination was then determined from the location of the Stokes V mag-

netic patches (sampled at the two heights; with an estimated height difference of 50 km) in a manner similar to our proposed approach for the intensity images, described earlier. This test confirmed that the inclination angles obtained from the measurements at the two heights on IMaX intensity images (14° on average; see Sect. 6.3.3) are consistent with the inclination of the flux tubes determined by connecting the centre of gravity of same magnetic elements in the Stokes V images made in the inner and outer flanks of the line (20° on average; a distribution's standard deviation of 18°). The values obtained from Stokes V directly have a larger uncertainty due to the significantly smaller height difference.

6.3.2 Inversions

In order to retrieve the magnetic field strength (B) and the field inclination angle (γ) from the observed polarisation signals, we use the results of three inversion codes: (a) SPINOR (Frutiger et al. 2000; Berdyugina et al. 2003) which computes the synthetic Stokes profiles based on the STOPRO routines (Solanki 1987), (b) SIR (Ruiz Cobo and del Toro Iniesta 1992), and (c) VFISV (Borrero et al. 2011). Both the SPINOR and SIR codes numerically solve the polarised radiative transfer equations under the assumption of local thermodynamic equilibrium (LTE) and iteratively minimise the difference between the computed and the observed profiles by modifying the initial model atmosphere using a response function-based Levenberg-Marquardt algorithm. The Harvard Smithsonian Reference Atmosphere (HSRA; Gingerich et al. 1971) was used as the initial model atmosphere for both inversion codes. The temperature in the SPINOR code is modified with three nodes at $\log\tau_{5000 \text{ \AA}} = 0, -0.9$ and -2.5 , while the SIR results are based on a temperature stratification in the range of $-4 < \log\tau_{5000 \text{ \AA}} < 0$ with two nodes in the temperature. The other parameters (i.e., B , γ , azimuth angle, line-of-sight velocity and micro-turbulent velocity) are height independent in both SPINOR and SIR codes. For details on the SIR inversion carried out on the same data as used in this chapter, we refer the reader to Guglielmino et al. (2012). The VFISV code analytically solves the radiative transfer equation based on the Milne-Eddington approximation of the solar atmosphere. A set of initial parameters are iteratively modified by all codes until the best match between the synthetic and observed Stokes profiles is achieved. A magnetic filling factor of unity has been assumed for all inversions.

We will refer to the inclination angles computed by the inversions as γ_i (i for inversion).

Figure 6.4 displays maps of different parameters around the sample MBP marked in Fig. 6.1. The CP and LP maps are based on (non-smoothed) non-reconstructed data, as described in Sect. 6.2. The plotted magnetic field parameters B_i and γ_i were also computed from the non-reconstructed Stokes profiles, using the SPINOR code. The overlaid (red) contours on all panels of Fig. 6.4 indicate the magnetic patches matching the 4σ noise level in CP and confirm the magnetic origin of the MBPs observed in the continuum and line-core intensity images. We further indicate the location of the MBP (crosses), determined at the formation height of the CP signal (located between the formation heights of continuum and line-core), in all maps. Note that the MBP in the continuum image is located on the right-hand side of the cross (with a 0.07 arcsec offset), while in the line-core filtergram it is located on the left-hand side of the cross (with a 0.04 arcsec offset); representing the inclined flux tube by the locations of its cross-sections in the three sampled heights. This is an example of the test for confirming the determined inclination angle

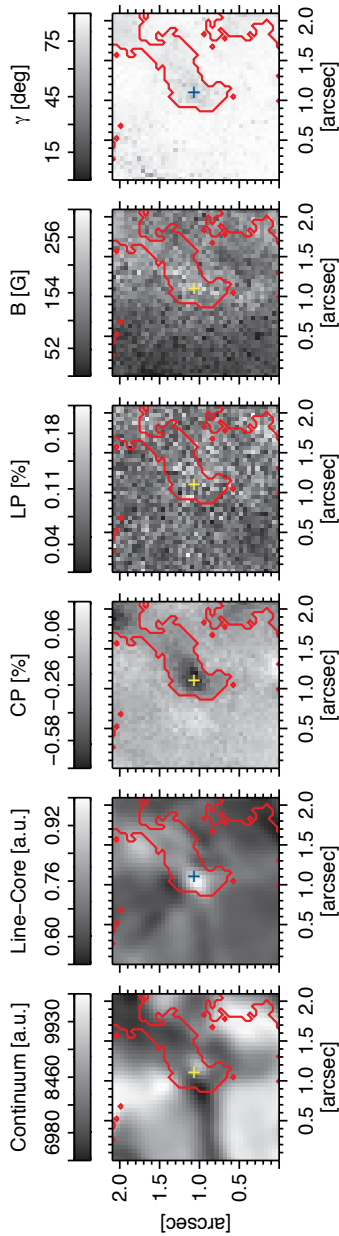


Figure 6.4: Example of a small magnetic bright point (MBP) marked in Fig. 6.1. From left to right: IMaX continuum intensity, IMaX line-core (see main text for a description), a measure of the strength of Stokes V (CP), total net linear polarisation (LP ; see main text), magnetic field strength (B) and field inclination (γ). The magnetic field parameters B and γ are computed using the SPINOR inversion code. Red contours outline magnetic regions and match the 4σ noise level in CP . Location of the centre of gravity of the CP distribution, is indicated by a cross in all panels. It facilitates comparing different maps.

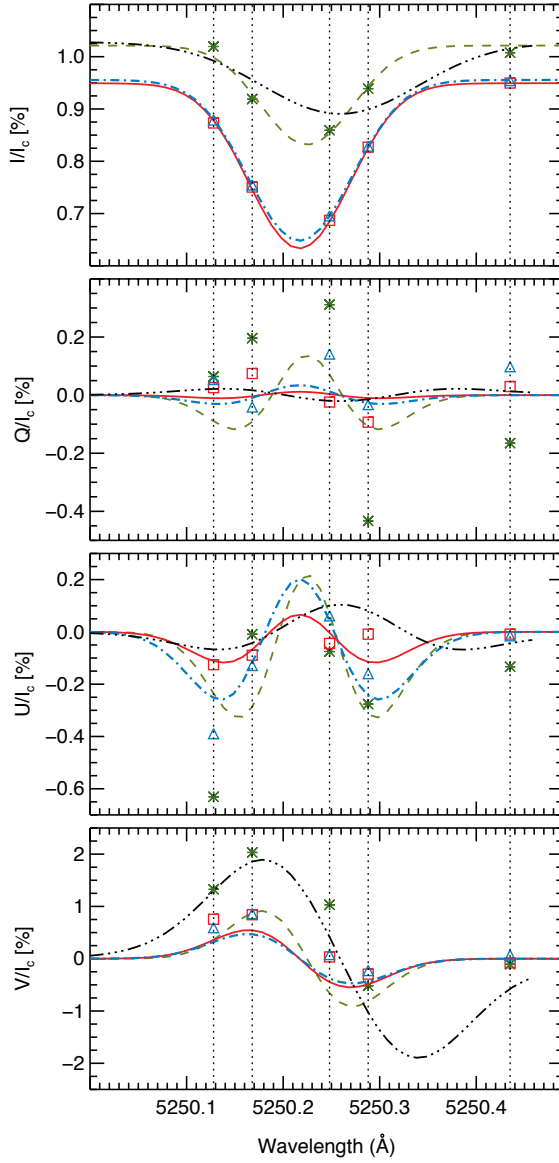


Figure 6.5: (Caption on the following page.)

Figure 6.5: Observed (symbols) and fitted (curves) Stokes I , Q , U , and V profiles for a sample MBP marked in Fig. 6.1. Red (squares and solid line): non-reconstructed, spatially smoothed IMAx data (see main text); fitted with the SPINOR inversion code. Blue (triangles and dot-dashed line): non-reconstructed data; fitted with the SPINOR code. Green (asterisks and dashed line): phase-diversity reconstructed data; fitted with the SPINOR code. Black (triple-dot-dashed line): fit to the phase-diversity reconstructed data returned by the SIR inversion code. The vertical dotted lines represent the IMAx filter wavelength positions. All profiles are normalised to the IMAx Stokes I continuum.

from our geometric approach (see Sect.6.3.1.1).

It is typical that although the magnetic field patch is bigger and more amorphous than the MBPs, its centre of gravity (marked by the cross) lies close to the MBPs' locations. The centre of gravity is measured within a small circle (diameter of ≈ 0.4 arcsec) centred at the pixel with maximum value (see Paper I for more detail) whose offset from the centre of gravity is ≈ 0.05 arcsec on the CP map, for this sample MBP. The LP signal in this map is almost everywhere below the 1σ noise level implying that both Stokes Q and U are not significant at the 1σ level at the position of our MBP. Hence, in principle only an upper limit on the inclination of the magnetic field in this MBP can be given.

The magnetic field strengths and inclination angles exhibit a wide range of values: $18 < B_i < 306$ G and $60^\circ < \gamma_i < 87^\circ$ among pixels with $CP \geq 4\sigma$ noise level, i.e., pixels inside the contours in Fig. 6.4. The large γ_i values may be a result of the noisy LP signal. The B_i and γ_i at the MBP's location (marked by the cross in Fig. 6.4) is found to be 194 G and 75° , respectively. The large γ_i returned by the inversion at the MBP's location is incompatible with the small γ_p (equal to $19 \pm 7^\circ$) returned by our measurements at the two heights.

In order to investigate the effect of noise level on the computed results, we performed inversions with the SPINOR code on three sets of differently treated data, described in Sect. 6.2; i.e., PD reconstructed, non-reconstructed and spatially smoothed (using a boxcar average of 3 pixels) non-reconstructed data. In addition, we used the results of the SIR inversion code performed on the phase-diversity reconstructed data as well as the results of the VFISV inversion code employed on both PD reconstructed and non-reconstructed data.

Figure 6.5 presents the Stokes I , Q , U , and V spectra recorded by IMAx for the sample MBP marked in Fig. 6.1. The different symbols represent the differently treated data: green asterisks for the PD reconstructed, blue triangles for the non-reconstructed and red squares for the spatially smoothed non-reconstructed data. The curves represent the corresponding best fits from the SPINOR inversion code: green dashed line for the PD reconstructed, blue dot-dashed line for the non-reconstructed and red solid line for the spatially smoothed non-reconstructed data. The best-fit profiles from the SIR inversion code applied to the phase-diversity reconstructed data are overlaid as black triple-dot-dashed lines. For simplicity, we have not over-plotted the profiles resulted from the VFISV inversion code, however, distributions of the magnetic field parameters that resulted from this inversion code will be later compared with similar distributions computed from the other inversion codes. Evidently the fits to the Stokes Q and U signals do not match the observed noisy profiles, which is not surprising given that the linear polarisation signal at

the position of this MBP lies below the 1σ noise level.

Comparing the original with the spatially smoothed non-reconstructed data indicates that the Stokes V signal is hardly affected by the spatially smoothing, while the Stokes Q and U signals are strongly affected by the smoothing of the non-reconstructed data. This is to be expected if the Q and U profiles are dominated by noise.

The magnetic field inclination and field strength values resulting from the inversions whose best-fit profiles were presented in Fig. 6.5 display a large range of values: 40° - 83° for γ_i and 194-587 G for B_i .

6.3.3 Statistics and discussion

Plotted in Fig. 6.6 are the distributions of the unsigned CP and the LP values (obtained from the least noisy spatially smoothed, non-reconstructed data; described in Sect. 6.2) in all 386 small MBPs studied here.

The triple-dot-dashed curve in Fig. 6.6a is an exponential fit to the CP histogram (for $CP > 0.45\%$) with an e-folding width of 0.48%. The CP histogram shows a lower limit of 0.13% which corresponds to the 4σ noise level as imposed as one of the selection criteria. In addition to the main distribution with a tail reaching to 1.9% CP , a few larger CP values of up to 4.3% (lying outside the range of this plot) were also obtained. The mean CP value of $0.68 \pm 0.48\%$ is given by the vertical solid line in Fig. 6.6a. This mean value (obtained from the spatially smoothed non-reconstructed data) is smaller by a factor of 2.8 than the mean CP measured from the PD reconstructed data, and by a factor of 3.6 than that of Riethmüller et al. (2013), who determined this parameter also from the PD reconstructed data. The small difference in CP values of MBPs to the work of Riethmüller et al. (2013) (if comparing the appropriate data) is easily explained by the fact that they considered MBPs with a larger range of sizes whereas we restrict ourselves to the smallest, point-like features.

In contrast to the strong CP signals at the position of our small MBPs, the distribution of LP , illustrated in Fig. 6.6b, shows LP signals which almost always lie below the 2σ noise level. In particular, 83% of the MBPs have $LP \leq 1\sigma$, 12% have $1\sigma < LP \leq 2\sigma$, 3% belong to the range of $2\sigma < LP \leq 3\sigma$ and only 2% corresponds to $LP > 3\sigma$. The exponential fit, with an e-folding width corresponding to an LP of 0.018%, is overlaid as a triple-dot-dashed line (fit limited to $LP \leq 0.08\%$). The largest LP values found in our sample reach up to 0.3% (not shown in the histogram). Therefore, the majority of our selected MBPs have a weak, mostly noise-dominated LP signal with a mean value of $0.024 \pm 0.018\%$ indicated by a vertical solid line in Fig. 6.6b. The too large fraction of MBPs with $LP < 1\sigma$ indicates that the deduced noise level is too large. This is to be expected since the noise is an average over the full IMAx field-of-view, whereas, by definition the MBPs are associated with a continuum enhancement and a weaker spectral line, i.e., with a larger photon flux, so that σ_{noise} at the MBPs is expected to be slightly lower.

In Fig. 6.7 the distributions of magnetic field inclination angle in 386 small and isolated internetwork MBPs, obtained from our geometric method, γ_p (black hashed histogram on the left side of the figure; from the IMAx/continuum-IMAx/line-core combination), and from the inversion of Stokes profiles, γ_i (all the remaining histograms), are plotted. They reveal a clear discrepancy between the almost vertical fields peaking at 14°

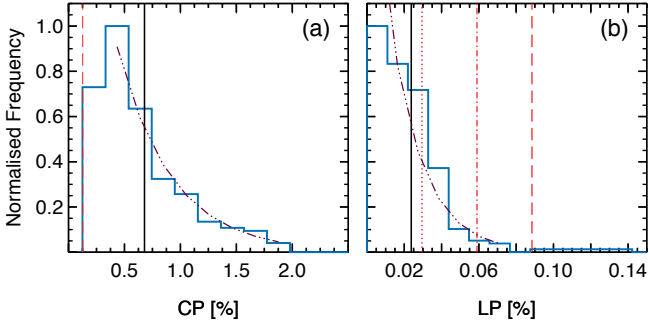


Figure 6.6: Distributions of the CP (panel *a*) and LP (panel *b*) at the positions of small SUNRISE/IMaX MBPs. The red dashed line in panel (*a*) marks the 4σ noise level and the vertical (black) solid lines in both panels represent the mean values of the histograms. The red dotted, dot-dashed and dashed vertical lines in panel (*b*) indicate the 1σ , 2σ and 3σ levels, respectively. The triple-dot-dashed curves represent the exponential fits to the histograms (see main text).

(mean γ_p of $14 \pm 6^\circ$) obtained from the intensity images and the nearly horizontal mag-

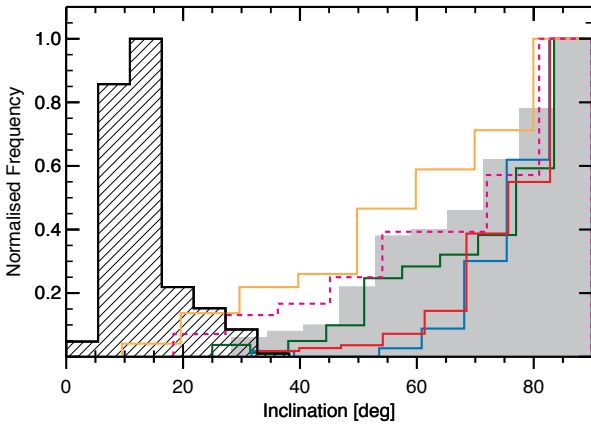


Figure 6.7: Distributions of inclination of MBPs. Inclinations, γ_p , obtained by comparing locations of MBPs in two layers (from the IMAx/continuum-IMAx/line-core combination; see main text) are represented by the (black) hashed histogram. Distributions of magnetic inclination angles, γ_i , of the same magnetic features computed by inverting Stokes data (see main text) are found in the right-hand-side of the plot. The different histograms result from inversions employing different codes and applying them to data treated in different ways (see main text for details).

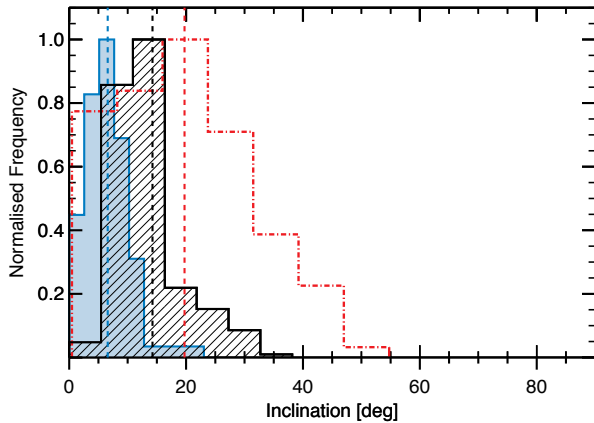


Figure 6.8: Distributions of inclination of MBPs obtained from the proposed geometric method, γ_p (see main text). The (black) hashed, (blue) shaded and (red; dot-dashed) outlined histograms show the distributions of γ_p obtained from combinations of two layers of the IMaX/continuum-IMaX/line-core, IMaX/continuum-SuFI/Ca II H and the IMaX Stokes V images made in the inner and outer flanks of the line, respectively. The vertical dashed lines indicate mean values of the histograms.

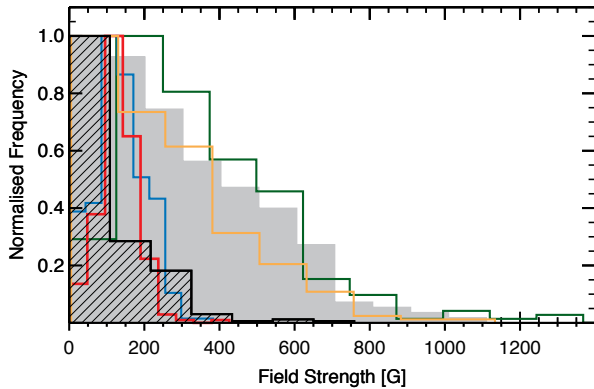


Figure 6.9: Distributions of the field strength B_i deduced in the same MBPs as in Fig. 6.7. The (black) hashed histogram shows the distribution of B obtained from the SPINOR inversion code with pre-determined inclination angles (γ_p) from measurements at two heights (see main text). Other histograms illustrate the distributions of the field strength of the same magnetic features computed by inverting differently treated data and using different inversion codes (see main text) without imposing γ .

netic fields (histograms in the right part of the figure), in the same magnetic elements, determined with the inversion codes. The gray shaded and yellow outlined histograms illustrate the distribution of γ_i obtained from inversions of PD reconstructed data made with the SIR and VFISV codes, respectively. The purple dashed-line identifies the distribution of γ_i obtained from inverting the non-reconstructed data with the VFISV code. The rest of the outlined histograms on the right-side of Fig. 6.7 represent distributions of γ_i computed with the SPINOR code from the differently treated data (described as in Sect. 6.2): (1) the non-reconstructed images (blue), (2) the spatially smoothed non-reconstructed data (red), and (3) PD reconstructed images (green). The fact that independent inversions carried out by three codes and applied to differently treated data with different noise levels produce qualitatively similar distributions of γ_i confirms that the difference between the inclination angles obtained from the geometric technique and those from the inversions are robust. There are, however, quantitative differences between the various histograms of γ_i . Thus the VFISV code returns somewhat less horizontal field than the other two codes. This indicates that Milne-Eddington inversions may be somewhat less affected by noise than a depth-dependant inversion.

In addition, we found (from our geometric method) that the magnetic elements are not inclined in any particular direction.

Our geometric method reveals the presence of nearly vertical internetwork magnetic fields, very much in contrast with the rather horizontal fields returned by inversions. The obviously too large inclinations returned by the inversions support the results of Borrero and Kobel (2011, 2012), who showed such a discrepancy between the results of inversion and both Monte Carlo and numerical simulations on the distribution of magnetic inclination angles.

For comparison, the distributions of γ_p obtained using different combinations of the two heights are plotted in Fig. 6.8. The black hashed histogram is the same distribution of γ_p showed on the left side of Fig. 6.7 (from the IMAx/continuum-IMaX/line-core images). The distributions of γ_p measured from the combinations of IMAx/continuum-SuFI/Ca II H and the IMAx Stokes V images made in the inner and outer flanks of the Fe I line are displayed as blue shaded and red (dot-dashed) outlined histograms, respectively. The vertical dashed lines in Fig. 6.8 indicate the average γ_p values, lying at 7° , 14° and 20° (with distributions' standard deviation of 4° , 6° and 18°) for the IMAx/continuum-IMaX/line-core, IMAx/continuum-SuFI/Ca II H and IMAx Stokes V images, respectively. The three distributions of γ_p give similar results, confirming the vertical fields of the MBPs. In Sect. 6.3.1.1 we discussed the possible causes for the differences among the three distributions of γ_p . In particular, we noted that a larger height difference between the two layers introduces a larger error/uncertainty in deducing the horizontal position on the derived γ_p .

We note that if the inversions derive an incorrect inclination, they possibly also deduce an incorrect pixel-averaged field strength B_i (which is at least partially determined by the amplitude of the Stokes profiles, so that an overestimate of the LP responsible for the overestimate of γ should also result in an overestimate of B). In order to obtain an improved value of B , we use the inclination obtained from our geometric method, γ_p , as an input to the inversion of the spectropolarimetric data. The inversion code is forced to ignore fitting the noise-dominated Stokes Q and U and hence, should provide more reliable magnetic field strength for small, internetwork magnetic elements compared to

those obtained from unconstrained inversions.

The distributions of B_i computed from spatially smoothed (red histogram) as well as non-smoothed non-reconstructed data (blue histogram) using the SPINOR code, presented in Fig. 6.9, have a mean value of 130 G. To avoid cluttering the figure, the distribution of the B_i obtained from inverting the non-reconstructed data with the VFISV code (with a mean value of 160 G) is not plotted. Inverting the PD reconstructed images results in a mean B_i in the range of 260 – 360 G, depending on the inversion code. A mean value of $B_p = 100$ G obtained from the SPINOR code with pre-determined inclination angles γ_p from non-reconstructed data (hashed histogram). This is obviously smaller than mean values obtained from unconstrained inversions.

A visual comparison between the distributions of γ_i obtained from different inversions in Fig. 6.7 shows that the results of the SPINOR inversion from the non-reconstructed data (i.e., from both non-smoothed and spatially smoothed data; blue and red histograms) represent larger γ compared to other distributions. Consequently, larger B_i values would be expected for the blue and red histograms in Fig. 6.9 compared to the others. However, their distributions show smaller B_i values. This non-compatibility arises from this fact that in the non-reconstructed data the magnetic field is more diffuse and is spread over a larger area. Hence, B_i in a single pixel (selected at the position of the MBPs) is expected to be smaller than the value in non-reconstructed data. The effect of the different spatial resolution more than offsets influences the difference in γ_i .

Let us now estimate by how much the contribution to the horizontal magnetic flux due to these MBPs is overestimated by inversions. Horizontal magnetic flux (Φ_h) at any given pixel can be obtained using the computed B and γ values, i.e., $\Phi_h \propto B \sin(\gamma)$. Hence, larger B and/or larger γ result in larger Φ_h . The ratio between the horizontal magnetic flux computed from the inversion results ($\Phi_{h,i}$) and the one obtained from our geometric method ($\Phi_{h,p}$) can be approximated as

$$\frac{\Phi_{h,i}}{\Phi_{h,p}} = \frac{B_i \sin(\gamma_i)}{B_p \sin(\gamma_p)}, \quad (6.2)$$

where B_i and γ_i are the estimated field strength and inclination angle from the inversions, respectively. $\gamma_p = 14^\circ$ is the mean inclination from the geometric technique and $B_p = 100$ G represents the field strength computed using the inversion with pre-determined γ_p . As a result, the mean values of the B_i and γ_i from different inversions reveal that the horizontal magnetic flux is overestimated by a factor of (roughly) 5 – 15 on average compared to $\Phi_{h,p}$.

However, note that none of these magnetic elements could be observed as MBPs unless they would be kG magnetic concentrations (e.g., Rutten et al. 2001; Vögler et al. 2005; Riethmüller 2013; Riethmüller et al. 2013). This means that these MBPs are likely not fully resolved and hence, all the field strength values that we computed using inversions were underestimated. Therefore, a much smaller filling factor than unity would be needed to obtain the true B values.

6.4 Conclusions

We propose a simple approach for determining the inclination of magnetic elements associated with bright points by comparing the locations of the MBPs in high spatial resolution intensity images sampling two heights, or, alternatively by comparing the locations of peak Stokes V signal at two heights. This technique is applied to SUNRISE/IMaX and SuFI data. The method offers, for the first time, an opportunity to determine the inclination angle in the small-scale magnetic features independently of inverting measured Stokes profiles. The new technique is of particular interest in the quiet-Sun since the Stokes profiles can be affected by noise there.

For a first application of our technique we selected small, point-like bright features (diameter smaller than 0.3 arcsec) displaying a CP (a measure of Stokes V strength) above the 4σ noise level. They turned out to have very weak linear polarisation signals, with LP , computed from Stokes Q and U profiles, lying almost always below the 2σ level.

The high spatial resolution and seeing-free data recorded by SUNRISE allowed the accurate position of a MBP associated with one and the same magnetic element to be determined in at least two different layers. We have employed the continuum position and the line-core of the SUNRISE/IMaX Fe I 5250.2 Å passband, but have also compared SUNRISE/SuFI Ca II H brightenings with those in the 5250.4 Å continuum. The inclination is obtained by connecting the coordinates of a pair of MBPs associated with the same magnetic feature (i.e., the same CP patch) and considering the formation heights of the passbands in which the MBPs are observed. There are a number of sources of uncertainty, such as the time difference between data recorded at different wavelengths and the fact that the formation heights depend on the atmospheric structure (e.g., temperature, electron pressure and magnetic field). However, using reasonable estimates of these and other uncertainties results in inclination angles accurate to better than 7° .

An application of this method to 386 small magnetic features in the internetwork quiet-Sun gives an average inclination of 14° and a standard deviation of only 6° . The small standard deviation suggest that our error estimate is relatively generous. There is very little overlap between the distributions of inclination obtained with our geometric technique and from the three Stokes inversion codes, which gave average inclinations γ_i of $66^\circ - 81^\circ$, with all γ_i distributions peaking at or close to 90° . The striking agreement between the various inversions supports the suggestion that inversion codes overestimate the inclination angles of features with noise-dominated Stokes Q and U signals (e.g., de Wijn et al. 2009; Borrero and Kobel 2011, 2012). Inversions of differently treated data (i.e., phase-diversity reconstructed, non-reconstructed and spatially smoothed non-reconstructed data) and three independent inversion codes gave similar results. Similarly, employing Ca II H line-core images (less sensitive to Zeeman effect and Doppler shifts) instead of the Fe I 5250.2 Å line-core gave very similar results, even providing somewhat more vertical fields ($\gamma_p \approx 7^\circ$ on average). Our results based on intensity images were generally confirmed by comparing spatial centre-of-gravity of the Stokes V signal at two different positions in the line, formed at somewhat different heights, giving $\gamma_p \approx 20^\circ$ on average. This last test is of particular important in spite of the larger errors it gives, due to the lower signals, less compact structures in Stokes V and the much smaller height difference, since it reveals that the geometric method applied to MBPs does provide a good estimate of the inclination of the magnetic field.

The results of such measurements at the two heights are also found to have a significant effect on determining the solar magnetic flux in horizontal fields, due to the studied small magnetic elements. Our work indicated that traditional inversion methods overestimate this parameter by an order of magnitude.

Furthermore, we found that the magnetic field strength (on the Sun) computed from the inversions of small, internetwork magnetic elements is overestimated. We showed that the inversions give a lower field strength by an average factor of ≈ 2 when the inclination angle, γ_p , obtained from our geometric method is imposed prior to inverting the data.

We have restricted ourselves to small magnetic elements that manifest themselves as BPs, which are expected to be kG magnetic concentrations (e.g., Spruit 1976). Only a concentrated field produces a sufficiently deep Wilson depression to allow enough excess radiation to enter the magnetic feature to produce a continuum BP. Thus, Riethmüller et al. (2013) use MHD simulations to demonstrate that only magnetic features with kG field produce significant continuum brightenings. The large expected intrinsic field strength is consistent with the small γ_p found here, since kG fields are expected to be relatively vertical due to their buoyancy (Schüssler 1986). The comparison of the deduced field strengths of roughly 100 G with the requirement of $B > 1000$ G mean that the area of the magnetic features studied here is on average smaller than $30 - 40 \text{ km}^2$ assuming a resolution element of SUNRISE/IMaX of 100 km (after reconstruction). Thus, although the high spatial resolution observations from SUNRISE/IMaX have allowed resolving magnetic elements in the quiet-Sun (Lagg et al. 2010), many small-scale magnetic elements observed by SUNRISE are believed to be spatially unresolved (Jafarzadeh et al. 2013a; Riethmüller et al. 2013).

It has recently been shown that only 1/4 of the IN areas have strong linear polarisation signals, i.e., signals above the 4.5σ noise level (Orozco Suárez and Bellot Rubio 2012). Therefore, the inclination of the magnetic vector in, at least, 3/4 of the IN area (i.e., the majority of the solar surface) is still not clear, with arguments being made for a mostly horizontal field (Bellot Rubio and Orozco Suárez 2012) as well as an isotropic distribution of weak fields (Asensio Ramos 2009; Bommier et al. 2009), or even predominantly vertical fields in the quiet-Sun (Stenflo 2010).

Our results demonstrate that at least some of the magnetic features interpreted in terms of horizontal fields by inversions are actually close to vertical (see Fig. 6.7). This requires a reassessment of the distribution of the magnetic field vector, especially in regions where Stokes Q and U are highly affected by noise. The method proposed here can help by providing inclinations for all magnetic features associated with MBPs (i.e., strong-field elements).

We can foresee a wide applicability of the new technique. Applying this method to higher contrast images, e.g., photospheric 2140 \AA and $\text{Ca II H } 3968 \text{ \AA}$ obtained by SUNRISE/SuFI (Riethmüller et al. 2010; Gandorfer et al. 2011), and loosening constraints on the size of the considered MBPs will result in better statistics. An even wider applicability of the new technique would result from measurements of the location of peaks (or centre-of-gravity) in the Stokes profiles (generally Stokes V due to its larger SNR value) at measurements made at different heights. We tested this by measuring the location of magnetic concentrations (centre-of-gravity) observed in the Stokes V images in two wavelength positions of the $\text{Fe I } 5250.2 \text{ \AA}$ line formed at somewhat different heights and found that the results are consistent with those obtained from the intensity images at two atmo-

spheric layers. Measurements in multiple spectral lines with sufficiently different heights of formation can increase the reliability of the method and may one day even allow the curvature of the magnetic elements (i.e., the bending of the axis of the underlying flux tube with height) to be determined.

7 Conclusions and outlook

We used several high-quality, (spatial and temporal) high-resolution time-series of images of the internetwork observed at disc-centre of the quiet Sun by the SUNRISE balloon-borne solar observatory. We studied the structure and dynamics of magnetic bright, point-like features (MBPs) in different solar atmospheric layers. We applied a set of stringent criteria within our analysis algorithm to (i) concentrate on the point-like features (i.e., MBPs smaller than 0.3 arcsec), (ii) separate the isolated MBPs (that do not merge or split in the course of their lifetimes) from other (non-magnetic) point-like brightenings (see Sect. 3.3). Although these criteria limited us to a relatively small number of MBPs (an average number density 0.03 (Mm)^{-2}), they secured measurements of the precise locations of the MBPs that are crucial for studying their dynamics.

We performed our investigations at heights sampled by the SuFI 3000 Å, IMAx Fe I 5250.2 Å and SuFI Ca II H 3968 Å passbands, which cover the lower solar atmosphere (i.e., approximately from the solar surface at $\tau_c = 1$ to the heights roughly corresponding to the temperature minimum/low-chromosphere). We investigated the magnetic properties of the MBPs using the all Stokes parameters measured by the SUNRISE/IMAx in the magnetically sensitive Fe I 5250.2 Å line, whenever available.

First, we tracked 107 MBPs identified in the Ca II H passband and determined their physical properties. We found mean values of $2.2 \pm 1.8 \text{ km s}^{-1}$, $0.2 \pm 0.02 \text{ arcsec}$ ($\approx 150 \text{ km}$), $1.48 \pm 0.3 \langle I_{Ca} \rangle$ and $673 \pm 526 \text{ sec}$ for distributions of horizontal velocity, diameter, intensity and lifetime of the MBPs, respectively (the uncertainties are the standard deviations of the parameters' distributions). We compared these values with those in the literature (Sect. 3.6) and found that, in particular, Ca II H MBPs live considerably longer than previously thought. Moreover, we obtained an anti-correlation between the maximum intensity and maximum horizontal velocity of the MBPs (Fig. 3.12). We also observed that the MBPs move at a supersonic speed for 3.5% of their lifetimes (on average) and several intermittent pulses (i.e., horizontal motions faster than $\approx 2 - 3 \text{ km s}^{-1}$, lasting less than $\approx 100 \text{ sec}$) in the horizontal velocity of the MBPs occur during their lifetimes. Such jerky motions are expected to be effective in exciting kink waves (Choudhuri et al. 1993a). We computed the total energy flux that can be potentially carried by the kink waves based on theoretical estimates ($\approx 310 \text{ W m}^{-2}$) and showed that it is marginally enough to heat the quiet corona. If such waves can reach these atmospheric layers at all (Sect. 3.5).

We then further investigated the MBPs identified in Chapter 3 as well as others found in other data sets using the criteria defined in Chapter 3. These investigations concentrated on three aspects of the properties of the MBPs:

1. We studied the trajectories of internetwork Ca II H MBPs to characterise their migra-

tion. We computed the diffusion parameters of MBPs and obtained a diffusion index of 1.69 ± 0.08 and a diffusion coefficient of $257 \pm 32 \text{ km}^2 \text{ s}^{-1}$, averaged over all MBPs. These values are, to our knowledge, among the largest values obtained so far. The former parameter (diffusion index) places the MBPs in the super-diffusive category. The calculated diffusion coefficients lie within the range of values deduced from the magnetic field's decay rate on the solar surface, from 3D MHD simulations. We further explored the nature of the distribution of the diffusion indices with the help of a Monte Carlo simulation, in which the migration of relatively short-lived MBPs (compared to the supergranular time-scale) are described as random walkers (caused by intergranular turbulence and granular evolution) superposed on a systematic velocity due to granular (and also meso- and super-granular) flows.

2. We investigated the presence of oscillations in both intensity and horizontal velocity at the position of the MBPs in two different atmospheric heights, sampled nearly simultaneously by the SuFI 3000 Å and SuFI Ca II H 3968 Å passbands (with a height difference of $430 \pm 30 \text{ km}$; both with a cadence of 12 sec). Seven MBPs could be tracked simultaneously in both filtergrams for a sufficiently long time (i.e., longer than 5 min). A wavelet analysis at the MBPs revealed the upward propagation of high-frequency (up to 30 mHz) fast waves of both compressible (sausage; manifested in intensity fluctuations) and incompressible (kink, observed in horizontal displacements perturbations) modes. The high frequency of the observed waves could be due to turbulence in intergranular areas (Hasan and van Ballegoijen 2008) where the MBPs are located. Observations of MHD fast waves at the height, roughly corresponding to the temperature minimum (sampled by the Ca II H bandpass), could be explained as the results of mode conversion at the $\beta \approx 1$ level, where the Alfvén and sound speeds coincide (e.g., Bogdan et al. 2003; Nutto et al. 2012). More importantly, the measured fast compressible (sausage) mode between the two atmospheric layers (at MBPs) can be due to the propagation path of the fast magnetic mode (Nutto et al. 2012). Such fast compressible waves have been shown not to reach the upper solar atmosphere, but are refracted due to the large gradient in the Alfvén speed (Nutto et al. 2012). We also found a decrease in the amplitudes of the horizontal velocities with height. This probably implies that the observed fast kink waves may not reach the corona, and therefore, either dissipate their energy in the lower layers, or are converted to another wave mode.
3. We introduced a new and simple method with which a proxy of the magnetic field's inclination can be determined directly from high resolution intensity images sampled at different heights. We applied this method on 386 small magnetic features found in the internetwork quiet Sun, while we also computed the magnetic inclination angle of the same magnetic features using inversions of simultaneously recorded Stokes profiles. We found that the almost vertical magnetic field from our geometric method is incompatible with the nearly horizontal field from the traditional inversion techniques. This has implications for the reliability of the inclination of magnetic fields obtained by inversions at low signal-to-noise ratios and for estimating the vertical and horizontal solar magnetic flux. We showed that the inversions overestimate the horizontal magnetic flux at small magnetic elements associated with MBPs (i.e., with concentrated field) by an order of magnitude.

More detailed results of the above mentioned studies, their thorough comparison with the literature, as well as further interpretations are provided in the conclusion sections of Chapters 3, 4, 5, and 6.

Furthermore, a close inspection of MBPs interacting with each other is being carried out. The merging and splitting of the MBPs can represent braiding of the flux tubes, if the two “merged” MBPs still remain distinct and move around each other. To this end, we are extending our developed code (employed for the so far investigations) to make use of some other image reconstruction algorithms (such as the so-called CLEAN method; Högbom 1974). This approach is an iterative procedure that minimise the effect of the point-spread-function in hiding the locations of “close” MBPs (e.g., apparently merged MBPs). Other possible (indirect) methods for indicating the braiding events are also considered.

Moreover, we plan to produce an easy-to-use graphical-user-interface of our developed algorithm that might help the community for similar investigations.

In addition, further research is being focused on:

- *Relationship between the rapid pulses found in Chapter 3 and the high-frequency kink waves studied in Chapter 5:* We have characterised the rapid pulses (the sudden acceleration of flux tubes by granules) studied in Chapter 3 (i.e., we know the times and locations of their occurrence). Hence, we aim to investigate whether the oscillatory power we found in the high-frequency kink waves (in Chapter 5) happens (or peaks) before, during, or just after such pulses. This can observationally identify rapid pulses, for the first time to our knowledge, as a major source of kink waves (the connection has been based on theory up to now).
- *Do the detected waves in Chapter 5 reach the high-chromosphere/corona?:* We have so far identified upward propagating high frequency waves at MBPs at the heights roughly corresponding to the temperature minimum/low chromosphere. Applying the same method used for such investigations on a larger range of simultaneously observed wavelengths (i.e., simultaneous sampling of several atmospheric layers from the low-photosphere to mid-chromosphere and possibly to the corona) will enable us to investigate their propagation, reflection or dissipation in the higher layers of the solar atmosphere. Fortunately, the SUNRISE balloon-borne solar observatory is scheduled to fly again this summer (June/July 2013) with additional chromospheric passbands, i.e., Ca II H 3968.4 Å and Mg II 2796.2 Å; with filter widths of 1.1 Å and 4.8 Å, respectively. Thus, a successful flight of this mission can provide datasets suitable for such an investigation.
- *Distribution of the magnetic field’s inclinations in internetwork areas:* We have shown that the inversion codes do not return the correct inclination of the magnetic field at the internetwork MBPs, where Stokes Q and U are adversely affected by noise. The results were consistent with inverting differently treated data with different noise levels. However, Bellot Rubio and Orozco Suárez (2012) showed that there is a large amount of linear polarisation signal everywhere in internetwork regions if the time series of images are integrated for long enough. Features with significant linear polarisation signals are, however, short lived (2.7 min on average; Danilovic et al. 2010b). Therefore, we are testing the results of Bellot Rubio and

Orozco Suárez (2012) and aim to obtain a more reliable distribution of the magnetic field's inclination; possibly by combining the results obtained from our proposed approach (based on the measurements of the MBPs' locations at two heights; Sect. 6.3.1) and those computed from inversions.

In summary, the original contribution and significance of our research to the field are:

- Structure, dynamics and an observational picture of the small-scale magnetic features in the lower solar atmosphere.
- Detection of jerky (sometimes supersonic) motions at the base of magnetic thin flux tubes that can excite kink waves along the tubes and produce (marginally) enough energy to heat the quiet corona.
- Provide the characteristics of the migration of MBPs across internetwork quiet-Sun.
- Identification of upward propagating, high-frequency, fast MHD waves, both compressible and incompressible, in the lower solar atmosphere.
- Introduce a new approach for determining reliable magnetic field inclinations of small magnetic elements in internetwork regions (independently of inversions of the Stokes parameters, affected by noise in the quiet Sun).

Bibliography

- Abramenko, V., Yurchyshyn, V., Goode, P., Kilcik, A., 2010, Statistical distribution of size and lifetime of bright points observed with the New Solar Telescope, *ApJ*, 725, L101
- Abramenko, V. I., Carbone, V., Yurchyshyn, V., Goode, P. R., Stein, R. F., Lepreti, F., Capparelli, V., Vecchio, A., 2011, Turbulent diffusion in the photosphere as derived from photospheric bright point motion, *ApJ*, 743, 133
- Abramenko, V. I., Yurchyshyn, V. B., Goode, P. R., Kitiashvili, I. N., Kosovichev, A. G., 2012, Detection of small-scale granular structures in the quiet Sun with the New Solar Telescope, *ApJ*, 756, L27
- Al, N., Bendlin, C., Kneer, F., 2002, Dynamics of small features in the solar chromosphere, *A&A*, 383, 283
- Antolin, P., Shibata, K., Kudoh, T., Shiota, D., Brooks, D., 2008, Predicting observational signatures of coronal heating by Alfvén waves and nanoflares, *ApJ*, 688, 669
- Aschwanden, M. J., Fletcher, L., Schrijver, C. J., Alexander, D., 1999, Coronal loop oscillations observed with the transition region and coronal explorer, *ApJ*, 520, 880
- Aschwanden, M. J., 2004, *Physics of the solar corona. An introduction* (Chichester: Praxis)
- Asensio Ramos, A., 2009, Evidence for quasi-isotropic magnetic fields from Hinode quiet-Sun observations, *ApJ*, 701, 1032
- Asensio Ramos, A., Manso Sainz, R., Martínez González, M. J., Viticchié, B., Orozco Suárez, D., Socas-Navarro, H., 2012, Model selection for spectropolarimetric inversions, *ApJ*, 748, 83
- Auer, L. H., House, L. L., Heasley, J. N., 1977, The determination of vector magnetic fields from Stokes profiles, *Sol. Phys.*, 55, 47
- Ayres, T. R., Testerman, L., Brault, J. W., 1986, Fourier transform spectrometer observations of solar carbon monoxide. II. Simultaneous cospatial measurements of the fundamental and first-overtone bands, and Ca II K, in quiet and active regions, *ApJ*, 304, 542

- Avrett, E. H., Loeser, R., 1992, The PANDORA atmosphere program, in *Cool Stars, Stellar Systems, and the Sun*, (Ed.) Giampapa, M. S. and Bookbinder, J. A., vol. 26 of ASP Conf. Ser. (San Francisco: ASP), p. 489
- Babcock, H. W., Babcock, H. D., 1952, Mapping the magnetic fields of the Sun, *PASP*, 64, 282
- Barthol, P., Gandorfer, A., Solanki, S. K., Schüssler, M., Chares, B., Curdt, W., Deutsch, W., Feller, A., Germerott, D., Grauf, B., Heerlein, K., Hinzberger, J., Kolleck, M., Meller, R., Müller, R., Riethmüller, T. L., Tomasch, G., Knölker, M., Lites, B. W., Card, G., Elmore, D., Fox, J., Lecinski, A., Nelson, P., Summers, R., Watt, A., Martínez Pillet, V., Bonet, J. A., Schmidt, W., Berkefeld, T., Title, A. M., Domingo, V., Gasent Blesa, J. L., Del Toro Iniesta, J. C., López Jiménez, A., Álvarez-Herrero, A., Sabau-Graziati, L., Widani, C., Haberler, P., Härtel, K., Kampf, D., Levin, T., Pérez Grande, I., Sanz-Andrés, A., Schmidt, E., 2011, The Sunrise mission, *Sol. Phys.*, 268, 1
- Baudin, F., Gabriel, A., Gibert, D., 1994, Time/frequency analysis of solar p-modes, *A&A*, 285, L29
- Baudin, F., Bocchialini, K., Koutchmy, S., 1996, Propagating magneto-acoustic waves in the solar chromosphere, *A&A*, 314, L9
- Beck, C., Schmidt, W., Rezaei, R., Rammacher, W., 2008, The signature of chromospheric heating in Ca II H spectra, *A&A*, 479, 213
- Beck, C., Rezaei, R., 2009, The magnetic flux of the quiet Sun internetwork as observed with the Tenerife infrared polarimeter, *A&A*, 502, 969
- Beckers, J. M., Milkey, R. W., 1975, The line response function of stellar atmospheres and the effective depth of line formation, *Sol. Phys.*, 43, 289
- Bello González, N., Flores Soriano, M., Kneer, F., Okunev, O., 2009, Acoustic waves in the solar atmosphere at high spatial resolution, *A&A*, 508, 941
- Bello González, N., Franz, M., Martínez Pillet, V., Bonet, J. A., Solanki, S. K., del Toro Iniesta, J. C., Schmidt, W., Gandorfer, A., Domingo, V., Barthol, P., Berkefeld, T., Knölker, M., 2010, Detection of large acoustic energy flux in the solar atmosphere, *ApJ*, 723, L134
- Bellot Rubio, L. R., Ruiz Cobo, B., Collados, M., 2000, Inversion of Stokes profiles from solar magnetic elements, *ApJ*, 535, 475
- Bellot Rubio, L. R., 2009, Detection of supersonic horizontal flows in the solar granulation, *ApJ*, 700, 284
- Bellot Rubio, L. R., Orozco Suárez, D., 2012, Pervasive linear polarization signals in the quiet Sun, *ApJ*, 757, 19
- Berdygina, S. V., Solanki, S. K., Frutiger, C., 2003, The molecular Zeeman effect and diagnostics of solar and stellar magnetic fields. II. Synthetic Stokes profiles in the Zeeman regime, *A&A*, 412, 513

- Berger, T. E., Schrijver, C. J., Shine, R. A., Tarbell, T. D., Title, A. M., Scharmer, G., 1995, New observations of subarcsecond photospheric bright points, *ApJ*, 454, 531
- Berger, T. E., Title, A. M., 1996, On the dynamics of small-scale solar magnetic elements, *ApJ*, 463, 365
- Berger, T. E., Löfdahl, M. G., Shine, R. S., Title, A. M., 1998a, Measurements of solar magnetic element motion from high-resolution filtergrams, *ApJ*, 495, 973
- Berger, T. E., Löfdahl, M. G., Shine, R. A., Title, A. M., 1998b, Measurements of solar magnetic element dispersal, *ApJ*, 506, 439
- Berger, T. E., Title, A. M., 2001, On the relation of G-band bright points to the photospheric magnetic field, *ApJ*, 553, 449
- Berkefeld, T., Schmidt, W., Soltau, D., Bell, A., Doerr, H. P., Feger, B., Friedlein, R., Gerber, K., Heidecke, F., Kentischer, T., von der Lühe, O., Sigwarth, M., Wälde, E., Barthol, P., Deutsch, W., Gandorfer, A., Germerott, D., Grauf, B., Meller, R., Álvarez-Herrero, A., Knölker, M., Martínez Pillet, V., Solanki, S. K., Title, A. M., 2011, The wave-front correction system for the Sunrise balloon-borne solar observatory, *Sol. Phys.*, 268, 103
- Biermann, L., 1948, Über die Ursache der chromosphärischen Turbulenz und des UV-Exzesses der Sonnenstrahlung, *ZAp*, 25, 161
- Bird, G. A., 1964, The propagation of acoustic waves through the solar chromosphere, *ApJ*, 140, 288
- Bloomfield, D. S., McAteer, R. T. J., Mathioudakis, M., Williams, D. R., Keenan, F. P., 2004, Propagating waves and magnetohydrodynamic mode coupling in the quiet-Sun network, *ApJ*, 604, 936
- Bogdan, T. J., Cattaneo, F., Malagoli, A., 1993, On the generation of sound by turbulent convection. I. A numerical experiment, *ApJ*, 407, 316
- Bogdan, T. J., Carlsson, M., Hansteen, V. H., McMurry, A., Rosenthal, C. S., Johnson, M., Petty-Powell, S., Zita, E. J., Stein, R. F., McIntosh, S. W., Nordlund, Å., 2003, Waves in the magnetized solar atmosphere. II. Waves from localized sources in magnetic flux concentrations, *ApJ*, 599, 626
- Bommier, V., Martínez González, M., Bianda, M., Frisch, H., Asensio Ramos, A., Gelly, B., Landi Degl'Innocenti, E., 2009, The quiet Sun magnetic field observed with ZIMPOL on THEMIS. I. The probability density function, *A&A*, 506, 1415
- Borrero, J. M., Solanki, S. K., 2008, Are there field-free gaps near $\tau = 1$ in sunspot penumbrae?, *ApJ*, 687, 668
- Borrero, J. M., Martínez-Pillet, V., Schlichenmaier, R., Solanki, S. K., Bonet, J. A., del Toro Iniesta, J. C., Schmidt, W., Barthol, P., Gandorfer, A., Domingo, V., Knölker, M., 2010, Supersonic magnetic upflows in granular cells observed with Sunrise/IMaX, *ApJ*, 723, L144

- Borrero, J. M., Kobel, P., 2011, Inferring the magnetic field vector in the quiet Sun. I. Photon noise and selection criteria, *A&A*, 527, A29
- Borrero, J. M., Tomczyk, S., Kubo, M., Socas-Navarro, H., Schou, J., Couvidat, S., Bogart, R., 2011, VFISV: Very Fast Inversion of the Stokes Vector for the helioseismic and magnetic imager, *Sol. Phys.*, 273, 267
- Borrero, J. M., Kobel, P., 2012, Inferring the magnetic field vector in the quiet Sun. II. Interpreting results from the inversion of Stokes profiles, *A&A*, 547, A89
- Bovelet, B., Wiehr, E., 2008, The quiet Sun's magnetic flux estimated from Ca II H bright inter-granular G-band structures, *A&A*, 488, 1101
- Brandt, P. N., Rutten, R. J., Shine, R. A., Trujillo Bueno, J., 1992, Dynamics of the quiet solar atmosphere: K_{2V} cell grains versus magnetic elements, in *Cool Stars, Stellar Systems, and the Sun*, (Ed.) Giampapa, M. S. and Bookbinder, J. A., vol. 26 of ASP Conf. Ser. (San Francisco: ASP), p. 161
- Brund, D., 1927, The period of simple vertical oscillations in the atmosphere, *Quart. J. Roy. Meteor. Soc.*, 53, 30
- Caccin, B., Gomez, M. T., Marmolino, C., Severino, G., 1977, Response functions and contribution functions of photospheric lines, *A&A*, 54, 227
- Cadavid, A. C., Lawrence, J. K., Ruzmaikin, A. A., 1999, Anomalous diffusion of solar magnetic elements, *ApJ*, 521, 844
- Cadavid, A. C., Lawrence, J. K., Berger, T. E., Ruzmaikin, A., 2003, Photospheric sources and brightening of the internetwork chromosphere, *ApJ*, 586, 1409
- Caligari, P., Moreno-Insertis, F., Schüssler, M., 1995, Emerging flux tubes in the solar convection zone. I. Asymmetry, tilt, and emergence latitude, *ApJ*, 441, 886
- Cally, P. S., 2007, What to look for in the seismology of solar active regions, *Astronomische Nachrichten*, 328, 286
- Cally, P. S., Hansen, S. C., 2011, Benchmarking fast-to-Alfvén mode conversion in a cold magnetohydrodynamic plasma, *ApJ*, 738, 119
- Cameron, R., Vögler, A., Schüssler, M., 2011, Decay of a simulated mixed-polarity magnetic field in the solar surface layers, *A&A*, 533, A86
- Carlsson, M., Stein, R. F., 1997, Formation of solar Calcium H and K bright grains, *ApJ*, 481, 500
- Carlsson, M., Stein, R. F., Nordlund, Å., Scharmer, G. B., 2004, Observational manifestations of solar magnetoconvection: Center-to-limb variation, *ApJ*, 610, L137
- Carlsson, M., Hansteen, V. H., de Pontieu, B., McIntosh, S., Tarbell, T. D., Shine, D., Tsuneta, S., Katsukawa, Y., Ichimoto, K., Suematsu, Y., Shimizu, T., Nagata, S., 2007, Can high frequency acoustic waves heat the quiet Sun chromosphere?, *PASJ*, 59, 663

- Carroll, B. W., Ostlie, D. A., 1996, *An introduction to modern astrophysics* (San Francisco: Pearson, Addison-Wesley)
- Cattaneo, F., Hurlburt, N. E., Toomre, J., 1989, Two and three-dimensional simulations of compressible convection, in *NATO ASIC Proc. 263: Solar and Stellar Granulation*, (Ed.) Rutten, R. J. and Severino, G. (Dordrecht: Kluwer), p. 415
- Centeno, R., Collados, M., Trujillo Bueno, J., 2006, Spectropolarimetric investigation of the propagation of magnetoacoustic waves and shock formation in sunspot atmospheres, *ApJ*, 640, 1153
- Centeno, R., Trujillo Bueno, J., Asensio Ramos, A., 2010, On the magnetic field of off-limb spicules, *ApJ*, 708, 1579
- Chae, J., Litvinenko, Y. E., Sakurai, T., 2008, Determination of magnetic diffusivity from high-resolution solar magnetograms, *ApJ*, 683, 1153
- Charbonneau, P., 1995, Genetic algorithms in astronomy and astrophysics, *ApJS*, 101, 309
- Charbonneau, P., 2005, Dynamo models of the solar cycle, *Living Rev. Solar Phys.*, 2, 2. URL: <http://www.livingreviews.org/lrsp-2005-2>
- Cheung, M. C. M., Schüssler, M., Moreno-Inertis, F., 2007, The origin of the reversed granulation in the solar photosphere, *A&A*, 461, 1163
- Chitta, L. P., van Ballegoijen, A. A., Ruppe van der Voort, L., DeLuca, E. E., Kariyappa, R., 2012, Dynamics of the solar magnetic bright points derived from their horizontal motions, *ApJ*, 752, 48
- Choudhuri, A. R., Auffret, H., Priest, E. R., 1993a, Implications of rapid footpoint motions of photospheric flux tubes for coronal heating, *Sol. Phys.*, 143, 49
- Choudhuri, A. R., Dikpati, M., Banerjee, D., 1993b, Energy transport to the solar corona by magnetic kink waves, *ApJ*, 413, 811
- Choudhuri, A. R., 2003, The solar dynamo as a model of the solar cycle, in *Dynamic Sun*, (Ed.) Dwivedi, B. N. and Parker, F. b. E. N. (Cambridge, UK: Cambridge University Press), p. 103
- Cranmer, S. R., van Ballegoijen, A. A., 2005, On the generation, propagation, and reflection of Alfvén waves from the solar photosphere to the distant heliosphere, *ApJS*, 156, 265
- Criscuoli, S., Del Moro, D., Giorgi, F., Romano, P., Berrilli, F., Ermolli, I., Viticchié, B., Zuccarello, F., 2012, Properties of G-band bright points derived from IBIS observations, *Memorie della Societa Astronomica Italiana Supplementi*, 19, 93
- Crocker, J. C., Grier, G., 1996, *Methods of digital video microscopy for colloidal studies*, *J. Colloid Interface Sci.*, 179, 298

- Crockett, P. J., Jess, D. B., Mathioudakis, M., Keenan, F. P., 2009, Automated detection and tracking of solar magnetic bright points, *MNRAS*, 397, 1852
- Crockett, P. J., Mathioudakis, M., Jess, D. B., Shelyag, S., Keenan, F. P., Christian, D. J., 2010, The area distribution of solar magnetic bright points, *ApJ*, 722, L188
- Danilovic, S., Gandorfer, A., Lagg, A., Schüssler, M., Solanki, S. K., Vögler, A., Katsukawa, Y., Tsuneta, S., 2008, The intensity contrast of solar granulation: Comparing Hinode SP results with MHD simulations, *A&A*, 484, L17
- Danilovic, S., Schüssler, M., Solanki, S. K., 2010a, Probing quiet Sun magnetism using MURaM simulations and Hinode/SP results: Support for a local dynamo, *A&A*, 513, A1
- Danilovic, S., Beeck, B., Pietarila, A., Schüssler, M., Solanki, S. K., Martínez Pillet, V., Bonet, J. A., del Toro Iniesta, J. C., Domingo, V., Barthol, P., Berkefeld, T., Gandorfer, A., Knölker, M., Schmidt, W., Title, A. M., 2010b, Transverse component of the magnetic field in the solar photosphere observed by Sunrise, *ApJ*, 723, L149
- Daubechies, I., 1990, The wavelet transform, time-frequency localization and signal analysis, *IEEE Trans. Inf. Theory*, 36, 961
- De Moortel, I., Ireland, J., Hood, A. W., Walsh, R. W., 2002, The detection of 3 and 5 min period oscillations in coronal loops, *A&A*, 387, L13
- De Pontieu, B., Erdélyi, R., James, S. P., 2004, Solar chromospheric spicules from the leakage of photospheric oscillations and flows, *Nature*, 430, 536
- De Pontieu, B., McIntosh, S. W., Carlsson, M., Hansteen, V. H., Tarbell, T. D., Schrijver, C. J., Title, A. M., Shine, R. A., Tsuneta, S., Katsukawa, Y., Ichimoto, K., Suematsu, Y., Shimizu, T., Nagata, S., 2007, Chromospheric Alfvénic waves strong enough to power the solar wind, *Science*, 318, 1574
- De Rosa, M. L., Toomre, J., 2004, Evolution of solar supergranulation, *ApJ*, 616, 1242
- de Wijn, A. G., Rutten, R. J., Haverkamp, E. M. W. P., Sütterlin, P., 2005, DOT tomography of the solar atmosphere. IV. Magnetic patches in internetwork areas, *A&A*, 441, 1183
- de Wijn, A. G., Lites, B. W., Berger, T. E., Frank, Z. A., Tarbell, T. D., Ishikawa, R., 2008, Hinode observations of magnetic elements in internetwork areas, *ApJ*, 684, 1469
- de Wijn, A. G., Stenflo, J. O., Solanki, S. K., Tsuneta, S., 2009, Small-scale solar magnetic fields, *Space Sci. Rev.*, 144, 275
- de Wijn, A. G., 2012, Measuring solar magnetism, *Science*, 338, 476
- DeForest, C. E., 2004, High-frequency waves detected in the solar atmosphere, *ApJ*, 617, L89
- Defouw, R. J., 1976, Wave propagation along a magnetic tube, *ApJ*, 209, 266

- Deinzer, W., Hensler, G., Schüssler, M., Weisshaar, E., 1984a, Model calculations of magnetic flux tubes. I. Equations and method, *A&A*, 139, 426
- Deinzer, W., Hensler, G., Schüssler, M., Weisshaar, E., 1984b, Model calculations of magnetic flux tubes. II. Stationary results for solar magnetic elements, *A&A*, 139, 435
- Del Moro, D., Giordano, S., Berrilli, F., 2007, 3D photospheric velocity field of a supergranular cell, *A&A*, 472, 599
- del Toro Iniesta, J. C., Ruiz Cobo, B., 1996, Stokes profiles inversion techniques, *Sol. Phys.*, 164, 169
- del Toro Iniesta, J. C., 2003, *Introduction to spectropolarimetry* (Cambridge, UK: Cambridge University Press)
- Deubner, F.-L., Gough, D., 1984, Helioseismology: Oscillations as a diagnostic of the solar interior, *ARA&A*, 22, 593
- Dorotovic, I., Erdélyi, R., Freij, N., Karlovsky, V., Marquez, I., 2013, On standing sausage waves in photospheric magnetic waveguides, arXiv:1210.6476
- Dunn, R. B., Zirker, J. B., 1973, The solar filigree, *Sol. Phys.*, 33, 281
- Duvall, Jr., T. L., Birch, A. C., 2010, The vertical component of the supergranular motion, *ApJ*, 725, L47
- Dybiec, B., Gudowska-Nowak, E., 2009, Discriminating between normal and anomalous random walks, *Phys. Rev. E*, 80, 061 122
- Eddy, J. A., 1976, The Maunder minimum, *Science*, 192, 1189
- Edwin, P. M., Roberts, B., 1982, Wave propagation in a magnetically structured atmosphere. III. The slab in a magnetic environment, *Sol. Phys.*, 76, 239
- Edwin, P. M., Roberts, B., 1983, Wave propagation in a magnetic cylinder, *Sol. Phys.*, 88, 179
- Eibe, M. T., Aulanier, G., Faurobert, M., Mein, P., Malherbe, J. M., 2002, Vertical structure of sunspots from THEMIS observations, *A&A*, 381, 290
- Einstein, A., 1905, Über die von der molekularkinetischen Theorie der Wärme geforderte Bewegung von in ruhenden Flüssigkeiten suspendierten Teilchen, *Ann. Phys.*, 322, 549
- Erdélyi, R., 2004, Coronal heating: Heating in the solar atmosphere, *Astronomy and Geophysics*, 45, 34
- Erdélyi, R., 2006, Magnetic seismology of the lower solar atmosphere, in *Proceedings of SOHO 18/GONG 2006/HELAS I, Beyond the spherical Sun*, vol. 624 of ESA Special Pub. (Sheffield: ESA SP), p. 15
- Erdélyi, R., Malins, C., Tóth, G., de Pontieu, B., 2007, Leakage of photospheric acoustic waves into non-magnetic solar atmosphere, *A&A*, 467, 1299

- Fan, Y., 2009, Magnetic fields in the solar convection zone, *Living Rev. Solar Phys.*, 6, 4, URL: <http://www.livingreviews.org/lrsp-2009-4>
- Farge, M., 1992, Wavelet transforms and their applications to turbulence, *Ann. Rev. Fluid Mech.*, 24, 395
- Ferriz-Mas, A., Schüssler, M., 1989, Radial expansion of the magnetohydrodynamic equations for axially symmetric configurations, *Geophys. Astrophys. Fluid Dynamics*, 48, 217
- Fick, A., 1855, Concerns diffusion and concentration gradient, *Ann. Phys. Lpz.*, 170, 59
- Finsterle, W., Jefferies, S. M., Cacciani, A., Rapex, P., 2004, Acoustic waves reveal the magnetic topology of the solar atmosphere, in *SOHO 14 Helio- and Asteroseismology: Towards a Golden Future*, (Ed.) Danesy, D., vol. 559 of ESA Special Pub. (New Haven: ESA SP), p. 223
- Fontenla, J. M., Avrett, E. H., Loeser, R., 1993, Energy balance in the solar transition region. III. Helium emission in hydrostatic, constant-abundance models with diffusion, *ApJ*, 406, 319
- Fontenla, J. M., Avrett, E., Thuillier, G., Harder, J., 2006, Semiempirical models of the solar atmosphere. I. The quiet- and active Sun photosphere at moderate resolution, *ApJ*, 639, 441
- Fontenla, J. M., Curdt, W., Haberreiter, M., Harder, J., Tian, H., 2009, Semiempirical models of the solar atmosphere. III. Set of non-LTE models for far-ultraviolet/extreme-ultraviolet irradiance computation, *ApJ*, 707, 482
- Frutiger, C., Solanki, S. K., Fligge, M., Bruls, J. H. M. J., 2000, Properties of the solar granulation obtained from the inversion of low spatial resolution spectra, *A&A*, 358, 1109
- Galsgaard, K., Nordlund, Å., 1996, Heating and activity of the solar corona. I. Boundary shearing of an initially homogeneous magnetic field, *J. Geophys. Res.*, 101, 13 445
- Gandorfer, A., Grauf, B., Barthol, P., Riethmüller, T. L., Solanki, S. K., Chares, B., Deutsch, W., Ebert, S., Feller, A., Germerott, D., Heerlein, K., Heinrichs, J., Hirche, D., Hirzberger, J., Kolleck, M., Meller, R., Müller, R., Schäfer, R., Tomasch, G., Knölker, M., Martínez Pillet, V., Bonet, J. A., Schmidt, W., Berkefeld, T., Feger, B., Heidecke, F., Soltau, D., Tischenberg, A., Fischer, A., Title, A., Anwand, H., Schmidt, E., 2011, The filter imager SuFI and the Image Stabilization and Light Distribution system ISLiD of the Sunrise balloon-borne observatory: Instrument description, *Sol. Phys.*, 268, 35
- Gingerich, O., Noyes, R. W., Kalkofen, W., Cuny, Y., 1971, The Harvard-Smithsonian reference atmosphere, *Sol. Phys.*, 18, 347
- Gizon, L., Duvall, T. L., Schou, J., 2003, Wave-like properties of solar supergranulation, *Nature*, 421, 43

- Goldreich, P., Kumar, P., 1990, Wave generation by turbulent convection, *ApJ*, 363, 694
- Gonsalves, R. A., Chidlaw, R., 1979, Wavefront sensing by phase retrieval, in *Applications of Digital Image Processing III*, (Ed.) A. G. Tescher, vol. 207 of SPIE Conf. Ser., p. 32
- Grigor'eva, S. A., Turova, I. P., Teplitskaia, R. B., 1991, Contribution and response functions for Ca II lines in different atmospheric models, *Sol. Phys.*, 135, 1
- Grinsted, A., Moore, J. C., Jevrejeva, S., 2004, Application of the cross wavelet transform and wavelet coherence to geophysical time series, *Nonlinear Process. Geophys.*, 11, 561
- Grossmann-Doerth, U., Larsson, B., Solanki, S. K., 1988, Contribution and response functions for Stokes line profiles formed in a magnetic field, *A&A*, 204, 266
- Grubbs, F., 1969, Procedures for detecting outlying observations in samples, *Technometrics*, 11, 1
- Gudiksen, B. V., Nordlund, Å., 2002, Bulk heating and slender magnetic loops in the solar corona, *ApJ*, 572, L113
- Gudiksen, B. V., Nordlund, Å., 2005a, An ab initio approach to the solar coronal heating problem, *ApJ*, 618, 1020
- Gudiksen, B. V., Nordlund, Å., 2005b, An ab initio approach to solar coronal loops, *ApJ*, 618, 1031
- Guglielmino, S. L., Martínez Pillet, V., Bonet, J. A., del Toro Iniesta, J. C., Bellot Rubio, L. R., Solanki, S. K., Schmidt, W., Gandorfer, A., Barthol, P., Knölker, M., 2012, The frontier between small-scale bipoles and ephemeral regions in the solar photosphere: Emergence and decay of an intermediate-scale bipole observed with Sunrise/IMaX, *ApJ*, 745, 160
- Gurtovenko, E. A., Sheminova, V. A., Sarychev, A. P., 1991, What is the difference between 'emission' and 'depression' contribution functions?, *Sol. Phys.*, 136, 239
- Hagenaar, H. J., Schrijver, C. J., Title, A. M., Shine, R. A., 1999, Dispersal of magnetic flux in the quiet solar photosphere, *ApJ*, 511, 932
- Hale, G. E., 1908, On the probable existence of a magnetic field in sun-spots, *ApJ*, 28, 315
- Hanle, W., 1924, Über magnetische Beeinflussung der Polarisation der Resonanzfluoreszenz, *Z. Phys.*, 30, 93
- Hansen, S. C., Cally, P. S., 2009, An exact test of generalised ray theory in local helioseismology, *Sol. Phys.*, 255, 193
- Hansteen, V. H., Leer, E., 1995, Coronal heating, densities, and temperatures and solar wind acceleration, *J. Geophys. Res.*, 100, 21 577

- Harvey, J. W., 2012, Chromospheric magnetic field measurements in a flare and an active region filament, *Sol. Phys.*, 280, 69
- Hasan, S. S., Sobouti, Y., 1987, Mode classification and wave propagation in a magnetically structured medium, *MNRAS*, 228, 427
- Hasan, S. S., Kalkofen, W., 1999, Excitation of oscillations in photospheric flux tubes through buffeting by external granules, *ApJ*, 519, 899
- Hasan, S. S., Kalkofen, W., van Ballegoijen, A. A., 2000, Excitation of oscillations in the magnetic network on the Sun, *ApJ*, 535, L67
- Hasan, S. S., Kalkofen, W., van Ballegoijen, A. A., Ulmschneider, P., 2003, Kink and longitudinal oscillations in the magnetic network on the Sun: Nonlinear effects and mode transformation, *ApJ*, 585, 1138
- Hasan, S. S., van Ballegoijen, A. A., Kalkofen, W., Steiner, O., 2005, Dynamics of the solar magnetic network: Two-dimensional MHD simulations, *ApJ*, 631, 1270
- Hasan, S. S., van Ballegoijen, A. A., 2008, Dynamics of the solar magnetic network. II. Heating the magnetized chromosphere, *ApJ*, 680, 1542
- Hathaway, D. H., Beck, J. G., Bogart, R. S., Bachmann, K. T., Khatri, G., Petitto, J. M., Han, S., Raymond, J., 2000, The photospheric convection spectrum, *Sol. Phys.*, 193, 299
- Hathaway, D. H., Beck, J. G., Han, S., Raymond, J., 2002, Radial flows in supergranules, *Sol. Phys.*, 205, 25
- Hathaway, D. H., 2010, The solar cycle, *Living Rev. Solar Phys.*, 7, 1. URL: <http://www.livingreviews.org/lrsp-2010-1>
- He, J., Marsch, E., Tu, C., Tian, H., 2009, Excitation of kink waves due to small-scale magnetic reconnection in the chromosphere?, *ApJ*, 705, L217
- Herschel, W., 1801, Observations tending to investigate the nature of the Sun, in order to find the causes or symptoms of its variable emission of light and heat; with remarks on the use that may possibly be drawn from solar observations, *Philos. Trans. R. Soc. London*, 91, 265
- Hirzberger, J., Vazquez, M., Bonet, J. A., Hanslmeier, A., Sobotka, M., 1997, Time series of solar granulation images. I. Differences between small and large granules in quiet regions, *ApJ*, 480, 406
- Hirzberger, J., Bonet, J. A., Vázquez, M., Hanslmeier, A., 1999, Time series of solar granulation images. II. Evolution of individual granules, *ApJ*, 515, 441
- Hirzberger, J., Feller, A., Riethmüller, T. L., Schüssler, M., Borrero, J. M., Afram, N., Unruh, Y. C., Berdyugina, S. V., Gandorfer, A., Solanki, S. K., Barthol, P., Bonet, J. A., Martínez Pillet, V., Berkefeld, T., Knölker, M., Schmidt, W., Title, A. M., 2010, Quiet-Sun intensity contrasts in the near-ultraviolet as measured from Sunrise, *ApJ*, 723, L154

- Hirzberger, J., Feller, A., Riethmüller, T. L., Gandorfer, A., Solanki, S. K., 2011, Performance validation of phase diversity image reconstruction techniques, *A&A*, 529, A132
- Hoekzema, N. M., Rimmele, T. R., Rutten, R. J., 2002, Small-scale topology of solar atmospheric dynamics. V. Acoustic events and internetwork grains, *A&A*, 390, 681
- Hofmann, J., Steffens, S., Deubner, F., 1996, K-grains as a three-dimensional phenomenon. II. Phase analysis of the spatio-temporal pattern, *A&A*, 308, 192
- Högbom, J. A., 1974, Aperture synthesis with a non-regular distribution of interferometer baselines, *A&AS*, 15, 417
- Hollweg, J. V., 1990, Heating of the solar corona, *Computer Phys. Rep.*, 12, 205
- Hunter, G. L., Edmond, K. V., Elsesser, M. T., Weeks, E. R., 2011, Tracking rotational diffusion of colloidal clusters, *Optics Express*, 19, 17 189
- Hunter, G. L., Weeks, E. R., 2012, The physics of the colloidal glass transition, *Rep. Prog. in Phys.*, 75, 066 501
- Ishikawa, R., Tsuneta, S., Ichimoto, K., Isobe, H., Katsukawa, Y., Lites, B. W., Nagata, S., Shimizu, T., Shine, R. A., Suematsu, Y., Tarbell, T. D., Title, A. M., 2008, Transient horizontal magnetic fields in solar plage regions, *A&A*, 481, L25
- Ishikawa, R., Tsuneta, S., 2009, Comparison of transient horizontal magnetic fields in a plage region and in the quiet Sun, *A&A*, 495, 607
- Ishikawa, R., Tsuneta, S., 2011, The relationship between vertical and horizontal magnetic fields in the quiet Sun, *ApJ*, 735, 74
- Jafarzadeh, S., Solanki, S. K., Feller, A., Lagg, A., Pietarila, A., Danilovic, S., Riethmüller, T. L., Martínez Pillet, V., 2013a, Structure and dynamics of isolated internetwork Ca II H bright points observed by Sunrise, *A&A*, 549, A116
- Jafarzadeh, S., Solanki, S. K., Lagg, A., Bellot Rubio, L. R., van Noort, M., Feller, A., Martínez-Pillet, V., Danilovic, S., Gandorfer, A., 2013b, Do inversions provide the correct inclinations of small quiet-Sun magnetic features?, Chapter 5 of this thesis
- Jenkins, M. C., Egelhaaf, S. U., 2008, Confocal microscopy of colloidal particles: Towards reliable, optimum coordinates, *Adv. Colloid Interface Sci.*, 136, 65
- Jess, D. B., Andić, A., Mathioudakis, M., Bloomfield, D. S., Keenan, F. P., 2007, High-frequency oscillations in a solar active region observed with the RAPID DUAL IMAGER, *A&A*, 473, 943
- Jess, D. B., Mathioudakis, M., Erdélyi, R., Crockett, P. J., Keenan, F. P., Christian, D. J., 2009, Alfvén waves in the lower solar atmosphere, *Science*, 323, 1582
- Jess, D. B., Shelyag, S., Mathioudakis, M., Keys, P. H., Christian, D. J., Keenan, F. P., 2012, Propagating wave phenomena detected in observations and simulations of the lower solar atmosphere, *ApJ*, 746, 183

- Jokipii, J. R., Parker, E. N., 1968, Random walk of magnetic lines of force in astrophysics, *Phys. Rev. Lett.*, 21, 44
- Kalkofen, W., 1997, Oscillations in chromospheric network bright points, *ApJ*, 486, L145
- Kalkofen, W., Hasan, S. S., Ulmschneider, P., 2003, The dynamics of the quiet solar chromosphere, p. 165
- Kato, Y., Steiner, O., Steffen, M., Suematsu, Y., 2011, Excitation of slow modes in network magnetic elements through magnetic pumping, *ApJ*, 730, L24
- Keller, C. U., 1992, Resolution of magnetic flux tubes on the Sun, *Nature*, 359, 307
- Keys, P. H., Mathioudakis, M., Jess, D. B., Shelyag, S., Crockett, P. J., Christian, D. J., Keenan, F. P., 2011, The velocity distribution of solar photospheric magnetic bright points, *ApJ*, 740, L40
- Khokhlova, V. L., 1959, A spectrophotometric investigation of the H and K Ca⁺ lines in the chromosphere and solar faculae, *Soviet Ast.*, 3, 59
- Khomenko, E. V., Collados, M., Solanki, S. K., Lagg, A., Trujillo Bueno, J., 2003, Quiet-Sun inter-network magnetic fields observed in the infrared, *A&A*, 408, 1115
- Khomenko, E. V., Martínez González, M. J., Collados, M., Vögler, A., Solanki, S. K., Ruiz Cobo, B., Beck, C., 2005, Magnetic flux in the internetwork quiet Sun, *A&A*, 436, L27
- Khomenko, E., Collados, M., Felipe, T., 2008, Nonlinear numerical simulations of magneto-acoustic wave propagation in small-scale flux tubes, *Sol. Phys.*, 251, 589
- Khomenko, E., Calvo Santamaria, I., 2013, Magnetohydrodynamic waves driven by p-modes, *arXiv:1302.4351*
- Kiselman, D., Rutten, R. J., Plez, B., 2001, The formation of G-band bright points. I. Standard LTE modelling, in *Recent Insights into the Physics of the Sun and Heliosphere: Highlights from SOHO and Other Space Missions*, (Ed.) Brekke, P. and Fleck, B. and Gurman, J. B., vol. 203 of IAU Symp. (San Francisco: ASP), p. 287
- Klimchuk, J. A., 2006, On solving the coronal heating problem, *Sol. Phys.*, 234, 41
- Kneer, F., von Uexkull, M., 1993, Oscillations of the Sun's chromosphere. VI. K grains, resonances, and gravity waves, *A&A*, 274, 584
- Kucera, A., Balthasar, H., Rybak, J., Woehl, H., 1998, Heights of formation of FeI photospheric lines, *A&A*, 332, 1069
- Lagg, A., Woch, J., Krupp, N., Solanki, S. K., 2004, Retrieval of the full magnetic vector with the He I multiplet at 1083 nm. Maps of an emerging flux region, *A&A*, 414, 1109

- Lagg, A., Solanki, S. K., Riethmüller, T. L., Martínez Pillet, V., Schüssler, M., Hirzberger, J., Feller, A., Borrero, J. M., Schmidt, W., del Toro Iniesta, J. C., Bonet, J. A., Barthol, P., Berkefeld, T., Domingo, V., Gandorfer, A., Knölker, M., Title, A. M., 2010, Fully resolved quiet-Sun magnetic flux tube observed with the Sunrise/IMaX instrument, *ApJ*, 723, L164
- Landi Degl’Innocenti, E., Landi Degl’Innocenti, M., 1977, Response functions for magnetic lines, *A&A*, 56, 111
- Lawrence, J. K., Schrijver, C. J., 1993, Anomalous diffusion of magnetic elements across the solar surface, *ApJ*, 411, 402
- Lawrence, J. K., Cadavid, A. C., Ruzmaikin, A., Berger, T. E., 2001, Spatiotemporal scaling of solar surface flows, *Phys. Rev. Lett.*, 86, 5894
- Lawrence, J. K., Cadavid, A. C., Christian, D. J., Jess, D. B., Mathioudakis, M., 2011, Rapid fluctuations in the lower solar atmosphere, *ApJ*, 743, L24
- Lawrence, J. K., Cadavid, A. C., 2012, Observed effect of magnetic fields on the propagation of magnetoacoustic waves in the lower solar atmosphere, *Sol. Phys.*, 280, 125
- Leenaarts, J., Wedemeyer-Böhm, S., 2005, DOT tomography of the solar atmosphere. III. Observations and simulations of reversed granulation, *A&A*, 431, 687
- Leenaarts, J., Rutten, R. J., Sütterlin, P., Carlsson, M., Uitenbroek, H., 2006, DOT tomography of the solar atmosphere. VI. Magnetic elements as bright points in the blue wing of $H\alpha$, *A&A*, 449, 1209
- Leenaarts, J., Carlsson, M., Hansteen, V., Gudiksen, B. V., 2011, On the minimum temperature of the quiet solar chromosphere, *A&A*, 530, A124
- Leenaarts, J., Carlsson, M., Rouppe van der Voort, L., 2012, The formation of the $H\alpha$ line in the solar chromosphere, *ApJ*, 749, 136
- Leighton, R. B., Noyes, R. W., Simon, G. W., 1962, Velocity fields in the solar atmosphere. I. Preliminary report, *ApJ*, 135, 474
- Leighton, R. B., 1964, Transport of magnetic fields on the Sun, *ApJ*, 140, 1547
- Leitzinger, M., Brandt, P. N., Hanslmeier, A., Pötzi, W., Hirzberger, J., 2005, Dynamics of solar mesogranulation, *A&A*, 444, 245
- Lemons, D. S., Gythiel, A., 1997, Paul Langevin’s 1908 paper “On the theory of brownian motion”, *Am. J. Phys.*, 65, 1079
- Lepreti, F., Carbone, V., Abramenko, V. I., Yurchyshyn, V., Goode, P. R., Capparelli, V., Vecchio, A., 2012, Turbulent pair dispersion of photospheric bright points, *ApJ*, 759, L17
- Lighthill, M. J., 1952, On sound generated aerodynamically. I. General theory, *Proc. R. Soc. Lond. A*, 211, 564

- Lin, H., 1995, On the distribution of the solar magnetic fields, *ApJ*, 446, 421
- Lin, H., Penn, M. J., Tomczyk, S., 2000, A new precise measurement of the coronal magnetic field strength, *ApJ*, 541, L83
- Lin, H., Kuhn, J. R., Coulter, R., 2004, Coronal magnetic field measurements, *ApJ*, 613, L177
- Lites, B. W., Rutten, R. J., Kalkofen, W., 1993, Dynamics of the solar chromosphere. I. Long-period network oscillations, *ApJ*, 414, 345
- Lites, B. W., Leka, K. D., Skumanich, A., Martínez Pillet, V., Shimizu, T., 1996, Small-scale horizontal magnetic fields in the solar photosphere, *ApJ*, 460, 1019
- Lites, B. W., Kubo, M., Socas-Navarro, H., Berger, T., Frank, Z., Shine, R., Tarbell, T., Title, A., Ichimoto, K., Katsukawa, Y., Tsuneta, S., Suematsu, Y., Shimizu, T., Nagata, S., 2008, The horizontal magnetic flux of the quiet-Sun internetwork as observed with the Hinode Spectro-Polarimeter, *ApJ*, 672, 1237
- Livingston, W., Harvey, J., 1971, The Kitt Peak magnetograph. IV. 40-channel probe and the detection of weak photospheric fields, in *Solar Magnetic Fields*, (Ed.) Howard, R., vol. 43 of IAU Symp. (Dordrecht: Reidel), p. 51
- Livingston, W. C., Harvey, J., 1975, A new component of solar magnetism - The inner network fields, *BAAS*, 7, 346
- Lockwood, M., Stamper, R., Wild, M. N., 1999, A doubling of the Sun's coronal magnetic field during the past 100 years, *Nature*, 399, 437
- Löfdahl, M. G., Scharmer, G. B., 1994, Wavefront sensing and image restoration from focused and defocused solar images, *A&AS*, 107, 243
- Löfdahl, M. G., Berger, T. E., Shine, R. S., Title, A. M., 1998, Preparation of a dual wavelength sequence of high-resolution solar photospheric images using phase diversity, *ApJ*, 495, 965
- Magain, P., 1986, Contribution functions and the depths of formation of spectral lines, *A&A*, 163, 135
- Manso Sainz, R., Martínez González, M. J., Asensio Ramos, A., 2011, Advection and dispersal of small magnetic elements in the very quiet Sun, *A&A*, 531, L9
- Martínez González, M. J., Collados, M., Ruiz Cobo, B., Solanki, S. K., 2007, Low-lying magnetic loops in the solar internetwork, *A&A*, 469, L39
- Martínez González, M. J., Bellot Rubio, L. R., 2009, Emergence of small-scale magnetic loops through the quiet solar atmosphere, *ApJ*, 700, 1391
- Martínez González, M. J., Bellot Rubio, L. R., Solanki, S. K., Martínez Pillet, V., Del Toro Iniesta, J. C., Barthol, P., Schmidt, W., 2012, Resolving the internal magnetic structure of the solar network, *ApJ*, 758, L40

- Martínez Pillet, V., Lites, B. W., Skumanich, A., 1997, Active region magnetic fields. I. Plage fields, *ApJ*, 474, 810
- Martínez Pillet, V., Del Toro Iniesta, J. C., Álvarez-Herrero, A., Domingo, V., Bonet, J. A., González Fernández, L., López Jiménez, A., Pastor, C., Gasent Blesa, J. L., Mellado, P., Piqueras, J., Aparicio, B., Balaguer, M., Ballesteros, E., Belenguer, T., Bellot Rubio, L. R., Berkefeld, T., Collados, M., Deutsch, W., Feller, A., Girela, F., Grauf, B., Heredero, R. L., Herranz, M., Jerónimo, J. M., Laguna, H., Meller, R., Menéndez, M., Morales, R., Orozco Suárez, D., Ramos, G., Reina, M., Ramos, J. L., Rodríguez, P., Sánchez, A., Uribe-Patarroyo, N., Barthol, P., Gandorfer, A., Knölker, M., Schmidt, W., Solanki, S. K., Vargas Domínguez, S., 2011, The Imaging Magnetograph eXperiment (IMaX) for the Sunrise balloon-borne solar observatory, *Sol. Phys.*, 268, 57
- Mathew, S. K., Martínez Pillet, V., Solanki, S. K., Krivova, N. A., 2007, Properties of sunspots in cycle 23. I. Dependence of brightness on sunspot size and cycle phase, *A&A*, 465, 291
- Mathew, S. K., Zakharov, V., Solanki, S. K., 2009, Stray light correction and contrast analysis of Hinode broad-band images, *A&A*, 501, L19
- Mathioudakis, M., Jess, D. B., Erdélyi, R., 2012, Alfvén waves in the solar atmosphere, *Space Sci. Rev.*, p. 94
- McIntosh, S. W., Smillie, D. G., 2004, Characteristic scales of chromospheric oscillation wave packets, *ApJ*, 604, 924
- McIntosh, S. W., De Pontieu, B., Carlsson, M., Hansteen, V., Boerner, P., Goossens, M., 2011, Alfvénic waves with sufficient energy to power the quiet solar corona and fast solar wind, *Nature*, 475, 477
- Mehlretter, J. P., 1974, Observations of photospheric faculae at the center of the solar disk, *Sol. Phys.*, 38, 43
- Metcalf, T. R., Leka, K. D., Barnes, G., Lites, B. W., Georgoulis, M. K., Pevtsov, A. A., Balasubramaniam, K. S., Gary, G. A., Jing, J., Li, J., Liu, Y., Wang, H. N., Abramenko, V., Yurchyshyn, V., Moon, Y.-J., 2006, An overview of existing algorithms for resolving the 180 degree ambiguity in vector magnetic fields: Quantitative tests with synthetic data, *Sol. Phys.*, 237, 267
- Mihalas, D., 1978, *Stellar atmospheres* (San Francisco: W. H. Freeman and Co.)
- Mihalas, B. W., Toomre, J., 1981, Internal gravity waves in the solar atmosphere. I. Adiabatic waves in the chromosphere, *ApJ*, 249, 349
- Mihalas, B. W., Toomre, J., 1982, Internal gravity waves in the solar atmosphere. II. Effects of radiative damping, *ApJ*, 263, 386
- Milano, L. J., Gomez, D. O., Martens, P. C. H., 1997, Solar coronal heating: AC versus DC, *ApJ*, 490, 442

- Monin, A. S., Iaglom, A. M., 1975, *Statistical fluid mechanics: Mechanics of turbulence* (Cambridge, MA: MIT Press), vol. 2
- Moreno-Insertis, F., 1986, Nonlinear time-evolution of kink-unstable magnetic flux tubes in the convective zone of the Sun, *A&A*, 166, 291
- Morton, R. J., Erdélyi, R., Jess, D. B., Mathioudakis, M., 2011, Observations of sausage modes in magnetic pores, *ApJ*, 729, L18
- Morton, R. J., Verth, G., Jess, D. B., Kuridze, D., Ruderman, M. S., Mathioudakis, M., Erdélyi, R., 2012, Observations of ubiquitous compressive waves in the Sun's chromosphere, *Nat. Commun.*, 3
- Möstl, C., Hanslmeier, A., Sobotka, M., Puschmann, K., Muthsam, H. J., 2006, Dynamics of magnetic bright points in an active region, *Sol. Phys.*, 237, 13
- Muller, R., 1983, The dynamical behavior of facular points in the quiet photosphere, *Sol. Phys.*, 85, 113
- Muller, R., Roudier, T., Vigneau, J., Auffret, H., 1994, The proper motion of network bright points and the heating of the solar corona, *A&A*, 283, 232
- Muller, R., Dollfus, A., Montagne, M., Moity, J., Vigneau, J., 2000, Spatial and temporal relations between magnetic elements and bright points in the photospheric network, *A&A*, 359, 373
- Nagata, S., Tsuneta, S., Suematsu, Y., Ichimoto, K., Katsukawa, Y., Shimizu, T., Yokoyama, T., Tarbell, T. D., Lites, B. W., Shine, R. A., Berger, T. E., Title, A. M., Bellot Rubio, L. R., Orozco Suárez, D., 2008, Formation of solar magnetic flux tubes with kG field strength induced by convective instability, *ApJ*, 677, L145
- Nakariakov, V. M., Verwichte, E., 2005, Coronal waves and oscillations, *Living Rev. Solar Phys.*, 2, 3. URL: <http://www.livingreviews.org/lrsp-2005-3>
- Narain, U., Ulmschneider, P., 1990, Chromospheric and coronal heating mechanisms, *Space Sci. Rev.*, 54, 377
- Narain, U., Ulmschneider, P., 1996, Chromospheric and coronal heating mechanisms II, *Space Sci. Rev.*, 75, 453
- Narayanan, A. S., 2013, *An introduction to waves and oscillations in the Sun* (New York: Springer)
- Nelson, G. D., 1978, A two-dimensional solar model, *Sol. Phys.*, 60, 5
- Nisenson, P., van Ballegooijen, A. A., de Wijn, A. G., Sütterlin, P., 2003, Motions of isolated G-band bright points in the solar photosphere, *ApJ*, 587, 458
- Nordlund, Å., 1984, Modelling of small-scale dynamical processes: Convection and wave generation, in *Small-Scale Dynamical Processes in Quiet Stellar Atmospheres*, (Ed. Keil, S. L. (Sunspot, NM: National Solar Obs.)), p. 181

- Nordlund, Å., 1985, Solar convection, *Sol. Phys.*, 100, 209
- Nordlund, Å., 2003, Solar photosphere and convection, in *Dynamic Sun*, (Ed.) Dwivedi, B. N. and Parker, F. b. E. N. (Cambridge, UK: Cambridge University Press), p. 148
- Nordlund, Å., Stein, R. F., Asplund, M., 2009, Solar surface convection, *Living Rev. Solar Phys.*, 6, 2. URL: <http://www.livingreviews.org/lrsp-2009-2>
- November, L. J., Toomre, J., Gebbie, K. B., Simon, G. W., 1981, The detection of meso-granulation on the Sun, *ApJ*, 245, L123
- Nutto, C., Steiner, O., Schaffenberger, W., Roth, M., 2012, Modification of wave propagation and wave travel-time by the presence of magnetic fields in the solar network atmosphere, *A&A*, 538, A79
- Ogurtsov, M. G., Nagovitsyn, Y. A., Kocharov, G. E., Jungner, H., 2002, Long-period cycles of the Sun's activity recorded in direct solar data and proxies, *Sol. Phys.*, 211, 371
- Okamoto, T. J., De Pontieu, B., 2011, Propagating waves along spicules, *ApJ*, 736, L24
- Orozco Suárez, D., Bellot Rubio, L. R., del Toro Iniesta, J. C., Tsuneta, S., Lites, B. W., Ichimoto, K., Katsukawa, Y., Nagata, S., Shimizu, T., Shine, R. A., Suematsu, Y., Tarbell, T. D., Title, A. M., 2007, Quiet-Sun internetwork magnetic fields from the inversion of Hinode measurements, *ApJ*, 670, L61
- Orozco Suárez, D., Bellot Rubio, L. R., Vögler, A., del Toro Iniesta, J. C., 2010, Applicability of Milne-Eddington inversions to high spatial resolution observations of the quiet Sun, *A&A*, 518, A2
- Orozco Suárez, D., Katsukawa, Y., 2012, On the distribution of quiet-Sun magnetic fields at different heliocentric angles, *ApJ*, 746, 182
- Orozco Suárez, D., Bellot Rubio, L. R., 2012, Analysis of quiet-Sun internetwork magnetic fields based on linear polarization signals, *ApJ*, 749
- Orozco Suárez, D., Katsukawa, Y., Bellot Rubio, L. R., 2012, The connection between internetwork magnetic elements and supergranular flows, *ApJ*, 758, L38
- Parker, E. N., 1972, Topological dissipation and the small-scale fields in turbulent gases, *ApJ*, 174, 499
- Parker, E. N., 1983, Magnetic neutral sheets in evolving fields. II. Formation of the solar corona, *ApJ*, 264, 642
- Parker, E. N., 1988, Nanoflares and the solar X-ray corona, *ApJ*, 330, 474
- Paxman, R. G., Schulz, T. J., Fienup, J. R., 1992, Joint estimation of object and aberrations by using phase diversity, *J. Opt. Soc. Am. A*, 9, 1072
- Peter, H., Gudiksen, B. V., Nordlund, Å., 2004, Coronal heating through braiding of magnetic field lines, *ApJ*, 617, L85

- Pietarila, A., Aznar Cuadrado, R., Hirzberger, J., Solanki, S. K., 2011, Kink waves in an active region dynamic fibril, *ApJ*, 739, 92
- Pietarila Graham, J., Danilovic, S., Schüssler, M., 2009, Turbulent magnetic fields in the quiet Sun: Implications of Hinode observations and small-scale dynamo simulations, *ApJ*, 693, 1728
- Pneuman, G. W., Solanki, S. K., Stenflo, J. O., 1986, Structure and merging of solar magnetic fluxtubes, *A&A*, 154, 231
- Pommois, P., Veltri, P., Zimbaro, G., 1999, Anomalous and Gaussian transport regimes in anisotropic three-dimensional magnetic turbulence, *Phys. Rev. E*, 59, 2244
- Press, W. H., Teukolsky, S. A., Vetterling, W. T., Flannery, B. P., 2007, *Numerical recipes: The art of scientific computing* (Cambridge, UK: Cambridge University Press)
- Priest, E., Forbes, T., 2000, *Magnetic reconnection : MHD theory and applications* (New York : Cambridge University Press)
- Rachkovsky, D. N., 1962, *Izv. Krymsk. Astrofiz. Obs.*, 28, 259
- Rappazzo, A. F., Velli, M., Einaudi, G., Dahlburg, R. B., 2008, Nonlinear dynamics of the Parker scenario for coronal heating, *ApJ*, 677, 1348
- Rast, M. P., 2003, Supergranulation: New observation, possible explanation, in *GONG+ 2002. Local and Global Helioseismology: the Present and Future*, (Ed.) Sawaya-Lacoste, H., vol. 517 of *ESA Special Pub.* (Noordwijk: ESA Publications Division), p. 163
- Reale, F., 2010, Coronal loops: Observations and modeling of confined plasma, *Living Rev. Solar Phys.*, 7, 5. URL: <http://www.livingreviews.org/lrsp-2010-5>
- Reeves, E. M., Timothy, J. G., Huber, M. C. E., 1977, Extreme UV spectroheliometer on the Apollo Telescope Mount, *Appl. Opt.*, 16, 837
- Ribeiro, H. V., Lenzi, E. K., Mendes, R. S., Santoro, P. A., 2011, Anomalous diffusion in a symbolic model, *Phys. Scr*, 83, 045 007
- Riethmüller, T. L., Solanki, S. K., Martínez Pillet, V., Hirzberger, J., Feller, A., Bonet, J. A., Bello González, N., Franz, M., Schüssler, M., Barthol, P., Berkefeld, T., del Toro Iniesta, J. C., Domingo, V., Gandorfer, A., Knölker, M., Schmidt, W., 2010, Bright points in the quiet Sun as observed in the visible and near-UV by the balloon-borne observatory Sunrise, *ApJ*, 723, L169
- Riethmüller, T. L., 2013, Investigations of small-scale magnetic features on the solar surface, Ph.D. thesis, Braunschweig University of Technology, Germany
- Riethmüller, T. L., Solanki, S. K., Berdyugina, S. V., Schüssler, M., Martínez Pillet, V., Hirzberger, J., Feller, A., Barthol, P., Gandorfer, A., Knölker, M., Schmidt, W., 2013, Comparison of solar photospheric bright points between Sunrise observations and MHD simulations, in preparation

- Rieutord, M., Rincon, F., 2010, The Sun's supergranulation, *Living Rev. Solar Phys.*, 7, 2.
URL: <http://www.livingreviews.org/lrsp-2010-2>
- Roberts, B., Ulmschneider, P., 1997, Dynamics of flux tubes in the solar atmosphere: Theory, in *European Meeting on Solar Physics*, (Ed.) Simnett, G. M. and Alissandrakis, C. E. and Vlahos, L., vol. 489 of *Lecture Notes in Phys.* (Berlin: Springer-Verlag), p. 75
- Roberts, B., 2000, Waves and oscillations in the corona, *Sol. Phys.*, 193, 139
- Roberts, B., 2004, MHD waves in the solar atmosphere, in *SOHO 13 Waves, Oscillations and Small-Scale Transients Events in the Solar Atmosphere: Joint View from SOHO and TRACE*, (Ed.) Lacoste, H., vol. 547 of *ESA Special Pub.* (Paris: ESA), p. 1
- Roberts, B., 2006, Slow magnetohydrodynamic waves in the solar atmosphere, *Philos. Trans. R. Soc. London A*, 364, 447
- Rosenthal, C. S., Bogdan, T. J., Carlsson, M., Dorch, S. B. F., Hansteen, V., McIntosh, S. W., McMurry, A., Nordlund, Å., Stein, R. F., 2002, Waves in the magnetized solar atmosphere. I. Basic processes and internetwork oscillations, *ApJ*, 564, 508
- Roudier, T., Muller, R., 1986, Structure of the solar granulation, *Sol. Phys.*, 107, 11
- Roudier, T., Rieutord, M., Brito, D., Rincon, F., Malherbe, J. M., Meunier, N., Berger, T., Frank, Z., 2009, Mesoscale dynamics on the Sun's surface from Hinode observations, *A&A*, 495, 945
- Ruiz Cobo, B., del Toro Iniesta, J. C., 1992, Inversion of Stokes profiles, *ApJ*, 398, 375
- Ruiz Cobo, B., del Toro Iniesta, J. C., 1994, On the sensitivity of Stokes profiles to physical quantities, *A&A*, 283, 129
- Rutten, R. J., 1990, Sun-as-a-star line formation, in *Cool Stars, Stellar Systems, and the Sun*, (Ed.) Wallerstein, G., vol. 9 of *ASP Conf. Ser.* (San Francisco: ASP), p. 91
- Rutten, R. J., Uitenbroek, H., 1991, Ca II H_{2V} and K_{2V} cell grains, *Sol. Phys.*, 134, 15
- Rutten, R. J., Kiselman, D., Rouppe van der Voort, L., Plez, B., 2001, Proxy magnetometry of the photosphere: Why are G-band bright points so bright?, in *Advanced Solar Polarimetry - Theory, Observation, and Instrumentation*, (Ed.) Sigwarth, M., vol. 236 of *ASP Conf. Ser.* (San Francisco: ASP), p. 445
- Rutten, R. J., de Wijn, A. G., Sütterlin, P., 2004, DOT tomography of the solar atmosphere. II. Reversed granulation in Ca II H, *A&A*, 416, 333
- Rutten, R. J., van Veelen, B., Sütterlin, P., 2008, DOT tomography of the solar atmosphere. VII. Chromospheric response to acoustic events, *Sol. Phys.*, 251, 533
- Rybicki, G. B., Hummer, D. G., 1991, An accelerated lambda iteration method for multilevel radiative transfer. I. Non-overlapping lines with background continuum, *A&A*, 245, 171

- Rybicki, G. B., Hummer, D. G., 1992, An accelerated lambda iteration method for multilevel radiative transfer. II. Overlapping transitions with full continuum, *A&A*, 262, 209
- Sánchez Almeida, J., 2003, Quiet Sun magnetic fields, in *Solar Wind Ten*, (Ed.) Velli, M. and Bruno, R. and Malara, F. and Bucci, B., vol. 679 of *AIP Conf. Proc.* (New York: AIP), p. 293
- Sánchez Almeida, J., 2004, The magnetism of the very quiet Sun, in *The Solar-B Mission and the Forefront of Solar Physics*, (Ed.) Sakurai, T. and Sekii, T., vol. 325 of *ASP Conf. Ser.* (San Francisco: ASP), p. 115
- Sánchez Almeida, J., Asensio Ramos, A., Trujillo Bueno, J., Cernicharo, J., 2001, G-band spectral synthesis in solar magnetic concentrations, *ApJ*, 555, 978
- Sánchez Almeida, J., Márquez, I., Bonet, J. A., Domínguez Cerdeña, I., Muller, R., 2004, Bright points in the internetwork quiet Sun, *ApJ*, 609, L91
- Sánchez Almeida, J., Bonet, J. A., Viticchié, B., Del Moro, D., 2010, Magnetic bright points in the quiet Sun, *ApJ*, 715, L26
- Sánchez Almeida, J., Martínez González, M., 2011, The magnetic fields of the quiet Sun, in *Solar Polarization 6*, (Ed.) Kuhn, J. R. and Harrington, D. M. and Lin, H. et al., vol. 437 of *ASP Conf. Ser.* (San Francisco: ASP), p. 451
- Sánchez Cuberes, M., Bonet, J. A., Vázquez, M., Wittmann, A. D., 2000, Center-to-limb variation of solar granulation from partial eclipse observations, *ApJ*, 538, 940
- Scharmer, G. B., Bjelksjo, K., Korhonen, T. K., Lindberg, B., Petterson, B., 2003, The 1-meter Swedish Solar Telescope, in *Society of Photo-Optical Instrumentation Engineers (SPIE) Conference Series*, (Eds.) S. L. Keil, S. V. Avakyan, vol. 4853 of *SPIE Conf. Ser.*, p. 341
- Schou, J., 2003, Wavelike properties of solar supergranulation detected in Doppler shift data, *ApJ*, 596, L259
- Schrijver, C. J., 1989, The effect of an interaction of magnetic flux and supergranulation on the decay of magnetic plages, *Sol. Phys.*, 122, 193
- Schrijver, C. J., Shine, R. A., Hagenaar, H. J., Hurlburt, N. E., Title, A. M., Strous, L. H., Jefferies, S. M., Jones, A. R., Harvey, J. W., Duvall, Jr., T. L., 1996, Dynamics of the chromospheric network: Mobility, dispersal, and diffusion coefficients, *ApJ*, 468, 921
- Schrijver, C. J., Hagenaar, H. J., Title, A. M., 1997, On the patterns of the solar granulation and supergranulation, *ApJ*, 475, 328
- Schrijver, C. J., Zwaan, C., 2000, *Solar and stellar magnetic activity* (New York: Cambridge University Press)
- Schunker, H., Cally, P. S., 2006, Magnetic field inclination and atmospheric oscillations above solar active regions, *MNRAS*, 372, 551

- Schüssler, M., 1986, MHD models of solar photospheric magnetic flux concentrations, in *Small Scale Magnetic Flux Concentrations in the Solar Photosphere*, (Ed.) Deinzer, W. and Knölker, M. and Voigt, H. H. (Göttingen: Vandenhoeck and Ruprecht), p. 103
- Schüssler, M., 1990, Theoretical aspects of small-scale photospheric magnetic fields, in *Solar Photosphere: Structure, Convection, and Magnetic Fields*, (Ed.) Stenflo, J. O., vol. 138 of IAU Symp. (Dordrecht: Kluwer), p. 161
- Schüssler, M., Caligari, P., Ferriz-Mas, A., Moreno-Insertis, F., 1994, Instability and eruption of magnetic flux tubes in the solar convection zone, *A&A*, 281, L69
- Schüssler, M., Shelyag, S., Berdyugina, S., Vögler, A., Solanki, S. K., 2003, Why solar magnetic flux concentrations are bright in molecular bands, *ApJ*, 597, L173
- Schüssler, M., Vögler, A., 2008, Strong horizontal photospheric magnetic field in a surface dynamo simulation, *A&A*, 481, L5
- Sheeley, N. R., 1967, Observations of small-scale solar magnetic fields, *Sol. Phys.*, 1, 171
- Shelyag, S., Schüssler, M., Solanki, S. K., Berdyugina, S. V., Vögler, A., 2004, G-band spectral synthesis and diagnostics of simulated solar magneto-convection, *A&A*, 427, 335
- Shelyag, S., Schüssler, M., Solanki, S. K., Vögler, A., 2007, Stokes diagnostics of simulated solar magneto-convection, *A&A*, 469, 731
- Shibata, K., 1983, Nonlinear MHD wave propagation in the solar chromosphere. I. The case of a uniform vertical magnetic field, *PASJ*, 35, 263
- Shimizu, T., Katsukawa, Y., Matsuzaki, K., Ichimoto, K., Kano, R., Deluca, E. E., Lundquist, L. L., Weber, M., Tarbell, T. D., Shine, R. A., Sôma, M., Tsuneta, S., Sakao, T., Minesugi, K., 2007, Hinode calibration for precise image co-alignment between SOT and XRT (2006 November-2007 April), *PASJ*, 59, 845
- Shine, R. A., Simon, G. W., Hurlburt, N. E., 2000, Supergranule and mesogranule evolution, *Sol. Phys.*, 193, 313
- Simon, G. W., Leighton, R. B., 1964, Velocity fields in the solar atmosphere. III. Large-scale motions, the chromospheric network, and magnetic fields, *ApJ*, 140, 1120
- Simon, G. W., Title, A. M., Weiss, N. O., 1995, Kinematic models of supergranular diffusion on the Sun, *ApJ*, 442, 886
- Sivaraman, K. R., Livingston, W. C., 1982, Ca II K_{2V} spectral features and their relation to small-scale photospheric magnetic fields, *Sol. Phys.*, 80, 227
- Skumanich, A., Lites, B. W., 1987, Stokes profile analysis and vector magnetic fields. I. Inversion of photospheric lines, *ApJ*, 322, 473
- Skumanich, A., Smythe, C., Frazier, E. N., 1975, On the statistical description of inhomogeneities in the quiet solar atmosphere. I. Linear regression analysis and absolute calibration of multichannel observations of the Ca⁺ emission network, *ApJ*, 200, 747

- Solanki, S. K., 1986, Velocities in solar magnetic fluxtubes, *A&A*, 168, 311
- Solanki, S. K., 1987, The photospheric layers of solar magnetic flux tubes, Ph.D. thesis, ETH Zürich, Switzerland
- Solanki, S. K., Steiner, O., Uitenbroeck, H., 1991, Two-dimensional models of the solar chromosphere. I. The Ca II K line as a diagnostic: 1.5-D radiative transfer, *A&A*, 250, 220
- Solanki, S. K., 1993, Small-scale solar magnetic fields - An overview, *Space Sci. Rev.*, 63, 1
- Solanki, S. K., Bruls, J. H. M. J., 1994, New contribution functions for Zeeman split spectral lines, *A&A*, 286, 269
- Solanki, S. K., Rueedi, I., Bianda, M., Steffen, M., 1996a, On the detection of shocks in the solar granulation, *A&A*, 308, 623
- Solanki, S. K., Zufferey, D., Lin, H., Rüedi, I., Kuhn, J. R., 1996b, Infrared lines as probes of solar magnetic features. XII. Magnetic flux tubes: evidence of convective collapse?, *A&A*, 310, L33
- Solanki, S. K., 1998, Structure of the solar photosphere, *Space Sci. Rev.*, 85, 175
- Solanki, S. K., Finsterle, W., Rüedi, I., Livingston, W., 1999, Expansion of solar magnetic flux tubes large and small, *A&A*, 347, L27
- Solanki, S. K., Schüssler, M., Fligge, M., 2000, Evolution of the Sun's large-scale magnetic field since the Maunder minimum, *Nature*, 408, 445
- Solanki, S. K., 2001, Small-scale photospheric structure of the solar magnetic fields outside sunspots, in *Magnetic Fields Across the Hertzsprung-Russell Diagram*, (Ed.) Mathys, G. and Solanki, S. K. and Wickramasinghe, D. T., vol. 248 of ASP Conf. Ser. (San Francisco: ASP), p. 45
- Solanki, S. K., Hammer, R., 2002, The solar atmosphere, in *The Century of Space Science, Vol. I*, (Ed.) Bleeker, J. A. and Geiss, J. and Huber, M. C. E. (Dordrecht: Springer - Kluwer), p. 1065
- Solanki, S. K., Lagg, A., Woch, J., Krupp, N., Collados, M., 2003, Three-dimensional magnetic field topology in a region of solar coronal heating, *Nature*, 425, 692
- Solanki, S. K., 2004, Structure of the solar chromosphere, in *Multi-Wavelength Investigations of Solar Activity*, (Ed.) Stepanov, A. V. and Benevolenskaya, E. E. and Kosovichev, A. G., vol. 223 of IAU Symp. (Cambridge, UK: Cambridge University Press), p. 195
- Solanki, S. K., Schüssler, M., 2004, Small-scale solar magnetic elements: Simulations and observations, in *The Solar-B Mission and the Forefront of Solar Physics*, (Ed.) Sakurai, T. and Sekii, T., vol. 325 of ASP Conf. Ser. (San Francisco: ASP), p. 105

- Solanki, S. K., Inhester, B., Schüssler, M., 2006, The solar magnetic field, *Rep. Prog. in Phys.*, 69, 563
- Solanki, S. K., 2009, Photospheric magnetic field: Quiet Sun, in *Solar Polarization 5: In Honor of Jan Stenflo*, (Ed.) Berdyugina, S. V. and Nagendra, K. N. and Ramelli, R., vol. 405 of *ASP Conf. Ser.* (San Francisco: ASP), p. 135
- Solanki, S. K., Barthol, P., Danilovic, S., Feller, A., Gandorfer, A., Hirzberger, J., Riethmüller, T. L., Schüssler, M., Bonet, J. A., Martínez Pillet, V., del Toro Iniesta, J. C., Domingo, V., Palacios, J., Knölker, M., Bello González, N., Berkefeld, T., Franz, M., Schmidt, W., Title, A. M., 2010, Sunrise: Instrument, mission, data, and first results, *ApJ*, 723, L127
- Solanki, S. K., Krivova, N. A., 2011, Analyzing solar cycles, *Science*, 334, 916
- Solanki, S. K., Barthol, P., Danilovic, S., Feller, A., Gandorfer, A., Hirzberger, J., Jafarzadeh, S., Lagg, A., Riethmüller, T. L., Schüssler, M., Wiegelmann, T., Bonet, J. A., González, M. J. M., Pillet, V. M., Khomenko, E., Yelles Chaouche, L., Iniesta, J. C. d. T., Domingo, V., Palacios, J., Knölker, M., González, N. B., Borrero, J. M., Berkefeld, T., Franz, M., Roth, M., Schmidt, W., Steiner, O., Title, A. M., 2012, First results from the Sunrise mission, in *4th Hinode Science Meeting: Unsolved Problems and Recent Insights*, (Ed.) Bellot Rubio, L. and Reale, F. and Carlsson, M., vol. 455 of *ASP Conf. Ser.* (San Francisco: ASP), p. 143
- Soltau, D., 1993, On intensity, magnetic field and velocities of small bright points in the Ca+ network, in *IAU Colloq. 141: The Magnetic and Velocity Fields of Solar Active Regions*, (Ed.) Zirin, H. and Ai, G. and Wang, H., vol. 46 of *ASP Conf. Ser.* (San Francisco: ASP), p. 225
- Souffrin, P., 1972, Radiative relaxation of sound waves in an optically thin isothermal atmosphere, *A&A*, 17, 458
- Spruit, H. C., 1976, Pressure equilibrium and energy balance of small photospheric flux-tubes, *Sol. Phys.*, 50, 269
- Spruit, H. C., 1977, Magnetic flux tubes and transport of heat in the convection zone of the Sun, Ph.D. thesis, University of Utrecht, The Netherlands
- Spruit, H. C., 1981a, Motion of magnetic flux tubes in the solar convection zone and chromosphere, *A&A*, 98, 155
- Spruit, H. C., 1981b, Magnetic flux tubes, *NASA Special Pub.*, 450, 385
- Spruit, H. C., 1982, Propagation speeds and acoustic damping of waves in magnetic flux tubes, *Sol. Phys.*, 75, 3
- Spruit, H. C., Nordlund, A., Title, A. M., 1990, Solar convection, *ARA&A*, 28, 263
- Stangalini, M., Del Moro, D., Berrilli, F., Jefferies, S. M., 2011, MHD wave transmission in the Sun's atmosphere, *A&A*, 534, A65

- Stangalini, M., Solanki, S. K., Cameron, R., Martínez Pillet, V., 2013, First evidence of interaction between longitudinal and transverse waves in solar magnetic elements, *A&A*, in press (arXiv:1304.7088)
- Steffens, S., Hofmann, J., Deubner, F. L., 1996, K-grains as a three-dimensional phenomenon. I. Statistics and spatial evolution, *A&A*, 307, 288
- Stein, R. F., 1967, Generation of acoustic and gravity waves by turbulence in an isothermal stratified atmosphere, *Sol. Phys.*, 2, 385
- Steiner, O., Hauschildt, P. H., Bruls, J., 2001, Radiative properties of magnetic elements. I. Why are G-band bright points bright?, *A&A*, 372, L13
- Stenflo, J. O., 1971, The interpretation of magnetograph results: The formation of absorption lines in a magnetic field, in *Solar Magnetic Fields*, (Ed.) R. Howard, vol. 43 of IAU Symp. (Dordrecht: Reidel), p. 101
- Stenflo, J. O., 1973, Magnetic-field structure of the photospheric network, *Sol. Phys.*, 32, 41
- Stenflo, J. O., 1975, A model of the supergranulation network and of active-region plages, *Sol. Phys.*, 42, 79
- Stenflo, J. O., 1989, Small-scale magnetic structures on the Sun, *A&A Rev.*, 1, 3
- Stenflo, J. O., 2010, Distribution functions for magnetic fields on the quiet Sun, *A&A*, 517, A37
- Stenflo, J. O., 2012, Basal magnetic flux and the local solar dynamo, *A&A*, 547, A93
- Stix, M., 2002, *The Sun: An introduction* (Berlin : Springer)
- Stodilka, M. I., 2008, On the detection of internal gravity waves in the solar photosphere, *MNRAS*, 390, L83
- Straus, T., Deubner, F.-L., Fleck, B., 1992, Is mesogranulation a distinct regime of convection?, *A&A*, 256, 652
- Straus, T., Fleck, B., Jefferies, S. M., Cauzzi, G., McIntosh, S. W., Reardon, K., Severino, G., Steffen, M., 2008, The energy flux of internal gravity waves in the lower solar atmosphere, *ApJ*, 681, L125
- Taroyan, Y., Erdélyi, R., 2009, Heating diagnostics with MHD waves, *Space Sci. Rev.*, 149, 229
- Thomas, J. H., 1985, in *Theoretical problems in high resolution solar physics*, (Ed.) Schmidt, H. U. (Munich: Max Planck Inst. Astrophys.)
- Title, A. M., Tarbell, T. D., Topka, K. P., Ferguson, S. H., Shine, R. A., SOUP Team, 1989, Statistical properties of solar granulation derived from the SOUP instrument on Spacelab 2, *ApJ*, 336, 475

- Title, A. M., Berger, T. E., 1996, Double-Gaussian models of bright points or why bright points are usually dark, *ApJ*, 463, 797
- Tomczyk, S., Card, G. L., Darnell, T., Elmore, D. F., Casini, R., Judge, P. G., Burkepile, J., 2004, Initial magnetic field measurements from the coronal multi-channel polarimeter, *BAAS*, 36, 686
- Torrence, C., Compo, G. P., 1998, A practical guide to wavelet analysis, *BAMS*, 79, 61
- Trujillo Bueno, J., 2001, Atomic polarization and the Hanle effect, in *Advanced Solar Polarimetry – Theory, Observation, and Instrumentation*, (Ed.) Sigwarth, M., vol. 236 of ASP Conf. Ser. (San Francisco: ASP), p. 161
- Trujillo Bueno, J., Shchukina, N., Asensio Ramos, A., 2004, A substantial amount of hidden magnetic energy in the quiet Sun, *Nature*, 430, 326
- Tsuneta, S., Ichimoto, K., Katsukawa, Y., Nagata, S., Otsubo, M., Shimizu, T., Suematsu, Y., Nakagiri, M., Noguchi, M., Tarbell, T., Title, A., Shine, R., Rosenberg, W., Hoffmann, C., Jurcevich, B., Kushner, G., Levay, M., Lites, B., Elmore, D., Matsushita, T., Kawaguchi, N., Saito, H., Mikami, I., Hill, L. D., Owens, J. K., 2008, The Solar Optical Telescope for the Hinode mission: An overview, *Sol. Phys.*, 249, 167
- Uitenbroek, H., Briand, C., 1995, The MG λ 285.21 nanometer line: An example of non-LTE line formation, *ApJ*, 447, 453
- Uitenbroek, H., 2001, Multilevel radiative transfer with partial frequency redistribution, *ApJ*, 557, 389
- Uitenbroek, H., 2003, The accuracy of the center-of-gravity method for measuring velocity and magnetic field strength in the solar photosphere, *ApJ*, 592, 1225
- Ulmschneider, P., 1970, On frequency and strength of shock waves in the solar atmosphere, *Sol. Phys.*, 12, 403
- Ulmschneider, P., 1971, On the propagation of a spectrum of acoustic waves in the solar atmosphere, *A&A*, 14, 275
- Ulmschneider, P., Zaehring, K., Musielak, Z. E., 1991, Propagation of nonlinear longitudinal-transverse waves along magnetic flux tubes in the solar atmosphere. I. Adiabatic waves, *A&A*, 241, 625
- Ulmschneider, P., Kalkofen, W., 2003, Heating of the solar chromosphere, in *Dynamic Sun*, (Ed.) Dwivedi, B. N. (Cambridge, UK: Cambridge University Press), p. 181
- Ulmschneider, P., Musielak, Z., 2003, Mechanisms of chromospheric and coronal heating, in *Current Theoretical Models and Future High Resolution Solar Observations: Preparing for ATST*, (Ed.) Pevtsov, A. A. and Uitenbroek, H., vol. 286 of ASP Conf. Ser. (San Francisco: ASP), p. 363
- Ulmschneider, P., Rammacher, W., Musielak, Z. E., Kalkofen, W., 2005, On the validity of acoustically heated chromosphere models, *ApJ*, 631, L155

- Unno, W., 1956, Line formation of a normal Zeeman triplet, *PASJ*, 8, 108
- Usoskin, I. G., Kovaltsov, G. A., 2004, Long-term solar activity: Direct and indirect study, *Sol. Phys.*, 224, 37
- Usoskin, I. G., 2013, A history of solar activity over Millennia, *Living Rev. Solar Phys.*, 10, 1. URL: <http://www.livingreviews.org/lrsp-2013-1>
- Utz, D., Hanslmeier, A., Muller, R., Veronig, A., Rybák, J., Muthsam, H., 2010, Dynamics of isolated magnetic bright points derived from Hinode/SOT G-band observations, *A&A*, 511, A39
- van Ballegooijen, A. A., Nisenson, P., Noyes, R. W., Löfdahl, M. G., Stein, R. F., Nordlund, Å., Krishnakumar, V., 1998, Dynamics of magnetic flux elements in the solar photosphere, *ApJ*, 509, 435
- van Ballegooijen, A. A., Asgari-Targhi, M., Cranmer, S. R., DeLuca, E. E., 2011, Heating of the solar chromosphere and corona by Alfvén wave turbulence, *ApJ*, 736, 3
- van Noort, M., 2012, Spatially coupled inversion of spectro-polarimetric image data. I. Method and first results, *A&A*, 548, A5
- van Noort, M., Lagg, A., Tiwari, S. K., Solanki, S. K., 2013, Peripheral downflows in sunspot penumbrae, submitted to *A&A*
- Vernazza, J. E., Avrett, E. H., Loeser, R., 1981, Structure of the solar chromosphere. III. Models of the EUV brightness components of the quiet-Sun, *ApJS*, 45, 635
- Vigeesh, G., Hasan, S. S., Steiner, O., 2009, Wave propagation and energy transport in the magnetic network of the Sun, *A&A*, 508, 951
- Vigeesh, G., Fedun, V., Hasan, S. S., Erdélyi, R., 2012, Three-dimensional simulations of magneto-hydrodynamic waves in magnetized solar atmosphere, *ApJ*, 755, 18
- Vitas, N., Fischer, C. E., Vögler, A., Keller, C. U., 2011, Fast horizontal flows in a quiet Sun MHD simulation and their spectroscopic signatures, *A&A*, 532, A110
- Vögler, A., Shelyag, S., Schüssler, M., Cattaneo, F., Emonet, T., Linde, T., 2005, Simulations of magneto-convection in the solar photosphere. Equations, methods, and results of the MURaM code, *A&A*, 429, 335
- Vögler, A., Schüssler, M., 2007, A solar surface dynamo, *A&A*, 465, L43
- Wall, J. V., Jenkins, C. R., 2003, *Practical statistics for astronomers* (Cambridge, UK: Cambridge University Press)
- Wang, H., 1997, Distribution of 2-D magnetic saddle points and morphology of flare kernels in solar active regions, *Sol. Phys.*, 174, 265
- Wang, H., Yan, Y., Sakurai, T., 2001, Topology of magnetic field and coronal heating in solar active regions, *Sol. Phys.*, 201, 323

- Wang, J., Wang, H., Tang, F., Lee, J. W., Zirin, H., 1995a, Flux distribution of solar intranetwork magnetic fields, *Sol. Phys.*, 160, 277
- Wang, T. J., Solanki, S. K., Curdt, W., Innes, D. E., Dammasch, I. E., Kliem, B., 2003, Hot coronal loop oscillations observed with SUMER: Examples and statistics, *A&A*, 406, 1105
- Wang, Z., Ulrich, R. K., Coroniti, F. V., 1995b, Acoustic wave propagation in the solar atmosphere I. Rediscussion of the linearized theory including nonstationary solutions, *ApJ*, 444, 879
- Wedemeyer-Böhm, S., Rouppe van der Voort, L., 2009, On the continuum intensity distribution of the solar photosphere, *A&A*, 503, 225
- Weeks, E. R., Crocker, J. C., Levitt, A. C., Schofield, A., Weitz, D. A., 2000, Three-dimensional direct imaging of structural relaxation near the colloidal glass transition, *Science*, 287, 627
- Wellstein, S., Kneer, F., von Uexkuell, M., 1998, Oscillations of the Sun's chromosphere. VIII. Horizontal motions of Ca II K bright points, *A&A*, 335, 323
- White, S. M., 2002, New radio instrumentation for the study of sunspots and starspots, *Astronomische Nachrichten*, 323, 265
- Wiegelmann, T., Lagg, A., Solanki, S. K., Inhester, B., Woch, J., 2005, Comparing magnetic field extrapolations with measurements of magnetic loops, *A&A*, 433, 701
- Wiegelmann, T., Sakurai, T., 2012, Solar force-free magnetic fields, *Living Rev. Solar Phys.*, 9, 5. URL: <http://www.livingreviews.org/lrsp-2012-5>
- Withbroe, G. L., Noyes, R. W., 1977, Mass and energy flow in the solar chromosphere and corona, *ARA&A*, 15, 363
- Wittmann, A., 1974, Computation and observation of Zeeman multiplet polarization in Fraunhofer lines. II. Computation of Stokes parameter profiles, *Sol. Phys.*, 35, 11
- Yelles Chaouche, L., Solanki, S. K., Schüssler, M., 2009, Comparison of the thin flux tube approximation with 3D MHD simulations, *A&A*, 504, 595
- Zeeman, P., 1897, The effect of magnetisation on the nature of light emitted by a substance, *Nature*, 55, 347
- Zhang, J., White, S. M., Kundu, M. R., 1998, The height structure of the solar atmosphere from the extreme-ultraviolet perspective, *ApJ*, 504, L127
- Zhugzhda, Y. D., Bromm, V., Ulmschneider, P., 1995, Propagation of nonlinear longitudinal-transverse waves along magnetic flux tubes in the solar atmosphere. II. The treatment of shocks., *A&A*, 300, 302
- Zimbaro, G., Veltri, P., Pommois, P., 2000, Anomalous, quasilinear, and percolative regimes for magnetic-field-line transport in axially symmetric turbulence, *Phys. Rev. E*, 61, 1940

Bibliography

- Zirin, H., 1985, Evolution of weak solar magnetic fields, *Aust. J. Phys.*, 38, 961
- Zirin, H., 1993, The interaction of weak and strong magnetic fields on the Sun, in IAU Colloq. 141: The Magnetic and Velocity Fields of Solar Active Regions, (Ed.) Zirin, H. and Ai, G. and Wang, H., vol. 46 of ASP Conf. Ser. (San Francisco: ASP), p. 215
- Zwaan, C., 1987, Elements and patterns in the solar magnetic field, *ARA&A*, 25, 83

Acknowledgements

First and foremost, I wish to express my deeply-felt gratitude to my supervisor, Prof. Sami K. Solanki, whose truly motivations, inspiring advices, warm encouragements and thoughtful guidance throughout my PhD research have enabled me not to only process the present work, but also to develop my knowledge in the field. I am also extremely grateful to him for correcting my manuscripts, from which, I have been learning scientific writing. In addition, I wish to express my sincere appreciation to him for trusting me to work independently while he has been always providing guidance, with his unsurpassed knowledge in the field, at key moments during the research.

I am also indebted to the other members of my thesis committee, Prof. Dr. Stefan Dreizler and Dr. Alex Feller, for their encouragement and insightful comments.

I have been sincerely privileged to get to know and to work with many colleagues within the SUNRISE science team and the MPS SLAM group, to only some of whom it is possible to give particular mention here. My extremely gratitude is extended to Dr. A. Lagg, Dr. M. van Noort, Dr. A. Pietarila, Dr. R. H. Cameron, Dr. A. Feller and Dr. M. Stangalini whose advices, useful discussions and comments have been invaluable on the progress of the present work. Also to Dr. S. Danilovic, Dr. J. Hirzberger, Dr. V. Martínez Pillet, Dr. L. R. Bellot Rubio, Dr. A. Gandorfer, T. L. Riethmüller and Dr. G. Narayan who have, in some way, contributed to the work.

In addition, I want to express my gratitude to my office-mate and good friend David Bühler, not only for making my lunch and free times enjoyable, but also for fascinating scientific discussions. My appreciation also goes to the other office-mate of mine, Jayant Joshi, all other PhD and postdoc researchers at the MPS as well as the staff members of the institute for providing a friendly environment and all supports I have needed during my PhD work. The supports from staff members of the Faculty of Physics of the Georg-August-Universität Göttingen, and in particular, of the Institute for Astrophysics could not be forgotten.

Furthermore, thanks are due to Dr. H. Uitenbroek, who provided his RH-code and the model atmospheres, and to A. Grinstead for providing his wavelet codes; that were both used for some parts of the analysis.

I take this opportunity to acknowledge my debt to Dr. Luc Rouppe van der Voort and Prof. Mats Carlsson of University of Oslo for teaching me the first steps in the field. I also developed a part of the image-alignment algorithm I used in this thesis during the time I spent at the Institute for Theoretical Astrophysics at the University of Oslo; supported by a Marie Curie Early Stage Research Training Fellowship of the European Community's Sixth Framework Programme under contract number MEST-CT-2005-020395: The USO-SP International School for Solar Physics.

A special mention goes to Prof. N. Riazi, my B.Sc. advisor at the Shiraz University, and

Prof. L. Lindegren, my M.Sc. supervisor at the Lund University, without whom, I could never be at this point. I have always tried to use my knowledge and experience I learnt from them during my PhD research.

In addition, Prof. Dainis Dravins deserves special recognition in this thesis. His enthusiastic lectures in “Stellar/Solar Atmosphere” during my master’s studies at the Lund University as well as his further supports and encouragements acted as first motivation for starting my scientific carrier in Solar Physics. This motivation was indeed completed with a three-month observing experience at the Swedish Solar Telescope (SST) in La Palma (in 2007), granted by the Institute for Solar Physics under the auspices of the Royal Swedish Academy of Sciences. I would like to thank Prof. G. Scharmer, Dr. D. Kiselman and Dr. M. Löfdahl for providing such a fantastic opportunity not only for gaining observing experience, but also for getting to know many great solar physicists during that period. Such an experience has led me to be involved in the MPS observing campaigns at the SST during the last three years. I am thankful to all my co-observers, student summer interns, and also Dr. P. Sütterlin of the SST, for their supports, enjoyable times and scientific discussions.

The work on this thesis was supported by the Max Planck Institute for Solar System Research and a PhD fellowship of the International Max Planck Research School on Physical Processes in the Solar System and Beyond. In particular, I would like to gratefully acknowledge the coordinator of the school, Dr. Dieter Schmitt, for all his kind helps and supports.

The work consists use of the SUNRISE data. The German contribution to SUNRISE is funded by the Bundesministerium für Wirtschaft und Technologie through the Deutsches Zentrum für Luft- und Raumfahrt e.V. (DLR), Grant No. 50 OU 0401, and by the Innovationsfond of the President of the Max Planck Society (MPG). The Spanish contribution has been funded by the Spanish MICINN under projects ESP2006-13030-C06 and AYA2009-14105-C06 (including European FEDER funds). The HAO contribution was partly funded through NASA grant NNX08AH38G.

Finally, I owe tremendous and deep gratitude to all my family members for their continuous and unconditional supports. To my parents who have always supported and encouraged me to pursue my interests. And last, but certainly not least, to my lovely and supportive wife, Shaghayegh Javadi, for always being there. To her, whose encouragements have been always powerful sources of inspiration and energy.

Shahin Jafarzadeh: Dynamics of magnetic bright points in the lower solar atmosphere

In this dissertation, we have investigated the structure and dynamics of small-scale magnetic bright points (MBPs) in quiet, internetwork regions of the lower solar atmosphere. Such MBPs are associated with small-scale, intense (generally kG) magnetic elements.

We used high spatial and temporal resolution observations, obtained by the SUNRISE balloon-borne solar observatory, to particularly address (1) observational properties of isolated internetwork Ca II H MBPs, (2) migration of Ca II H MBPs in the internetwork areas, (3) propagation of high-frequency fast waves in small magnetic elements in the lower solar atmosphere, and (4) distribution of magnetic field's inclination in small quiet-Sun magnetic features.

The results of these studies have implications for, e.g., our understanding of the heating mechanisms in the higher layers of the solar atmosphere, estimates of the solar magnetic flux as well as the structure of the convection flows (within a supergranule) advecting small magnetic elements.



9 783942 171755